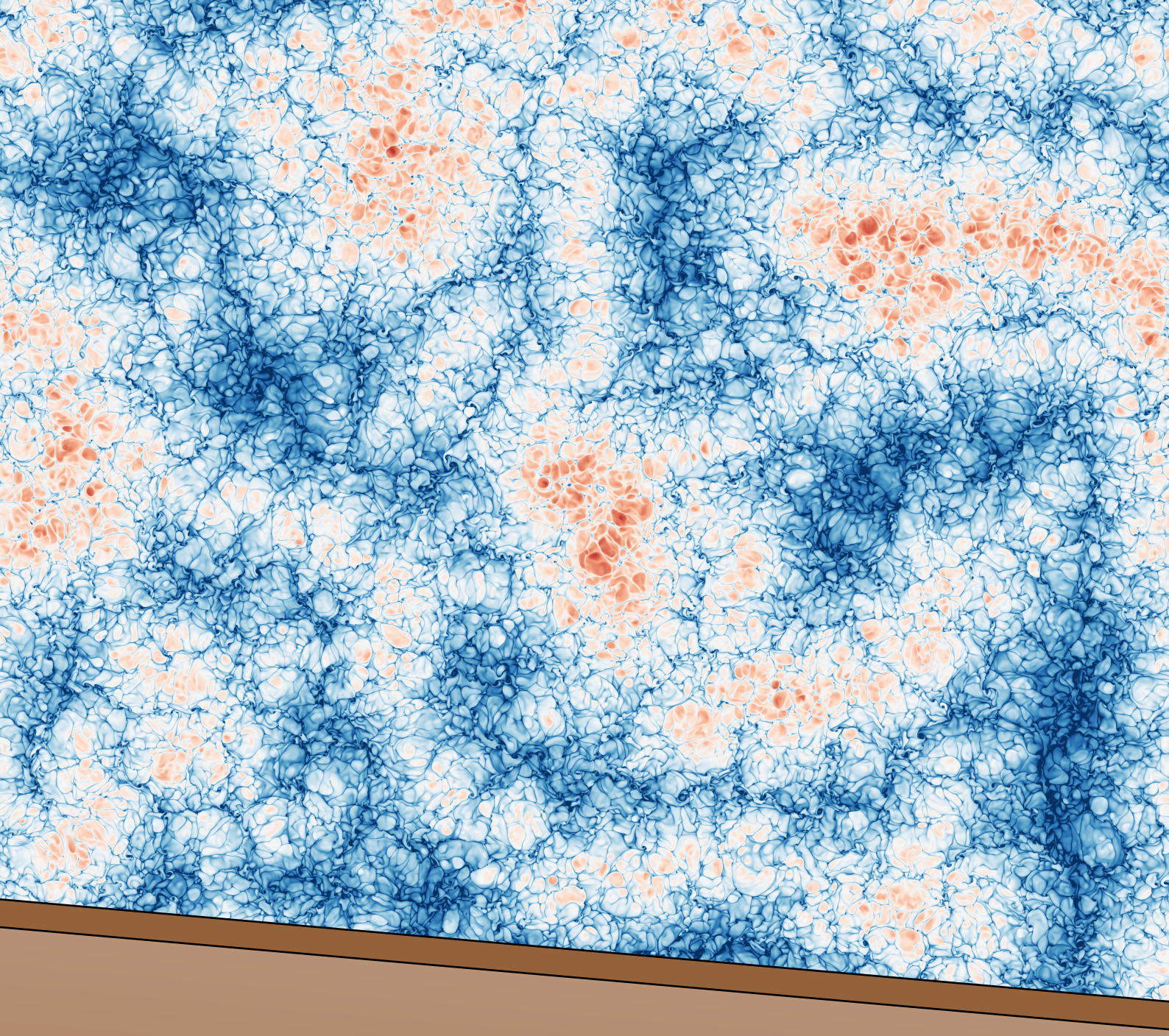

Large-scale flow structures in turbulent Rayleigh-Bénard convection

Dynamical origin, formation, and role in material transport

a PhD thesis by

Philipp Patrick Vieweg

M. Sc. Philipp Patrick Vieweg

Large-scale flow structures in turbulent Rayleigh-Bénard convection: Dynamical origin, formation, and role in material transport

Dissertation
for award of the academic degree **Doktoringenieur (Dr.-Ing.)**

carried out at the
Institute of Thermodynamics and Fluid Mechanics
and submitted at the
Department of Mechanical Engineering
University of Technology Ilmenau.

1st assessor: Prof. Dr. rer. nat. habil. Jörg Schumacher	*Theor. Fluid Mechanics*
2nd assessor: Prof. Dr. rer. nat. Kathrin Padberg-Gehle	*Applied Mathematics*
3rd assessor: Prof. Dr. Janet D. Scheel	*Physics*

Day of submission: 25/01/2023
Day of scientific disputation: 12/07/2023

DOI: 10.22032/dbt.58334
URN: urn:nbn:de:gbv:ilm1-2023000228

Abstract

Thermal convection is the essential mechanism by which heat is transported in many natural flows and reveals often a hierarchy of different flow structures. Any of the present environments may offer its own set of specific boundary conditions, whereas the solar convection zone represents one of the most prominent examples for a natural convection flow that exhibits a distinguished pattern hierarchy. The formation of the latter and the role of its involved flow structures on material transport are important open questions in science.

This thesis at hand (1) expands our understanding of the alteration of large-scale flow structures by different boundary conditions, and (2) investigates the former from a Lagrangian material transport perspective. To this end, Rayleigh-Bénard convection – a paradigm of natural thermal convection – is studied via direct numerical simulations.

The first main result is obtained by an explorative study with respect to idealised mechanical and thermal boundary conditions. It is shown that the latter fundamentally determine the nature of large-scale flow structures, opening an entirely new path for more detailed studies. If the flow is driven by a constant heat flux, the gradual aggregation of smaller convection cells to a domain-filling convection structure – which is in reminiscence to the astrophysical motivation termed supergranule – can be observed for all accessible Rayleigh and Prandtl numbers. It is furthermore shown that weak rotation around the vertical axis is capable of limiting this aggregation process, and the scaling of the resulting pattern size is investigated. The dynamical origin and formation of the supergranules is analysed in the context of instabilities and spectral cascades.

The second main result is obtained by examining the evolution of massless Lagrangian particles in the classical, constant temperature-driven scenario. Unsupervised machine learning is used to identify coherent spatial regions, the latter of which are subsequently related to the large-scale flow patterns and analysed in terms of their heat transport across different working fluids. A new evolutionary clustering method, which overcomes observation window restrictions of previous approaches, is developed. It is part of future work to apply this technique to the gradual supergranule aggregation.

This thesis describes a new mechanism of self-organisation of flows and significantly expands our understanding of large-scale flow structures in thermal convection. Due to the simplicity of the underlying dynamical system, it applies to various natural flows and allows to interpret their extremely complex nature more successfully.

Kurzzusammenfassung

Thermische Konvektion ist der essentielle Mechanismus durch welchen Wärme in vielen natürlichen Strömungen übertragen wird und weist zugleich oftmals eine Hierarchie von verschiedenen Strömungsstrukturen auf. Jedes Umfeld kann dabei über seine eigenen charakteristischen Randbedingungen verfügen, wobei die solare Konvektionszone das wohl bekannteste Beispiel mit ausgeprägter Strukturhierarchie repräsentiert. Die Entstehung Letzterer und die Rolle der involvierten Strömungsmuster bzgl. des materiellen Transports stellen wichtige offene Fragen der Wissenschaft dar.

Die vorliegende Arbeit (1) erweitert unser Verständnis von der Beeinflussung großskaliger Strömungsstrukturen durch verschiedene Randbedingungen und (2) untersucht diese Muster aus der Perspektive materiellen Transports. Zu diesem Zweck wird Rayleigh-Bénard Konvektion – ein Paradigma natürlicher thermischer Konvektion – mittels direkter numerischer Simulationen untersucht.

Das erste wesentliche Ergebnis wird durch eine explorative Studie verschiedener idealisierter mechanischer und thermischer Randbedingungen erreicht. Es wird gezeigt, dass Letztere die Natur der großskaligen Strömungsstrukturen fundamental bestimmen. Wird eine konstante Wärmestromdichte aufgeprägt, so kann eine allmähliche Aggregation kleinerer Konvektionszellen zu einer die gesamte Domäne füllenden Konvektionsstruktur – welche in Analogie zur astrophysikalischen Motivation als Supergranule bezeichnet wird – für alle zugänglichen Rayleigh- und Prandtl-Zahlen beobachtet werden. Es wird zudem gezeigt, dass schwache Rotation um die vertikale Achse imstande ist, den Aggregationsprozess zu beschränken. Der dynamische Ursprung und die Formierung der Supergranulen werden im Kontext von Instabilitäten und spektralen Kaskaden analysiert.

Das zweite wesentliche Ergebnis wird durch die Analyse der Entwicklung von masselosen Lagrange'schen Partikeln im klassischen, durch konstante Temperaturen angetriebenen Szenario erzielt. Unüberwachtes maschinelles Lernen wird dazu benutzt, kohärente Regionen zu identifizieren, welche anschließend mit den großskaligen Strömungsstrukturen in Verbindung gebracht und bzgl. ihres Wärmetransportes in verschiedenen Fluiden analysiert werden. Abschließend wird eine neue evolutionäre Clustering-Methode entwickelt, welche künftig auf die Supergranulenaggregation angewendet werden kann.

Diese Arbeit beschreibt einen neuen Mechanismus der Selbstorganisation von Strömungen und erweitert damit unser Verständnis großskaliger Strömungsstrukturen thermischer Konvektion. Die Einfachheit des untersuchten dynamischen Systems erlaubt eine Übertragung auf verschiedenste natürliche Strömungen sowie deren erfolgreichere Interpretation.

Acknowledgements

Albeit scientific discoveries might be the result of curiosity, diligence and stamina of a single person, their significance is surely promoted by an inspiring and supporting environment. This doctoral thesis would not be the same if I would not have been in such a fortunate situation here among my colleagues at the *Institute of Thermodynamics and Fluid Mechanics* at *University of Technology Ilmenau* (Technische Universität Ilmenau).

First, I gratefully acknowledge financial support by the *German Research Foundation* (Deutsche Forschungsgemeinschaft, DFG) within the *Priority Programme DFG-SPP 1881* on *Turbulent Superstructures*. This funding has put me in the extremely lucky situation to be able to travel (more than once) to international conferences, even on the other side of the Atlantic, and to publish articles in open-access journals – aspects, which definitely promote scientific exchange and thus progress.

This funding gave me further the chance to participate at the *Boulder Summer School for Condensed Matter and Materials Physics 2022* with the perfectly matching topic 'Hydrodynamics Across Scales'. This 4 week event was supported by a grant from the *National Science Foundation* (NSF), with additional funding provided by the *University of Colorado*. My time spent at this summer school was definitely the most vibrant and inspiring time of my entire PhD, which I will surely yearn back for a long time. It was really fun to interact and connect with the many other young scientists. A special thank goes to Leo Radzihovsky as the leading local organiser.

Nowadays' computational technology grants unseen possibilities to humans, but its advantages can only be exploited when having access to it. Almost all simulations reported in this thesis would not have been possible without the millions of CPU-hours of quota on various up-to-date high performance computing resources. I therefore thankfully acknowledge the *Gauss Centre for Supercomuting e.V.* for funding my work by providing computing resources on the GCS supercomputer SuperMUC-NG at Leibnitz Supercomputing Centre within project pn68ni and through the John von Neumann Institute for Computing (NIC) on the GCS supercomputer JUWELS at Jülich Supercomputing Center (JSC) within projects chil12 and mesoc. Additionally, I acknowledge the computing centre of the *University of Technology Ilmenau* for providing access to, as well as computing and storage resources on its compute cluster MaPaCC4. Here in particular, I thank Henning Schwanbeck for his generous technical support and his understanding for my constant need for additional storage.

Nobody needs to reinvent the wheel, and making use of the past work of others was never easier before thanks to all the open-source projects. This thesis has benefited

at many places from such – from the Nek5000 spectral element simulation code to the Python programming language and its many professional libraries like SciPy, NumPy and Matplotlib to the Scientific Python Development Environment Spyder. One can barely sufficiently appreciate the work of all its contributors. I would like to thank at this place my former colleague Sandeep Pandey who introduced me to Python and its world free of license fees.

This entire above-mentioned surrounding academic environment would definitely not have been accessible for me without the work and success of one single person: my supervisor Jörg Schumacher. It is him that acquired the necessary funding, gave me the chance to be part of his team, believed constantly in my strengths, and strongly promoted my theoretical background in fluid mechanics. With his help and mentoring, I dived into topics which I thought are unreachable. Furthermore, I thank Colette Wilhelm for her extensive help with all the bureaucracy.

Last, but not least, I want to thank my girlfriend, family and friends for the necessary diversion in busy and challenging times and their valuable support which began long before the start of my PhD. Ultimately, it might have been them that directed the trajectory of my life into this great environment.

Philipp Patrick Vieweg
January 2023

Contents

Nomenclature

Abbreviations

Acronym	Meaning
BC	boundary condition
DNS	direct numerical simulation
GLL	Gauss-Lobatto-Legendre
GQL	generalised quasilinear
LES	large-eddy simulation
PDF	probability density function
RANS	Reynolds-averaged Navier-Stokes

Non-dimensional numbers

Acronym	Meaning	Defined in or on
CFL	Courant-Friedrich-Lewy number	eq. (2.9)
Ek	Ekman number	p. 32
Nu	Nusselt number	eq. (1.19)
$\mathrm{Nu_L}$	Lagrangian Nusselt number	p. 88
Pr	Prandtl number	eq. (1.9)
Ra	Rayleigh number	eq. (1.10)
Re	Reynolds number	eq. (1.20)
Ro	Rossby number	eq. (1.11)
Sc	Schmidt number	p. 40
St	Stokes number	p. 74
Ta	Taylor number	eq. (3.10)

Selected mathematical notation and symbols

Symbol	Description
$\tilde{\Phi}$	non-dimensional quantity
$\hat{\Phi}$	Fourier coefficient
Φ^T	transpose
Φ^*	complex conjugate

Symbol	Description
$\mathfrak{R}$	real part
$\mathfrak{I}$	imaginary part
$\imath$	imaginary number

Frequently used Latin characters

Symbol	Description
A	horizontal cross-section (area)
c	some constant
c_p	specific heat capacity at constant pressure
d_{cut}	cut-off distance, sparsification parameter
d_{icut}	intermediate cut-off distance
d_{ij}	time-averaged distance between particles i and j
$E_{\Phi_1\Phi_2}$	energy
$\boldsymbol{e}_{x,\,y,\,z}$	unit vectors
f	some function
g	acceleration due to gravity
H	vertical separation of the plates
i, j, k	integer or natural number
$\boldsymbol{K}$	graph kernel matrix
$\boldsymbol{k}$	wave number, coordinate in spectral space with $\boldsymbol{k} = (k_x, k_y, k_z)$ (similarly $\boldsymbol{p}$ and $\boldsymbol{q}$)
k'	threshold wave number
$\boldsymbol{L}$	graph Laplacian rate matrix
L	horizontal extent of the flow domain
m	integer or natural number
N	polynomial order
N_{dof}	total number of degrees of freedom of the discrete dynamical system
N_{e}	total number of spectral elements with $N_{\mathrm{e}} = N_{\mathrm{e},\,x} \times N_{\mathrm{e},\,y} \times N_{\mathrm{e},\,z}$
N_{p}	total number of advected Lagrangian particles
n	integer or natural number
n_{cf}	number of coherent features
n_{ep}	number of evaluated particles
p	pressure
$S_{u,\Theta}$	rate of mode-to-mode energy transfer
T	temperature
t	time
t_{Lr}	total Lagrangian runtime of particle advection (being a fraction of t_{r})
t_{r}	total runtime of the simulation
$\boldsymbol{u}$	velocity with $\boldsymbol{u} = (u_x, u_y, u_z)$
$\boldsymbol{u}_i$	velocity of particle with index i
V	volume
$\boldsymbol{x}$	position, coordinate in physical space with $\boldsymbol{x} = (x, y, z)$
$\boldsymbol{x}_i$	trajectory of particle with index i

Frequently used Greek characters

Symbol	Description
α	volumetric thermal expansion coefficient at constant pressure
β	(negative) applied vertical temperature gradient at the plates
Γ	aspect ratio
ΔT	(average) dimensional temperature difference between the plates
ΔT_{D}	(average) non-dimensional ΔT in the Dirichlet case
ΔT_{N}	average non-dimensional ΔT in the Neumann case
Δt_{ow}	temporal width of the observation window
$\delta\Phi$	perturbation variable
δ_T	thermal boundary layer thickness
ε	kinetic energy dissipation rate
$\varepsilon_{\mathrm{ks}}$	kernel scale
ζ	hard clustering threshold
η	dynamic viscosity
$\eta_{\mathrm{B,\,C,\,K}}$	Batchelor, Corrsin or Kolmogorov scale
Θ	temperature deviation from the linear conduction profile
κ	thermal diffusivity
Λ_T	integral length scale of the temperature field
Λ_{to}	characteristic turnover wavelength
λ	wavelength
λ_{t}	thermal conductivity
ν	kinematic viscosity
$\boldsymbol{\Xi}_n$	orthonormal eigenvector
$\Pi_{u,\Theta}$	spectral energy flux
ρ	mass density
τ	time scale
Φ	some quantity
$\boldsymbol{\Psi}_{\max}$	maximum likelihood of feature affiliation
$\boldsymbol{\Psi}_n$	sparse feature vector in a sub-space close to the eigenspace
$\boldsymbol{\Omega}$	angular velocity with $\boldsymbol{\Omega} = (\Omega_x, \Omega_y, \Omega_z)$ and here in particular $\Omega_z \equiv \Omega$

General abbreviations used in subscripts

Acronym	Meaning	Acronym	Meaning
ce	cosine expansion	marg	marginal stability
cf	coherent features	N	Neumann
char	characteristic	pp	partner particle
crit	critical	rms	root-mean-square
D	Dirichlet	rs	re-scaled
f	free-fall	se	sine expansion
h	horizontal	to	turnover
ib	incoherent background	v	vertical

'*The experiment is the mightiest and most reliable lever through which we can wrest its secrets from nature.*'

– Wilhelm Conrad Röntgen, 2nd January 1894
(translated from German [1])

Mr Röntgen was the discoverer of X-Rays (also called Röntgen radiation) and grantee of the first Nobel Prize in Physics in 1901. What if we could show him nowadays the possibility of measuring numerical experiments even without the use of rays?

Chapter 1

Introduction

1.1 Motivation

Gravity — the weakest of the four fundamental interactions in physics — pervades the whole universe while being inescapable by acting as a body force. In contrast to electromagnetic interactions, which may act on similar length scales and can be considered as being 10^{39} times stronger than gravitational interactions[1], there are no negative gravitational masses [2]. This fact that gravity cannot be neutralised grants it a very special omnipresent role, especially on large scales.

The interplay of gravity with mass density inhomogeneities, typically caused by thermal heterogeneities, is called *buoyancy* and induces without any further help *natural (thermal) convection* – the latter of which represents the essential mechanism by which heat is transported in natural flows [3]. On the one hand, such a convective heat transfer is much more efficient than pure heat *conduction*, whereas on the other hand the existence of a fluid is mandatory to absorb and release heat. If this is not present, *radiation* as a third mechanism may transfer heat even without any transmitting matter and becomes dominant especially when the surface temperature of a body is extraordinary high.

Examples for such natural convection processes driven by heat transfer can be found on Earth throughout its layers from mantle convection [4] over deep ocean convection [5] up to convection in its atmosphere [6], eventually determining local and global aspects of weather and climate. But natural convection is not only an effect that accompanies humans, it can also be used and exploited by us through engineering. For instance, natural thermal convection can be used to cool electrical devices without the need of an additional fan and thus a plus of energy input. Vice versa, wind turbines may exploit the pressure gradients across the Earth's atmosphere by translating kinetic energy into electricity.

Thermal convection flows reveal often a hierarchy of different structures and flow patterns, e.g. as clusters of clouds over the warm ocean in the tropics of Earth [7]. The *solar convection zone* in the outer 30% of the Sun [8], see also figure 1.1, might represent

[1] Considering exemplary the attracting forces between a proton and electron.

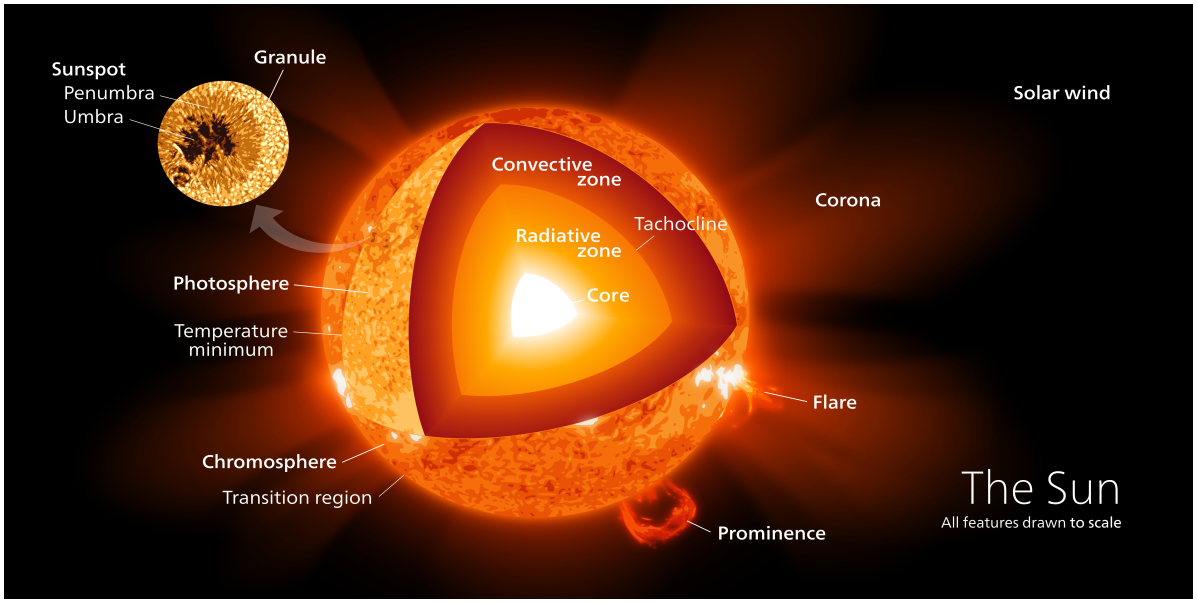

Figure 1.1: Schematic structure of the Sun [9]. Heat that is generated in its core is transferred through the convection zone and eventually radiated at its photosphere into space. A prominent hierarchy of different patterns at and close to its surface is observable from Earth.

one of the most prominent astrophysical examples of such a hierarchy formation. So-called *granules*, i.e. small convection cells with typical horizontal extensions of $l_{\mathrm{G}} \sim 10^3$ km that exhibit lifetimes of about 10 minutes, represent the first stage and form the basic pattern at the solar surface where a heat flux drives convection [8, 10]. The next larger building block in this hierarchy is termed *supergranules*, offering extensions of $l_{\mathrm{SG}} \sim 30 l_{\mathrm{G}}$ and lifetimes of a day. Finally, observed *giant long-living fluid motions* [11], that extend with $l_{\mathrm{GM}} \sim 200 l_{\mathrm{G}}$ across major parts of the solar convection zone and exhibit lifetimes of more than a month, represent a third stage in this hierarchy [8]. However, our understanding of this hierarchy's origins is still far from complete [12].

Supergranules as part of this hierarchy are known to be connected to magnetic networks such as sunspots [8, 10, 13, 14], the latter of which are directly related to the solar cycle. On the one hand, this cycle impacts the solar radiation [10] and thus – besides other cycles that originate in the orbital parameters of Earth [15–17] – the thermal forcing of weather and climate on Earth. On the other hand, and even more important, such magnetic networks are related to coronal mass ejections and thus to adverse space weather. In other words, supergranules are related to accelerated and from the Sun ejected particles, which can in turn pose severe danger to humans and their technology [8, 18]. From this point of view it becomes clear that such hierarchies in natural flows are of particular interest in research.

The phenomenon of natural convective heat transfer with its many facets is crucial for many processes – so does it not surprise that the idea of convection is quite old and that first quantitative experiments have already been performed around the year

1900 by Henri Bénard [19, 20]. He studied the stability of a thin fluid layer with a free surface, influenced by a vertical temperature gradient. Later in 1916, Lord Rayleigh studied convection between two plates in more detail and developed a complete linear stability analysis for selected boundary conditions [21]. Many scientists followed the works of Bénard and Rayleigh in the last century while focussing on the thermally driven turbulent convection – but still a large number of questions remains open, even for the simplest experimental setup of so-called *Rayleigh-Bénard convection* [3, 20].

1.2 Fundamentals of Rayleigh-Bénard convection

1.2.1 Basic experimental setup

Rayleigh-Bénard convection is the simplest paradigm for research of thermal convection and thus of thermally driven turbulence [3, 22]. There, 'a continuous medium, whose equilibrium state is uniform, is contained between two parallel uniform plates [...] whose width L is large compared to their [vertical] separation H. The medium is driven out of equilibrium [...] by gradients of temperature [...]. Because the plates are uniform, the gradients are normal to the plates and independent of their position along the plates' [23]. In other words, heat shall be transferred across a layer of fluid that gets confined between two horizontal planes – the bottom plane is heated whereas the top plane is cooled. Because of the variation of mass density with temperature, this may destabilise the fluid once the system is subjected to gravity. This is all that is necessary and thus the reason for the simplicity of this setup.

Although already complicated in its own, various extensions can be made to include further physical mechanisms into this dynamical system. Examples of such extensions that are of particular importance to geo- and astrophysical flows include complex fluid property dependencies [24–26], phase changes [27, 28], rotation around some axis [29, 30] or magnetohydrodynamic effects [31–33].

This present thesis deals mostly with the very basic setup of Rayleigh-Bénard convection and includes rotation around the vertical axis at selected places as the only extension. If not mentioned explicitly, rotation is not included. The underlying experimental setup is visualised in figure 1.2.[2]

It should be stressed that this experimental setup of Rayleigh-Bénard convection is in contrast to the more complex *Bénard-Marangoni convection*, which is the original setup used by Henri Bénard. The key difference is that Bénard-Marangoni convection offers a free surface at the top such that the flow is driven by surface tension instead of buoyancy. Thus, it works even in a zero-gravity environment [20, 34–36].

When the applied temperature gradient between the plates in Rayleigh-Bénard convection is increased starting from zero and eventually exceeds a certain point, the fluid that was at rest before begins to move. If this thermal driving is constant over time, the system might even enter a *non-equilibrium statistically steady state*. The strength

[2] Figure 3.12 and section 3.4.2.2 will point out and discuss in more detail how this Cartesian domain is related to the motivating geo- and astrophysical objects.

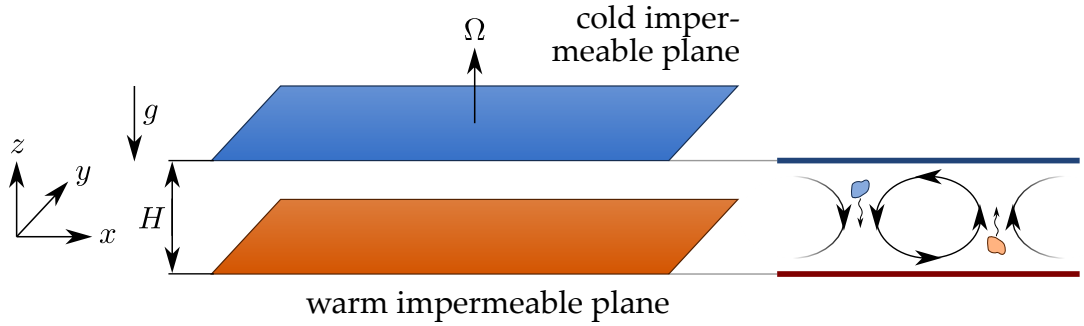

Figure 1.2: Basic setup of Rayleigh-Bénard convection in Cartesian coordinates. A fluid is confined between two horizontal planes, the latter of which prescribe a temperature gradient, and subjected to gravity. Rotation around the vertical axis with angular velocity Ω is optional. If $\mathrm{Ra} \geq \mathrm{Ra}_{\mathrm{crit}}$, flow structures manifest that are driven by hot ascending and cold descending fluid just as sketched on the right side.

of thermal driving can be quantified by the so-called Rayleigh number Ra, and so the before-mentioned critical point is then given by the critical Rayleigh number $\mathrm{Ra}_{\mathrm{crit}}$ which is typically of order $\mathcal{O}(10^3) - \mathcal{O}(10^4)$, see table 1.1. This point of *onset of convection* solely depends on boundary conditions [37, 38], the aspect ratio Γ of the domain [20, 23, 35], and (if present) the strength of rotation [39, 40] which can be quantified by the Rossby number Ro. In contrast, it is mostly independent of the working fluid[3] which can be characterised by the Prandtl number Pr. These four dimensionless quantities represent the fundamental system parameters that govern the entire fluid flow and will be defined in section 1.2.2.

It is peculiar that a fluid suddenly gets in motion after the Rayleigh number is increased beyond its critical value. At first thought one could expect that the unstable thermal arrangement of the fluid, whose mass density becomes larger at the colder top but smaller at the hotter bottom of the fluid layer, causes immediately a convective motion [37]. In fact, this is not the case. Suppose for this a quiescent state with $\mathrm{Ra} < \mathrm{Ra}_{\mathrm{crit}}$. If a volume element is moved due to a random fluctuation e.g. upwards – see also figure 1.2 –, it is hotter than its vicinity. Due to the heat conduction in the fluid, this temperature difference will get balanced and also by friction, the volume element gets slowed down and will stagnate. But if the temperature gradient gets increased beyond a certain critical value, implying $\mathrm{Ra} \geq \mathrm{Ra}_{\mathrm{crit}}$, the stabilising mechanisms of heat conduction and viscosity will not suffice any more. The hotter particle is also less dense than its vicinity, leading to a buoyancy that strengthens the initial random fluctuation. The particle reaches even colder vicinities, leading to a further enhanced buoyancy. The same is also valid for a volume element which is moved downwards: it reaches hotter vicinities and thus its density is higher than the density of its neighbouring volume elements. In the end also this particle will continue to move downwards [41]. Nothing but this proportion between buoyancy on the one side and dissipation through viscosity and heat conduction on the other side is quantified by the Rayleigh number.

[3] This vague introductory statement will be rendered more precisely in section 3.2.1.

Mechanical BC	$\mathrm{Ra}_{\mathrm{crit}}$	k_{crit}	λ_{crit}	Reference
Thermal BC: Dirichlet / constant temperature				
no-slip	1707.8	3.13	2.01	[42]
free-slip	$\frac{27}{4}\pi^4 \approx 657.5$	$\frac{\pi}{\sqrt{2}} \approx 2.221$	$2\sqrt{2} \approx 2.828$	[21]
Thermal BC: Neumann / constant heat flux				
no-slip	$6! = 720$	0	∞	[38]
free-slip	$5! = 120$	0	∞	[38]

Table 1.1: Critical parameters at the onset of convection. The critical Rayleigh number $\mathrm{Ra}_{\mathrm{crit}}$, horizontal wave number $k_{\mathrm{crit}} \equiv k_{\mathrm{h,\,crit}}$, and horizontal wavelength $\lambda_{\mathrm{crit}} \equiv \lambda_{\mathrm{h,\,crit}}$ with $\lambda = 2\pi/k$ are provided for selected combinations of thermal and mechanical boundary conditions, the latter of which will be explained in section 1.2.2.4. These numbers hold for the non-rotating scenario with $\Gamma \to \infty$ only.

1.2.2 Mathematical model

1.2.2.1 Oberbeck-Boussinesq approximation

Although more than a century old, the basic concept of Lord Rayleigh's theoretical treatment has not become outdated – he described the fluid flow as a continuum based on the so-called *Oberbeck-Boussinesq approximation* [43, 44]. In general, material parameters depend on the temperature T and pressure p. The key idea of this approximation is now that their dependence on 'pressure is unimportant and that even the variation with temperature may be disregarded except in so far as it modifies the operation of gravity' [21]. As a consequence, the mass density ρ becomes a linear function of only the temperature such that [3, 45]

$$\rho(T,p) = \rho(T) \simeq \rho_{\mathrm{ref}}\left[1 - \alpha\left(T - T_{\mathrm{ref}}\right)\right] \qquad \text{with} \qquad \alpha = \frac{1}{V}\frac{\partial V}{\partial T}\bigg|_p = -\frac{1}{\rho}\frac{\partial \rho}{\partial T}\bigg|_p , \quad (1.1)$$

where α represents the volumetric thermal expansion coefficient at constant pressure, V the volume and $\rho_{\mathrm{ref}} = \rho(T_{\mathrm{ref}})$ the density at a reference temperature T_{ref} – the latter is typically chosen as the mean temperature in the system. This equation (1.1) comes only into play when the mass density acts together with gravity, otherwise the fluid is considered to be incompressible with $\rho = \rho_{\mathrm{ref}}$.

Physically, this incompressibility implies that and may be used only if the flow is highly subsonic, as well as the height of the convection layer is small enough to assume a uniform and constant background density [3, 10, 46]. In addition, the Oberbeck-Boussinesq approximation might allow for 'small' temperature differences only [47, 48] due to the linearisation in eq. (1.1) and the elsewhere assumed temperature-independent fluid properties. Despite these restrictions, the approximation remains valid for many practical flows and is thus commonly used even today.

1.2.2.2 Dimensional governing equations

Based on the Oberbeck-Boussinesq approximation, the fundamental governing equations of rotating thermal convection are [45, 48–52]

$$\nabla \cdot \boldsymbol{u} = 0, \tag{1.2}$$

$$\frac{\partial \boldsymbol{u}}{\partial t} + (\boldsymbol{u} \cdot \nabla)\, \boldsymbol{u} + 2\Omega\, \boldsymbol{e}_z \times \boldsymbol{u} = -\frac{1}{\rho_{\mathrm{ref}}} \nabla p + \nu\, \nabla^2 \boldsymbol{u} + \alpha g\, (T - T_{\mathrm{ref}})\, \boldsymbol{e}_z, \tag{1.3}$$

$$\frac{\partial T}{\partial t} + (\boldsymbol{u} \cdot \nabla)\, T = \kappa\, \nabla^2 T. \tag{1.4}$$

Here, $\boldsymbol{u} = \boldsymbol{u}(\boldsymbol{x}, t)$ with $\boldsymbol{u} = (u_x, u_y, u_z)$ is the velocity field, $T = T(\boldsymbol{x}, t)$ the absolute temperature field and $p = p(\boldsymbol{x}, t)$ the pressure variation field around the hydrostatic equilibrium profile that is further modified under the action of rotation. $\boldsymbol{x} = (x, y, z)$ represents the spatial coordinate and t the time. The coordinate system is chosen such that the acceleration due to gravity g points against the z-axis, see also figure 1.2, therefore $\boldsymbol{e}_z$ represents the unity vector along this axis. Rotation is, if present at all, considered to be aligned along the vertical axis, anti-parallel to the direction of gravity, constant in space and time, and explicitly included with respect to the Coriolis acceleration only – the centrifugal acceleration term is not neglected but just absorbed in the pressure field [53–56].[4] Further, Ω represents the angular velocity around the vertical axis, ν the kinematic viscosity, and $\kappa = \lambda_{\mathrm{t}} / (\rho_{\mathrm{ref}} c_p)$ the thermal diffusivity with λ_{t} as the thermal conductivity and c_p as the specific heat capacity at constant pressure.

The outstanding generality of the above equations is provided by the fact that the *continuity equation* (1.2), the *Navier-Stokes equation* (1.3), and the *energy equation* (1.4) represent *conservation equations* for the mass density, the momentum density, and the internal energy density of any incompressible Newtonian fluid, respectively [57]. Crucially, the temperature represents an *active* scalar as it enters the Navier-Stokes equation – so, these equations are *coupled*.

1.2.2.3 Non-dimensional governing equations

The large number of parameters in equations (1.2) – (1.4) hampers a systematic study capturing the relative strengths of the various terms in these equations. However, a dimensional analysis reveals that the problem can be reduced to only three parameters which can be obtained by non-dimensionalising the field variables based on characteristic length, time, temperature, and thus also velocity scales.

In general, the height H of the fluid layer represents the characteristic length scale of the Rayleigh-Bénard convection system. In contrast, the velocity scale can be chosen from several options and depends on arguments of the strength of selected terms to each other [56]. For large-scale structures in turbulent flows at high Rayleigh numbers, diffusion becomes unimportant and the *free-fall inertial balance* will be achieved – i.e., the forcing in eq. (1.3) through buoyancy is balanced by the non-linear term. Thus, $(\boldsymbol{u} \cdot \nabla)\, \boldsymbol{u} \sim \alpha g T \boldsymbol{e}_z$

[4] A more detailed explanation on this is provided in section 3.4.2.

and so $U_{\mathrm{char}}^2/H \sim \alpha g T_{\mathrm{char}}$, which leads after solving for the characteristic velocity U_{char} to the so-called free-fall velocity $U_{\mathrm{char}} \sim U_{\mathrm{f}} := \sqrt{\alpha g T_{\mathrm{char}} H}$ [52]. As will become clear when defining the boundary conditions in section 1.2.2.4, the characteristic temperature T_{char} can be either the applied constant temperature difference ΔT between the plates such that $T_{\mathrm{char}} \sim \Delta T$, or obtained via the applied constant temperature gradient β which leads to $T_{\mathrm{char}} \sim \beta H$. With this diffusivity-free velocity scale, the corresponding time scale becomes the so-called inertial *free-fall time scale* $\tau_{\mathrm{f}} := H/U_{\mathrm{f}} = \sqrt{H/\left(\alpha g T_{\mathrm{char}}\right)}$. The pressure scale results in $p_{\mathrm{f}} := U_{\mathrm{f}}^2 \rho_{\mathrm{ref}}$. Thus, in a nutshell,

$$\boldsymbol{x} = H\,\tilde{\boldsymbol{x}}, \qquad \boldsymbol{u} = U_{\mathrm{f}}\,\tilde{\boldsymbol{u}}, \qquad T = T_{\mathrm{char}}\,\tilde{T}, \qquad t = \tau_{\mathrm{f}}\,\tilde{t}, \qquad p = p_{\mathrm{f}}\,\tilde{p}, \tag{1.5}$$

with variables exhibiting tildes being non-dimensional – these tildes are, as is common, dropped in the following.

A subsequent non-dimensionalisation translates equations (1.2) – (1.4) to [58, 59]

$$\nabla \cdot \boldsymbol{u} = 0, \tag{1.6}$$

$$\frac{\partial \boldsymbol{u}}{\partial t} + (\boldsymbol{u}\cdot\nabla)\,\boldsymbol{u} + \frac{1}{\mathrm{Ro}}\,\boldsymbol{e}_z \times \boldsymbol{u} = -\nabla p + \sqrt{\frac{\mathrm{Pr}}{\mathrm{Ra}}}\,\nabla^2 \boldsymbol{u} + T\boldsymbol{e}_z, \tag{1.7}$$

$$\frac{\partial T}{\partial t} + (\boldsymbol{u}\cdot\nabla)\,T = \frac{1}{\sqrt{\mathrm{RaPr}}}\,\nabla^2 T. \tag{1.8}$$

Starting here and throughout the remainder of this thesis, all field variables $\boldsymbol{u}$, p, T as well as times and lengths are (unless otherwise noted) non-dimensional, i.e. they do not exhibit a physical unit any more – instead, their unit is 1. Velocities, times and temperatures are measured in units of the above-introduced free-fall velocity, free-fall time and characteristic temperature of the system, respectively, whereas the lengths are measured in units of the height of the fluid layer.[5]

Comparing equations (1.6) – (1.8) with (1.2) – (1.4) highlights the vast reduction of the parameter space. The whole dynamics is now described by the following three non-dimensional parameters only. The (molecular [61] or thermal [8]) *Prandtl number*

$$\mathrm{Pr} := \frac{\nu}{\kappa} \tag{1.9}$$

represents the ratio of viscous to thermal diffusion and characterises the working fluid. The *Rayleigh number* Ra, whose definition [58, 62] depends on the choice of the thermal boundary condition – Dirichlet (D) or Neumann (N), see section 1.2.2.4 –, is given by

$$\mathrm{Ra_D} := \frac{\alpha g \Delta T H^3}{\nu\kappa} \qquad \text{or} \qquad \mathrm{Ra_N} := \frac{\alpha g \beta H^4}{\nu\kappa}, \tag{1.10}$$

[5] In contrast to this non-dimensionalisation based on the free-fall velocity U_{f}, it can also be performed based on a diffusivity. This results in either the *viscous* or the *thermal vertical diffusion time scale*, $\tau_\nu := H^2/\nu \equiv \sqrt{\mathrm{Ra/Pr}}\,\tau_{\mathrm{f}}$ or $\tau_\kappa := H^2/\kappa \equiv \sqrt{\mathrm{RaPr}}\,\tau_{\mathrm{f}}$, respectively. Finally, the Rayleigh and Prandtl number comprise all these time scales as $\mathrm{Ra} = \tau_\nu\tau_\kappa/\tau_{\mathrm{f}}^2$ and $\mathrm{Pr} = \tau_\kappa/\tau_\nu$ [60]. More information on time scales especially corresponding to rotation are provided in section 3.4.2.

repectively, and quantifies the strength of the thermal driving compared to diffusion of momentum and heat. Finally, the (convective [52, 63] or gravitational [64]) *Rossby number*

$$\mathrm{Ro} := \frac{U_\mathrm{f}}{2\Omega H} \tag{1.11}$$

represents the ratio between the freely falling convective inertia to the system's rotational inertia [52]. This comes only into play if rotation around the vertical axis is considered – otherwise $\mathrm{Ro} = \infty$ and the Coriolis acceleration term vanishes.

One might wonder why scientists need to put so much effort in solving these equations that obey only three control parameters – the reasons here are two-fold. Firstly, the Navier-Stokes equation contains the *non-linear* term which prohibits applying the superposition principle for a general analytic solution [65]. Secondly, the solution of the Navier-Stokes equation is *non-local* due to the involved pressure field, the latter of which needs to be computed based on the knowledge of the field variables across the entire domain (see also eq. (1.18)). This in particular is caused by the incompressibility which implies to set the speed of sound to $c_\mathrm{s} \to \infty$. Because of these two reasons, researchers are asked to perform complex simulations or experiments to study the particular system of interest.

1.2.2.4 Boundary conditions

Many natural buoyancy-driven convection processes, see also again section 1.1, can be described by the governing equations (1.6) – (1.8). However, this set of equations must always be complemented by appropriate *boundary conditions* (BCs) specifying the environment in which it may then describe the actual flow.

First of all, the domain geometry needs to be defined. This can be very complex in nature and systematic research relies on mathematical idealisations. These may range from spherical shells – approximating, e.g., the entire solar convection zone – up to Cartesian boxes, the latter of which might represent in the same example one particular section of this zone while neglecting the spherical character (see also figure 3.12 and section 3.4.2.2). Every such flow domain introduces at least one additional non-dimensional parameter, the *aspect ratio*

$$\Gamma := \frac{L}{H}, \tag{1.12}$$

describing the ratio of the typical horizontal length scale L of the flow domain to the vertical length scale H.

Further, the variety of convection processes in nature and technology exhibits combinations of different mechanical and thermal boundary conditions. Although sometimes more a valid approximation than a perfect description of reality, the following ones [56, 65] capture typical scenarios.

On the one hand, boundary conditions for the velocity field demand always – due to the nature of the experiment – impermeable top and bottom planes. However, the role of tangential stress can be very different ranging from 'as large as necessary to prevent any fluid motion' as one limit to 'being absent' as the complementary limit. The former is

called *no-slip* (or rigid) boundary condition. Physically, this means that the fluid sticks perfectly to the planes and so this is the typical boundary condition that laboratory experiments or technological applications obey. It can mathematically be described by

$$\boldsymbol{u}\ (z \in \{0, H\}) = 0 \qquad \text{or} \qquad \tilde{\boldsymbol{u}}\ (\tilde{z} \in \{0, 1\}) = 0 \tag{1.13}$$

for dimensional or non-dimensional quantities, respectively. In contrast, the latter is called *free-slip* (or stress-free) boundary condition. This can be the case when one fluid flows over another one and has practical relevance in many geo- and astrophysical settings [8, 66, 67]. It implies that

$$u_z\ (z \in \{0, H\}) = 0, \qquad \frac{\partial u_{x,y}}{\partial z}\ (z \in \{0, H\}) = 0 \qquad \text{or} \tag{1.14a}$$

$$\tilde{u}_z\ (\tilde{z} \in \{0, 1\}) = 0, \qquad \frac{\partial \tilde{u}_{x,y}}{\partial \tilde{z}}\ (\tilde{z} \in \{0, 1\}) = 0. \tag{1.14b}$$

Navier-slip boundary conditions [49, 68] represent an interpolation between these two limits of tangential stress [69] and are, e.g., often used in microfluidics [70].

On the other hand, boundary conditions on the temperature field at the top and bottom planes depend critically on the choice of working materials. Physically, this depends on the ratio of thermal diffusivities $\kappa_\mathrm{F}/\kappa_\mathrm{S}$ between the fluid (F) and solid plate (S) [37, 38, 62, 71]. If $\kappa_\mathrm{F}/\kappa_\mathrm{S} \to 0$, temperature inhomogeneities in the solid top or bottom plate relax much more rapidly by thermal diffusion than in the fluid such that their temperature can be assumed to be constant. Thus, this case is called *constant temperature* (or iso-thermal) boundary condition and of *Dirichlet* type. Mathematically,

$$T\ (z = 0) = T_\mathrm{bot} = T_\mathrm{top} + \Delta T, \qquad T\ (z = H) = T_\mathrm{top} \qquad \text{or} \tag{1.15a}$$

$$\tilde{T}\ (\tilde{z} = 0) = 1, \qquad \tilde{T}\ (\tilde{z} = 1) = 0 \tag{1.15b}$$

with the fixed temperature difference between the plates $\Delta T > 0$. In the complementary case of $\kappa_\mathrm{F}/\kappa_\mathrm{S} \to \infty$, the plates act – relative to the fluid – as thermal insulators which prescribe a heat flux independently of the fluid motion. This case is called *constant heat flux* (or iso-flux) boundary condition and of *Neumann* type. It is described by

$$\frac{\partial T}{\partial z}\ (z \in \{0, H\}) = -\beta \qquad \text{or} \qquad \frac{\partial \tilde{T}}{\partial \tilde{z}}\ (\tilde{z} \in \{0, 1\}) = -1 \tag{1.16}$$

with the fixed vertical temperature gradient $\beta > 0$. Robin boundary conditions [72] cover the range between these two extreme cases [58].

The lateral boundaries may either close the domain – i.e. they exhibit similar velocity or temperature boundary conditions to any of the above-mentioned, which is for instance the case in laboratory experiments – or be periodic. *Periodic* boundary conditions are often appropriate for geo- and astrophysical settings and indicate that the domain is topologically equivalent to a ring [23]. Mathematically, this means that any quantity Φ is repeated after the periodic length L such that

$$\Phi\ (\boldsymbol{x}) = \Phi\ (\boldsymbol{x} + i_x L_x \boldsymbol{e}_x + i_y L_y \boldsymbol{e}_y) \qquad \text{or} \tag{1.17a}$$

$$\tilde{\Phi}\ (\tilde{\boldsymbol{x}}) = \tilde{\Phi}\ (\tilde{\boldsymbol{x}} + i_x \Gamma_x \boldsymbol{e}_x + i_y \Gamma_y \boldsymbol{e}_y) \tag{1.17b}$$

for arbitrary integers $i \in \mathbb{Z}$ [23, 55, 56, 65].

The pressure field as the last of the three fields in equations (1.6) – (1.8) becomes under the Oberbeck-Boussinesq approximation an enslaved field only – it is not independent any more but instead directly coupled to the velocity and temperature field. Its governing *pressure equation* can be obtained by taking the divergence of the Navier-Stokes equation (1.7) with the continuity equation (1.6) acting as a boundary condition and reads

$$\nabla^2 p = -\nabla \cdot \left[(\boldsymbol{u} \cdot \nabla)\, \boldsymbol{u} + \frac{1}{\mathrm{Ro}}\, \boldsymbol{e}_z \times \boldsymbol{u} - T \boldsymbol{e}_z \right], \tag{1.18}$$

representing mathematically a Poisson equation. Thus, the before-mentioned boundary conditions from the velocity and temperature fields affect immediately the pressure field.

1.2.3 Heat and momentum transport and the role of large-scale flow structures

As vividly explained in section 1.2.1, convection sets in once $\mathrm{Ra} \geq \mathrm{Ra}_{\mathrm{crit}}$ that eventually supports the conductive heat transfer across the fluid layer. When Rayleigh-Bénard convection is progressively driven out of equilibrium state, it becomes increasingly dynamic and chaotic as the dissipative viscous effects compete only at small length scales effectively with the strong thermal driving. This implies that a large number of degrees of freedom participates in the dynamics [23].

Right at the onset of convection, a well-ordered flow structure establishes which consists of straight convection rolls [39–41] with characteristic horizontal length scales dependent of the boundary conditions [37–40]. For increased thermal forcing, these rolls become susceptible to instabilities towards more complex structures and the flow gets strongly influenced by the Prandtl number Pr [73–75]. Once Rayleigh-Bénard convection is driven far from the onset such that $\mathrm{Ra} \gg \mathrm{Ra}_{\mathrm{crit}}$, disorder in space and time establishes due to the influence of instabilities and defects on each other, as well as uncontrolled initial conditions [23]. This leads finally to fully developed, chaotic turbulence in the flow. However, recent research showed that not a completely disordered state manifests but instead a large-scale order in the form of rolls and cells re-appears once the instantaneous fluctuations of temperature and velocity are removed. These structures are termed *large-scale circulation* [76] or *turbulent superstructures* [75] if $\Gamma \approx 1$ or $\Gamma \gg 1$, respectively. While both exhibit typical horizontal length scales of order $\mathcal{O}(H)$, the latter are even reminiscent to those patterns known from slightly above the onset of convection [75].

This dynamical response of the convection system – defined by its input parameters Ra, Pr, Ro and Γ, as well as boundary conditions; see table 1.2 for typical values in geo- and astrophysical flows – with respect to the resulting heat and momentum transport is at the heart of modern research.

Heat transport comprises both diffusive and convective contributions and varies in space and time. The (classical) *Nusselt number* quantifies the ratio of the (average) total heat current $\boldsymbol{J} = \boldsymbol{u}T + \boldsymbol{J}_{\mathrm{diff}}$ across the fluid layer to the diffusive heat current

	Ra	Pr	Ro	...
Mantle convection	$10^6 - 10^9$	$10^{22} - 10^{25}$	–	...
Deep ocean convection	$10^{24} - 10^{31}$	7	$10^{-2} - 10^0$	...
Shallow atmosphere convection	$10^{18} - 10^{21}$	0.7	$10^{-1} - 10^1$	...
Earth's outer core	$10^{23} - 10^{27}$	$10^{-2} - 10^{-1}$	$10^{-7} - 10^{-5}$	...
Solar convection zone	$10^{12} - 10^{24}$	$10^{-13} - 10^{-3}$	$10^0 - 10^5$	...

...	Γ	mechanical BCs	thermal BCs	References
...	54	fs	D	[3, 4, 56, 77–79]
...	$10^2 - 10^3$	ns, fs	N	[3, 5, 80–82]
...	10^2	ns, fs	D, N	[3, 6, 83–86]
...	$10^0 - 10^1$	ns	D	[56, 87–89]
...	10	fs	N	[3, 8, 14, 90–92]

Table 1.2: Geo- and astrophysical thermal convection systems. Examples and estimates of corresponding parameters and best matching boundary conditions (ns = no-slip, fs = free-slip, D = Dirichlet, N = Neumann). Note that the estimated parameter ranges are subject to partly large uncertainties.

$\boldsymbol{J}_{\text{diff}} = -\nabla T/\sqrt{\text{RaPr}}$ that would take place in case of pure heat conduction,

$$\text{Nu}\,(t) := \frac{\langle \boldsymbol{J} \cdot \boldsymbol{e}_z \rangle_\Phi}{\langle \boldsymbol{J}_{\text{diff}} \cdot \boldsymbol{e}_z \rangle_\Phi} = -\frac{\partial \langle T \rangle_A}{\partial z} + \sqrt{\text{RaPr}}\,\langle u_z T \rangle_A \tag{1.19a}$$

$$= 1 + \sqrt{\text{RaPr}}\,\langle u_z T \rangle_V, \tag{1.19b}$$

and can be derived from eq. (1.8) [93]. $\langle\cdot\rangle_\Phi$ represents an average over the quantity Φ, the latter of which can be the horizontal cross-section $A = \Gamma \times \Gamma$ or the entire volume $V = A \times 1$.[6] Hence by definition, $\text{Nu} = 1$ for $\text{Ra} < \text{Ra}_{\text{crit}}$ and $\text{Nu} > 1$ else. The individual terms on the right side represent the diffusive and convective vertical heat transport. Although they depend on the vertical coordinate in eq. (1.19a), their sum is constant for all z allowing for the equivalent definition (1.19b). These above definitions hold for Dirichlet boundary conditions, as well as for the re-scaled fields (see section 3.1.2) in the Neumann case.

In contrast, momentum transport can be quantified by the *Reynolds number*

$$\text{Re} := \sqrt{\frac{\text{Ra}}{\text{Pr}}}\,U_{\text{char}} \tag{1.20}$$

through the ratio of inertial to viscous forces in eq. (1.7). U_{char} represents a characteristic velocity and is in simulations typically chosen as the root-mean-square velocity $U_{\text{char}} = u_{\text{rms}} := \sqrt{\langle \boldsymbol{u}^2 \rangle_V}$ in the numerical domain [75, 94].

Researchers aim to predict these transports through scaling laws such as [8]

$$\text{Nu} = f_1\,(\text{Ra}, \text{Pr}, \text{Ro}, \Gamma, \text{BCs}) \qquad \text{and} \qquad \text{Re} = f_2\,(\text{Ra}, \text{Pr}, \text{Ro}, \Gamma, \text{BCs}) \tag{1.21}$$

[6] One may also omit the averaging and define a local Nusselt number, see eq. (4.11).

with commonly observed functional forms like [95]

$$\mathrm{Nu} = c\,\mathrm{Pr}^{\gamma_1}\left(\frac{\mathrm{Ra}}{\mathrm{Ra}_{\mathrm{crit}}}\right)^{\gamma_2}\mathrm{Ro}^{\gamma_3}. \tag{1.22}$$

Here, c is some constant and the exponents

$$\gamma_1 := \frac{\partial \ln(\mathrm{Nu})}{\partial \ln(\mathrm{Pr})}, \qquad \gamma_2 := \frac{\partial \ln(\mathrm{Nu})}{\partial \ln(\mathrm{Ra})}, \qquad \gamma_3 := \frac{\partial \ln(\mathrm{Nu})}{\partial \ln(\mathrm{Ro})} \tag{1.23}$$

with ln representing the natural logarithm. As the coefficient and these exponents may depend on the range of input parameters and boundary conditions, such a question for the response of the dynamical system becomes challenging.

Nevertheless, such scaling laws can be deduced either empirically or theoretically [95] and are of particular interest for several reasons. Firstly, they may offer insights into force balances in the governing equations. Once such balances are known and understood, they allow for model reductions based on the identified key dynamics [95] which in turn may let expensive experiments or numerical simulations become dispensable. Secondly, scaling laws and knowledge about their range of validity permit extrapolations to study even settings that are not accessible for experiments and direct numerical simulations. This is of particular importance in geo- and astrophysical settings where extreme Pr and Ra can be found [95]. Thirdly, the question of interest can especially in these settings just be the opposite of eq. (1.21) – the heat transfer through the convection layer is known but one would like to understand the flow structure that enables this heat transfer to occur [8].

Interestingly, it is the above-mentioned large-scale flow structures that predominantly cause the heat transport in the turbulent regime [96], raising and highlighting their crucial role in current research.

1.3 Scientific objectives of the present thesis

The variety of natural flows with their different boundary conditions in the presence of large aspect ratios, as summarised in table 1.2, stresses the complexity in research and detection of large-scale flow structures, as well as the subsequent understanding of heat transport across a fluid layer.

The twofold goal of the thesis at hand is thus

1. to understand how large-scale flow structures are altered by different boundary conditions, as well as

2. to infer these large-scale flow structures from a Lagrangian material transport perspective.

In general, fluid flows can be studied analytically, by the use of numerical simulations, or by performing laboratory experiments. Analytical solutions, however, are limited to the

onset of convection and right above, providing no chance of studying turbulent large-scale flow structures. Instead, numerical simulations offer several advantages over laboratory experiments that are beneficial for achieving the above-mentioned objectives. For instance, boundary conditions can be flexibly chosen, easily modified and hold perfectly. Furthermore, any global or even local quantity can be measured without interfering the fluid flow, and material properties can be chosen at will allowing the Oberbeck-Boussinesq approximation to be ideally satisfied [97]. Moreover, physical mechanisms of arbitrary strength – such as rotation around some axis – can be implemented easily. In contrast, laboratory experiments allow for inexpensive long-term investigations of the slow dynamics of large-scale flow structures, realistic fluid properties and partly broader parameter ranges [98, 99]. These drawbacks of numerical simulations are not expected to cause serious limitations for reaching the goals of the present thesis, rendering this method ideally suited. Fundamentals of the applied numerical method are provided in chapter 2. In order to comply with the objectives, the following scientific contributions were made.

The impact of different boundary conditions is investigated in an explorative study with respect to idealised cases of velocity and temperature boundary conditions in chapter 3. This part of the thesis offers predominantly an Eulerian perspective to allow for a bird's eye view on the entire flow. It is found and explained in section 3.1 that switching the thermal boundary conditions changes the nature of the large-scale flow structures fundamentally, opening an entirely new path for more detailed studies. In case of constant heat flux boundary conditions, the gradual aggregation of smaller convection cells to a domain-filling convection structure, the latter of which is termed supergranule in reminiscence to the astrophysical motivation of this thesis, can be observed for all accessible Ra (and Pr, see section 3.3). A subsequent leading Lyapunov vector (stability) analysis, see section 3.2, reveals similarities between pattern formation in the turbulent regime and the stability of convection rolls slightly above the onset of convection – in both scenarios, patterns at intermediate scale give continuously rise to new patterns at larger scale. The resulting hierarchy of flow structures is only in accordance with natural examples when this aggregation process stops at some intermediate scale. Rotation around the vertical axis is thus added in section 3.4 as an additional physical mechanism. It is shown that this limits the aggregation process effectively and that the Rossby number serves as control parameter for the resulting supergranule size. Ultimately, an energy transfer analysis in spectral space, see section 3.5, shows that the gradual supergranule aggregation represents an inverse cascade in the subset of two-dimensional modes within the fully three-dimensional flow which can be limited by the effect of rotation. To the best knowledge of the author, this is the first time that such an inverse cascade is proven in naturally forced three-dimensional convection. Hence, these studies investigate the gradual supergranule aggregation across the three-dimensional control parameter space and analyse the former in particular with respect to its dynamical origin and transient formation.

Insights on large-scale flow structures from a Lagrangian material transport perspective are obtained in chapter 4. This part of the thesis obtains major results by advecting massless particles that follow the turbulent flow perfectly, see sections 4.1 and 4.2. Such a

material transport perspective represents a Lagrangian description of the flow. In section 4.3, coherent spatial regions in the flow are identified via unsupervised machine learning for the case of classical thermal boundary conditions. These regions are related to the turbulent superstructures, and their significantly reduced heat transport is detected. Current Lagrangian analysis methods are limited to short observation time windows and do not allow for investigations of gradually evolving structures over long periods of time. To overcome this hitherto restriction, a new evolutionary clustering method is developed and applied for the same case in section 4.4. It is part of future work to apply this technique to the gradual supergranule aggregation found in this thesis to study for instance how heat transport is altered during such a gradual long-term process from a material perspective.

Finally, this thesis finishes with some concluding remarks and perspectives in chapter 5, underlining the extensive character of the present work.

As many results and details have already been published – or should probably be published in the near future – in peer-reviewed journals, the general spirit of this thesis at hand elaborates more on the fundamentals of the underlying concepts that offer a more general picture. Hence, it should serve as a read-worthy and valuable accompanying source of information.

Chapter 2

Fundamentals of the applied numerical method

All numerical studies in the present thesis are carried out as direct numerical simulations using the open-source spectral element solver *Nek5000*.[1] In the following, a brief introduction into key aspects of this numerical method is given.

2.1 General classification

From a more distant perspective, two points of the above statement are of particular importance when comparing different numerical methods with each other.

Firstly, the actually solved equations. *Direct numerical simulations* (DNSs), in contrast to *large-eddy simulations* (LESs) and *Reynolds-averaged Navier-Stokes* (RANS) *simulations*, provide access to the full information from all dynamically relevant scales of the flow. This is not the case for its two alternatives. On the one side, LES filter the flow spatially, resolving only the larger energy-containing structures of the flow on coarse meshes while incorporating contributions of smaller structures through sub-grid approximations. On the other side, RANS simulations follow the philosophy of the Reynolds decomposition [100], splitting the fields into their (typically) temporal means and fluctuations. The resulting equations contain the so-called Reynolds stress tensor as the only term that depends on the (unknown) fluctuations. This is known as the closure problem and requires approximations based on the mean values. Hence, both the LES and RANS simulations rely on modelling of (either spatial or temporal) small-scale components of the flow to reduce the complexity of the simulation [101–103]. The recently developed *generalised quasilinear* (GQL) *approximation* can be seen as a combination of RANS and LES as it decomposes the flow into low and high wave number modes while circumventing the closure problem by excluding selected spectral interactions [104]. However, this thesis aims to answer questions for which it is necessary to include all possible interactions, i.e. any conceivable energy transfer, and hence to resolve even the

[1] Nek5000 version 17.0. Argonne National Laboratory, Illinois. `http://nek5000.mcs.anl.gov`

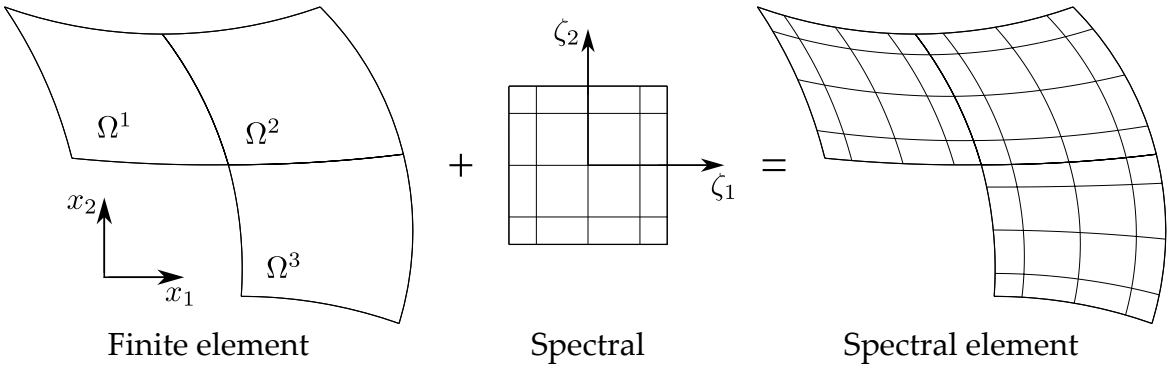

Figure 2.1: Spectral element discretisation. Two-dimensional example for $N_\mathrm{e} = 3$ spectral elements and polynomial order $N = 4$. Inside each spectral element, the GLL nodal lines are indicated. The spectral element method combines complex geometries from finite elements with high accuracies from spectral methods. Figure based on [101].

finest scale of the flow – namely the Kolmogorov η_K or Batchelor scale η_B – without further assumptions or models.

Secondly, the numerical discretisation for solving the underlying equations. The options range from the finite difference method over the finite element method or finite volume method to the spectral method. Especially the finite element and volume methods allow easily for complex geometries and thus a variety of problems, representing in contrast a weak point of spectral methods. However, the latter offer excellent spatial accuracy due to the choice of high-order basis functions. A hybrid approach is the spectral element method, combining the advantages of the generality and the accuracy from finite element and spectral methods, respectively, into one framework [103, 105]. These high accuracies are indispensable in fundamental research.

Nek5000 is used, benchmarked and validated for many years in fundamental research of turbulent thermal convection [75, 106–108]. This well-established tool allows efficient parallelisations exploitable on high-performance computing systems and is thus perfectly suited for this present thesis.

2.2 Domain discretisation

Figure 2.1 visualises the characteristic domain decomposition applied in Nek5000, stressing the key concept of spectral element methods. First, the global domain Ω is split into N_e non-overlapping sub-domains (elements) Ω^i with $i = 1 \dots N_\mathrm{e}$. Second, a spectral method is applied within each element individually, placing $(N + 1)$ collocation points along each direction. Global and local coordinates can be translated into each other by a proper mapping.

For a one-dimensional example, the spectral element approximation Φ_N^i of a quantity

Φ within one element Ω^i can be written as [101]

$$\Phi_N^i(\zeta) = \sum_{j=0}^{N} \Phi_j^i \; Z_j(\zeta) \qquad \text{with } \zeta \in \Omega^i. \tag{2.1}$$

Obviously, the quality of this approximation along the local coordinate $\zeta \in [-1, 1]$ depends on the polynomial order N and the size of the sub-domain. Z_j are orthogonal basis functions – more precisely, they represent so-called Lagrangian interpolation basis functions, i.e. $Z_j\,(\zeta = \zeta_k) = \delta_{jk}$ at the collocation points with coordinates ζ_k (see below) with the Kronecker delta δ_{jk} and $k = 0 \dots N$. Thus, the basis coefficients Φ_j^i represent nodal values of the unknown. The present implementation exploits Legendre polynomials of order N which are given by

$$L_N(\zeta) = \sum_{k=0}^{\lfloor N/2 \rfloor} (-1)^k \, \frac{(2N-2k)!}{(N-k)!\;(N-2k)!\;k!\;2^N} \, \zeta^{N-2k} = \frac{1}{2^N\;N!} \, \frac{d^N}{d\zeta^N} \left[\left(\zeta^2 - 1\right)^N \right] \tag{2.2}$$

to construct these basis functions. Note that the expression on the right is the so-called *Rodrigues's formula*. The ordered set of $(N + 1)$ discrete collocation points – with $\zeta_k \in [-1, 1]$, $\zeta_0 = -1$ and $\zeta_N = 1$ – is crucial for the Lagrangian interpolation basis and determined from solutions of

$$\left(1 - \zeta^2\right) \; L'_N(\zeta) = 0 \qquad \text{with } \zeta \in \Omega^i \tag{2.3}$$

where L'_N is the derivative of the corresponding Legendre polynomial. These points are called *Gauss-Lobatto-Legendre* (GLL) *quadrature nodes*. Finally, the resulting elements of the spectral basis are given by combining the information on the Legendre polynomials and the collocation points via

$$Z_j(\zeta) = \frac{-1}{N(N+1)} \frac{(1-\zeta^2)\;L'_N(\zeta)}{(\zeta - \zeta_j)\;L_N(\zeta_j)} \qquad \text{for } j = 0 \dots N, \quad \zeta \in \Omega^i. \tag{2.4}$$

Figure 2.2 visualises such a set of basis functions together with the corresponding GLL nodes for $N = 4$ (see also again figure 2.1). Although the GLL nodes result in non-uniform grids which are more dense at the element boundaries, the final approximation benefits from a good conditioning and minimal round-off errors compared to uniform node placements. In particular, these benefits originate in avoiding Runge's phenomenon, i.e. the increasing divergence of the polynomial interpolation due to oscillations close to the element boundaries for an increasing polynomial order when using uniform node distributions [109, 110].

From a more practical perspective it is worth to mention that while the elements Ω^i are configured during the mesh generation in advance of a simulation run, the polynomial order N can be set flexibly during the simulation to adjust the grid spacing to the simulation's needs. With increasing N, the user implicitly benefits from the exponential convergence – i.e., exponentially increasing accuracy – that spectral element methods offer [103, 108].

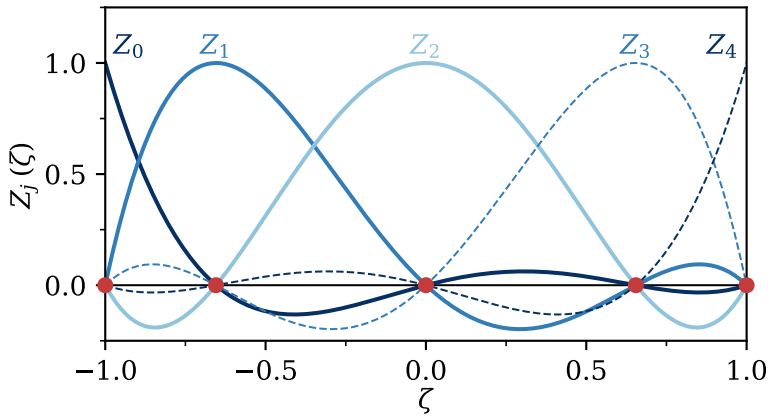

Figure 2.2: Legendre spectral element basis functions, exemplary for a polynomial order $N = 4$ (see also figure 2.1). The Gauss-Lobatto-Legendre collocation points are provided as red dots along the abscissa, highlighting their non-uniform distribution and the characteristics of Lagrangian interpolation basis functions.

2.3 Adaptation and solution of provided equations

For incompressible flows, Nek5000 provides the following set of equations [111]

$$\nabla \cdot \boldsymbol{u} = 0, \tag{2.5}$$

$$\rho \left[\frac{\partial \boldsymbol{u}}{\partial t} + (\boldsymbol{u} \cdot \nabla)\, \boldsymbol{u} \right] = -\nabla p + \eta\, \nabla^2 \boldsymbol{u} + \rho \boldsymbol{f}_{\text{vol}}, \tag{2.6}$$

$$\rho c_p \left[\frac{\partial T}{\partial t} + (\boldsymbol{u} \cdot \nabla)\, T \right] = \nabla \cdot (\lambda_{\text{t}}\, \nabla T) + q_{\text{vol}}. \tag{2.7}$$

Here, $\boldsymbol{f}_{\text{vol}}$ and q_{vol} represent volume forces and volumetric heat sources, respectively, and the dynamic viscosity $\eta = \nu\rho$. To adapt these equations to any problem, the coefficients ρ, η, ρc_p and λ_{t}, as well as $\boldsymbol{f}_{\text{vol}}$ and q_{vol} can be defined.

These equations can be translated into equations (1.6) – (1.8) by setting the coefficients $\rho \to 1$, $\eta \to \sqrt{\text{Pr}/\text{Ra}}$, $\rho c_p \to 1$, $\lambda_{\text{t}} \to 1/\sqrt{\text{RaPr}}$, the volumetric heat source $q_{\text{vol}} \to 0$, and the volume forces $\boldsymbol{f}_{\text{vol}} \to T\boldsymbol{e}_z - (u_x \boldsymbol{e}_y - u_y \boldsymbol{e}_x)/\text{Ro}$. In the non-rotating case, the Coriolis acceleration is omitted in the latter. As a consequence, non-dimensional fields manifest naturally.

Equations (2.6) and (2.7) represent evolution equations of the velocity and temperature, implying that these fields need to be advanced in time – numerically, this is done by the so-called time marching. Generally, the time marching $\partial\Phi/\partial t = f(\Phi)$ of a quantity Φ can be performed either explicitly or implicitly, i.e. $\Phi_{n+1} = f(\Phi_n, \Phi_{n-1}, \dots)$ or $\Phi_{n+1} = f(\Phi_{n+1}, \Phi_n, \Phi_{n-1}, \dots)$, respectively, with some functions f and n denoting here the discrete time step. These approaches follow thus the philosophy of either a forward or backward difference in time. Although the latter requires solving a linear system of equations to obtain the corresponding field at the next time step – which is not necessary

in case of the former and thus much more expensive –, it benefits from an increased numerical stability. This, in turn, allows for larger discrete time steps [101, 103, 112].

Nek5000 performs the time marching using a k-th order backwards differentiation formula BDFk with $k = 2$ in this work. The non-linear term, as well as user-provided right-hand-side terms (i.e. here the buoyancy and Coriolis terms) are incorporated explicitly using high order extrapolations EXTk – in contrast, the linear terms are treated implicitly. The pressure field can be either obtained via a Poisson equation from the velocity field with special boundary conditions, or solved in a coupled manner together with the velocity field. An algebraic multigrid is used as part of the pressure pre-conditioner to enhance performance [105, 108, 109].

In order to make use of discretised versions of equations (2.5) – (2.7) at all, these are transformed into a weak formulation using Galerkin methods. Afterwards, the latter are spatially and temporally discretised using the basis functions outlined in section 2.2 and the methods described above, respectively. This allows for exact evaluations of integrals in the scalar products based on Gauss's theorem and translates the equations into big matrix systems [108, 113].

Such numerical procedures represent discrete approximations of the continuous equations and are thus subject to residuals. The (weighted) residual tolerances are set based on past experience of the research department to 10^{-4}, 10^{-6} and 10^{-6} for the pressure, velocity and temperature field, respectively.

2.4 Methodical details

All simulations will take place in Cartesian domains, thus the spatial domain will get subdivided into $N_\mathrm{e} = N_{\mathrm{e},\,x} \times N_{\mathrm{e},\,y} \times N_{\mathrm{e},\,z}$ spectral elements. While their spacing is uniform along the horizontal directions, it is non-uniform in the vertical direction to allow for a more detailed representation of the boundary layers close to the top and bottom planes. The final resolution – and thus the total number of discrete grid points – is determined by the combination of this spatial subdivision and the number of GLL collocation points placed inside each element. The latter can be controlled via lx1 $= N+1$ with lx1 representing a simulation configuration parameter.

The spacing of the discrete numerical grid is crucial for the CPU and memory consumption during the simulation runtime as the total number of grid points $N_\mathrm{tot} \simeq N_\mathrm{e} N^3$. Thus, the grid should be as fine as necessary but as coarse as possible. The smallest observable scales in the flow are given by either the Kolmogorov or the Batchelor scale – η_K or η_B, see section 3.3.1 – for $\mathrm{Pr} \leq 1$ or $\mathrm{Pr} \geq 1$, respectively. To resolve them sufficiently, it is common to apply the (refined) *Grötzbach criterion* [108]

$$\frac{\Delta z}{\langle \eta_\mathrm{K} \rangle_{A,t}} \lesssim \frac{\pi}{2} \quad \text{for } \mathrm{Pr} \leq 1, \qquad \text{or} \qquad \frac{\Delta z}{\langle \eta_\mathrm{B} \rangle_{A,t}} \lesssim \frac{\pi}{2} \quad \text{for } \mathrm{Pr} \geq 1 \tag{2.8}$$

with the vertical grid spacing Δz.

The spatial grid spacing affects also the stability of the numerical time integration.

The *Courant-Friedrich-Lewy* (CFL) *number* [101]

$$\mathrm{CFL} := \max_{u,\Delta x} \left| \frac{u\,\Delta t}{\Delta x} \right| \tag{2.9}$$

quantifies the ratio of the distance a fluid parcel travels in a given time step to the local grid spacing and is here of particular importance. Interpreting this as a propagation of information across the numerical grid within one time step makes clear, why this quantity affects the stability of the numerical time integration. Stability of the Navier-Stokes equation in Nek5000 requires $\mathrm{CFL} \lesssim 0.5$ [109, 111]. This shows that the spatial and temporal grid spacings are coupled to some extend – typical time step sizes are of order $\mathcal{O}\left(10^{-3}\tau_\mathrm{f}\right)$ – $\mathcal{O}\left(10^{-2}\tau_\mathrm{f}\right)$.

This time advancement of numerical simulations always starts with well-defined *initial conditions* that are typically given by

$$\boldsymbol{u}\left(\boldsymbol{x}, t=0\right) = 0 \qquad \text{and} \qquad T\left(\boldsymbol{x}, t=0\right) = 1 - z + \Upsilon. \tag{2.10}$$

$\Upsilon = \Upsilon\left(\boldsymbol{x}\right)$ represents small random thermal fluctuations of size $0 \leq \Upsilon \leq 10^{-3}$ that are added on top of the linear conduction profile to accelerate the attraction of the dynamical system towards the fully developed flow. Note that this initialisation provides a global mean temperature of $\langle T\left(t=0\right)\rangle_V = 0.5 + \langle\Upsilon\rangle_V$.

The above introduced requirements on the spatial and temporal discretisation become even more challenging when considering that the (numerically discrete) total number of degrees of freedom N_dof of the dynamical system is $N_\mathrm{dof} = 3N_\mathrm{tot}$. The coefficient 3 is due to two velocity components (the third one is enslaved due to incompressibility) and the additional scalar temperature field. This asks for professional computing resources – thus, all numerical simulations of the present thesis were performed on either the local compute cluster MaPaCC4, or on the national supercomputing machines JUWELS and SuperMUC-NG. The largest simulation run – see simulation Nfs2_Pr001 in table 3.3 – occupied 131,072 CPUs in parallel with a peak memory footprint of 181 TB during runtime and $N_\mathrm{dof} \approx 7.2 \times 10^{10}$. At the time of writing, this represents almost half of the largest[2] national supercomputer SuperMUC-NG. These numbers underline the tremendous complexity of research of thermal convection flows, as well as its need for efficient, highly parallelisable solvers like Nek5000 and extensive access to supercomputing systems.

[2]Measured in terms of CPU resources.

Chapter 3

Large-scale flow structures at different boundary conditions

As highlighted in chapter 1, the enormous variety of thermal convection settings present in nature exhibits a variety of different combinations of thermal and mechanical boundary conditions especially at large aspect ratios.

Historically, past research started several decades ago to investigate the influence of many different boundary conditions analytically with respect to the onset of convection. However, this scenario is far off the before-mentioned examples. The emergence of precise measurement techniques for experimental setups on the one hand, and computational resources that allow to perform numerical simulations for increasingly disordered flows on the other hand, paved the way to study thermal convection even for turbulent flows far beyond the onset of convection. Unfortunately, these previous studies are typically restricted to constant temperature boundary conditions – which is why this can be seen as the 'classical' thermal boundary condition – and do not offer a systematic comparison of various thermal and mechanical boundary conditions at large aspect ratios at once.

This chapter investigates the impact of boundary conditions in a first systematic approach – in contrast to the Lagrangian material transport perspective from chapter 4, most of the analyses here follow an Eulerian approach. The first section 3.1 aims to answer the open question in research, how long-living large-scale flow structures – that coexist with local turbulence acting on very short time scales – are altered by variations of boundary conditions. It comes out that thermal boundary conditions play a crucial role in defining the nature of large-scale flow structures, which is the reason why subsequent sections are dedicated to studying flow structures in case of the complementary constant heat flux boundary conditions in much more detail. Here, the transient process of the gradual pattern formation and its dynamical origin represent aspects of particular interest.

Many parts of this chapter have already been published [V1, V5] or extended [V6] – these publications may provide even additional information as for instance resolution studies or the interpretation of laboratory experiment results.

3.1 The impact of thermal and mechanical boundary conditions

3.1.1 General considerations and remarks

The flow that establishes in the dynamical system of Rayleigh-Bénard convection is inherently biased by the available numerical domain as the latter prescribes the largest accessible length scale – this holds equally for closed and periodic domains. Thus, the domain represents an important aspect of scientific studies. An infinite aspect ratio is only hypothetically possible in analytical treatises, whereas numerical studies rely on finite geometries. Generally, the influence of lateral boundaries on the flow decreases rapidly with $\mathcal{O}\left(\Gamma^{-2}\right)$ [20, 23, 35] and containers with $\Gamma \gtrsim 20$ are presumed to represent fairly close approximations of infinite fluid layers for which the effect of lateral boundaries practically disappears [22, 35, 96].

Here, the impact of boundary conditions on large-scale flow structures is studied in a Cartesian domain with square cross-section and an extraordinary large aspect ratio $\Gamma = \Gamma_x = \Gamma_y = 60$, while the lateral boundaries are decided to be periodic (see eq. (1.17)). This releases the dynamical system from the lateral bounds and simultaneously ensures an isotropy in both horizontal directions x and y.

This fundamental analysis starts with the non-rotating scenario, i.e. $\mathrm{Ro} = \infty$. Furthermore, the Prandtl number be $\mathrm{Pr} = 1$ which roughly approximates air ($\mathrm{Pr} = 0.7$ [56]) as working medium.

3.1.2 Constructing sets of boundary condition combinations

Varying the thermal and mechanical boundary conditions, each between two idealised options as set out in section 1.2.2.4, leads to a set of four possible combinations – a subsequent systematic comparison between all of these options relies thus on a well-defined scaling. Figure 3.1 visualises the scaling and comparison scheme that is applied in this thesis.

The combination of the classical thermal Dirichlet with mechanical no-slip boundary conditions, the latter of which apply to laboratory experiments, serves as starting point for this scaling where Ra is varied in powers of 10. Pattern formation in Rayleigh-Bénard convection depends at a given Pr on the distance of the applied Rayleigh number to the critical Rayleigh number [23]. As the latter depends on the boundary conditions, the Dirichlet free-slip case is obtained by keeping this distance or supercriticality $r := \mathrm{Ra}/\mathrm{Ra}_{\mathrm{crit}}$ fixed (see also eq. (1.22) where this ratio was already used).

The relation of the Neumann scenario to the corresponding Dirichlet case can again – similar to the mechanical boundary conditions above – be performed based on either the supercriticality r, or the Rayleigh number Ra. Taking the linear stability (see again table 1.1) as a first guess of emerging patterns, one might expect the latter to manifest very differently for varying thermal boundary conditions. Thus, a scaling based on Ra is preferred in favour of r. Here, it becomes important to understand the relation between both definitions of Ra from eq. (1.10) as they do generally not equal.

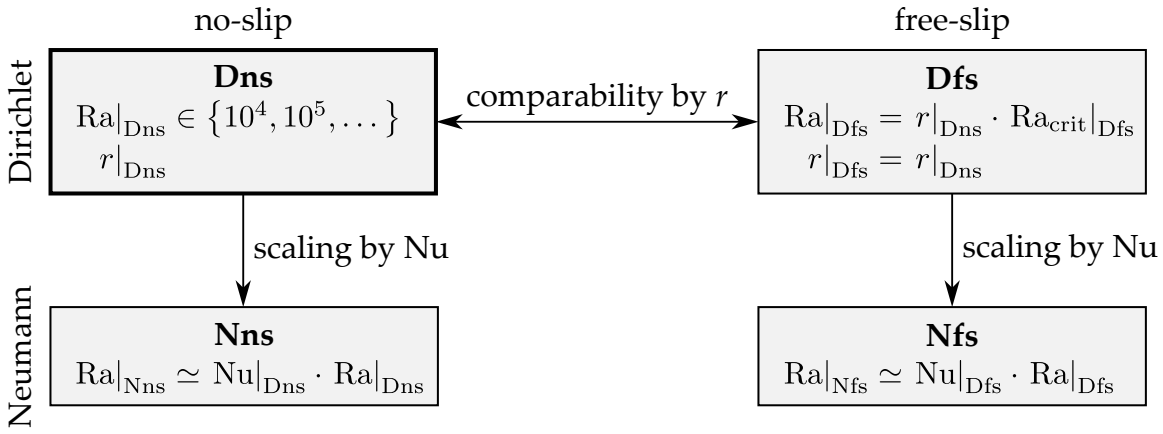

Figure 3.1: Scaling scheme for different boundary conditions allowing for a systematic comparison of the set of four different combinations of thermal and mechanical boundary conditions. The abbreviation for each case is printed in bold at the top of each box and will be used throughout this thesis. The most common scenario Dns serves as reference, providing the initial Ra_{D} from which all other Ra will be derived.

In the Dirichlet case, the applied temperature difference ΔT is used as characteristic parameter – thus, the non-dimensional temperature difference between the plates is $\Delta T_{\mathrm{D}} := \langle T\,(z=0) - T\,(z=1)\rangle_A = T\,(z=0) - T\,(z=1) = 1$ as indicated by eq. (1.15). However, in the Neumann case the applied temperature gradient β serves as characteristic parameter as shown in eq. (1.16), so the non-dimensional temperature difference between the plates $\Delta T_{\mathrm{N}} := \langle T(z=0) - T(z=1)\rangle_A \leq 1$ is consequently not specified. Yet, based on dimensional arguments it is possible to relate both cases via [93]

$$\Delta T = \langle T\,(z=0) - T\,(z=H)\rangle_A \tag{3.1a}$$

$$= \beta H \underbrace{\langle \tilde{T}\,(\tilde{z}=0) - \tilde{T}\,(\tilde{z}=1)\rangle_{\tilde{A}}}_{=\Delta T_{\mathrm{N}}}. \tag{3.1b}$$

Note that this simply represents a non-dimensionalisation of the dimensional ΔT based on the characteristic parameters from the Neumann case. This relation, connected with eq. (1.10), leads naturally to

$$\mathrm{Ra}_{\mathrm{D}} = \mathrm{Ra}_{\mathrm{N}}\,\Delta T_{\mathrm{N}} = \frac{\mathrm{Ra}_{\mathrm{N}}}{\mathrm{Nu}_{\mathrm{N}}}. \tag{3.2}$$

Here, the right-most expression makes use of another important relation: In case of periodicity at the lateral boundaries and thermal Neumann boundary conditions, it can be deduced from the definition of the Nusselt number in eq. (1.19) that [93, 114]

$$\mathrm{Nu}_{\mathrm{N}} = \frac{\beta H}{\Delta T} = \frac{1}{\Delta T_{\mathrm{N}}}. \tag{3.3}$$

It should be stressed that relation (3.2) only connects both Rayleigh numbers such that they represent a comparable thermal driving – however, this does not imply that the

resulting Nusselt numbers of the individual flows will equal. Unfortunately, the Nusselt number is known *a posteriori* only, which asks for a slight variation from relation (3.2) to allow for an *a priori* scaling and comparison scheme that uses the Dirichlet scenario as starting point – here, presuming $\mathrm{Nu_N} \simeq \mathrm{Nu_D}$ (which holds in particular at large Ra [62]) suffices.

As pointed out in section 1.2.2, different thermal boundary conditions ask for different characteristic temperatures for the non-dimensionalisation. Consequently, the resulting temperature drop ΔT_N across the fluid layer may vary. Contrasting different simulations might thus ask for a re-scaling of the flow field – typically, this is done via eq. (3.1). The non-dimensional quantities can thereto be re-scaled as follows: $\boldsymbol{x}_\mathrm{rs} = \boldsymbol{x}$, $\boldsymbol{u}_\mathrm{rs} = \boldsymbol{u}/\sqrt{\Delta T_\mathrm{N}}$, $T_\mathrm{rs} = (T - \langle T \rangle_V)/\Delta T_\mathrm{N} + \langle T \rangle_V$, $t_\mathrm{rs} = t\sqrt{\Delta T_\mathrm{N}}$, and $p_\mathrm{rs} = p/\Delta T_\mathrm{N}$. Note that consequently $0 \leq \langle T_\mathrm{rs} \rangle_A \leq 1$. Such a re-scaling (from, e.g., $\tau_{\mathrm{f,\,N}}$ to $\tau_{\mathrm{f,\,D}}$) is not always necessary and applied only at selected parts of the present thesis – if so, this will be explicitly signified.

3.1.3 Rayleigh-Bénard convection at various boundary conditions

The investigation of the impact of boundary conditions starts with scenarios at $\mathrm{Ra_D} \in \{10^4, 10^5, 10^6, 10^7\}$ in the no-slip case – as the corresponding $\mathrm{Ra_N}$ are subsequently derived based on the simulations' $\mathrm{Nu_D}$, the actual Ra differ significantly. Table 3.1 summarises the important parameters for all simulations relevant for this section 3.1, underlining that they cover the weakly non-linear up to the fully turbulent regimes independently of the combination of boundary conditions.

3.1.3.1 Comparison of the global heat and momentum transport

Every simulation is run as long as necessary to relax into a statistically stationary regime, which may – depending on especially the thermal boundary condition – require up to $\mathcal{O}(10^4 \tau_\mathrm{f})$. From a qualitative point of view, the global heat and momentum transport – as measured by Nu and Re – increase when substituting no-slip by free-slip conditions. This is due to the weaker impact of the plates on the flow in case of the latter, allowing higher velocities and thus an increased heat transfer. The qualitative change of the global transport is similar when replacing the Dirichlet with Neumann boundary conditions, as well as when the Rayleigh number is increased while the specific combination of boundary conditions is fixed. Overall, these global measures taken at the final phase of the simulations confirm that the scaling scheme introduced above is well-chosen.

The quantitative scaling of the Nusselt number is visualised in figure 3.2 (a, b) for all simulations. As can be seen, the estimated scaling exponents for $\mathrm{Ra_N}$ in the Neumann scenarios differ significantly from the ones obtained for $\mathrm{Ra_D}$ at Dirichlet conditions. However, re-scaling $\mathrm{Ra_N}$ to $\mathrm{Ra_D}$ via eq. (3.2) – yielding scaling exponents of roughly $\gamma_{2,\mathrm{Nns}} \approx 0.223$ and $\gamma_{2,\mathrm{Nfs}} \approx 0.251$, see also the dashed lines in the panels – supports the expected increasing congruence [62] at large Ra. The vertical profiles of the temperature fields confirm this similarity by an extended mixed bulk of the fluid layer. The *bulk* is a region close to the midplane (i.e. $z = 0.5$) which is mostly unaffected by the (thermal) *boundary layers* – the characteristic thickness of the latter is given by $\delta_T = 1/(2\,\mathrm{Nu})$.

Run	Ra	Γ	N_e	N	t_r	Nu	Re	Λ_T
Dns1	$10,000$	60	$200^2 \times 4$	7	$2,300$	2.22 ± 0.01	17.3 ± 0.0	4.55 ± 0.04
Dns2	$100,000$	60	$200^2 \times 4$	11	$1,450$	4.34 ± 0.02	68.6 ± 0.1	4.60 ± 0.07
Dns3	$1,000,000$	60	$400^2 \times 8$	7	$1,100$	8.30 ± 0.03	219.2 ± 0.3	5.06 ± 0.05
Dfs1	$3,850$	60	$200^2 \times 4$	7	$1,250$	2.71 ± 0.02	21.6 ± 0.1	5.25 ± 0.09
Dfs2	$38,501$	60	$200^2 \times 4$	11	$1,450$	5.29 ± 0.04	74.2 ± 0.2	5.30 ± 0.17
Dfs3	$385,014$	60	$400^2 \times 8$	7	$1,100$	10.21 ± 0.04	215.8 ± 0.5	5.34 ± 0.10
Dfs4	$3,850,139$	20	$280^2 \times 16$	7	200	19.97 ± 0.26	608.7 ± 4.5	6.17 ± 0.14
Nns1	$22,263$	60	$200^2 \times 4$	7	$7,000$	3.03 ± 0.01	18.9 ± 0.0	59.75 ± 0.00
Nns2	$434,290$	60	$200^2 \times 4$	11	$14,500$	4.87 ± 0.04	73.3 ± 0.4	59.75 ± 0.01
Nns3	$8,310,000$	60	$400^2 \times 8$	7	$21,400$	8.93 ± 0.04	229.6 ± 0.5	59.76 ± 0.01
Nfs1	$10,432$	60	$200^2 \times 4$	7	$4,000$	3.93 ± 0.12	26.4 ± 0.4	59.66 ± 0.04
Nfs2	$203,576$	60	$200^2 \times 4$	11	$6,500$	6.74 ± 0.10	81.4 ± 0.7	59.66 ± 0.02
Nfs3	$3,928,297$	60	$400^2 \times 8$	7	$10,000$	12.29 ± 0.16	229.0 ± 1.4	59.72 ± 0.02
Nfs4	$76,887,279$	60	$830^2 \times 16$	7	$19,000$	23.47 ± 0.24	635.9 ± 3.1	59.68 ± 0.02

Table 3.1: Simulation parameters of the direct numerical simulations studying the impact of different thermal and mechanical boundary conditions – the Prandtl number $\mathrm{Pr} = 1$ for all runs. The table contains the Rayleigh number Ra, the aspect ratio Γ, the total number of spectral elements N_e in the simulation domain via $N_{\mathrm{e},\,x} \times N_{\mathrm{e},\,y} \times N_{\mathrm{e},\,z}$, the polynomial order N on each spectral element, the total runtime of the simulation t_r in units of the corresponding free-fall times τ_f, the resulting Nusselt number Nu, the Reynolds number Re, and the integral length scale Λ_T (see eq. (3.4)) of the temperature field at midplane. All values correspond to the late state of the flow where the large-scale flow structures are completely established. Nu, Re and Λ_T are typically determined from 50 snapshots within the last $500\tau_\mathrm{f}$ of each simulation, while error bars are determined by the standard deviation.

Such profiles are exemplified for one pair of simulations in panel (c). Interestingly, the Neumann runs exhibit a (weak) stable stratification close to the midplane. As this corresponds to a density stratification that is counter-directed to the applied inverse one which initially causes the convective motion in Rayleigh-Bénard convection, this observation suggests to analyse the flow structure in the following in more detail.

3.1.3.2 Comparison of instantaneous temperature fields at the midplane

The generated dataset provides three complete sets of simulations for which all four combinations of boundary conditions, just as shown by figure 3.1, are available. Figure 3.3 visualises the temperature field of one instantaneous snapshot at the midplane for all of them.

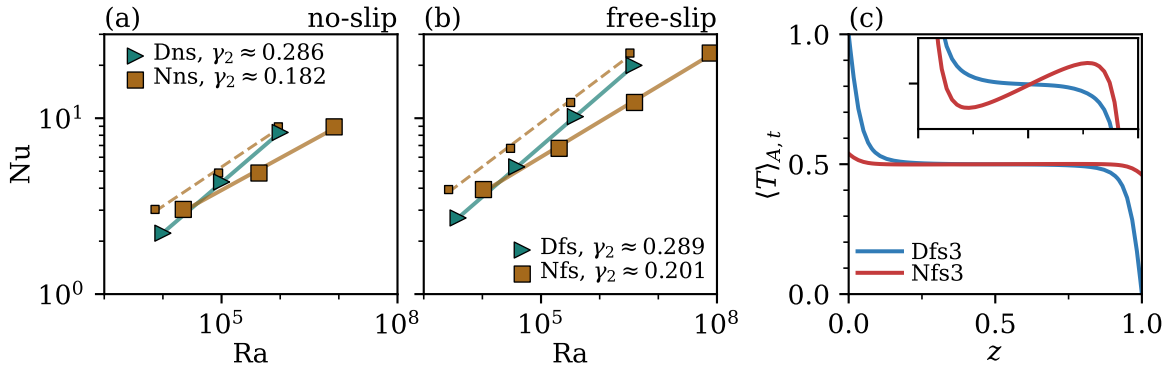

Figure 3.2: Heat transfer at different boundary conditions. (a, b) The global heat transport scales differently with $\mathrm{Ra_D}$ or $\mathrm{Ra_N}$ for different combinations of boundary conditions. The legends include the estimated scaling exponents from eq. (1.23), whereas the smaller brown markers result from re-scaling $\mathrm{Ra_N}$ via eq. (3.2). (c) Vertical profiles of the temperature field indicate the extended bulk region and thermal boundary layers independently of the thermal boundary condition. The inset highlights the slight stable stratification in this bulk for the Neumann scenario by plotting the re-scaled temperature profile $\langle T_{\mathrm{rs}} \rangle_{A,t}$.

The temperature pattern of Dirichlet simulation run Dns1 offers pretty regular and only weakly time-dependent structures – these are called *spiral defect chaos* and reminiscent of the straight convection rolls at the onset of convection. In this case, the temperature and velocity fields are closely connected as (up-) down-welling fluid corresponds to (hot) cold regions. As the Rayleigh number is increased, the flow becomes successively more affected by fluctuations. The observation is similar for the Dfs scenario. Hence, independently of the mechanical boundary condition, the flow evolves towards the recently studied turbulent superstructures [75].

The flow structures transform fundamentally once the Neumann boundary conditions are applied instead. All flows evolve in a characteristic way, exhibiting in the final state basically one cold and one hot spot which both span across extremely extended parts of the domain. As will be shown later in section 3.1.3.3, it is the gradual aggregation process towards these structures that requires the extraordinary long evolution times of all the Neumann simulations. These spots represent the thermal footprint of domain-sized counter-rotating convection cells in x- and y-direction that are superposed by smaller structures especially for larger Rayleigh numbers. Their arrangements indicate that they represent the largest wavelength possible for the present domain – the rotated square pattern is thus nothing but a final adjustment of the flow to the periodic boundary conditions in the lateral directions. Simultaneously, the critical mode from the onset of convection offers independently of mechanical boundary conditions an infinite wavelength (see table 1.1), which suggests to interpret this large-scale pattern as a finite-size relic of the critical mode. Remarkably, this critical mode seems not to be forgotten by the dynamical system even far beyond $\mathrm{Ra_{crit}}$ and dominates still the fully turbulent flows.

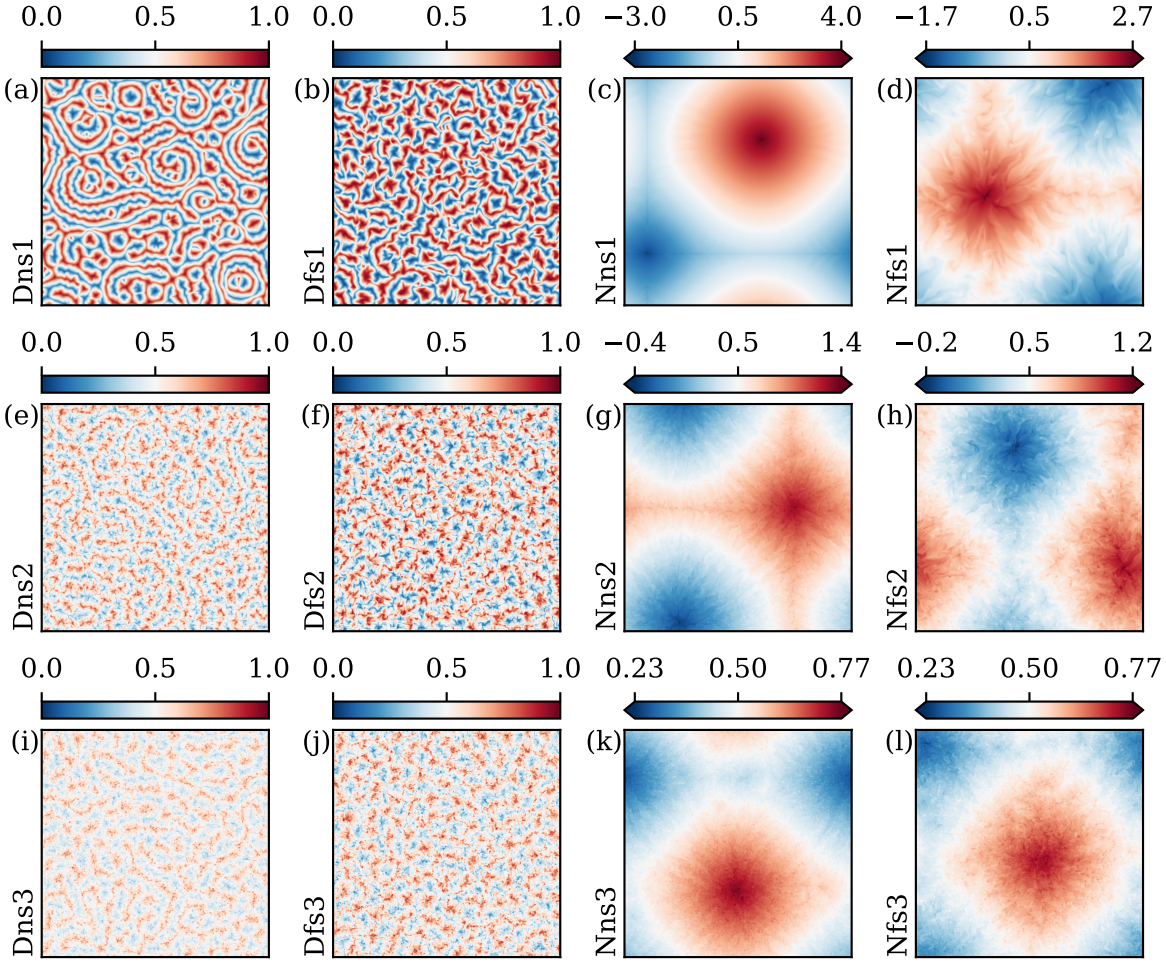

Figure 3.3: Flow patterns at midplane for all boundary conditions. All panels visualise the temperature field $T(x, y, z = 0.5)$ across the entire horizontal cross-section from the final statistically stationary state. Different combinations of boundary conditions are arranged in different columns, whereas the Rayleigh numbers increase from top to bottom. Obviously, the thermal boundary conditions rule the large-scale flow structure. See table 3.1 for detailed information on the simulations.

Figure 3.4 (a) proves the existence of this large-scale cell for the highest accessible Rayleigh number. Enlarging a small fraction from within the thermal boundary layer close to the top plane, see figure 3.4 (b), underlines the coexistence of very differently sized structures in this flow. In analogy to the astrophysical motivation – for which the free-slip boundary conditions are closest too –, the large-scale convection cell will be termed *supergranule* whereas the significantly smaller fine-scale pattern will be termed *granules*. As will be shown in section 3.1.3.3, these two hierarchical stages correspond to different spectral peaks, whereas the granules will be related to instabilities of the thermal boundary layer and the associated thermal plume formation later in section 3.2.2.3.

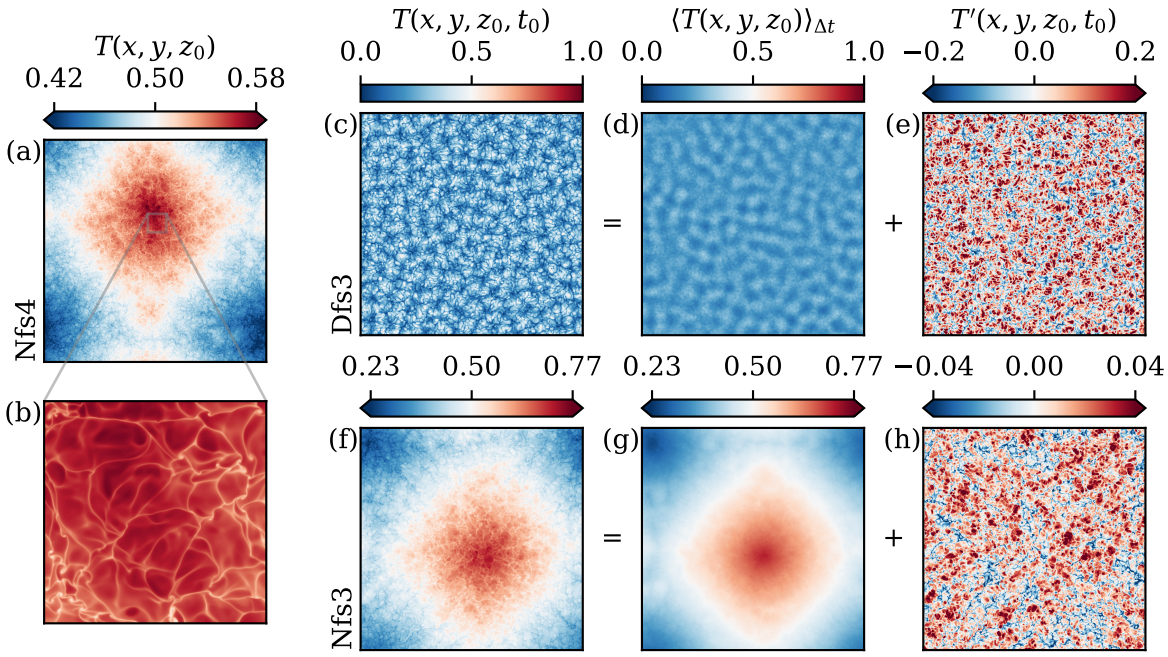

Figure 3.4: Hierarchies of flow structures. (a, b) The supergranule emerges even for the highest accessible Ra and is superposed by finer granule patterns. The zoom enlarges a region of size 5×5. (c – h) Reynolds decomposition of one Dirichlet and one Neumann flow field. Panels (d, g) highlight the striking differences between turbulent superstructures and the supergranule. All fields are taken close to the top plane at $z_0 = 1 - \delta_T/2$ with t_0 located in the final phase of the simulation and $\Delta t = 500$. Unless otherwise noted, all panels visualise the entire horizontal cross-section.

The different character between turbulent superstructures known from the Dirichlet case, and the supergranule discovered for the Neumann case is underlined by figure 3.4 (c – h). Here, a Reynolds decomposition is applied to the temperature field such that $T(\boldsymbol{x}, t) = \langle T(\boldsymbol{x})\rangle_{\Delta t} + T'(\boldsymbol{x}, t)$. With $\Delta t = 500$, this temporal filter separates the slowly evolving characteristics of the flow from the rapid fluctuations. In the Dirichlet case, this allows to differentiate between the turbulent superstructures and a fine skeleton of plume ridges. Both of these structures are in terms of their horizontal extension definitely related. In contrast, in the Neumann case the supergranule is now clearly revealed. Although the instantaneous fluctuations are more similar to the Dirichlet case, their horizontal extension differs significantly from that of the supergranule.

This systematic comparison shows unambiguously that Rayleigh-Bénard convection as the paradigm of thermal convection is governed by the thermal boundary conditions. Albeit the mechanical boundary conditions impact the flow to some extend, the thermal ones transform the flow exceptionally. The similarity of the large-scale cell to the critical structure known from the onset of convection is striking, however previous studies have not recognised such fundamental differences to the Dirichlet scenario in the turbulent regime. This might be attributed to the following three important aspects in which the

present study differs from the majority of previous numerical studies:

1. Neumann boundary conditions are applied to the temperature field.
2. The simulations are performed for extraordinary long evolution times $\mathcal{O}\left(10^4 \tau_\mathrm{f}\right)$.
3. A horizontally widely extended domain is considered.

This clearly asks to study the emergence of this large-scale structure in more detail.

3.1.3.3 Time-dependent gradual supergranule aggregation

Figure 3.5 visualises the investigation of the entire evolution of simulation run Nfs1 from the initial condition over the transient state into the statistically stationary regime. Panels (a – e) prove that the supergranule is the result of the gradual aggregation of smaller flow structures. This process ceases only when the growing circulation rolls reach domain size and is most easily detectable from the temperature field.

Interestingly, the global measures of heat and momentum transport, Nu and Re, stay mostly unaffected during this process as shown in panel (f). However, as demonstrated in [V1], the fraction of the convective heat flux transported by the supergranule shifts throughout the slow formation and makes up eventually up to 40%.

To measure the growth of the patterns, the so-called integral length scale [115]

$$\Lambda_T\left(z_0, t\right) := 2\pi \frac{\int_{k_\mathrm{h}} \left[E_{TT}\left(k_\mathrm{h}, z_0, t\right)/k_\mathrm{h}\right] dk_\mathrm{h}}{\int_{k_\mathrm{h}} E_{TT}\left(k_\mathrm{h}, z_0, t\right) dk_\mathrm{h}} \tag{3.4}$$

based on the azimuthally averaged Fourier energy spectrum (see below) of the temperature variance, $E_{TT}\left(k_\mathrm{h}, z_0, t\right)$, is computed throughout the evolution. As indicated in panel (g), this quantity converges during the transient towards the horizontal periodic length given by the aspect ratio and finally indicates the numeric bound on the pattern size. Its value for the statistically stationary state is given in table 3.1.

In spite of the converging pattern size for $t \gtrsim 1,500$, the aggregation has not completely finished as the thermal variance of the flow field still increases until $t \approx 3,000$. To measure this, the temperature field is decomposed into the linear temperature profile $T_\mathrm{lin}\left(z\right) := 1 - z$ which manifests in case of pure heat conduction, and its deviation $\Theta\left(\boldsymbol{x}, t\right)$ such that

$$\Theta\left(\boldsymbol{x}, t\right) := T\left(\boldsymbol{x}, t\right) - T_\mathrm{lin}\left(z\right). \tag{3.5}$$

The standard deviation – also known as the root-mean-square value – of the *temperature deviation field* $\Theta_\mathrm{rms} := \sqrt{\langle \Theta^2 \rangle_V}$ is included in panel (g). Its convergence marks the reach of the statistically stationary regime of the flow.

This supergranule aggregation cannot only be observed in physical space, but also in spectral space. Any horizontally periodic quantity can be expanded in a *Fourier series* of the form

$$\Phi\left(\boldsymbol{x}_\mathrm{h}, z_0, t\right) = \sum_{\boldsymbol{k}_\mathrm{h}} \hat{\Phi}\left(\boldsymbol{k}_\mathrm{h}, z_0, t\right) \; e^{\imath \boldsymbol{k}_\mathrm{h} \cdot \boldsymbol{x}_\mathrm{h}} \tag{3.6}$$

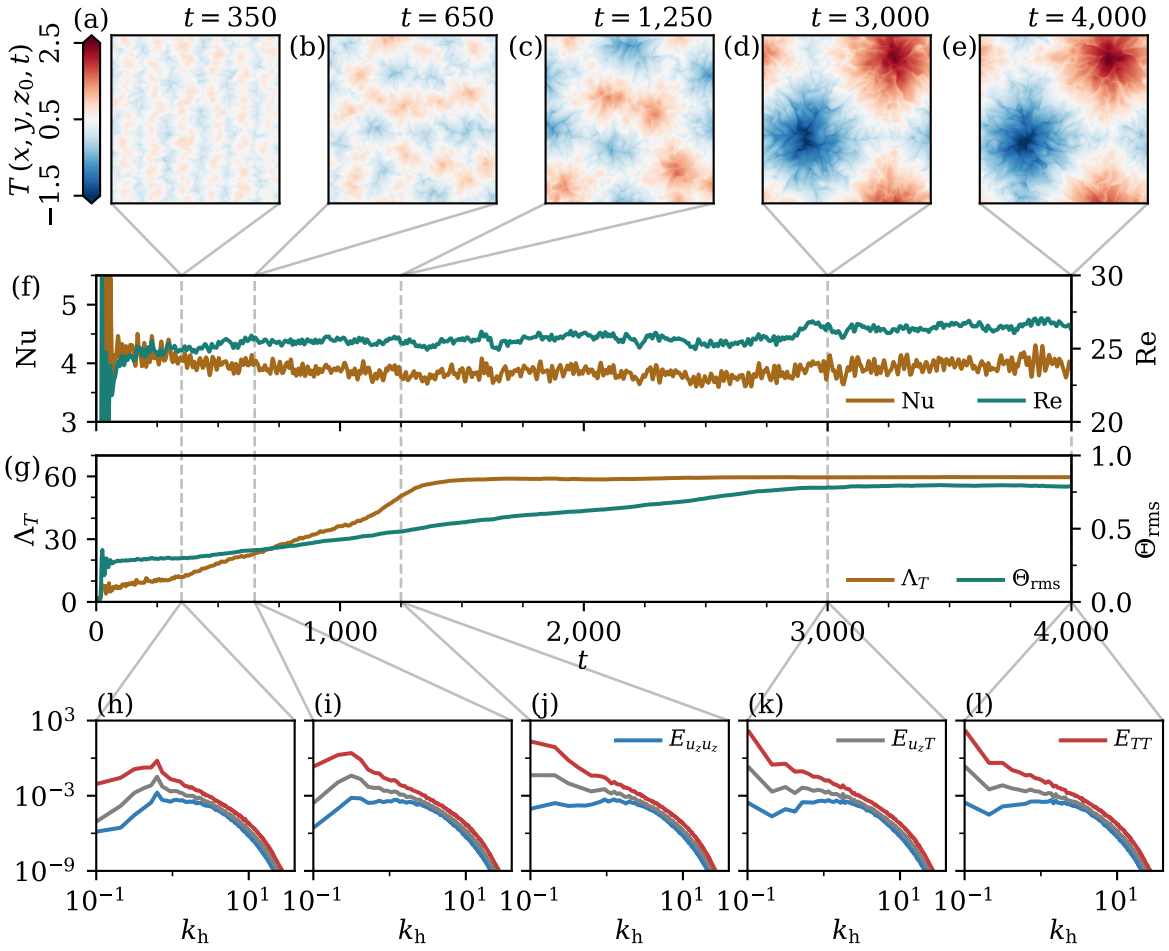

Figure 3.5: Gradual supergranule aggregation. The final supergranule of simulation run Nfs1 establishes after a long initial transient that takes until $t \approx 3,000$ and is statistically stationary just afterwards. (a – e) Horizontal slices of the instantaneous temperature field at $z_0 = 1 - \delta_T/2$ visualise the gradual pattern formation across the entire horizontal cross-section. (f) The global heat and momentum transport remain mostly unaffected during the entire evolution. (g) In contrast, the integral length scale of the temperature field $\Lambda_T(z_0)$, as well as the standard deviation Θ_{rms} of the temperature deviation field indicate an ongoing transient process. (h – l) Azimuthally averaged instantaneous Fourier spectra at z_0 – corresponding to the kinetic energy with respect to the vertical velocity component $E_{u_z u_z}$, the co-spectrum of the turbulent convective heat flux $E_{u_z T}$, and the temperature variance E_{TT} – exhibit a shift of energy towards large scales.

with the imaginary number $\imath$, as well as the vectors of horizontal wave numbers $\boldsymbol{k}_\mathrm{h} = (k_x, k_y)$ and coordinates $\boldsymbol{x}_\mathrm{h} = (x, y)$. The numerically discrete wave numbers, here exemplary along the x-direction, are given by $k_{x,n} := 2\pi\ n/L_x$ with $n \in \mathbb{N}$ and $L_x = \Gamma_x$. Thus, n represents the number of complete waves over the non-dimensional periodic length L_x. $\hat{\Phi} = \mathcal{F}(\Phi) \in \mathbb{C}$ is the so-called *Fourier coefficient* with the *Fourier transform* $\mathcal{F}(\cdot)$. With this in mind, the two-dimensional (co-)spectrum of the quantities Φ_1 and Φ_2 is defined by

$$E_{\Phi_1\Phi_2}(\boldsymbol{k}_\mathrm{h}, z_0, t) := \frac{1}{2}\,\Re\left[\hat{\Phi}_1(\boldsymbol{k}_\mathrm{h}, z_0, t)\ \hat{\Phi}_2^*(\boldsymbol{k}_\mathrm{h}, z_0, t)\right] \tag{3.7}$$

where $\Re$ denotes the real part and the asterisk Φ^* the complex conjugate. In the present domain, both horizontal directions are isotropic and so it might be equally expressed as $E_{\Phi_1\Phi_2}(\boldsymbol{k}_\mathrm{h}, z_0, t) \equiv E_{\Phi_1\Phi_2}(k_\mathrm{h}, \phi, z_0, t)$ with the absolute horizontal wave number $k_\mathrm{h} := |\boldsymbol{k}_\mathrm{h}|$ and the azimuthal angle ϕ. Due to the horizontal isotropy, the azimuthally averaged spectra $E_{\Phi_1\Phi_2}(k_\mathrm{h}, z_0, t) := \langle E_{\Phi_1\Phi_2}(k_\mathrm{h}, \phi, z_0, t)\rangle_\phi$ will be studied in the following.

Panels (h – l) of figure 3.5 plot the spectrum of the kinetic energy with respect to the vertical velocity component $E_{u_z u_z}$, the co-spectrum of the turbulent convective heat flux $E_{u_z T}$, and the temperature variance E_{TT} at several times throughout the flow evolution. During the transient, there is a clear shift of spectral energy from larger to smaller wave numbers, i.e., from structures of smaller to larger horizontal extension, which eventually accumulates at the smallest available wave number $k_\mathrm{min} = 2\pi/\Gamma \approx 0.1$. Although the supergranule is most prominent in the temperature field, it leaves its footprint even in the vertical velocity field as indicated by $E_{u_z u_z}$. Panels (k, l) underline once more the reach of the statistically stationary regime at late times.

The analysis of the full evolution of simulation run Nfs1 from above highlights the complexity of the supergranule establishment. The transient process alters both the velocity and temperature field, although global measures remain mostly unaffected. Based on Λ_T and Θ_rms, the pattern size seems to increase roughly linearly. This process proceeds very slowly – interestingly, it seems not to be related to either a *vertical or horizontal diffusion time scale*, $\tau_\Phi = \tau_{\nu,\kappa}$ or $\tau_{\Phi,\mathrm{h}} := \Gamma^2\tau_\Phi$, respectively.

This supergranule formation was not studied previously and is thus an original result of this comparison of different boundary conditions in Rayleigh-Bénard convection. Hence, the subsequent sections in this chapter are dedicated to investigate its enthralling character in more detail and even throughout the multi-dimensional parameter space. As mechanical boundary conditions show relatively little impact, the focus is in the following on the free-slip boundary condition in reminiscence to the astrophysical motivation.

3.2 Relating supergranule aggregation to stability mechanisms

The previous section 3.1.3 revealed that the final supergranule – which establishes in the Neumann case only – can be interpreted as the finite size relic of the critical mode from the onset of convection which is included in table 1.1. This suggests to analyse the stability properties of the flow in more detail.

3.2.1 Linear stability at the onset of convection

The *primary* instability of a flow at rest towards convection can be studied analytically by a *linear stability analysis*. In fact, this is the method that already Lord Rayleigh used back in 1916 to analyse Rayleigh-Bénard convection – the experimental setup that is now named after him to honour his contributions – and to successfully explain the onset of convection [116].

The key idea of such an analysis is to study the time-dependence of tiny perturbations that are added onto a base (quiescent) state. As these perturbations are very small, only the leading (linear) contribution is retained – disturbances of higher order become successively smaller and are thus neglected. This terms the analysis *linear*. The fluid at rest represents the equilibrium state in Rayleigh-Bénard convection from which perturbations may either decay, persist or grow. This can be quantified by the growth rate $\sigma = \sigma_\mathrm{r} + \imath\sigma_\mathrm{i} \in \mathbb{C}$, see also eq. (A.37). Excluding oscillatory motions, i.e. $\sigma_\mathrm{i} = 0$, the case of $\sigma_\mathrm{r} = \sigma = 0$ is of particular importance as this marks the transition of the system from being stable to being unstable against disturbances. In case of the latter, the base state is left and perturbations grow over time. The transition state itself marks eventually the neutral (or marginal) stability.

The linear stability analysis for (rotating) Rayleigh-Bénard convection with free-slip boundary conditions is provided in appendix A step-by-step for stationary modes. The solution is independent of the Prandtl number[1] but depends on the thermal boundary conditions. In the Dirichlet case, the marginal state is given by [39]

$$\mathrm{Ra}_\mathrm{D,\,marg} = \frac{1}{k_\mathrm{h}^2}\left[\left(k_\mathrm{h}^2 + \pi^2\right)^3 + \mathrm{Ta}\;\pi^2\right], \tag{3.8}$$

whereas in the Neumann case [29]

$$\mathrm{Ra}_\mathrm{N,\,marg} = \frac{\pi^2}{8}\left[\left(k_\mathrm{h}^2 + \pi^2\right)^2 + \frac{\mathrm{Ta}\;\pi^2}{k_\mathrm{h}^2 + \pi^2}\right] \tag{3.9}$$

can be derived for a truncated system. The *Taylor number*

$$\mathrm{Ta} := \frac{4\Omega^2 H^4}{\nu^2} \equiv \frac{\mathrm{Ra}}{\mathrm{Pr}}\,\mathrm{Ro}^{-2} \tag{3.10}$$

represents the squared ratio of the system's Coriolis to viscous forces [52] and can be related to the Rossby number as seen in eq. (3.10). Its appearance clearly indicates the importance of viscous interactions at the onset of convection (in favour of the free-fall inertial balance).[2]

[1] The situation is actually very subtle. In the rotating scenario, oscillatory modes (i.e. $\sigma_\mathrm{r} = 0$ but $\sigma_\mathrm{i} \neq 0$) might set in earlier than stationary modes (i.e. $\sigma = 0$) if $\mathrm{Pr} < \mathrm{Pr}_\mathrm{crit}$ with $\mathrm{Pr}_\mathrm{crit} \simeq 0.677$ and rotation is strong enough. In contrast, stationary modes will always set in first if $\mathrm{Pr} \geq \mathrm{Pr}_\mathrm{crit}$. In the non-rotating scenario, stationary modes dominate independently of Pr [29, 39, 40].

[2] This can be further understood by a closer look at the definition of the Taylor number – it represents in fact the squared ratio of the vertical viscous diffusion time scale to the (Coriolis) rotation time scale, $\mathrm{Ta} = \tau_\nu^2/\tau_\Omega^2$. The *Ekman number* $\mathrm{Ek} = \tau_\Omega/\tau_\nu \equiv \mathrm{Ta}^{-1/2}$ represents just another popular parameter which can be used equivalently. More information on time scales related to rotation are provided in section 3.4.2.

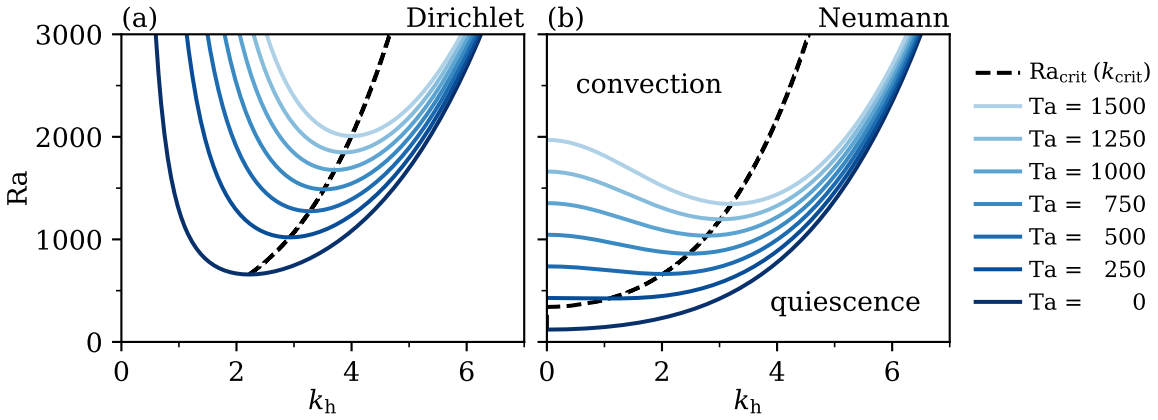

Figure 3.6: Linear stability for varying thermal boundary conditions. The primary instability is governed by the thermal boundary condition as highlighted by slices at different Ta within the three-dimensional Ra–Ta–k_h parameter space (see eq. (3.8) and (3.9)). The dashed lines trace the global minimum, indicating the course of the critical values. Free-slip boundary conditions are applied throughout.

Figure 3.6 visualises the neutral stability curves for both thermal boundary conditions. The global minimum of the individual curves mark the *critical point* at the onset of convection – this is exactly what is provided in table 1.1 for the non-rotating scenario. It is easy to realise that there is a striking qualitative difference between Dirichlet and Neumann conditions already in this case.

Additional rotation around the vertical axis generally stabilises the fluid independently of the thermal boundary conditions. However, while the critical wave number at the onset of convection steadily increases in the Dirichlet case, the Taylor number needs to surpass the critical value $\mathrm{Ta}_{\mathrm{crit}} \simeq 180.15$ [29, 40] to move the critical wave number off zero in the Neumann case. In other words, the critical wavelength at the onset of Rayleigh-Bénard convection with Neumann boundary conditions becomes finite if rotation is only strong enough. The dashed black lines in figure 3.6 trace the critical point through the parameter space and underline the qualitative differences between both thermal boundary conditions once more. These differences vanish in the asymptotic limit of strong rotation [29, 117], i.e. $\mathrm{Ro} \to 0$ or $\mathrm{Ta} \to \infty$.

A further very interesting result is obtained by an analytical, fully non-linear stability analysis of two-dimensional convection rolls in non-rotating Rayleigh-Bénard convection with Neumann boundary conditions slightly above the onset of convection with $\mathrm{Ra} \gtrsim \mathrm{Ra}_{\mathrm{crit}}$. Such a study of *secondary* instabilities reveals 'that each mode is unstable to one of longer wavelength than itself, so that any long box will eventually contain a single roll' [118]. This implies that flow structures slightly above the onset of convection tend to extend horizontally towards the largest possible scale. This seems to be a striking analogy to the growing size of the supergranule during its aggregation process, although the latter takes place even far beyond the onset of convection.

3.2.2 Leading Lyapunov vector analysis

The non-linearity of the Navier-Stokes equation and the resulting complexity of its solutions in the turbulent regime far off the onset of convection render an analytical solution intractable. Thus, the stability analysis in this extended region of the parameter space asks for different methods. One method to analyse the stability of complex flows is the so-called *leading Lyapunov vector analysis*.

3.2.2.1 Conceptual framework

In the framework of dynamical systems (in which this analysis is well-established), the evolution of the turbulent convection flow is seen as a trajectory in the very high-dimensional (phase or) state space. In this space, the state of the fluid flow can be described by the column vector $\boldsymbol{y}(t) = [\boldsymbol{u}(\boldsymbol{x}_i, t), T(\boldsymbol{x}_i, t)]$ which combines the velocity and scalar temperature field for all discrete grid points $\boldsymbol{x}_i$ with $i = 1 \dots N_\mathrm{e} N^3$ (in different rows) for any time. The non-linear governing equations (1.6) – (1.8) can thus be seen as an operator $\boldsymbol{F}$ that acts on this vector $\boldsymbol{y}$ such that [119, 120]

$$\frac{d\,\boldsymbol{y}(t)}{dt} = \boldsymbol{F}[\boldsymbol{y}(t)]. \tag{3.11}$$

Rayleigh-Bénard convection represents a chaotic dynamical system [121–123], i.e. its trajectory depends sensitively on the initial conditions [119, 123]. The key idea of the leading Lyapunov vector analysis[3] is now to probe the strength of the exponential separation of two initially very close system trajectories $\boldsymbol{y}(t)$ and $\boldsymbol{y}(t) + \delta\boldsymbol{y}(t)$ in this high-dimensional state space [57, 123] – see figure 3.7. The perturbation field or separation vector $\delta\boldsymbol{y}(t) = [\delta\boldsymbol{u}(\boldsymbol{x}_i, t), \delta T(\boldsymbol{x}_i, t)]$ of these two trajectories develops out of the random, infinitesimal initial perturbation $\delta\boldsymbol{y}(0)$ due to the chaotic nature of the system via [119]

$$\frac{d\,\delta\boldsymbol{y}(t)}{dt} = \boldsymbol{J}(\boldsymbol{y})\,\delta\boldsymbol{y} + \boldsymbol{G}(\boldsymbol{y}, \delta\boldsymbol{y}) \simeq \boldsymbol{J}(\boldsymbol{y})\,\delta\boldsymbol{y}. \tag{3.12}$$

Here, $\boldsymbol{J}(\boldsymbol{y})\,\delta\boldsymbol{y}$ represent the tangent linear terms with the Jacobian $\boldsymbol{J} = \partial\boldsymbol{F}/\partial\boldsymbol{y}$ and $\boldsymbol{G}(\boldsymbol{y}, \delta\boldsymbol{y})$ covers the high-order non-linear terms [119]. As the perturbation is infinitesimal, one can presume that its evolution is captured sufficiently by the linear terms which avoids the complexity of the non-linear problem and leads to the expression on the right

[3] Theoretically it would be possible to evolve $n \leq N_\mathrm{dof}$ orbiting trajectories along with the original system trajectory [57]. However, due to the computational complexity this becomes quickly impossible as this requires to solve n versions of equations (3.13) – (3.15) for n different initial perturbations $\delta\boldsymbol{y}_n(0)$ simultaneously with the original equations (1.6) – (1.8). Furthermore, to avoid numerical overflows as well as errors that might originate from the tendency that all perturbation vectors point towards the direction of fastest growth in the tangent space, these $\delta\boldsymbol{y}_n$ are periodically re-orthonormalised using a Gram-Schmidt (GS) procedure [57, 122, 123]. Consequently the *leading* Lyapunov vector $\delta\boldsymbol{y} \equiv \delta\boldsymbol{y}_1$ represents the only one that points in a physically important direction [122]. This underlines the importance of the leading perturbation vector and justifies the restriction to its analysis.

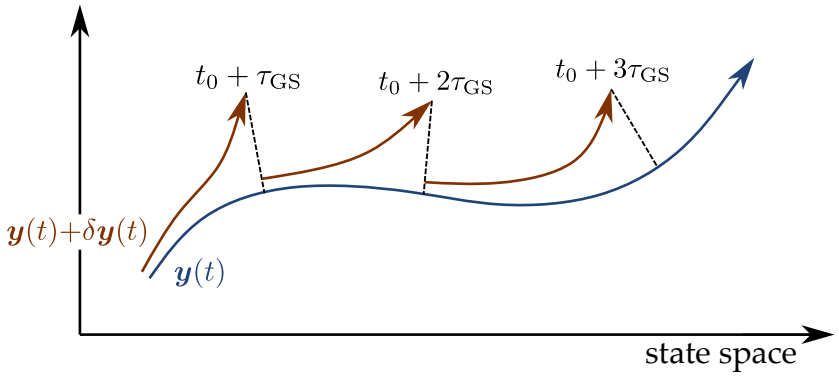

Figure 3.7: Concept of the leading Lyapunov vector analysis. The original system trajectory $\boldsymbol{y}(t)$ is orbited in the high-dimensional state space by another very close trajectory $\boldsymbol{y}(t) + \delta\boldsymbol{y}(t)$. The separation $\delta\boldsymbol{y}(t)$ quantifies eventually the former's susceptibility to infinitesimal perturbations and is periodically re-orthonormalised (see the footnote on page 34) as indicated by τ_{GS}.

of eq. (3.12) [119, 124]. In the particular Rayleigh-Bénard convection scenario at hand, this set of linearised governing equations is given by [111, 124]

$$\nabla \cdot \delta\boldsymbol{u} = 0, \tag{3.13}$$

$$\frac{\partial\, \delta\boldsymbol{u}}{\partial t} + (\boldsymbol{u}\cdot\nabla)\,\delta\boldsymbol{u} + (\delta\boldsymbol{u}\cdot\nabla)\,\boldsymbol{u} + \frac{1}{\mathrm{Ro}}\,\boldsymbol{e}_z \times \delta\boldsymbol{u} = -\nabla\delta p + \sqrt{\frac{\mathrm{Pr}}{\mathrm{Ra}}}\,\nabla^2\delta\boldsymbol{u} + \delta T\boldsymbol{e}_z, \tag{3.14}$$

$$\frac{\partial\, \delta T}{\partial t} + (\boldsymbol{u}\cdot\nabla)\,\delta T + (\delta\boldsymbol{u}\cdot\nabla)\,T = \frac{1}{\sqrt{\mathrm{RaPr}}}\,\nabla^2\delta T. \tag{3.15}$$

This time-dependent separation $\delta\boldsymbol{y}$ of the two nearby trajectories quantifies the system trajectory's susceptibility to infinitesimal perturbations. If this separation grows over time, the system trajectory depends sensitively on the initial conditions and the system can thus be termed chaotic. The resulting exponential growth can be quantified by the instantaneous leading Lyapunov exponent [124]

$$\lambda(t) \equiv \lambda_1(t) := \frac{d}{dt}\ln\left[\frac{\|\delta\boldsymbol{y}(t)\|}{\|\delta\boldsymbol{y}(0)\|}\right] \tag{3.16}$$

and implies $\lambda > 0$ for a chaotic system [122, 123] with a norm that is given by

$$\|\delta\boldsymbol{y}(t)\| = \sqrt{\frac{1}{V}\int_V \left[\delta\boldsymbol{u}^2(t) + \delta T^2(t)\right] dV}. \tag{3.17}$$

Besides this global aspect, the perturbation field $\delta\boldsymbol{y}$ allows even further insights as it is the local magnitude of its components that encodes the regions of largest susceptibility to local instabilities out of the present (turbulent) state [122]. Hence, it should contain the essential information to relate the supergranule aggregation to instability mechanisms.

Run	Ra	Γ	N_e	N	t_r	Nu	Re	Λ_T
Dfs2_L	$38,501$	60	$200^2 \times 4$	7	785	5.29 ± 0.03	74.0 ± 0.3	5.27 ± 0.12
Nfs2_L	$203,576$	60	$200^2 \times 4$	7	$6,770$	6.71 ± 0.10	80.2 ± 0.5	59.37 ± 0.06

Table 3.2: Simulation parameters of the direct numerical simulations performing a leading Lyapunov vector analysis – the Prandtl number $\mathrm{Pr} = 1$ and free-slip boundary conditions are applied for all runs. Nu, Re and Λ_T are determined from several hundreds of snapshots within the last $500\tau_f$ of each simulation. For more information, see table 3.1.

3.2.2.2 Associating the temperature perturbation vector with flow instabilities

To study stability mechanisms in Rayleigh-Bénard convection through a leading Lyapunov vector analysis, selected simulations from section 3.1 with free-slip boundary conditions are repeated with a simultaneous evolution of the orbiting trajectory – table 3.2 summarises important parameters for these additional simulation runs.

Figure 3.8 exhibits in panels (a – d) the temporal evolution of a local defect generation that can be detected in the temperature field $T(x, y, z_0 = 0.5, t)$ at midplane. In particular, the split of a turbulent convection roll as part of turbulent superstructures in the Dirichlet case can be observed. Interestingly, this change in the flow structure can also be detected based on the corresponding dynamical sequence of the temperature perturbation field's magnitude $|\delta T(x, y, z_0 = 0.5, t)|$, see panels (e – h).

This observation proves that the leading Lyapunov vector analysis – which got established in the past for the weakly non-linear regime of Rayleigh-Bénard convection only [120–122, 125] – is a useful tool even for a fully turbulent flow as it connects the separation of the two nearby system trajectories with local instabilities. Moreover, the detected instabilities are very similar to those found in the weakly non-linear regime.

As pointed out above in section 3.2.2.1, the magnitude of the perturbation field $\delta\boldsymbol{y}$ encodes the regions of largest susceptibility to instabilities. Although the described dynamical sequence is taken at the midplane where such a defect generation can be related most easily to turbulent superstructures, it follows that horizontal slices at very different vertical positions are most susceptible in the flow. In particular, in case of Dirichlet boundary conditions the most sensitive regions can be found at the top of the thermal boundary layer, whereas it is the top and bottom planes that are most sensitive in the Neumann case [V1].

The dynamical sequence from above is thus repeated for $z_1 = 1 - 2/3\ \delta_T$ in figure 3.8 (i – p). It can be found that instabilities in the Dirichlet case are largest close to (but not at) the downflow regions.

This is in contrast to the Neumann case for which a temporal evolution is provided in figure 3.8 (q – x) for a horizontal slice close to the top plane at $z_2 = 1 - \delta_T/2$. Here, the most unstable regions are found to coincide with the downflow regions. Interestingly, the temperature perturbation field consists of a connected pattern of high-amplitude ridges with a coarser spacing indicating a larger scale of instability.

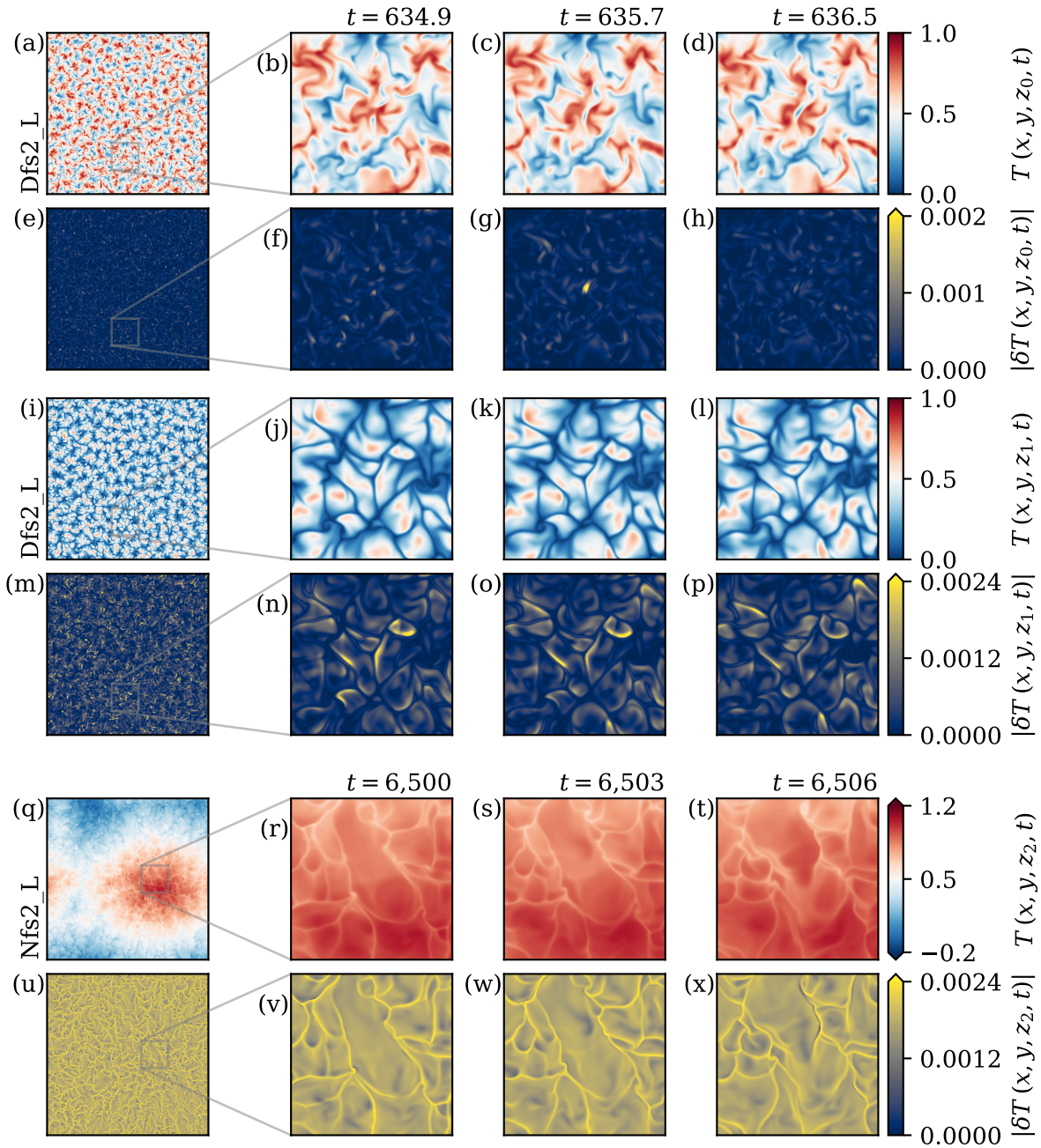

Figure 3.8: Leading Lyapunov vector analysis. (a – h) The temperature perturbation vector comprises information on pattern susceptibility in space and time as shown here for a roll split at midplane, i.e., $z_0 = 0.5$. The most susceptible region depends on the thermal boundary condition. (i – p) The same Dirichlet simulation as in (a – h) but here for $z_1 = 1 - 2/3\ \delta_T$. (q – x) The Neumann scenario offers different and stronger susceptibilities at $z_2 = 1 - \delta_T/2$. The first column visualises the entire horizontal cross-section, whereas the remaining panels highlight dynamical sequences via enlarged regions of interest of size 10×10.

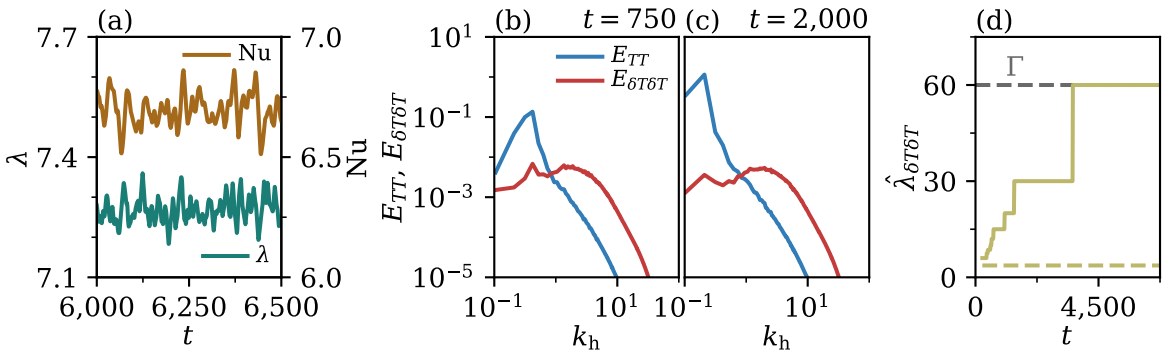

Figure 3.9: Scales of instability in the Neumann scenario Nfs2_L. (a) Global measures of instability and heat transfer vary over time. (b, c) Azimuthally averaged spectra $E_{\Phi\Phi}(k_\mathrm{h}, z_2 = 1 - \delta_T/2, t)$ offer a time-dependent peak during the transient supergranule aggregation. (d) This is captured by the temporal evolution of the unstable wavelengths $\hat{\lambda}_{\delta T \delta T}$ that correspond to local maxima in $E_{\delta T \delta T}$. The spectra are time-averaged over $50\tau_\mathrm{f}$ and $E_{\delta T \delta T}$ is multiplied by 10^6 for better comparability.

3.2.2.3 Scales of instability

The striking differences of unstable structures between the Dirichlet and Neumann flow – see again figure 3.8 (m – p) and (u – x), respectively – ask for a more detailed analysis of the perturbation field. Hence, figure 3.9 provides additional information on the instabilities and corresponding scales.

From a *global* perspective it can be confirmed that the leading Lyapunov exponent $\lambda(t)$ fluctuates – as a global measure of instability – over time similar to the Nusselt number $\mathrm{Nu}(t)$ – as a global measure of heat transfer – around a mean value. Both these measures are contrasted in figure 3.9 (a). The fact that $\lambda > 0$ proves the flow to be chaotic even in the Neumann case.

In contrast from a *local* perspective, the particular scales of instability are studied via the azimuthally averaged spectrum of the temperature perturbation vector $E_{\delta T \delta T}(k_\mathrm{h}, z_2 = 1 - \delta_T/2, t)$ in panels (b, c). Interestingly, this scale analysis seems to offer again a hierarchy of two separate instabilities. First, there is a large-wave-number bump with a peak at $\hat{k}_\mathrm{h} \approx 2$ which can be related to instabilities of the fine granule patterns visualised in figure 3.4 (b). While these instabilities are time-independent, a second but time-dependent peak $\hat{k}_\mathrm{h}(t)$ can be found to move gradually towards larger scales. A comparison of $E_{\delta T \delta T}$ with E_{TT} confirms that this instability corresponds to the gradual supergranule aggregation that yields eventually the supergranule pattern as another step in the pattern hierarchy and is visualised in figure 3.4 (a). This gradual shift suggests finally that the turbulent flow develops instabilities at an increasingly larger scale.

These two scales of instability are given by their corresponding peak wavelength $\hat{\lambda}_{\delta T \delta T} = 2\pi/\hat{k}_\mathrm{h}$ and plotted over time in figure 3.9 (d). In fact, this underlines that the instability mechanism corresponding to the supergranule formation moves steadily to larger wavelengths and ceases only artificially when domain size is reached. It is worth to

stress that the discrete nature of its growth in this panel is just a result of the coarsening of the spectral coordinates at large scales.

Interestingly, this dynamical behaviour of instability mechanisms, especially the time-dependent character, is fundamentally different to the Dirichlet case. For the latter, no time-dependent peak can be found in the temperature perturbation spectrum $E_{\delta T \delta T}$ [V1]. In other words, the crucial distinction seems to be the lack of a hierarchy of instabilities that eventually prevents the formation of a related hierarchy of patterns.

The above leading Lyapunov vector analysis evaluates the dynamical system from a Lagrangian perspective in the very high-dimensional state space. This allows to identify the basic instability mechanism that eventually yields the supergranule as a separate flow structure at a separate scale. It is found that the fully turbulent flow develops instabilities at increasingly larger wavelengths – crucially, this is analogous to secondary instabilities which can be found analytically for slightly above the onset of convection (see section 3.2.1 and [118]). Thus, in addition to the critical mode from the onset of convection, even this formation mechanism seems to persist far into the turbulent regime at $\mathrm{Ra} \gg \mathrm{Ra}_{\mathrm{crit}}$.

In this regime, the Prandtl number becomes typically very important for the dynamics [56, 75, 97] which asks to extend the study of the supergranule along this second control parameter in the following section.

3.3 Supergranule aggregation across various fluids

The comparison of the impact of different thermal boundary conditions in section 3.1 revealed their striking effect on large-scale flow patterns. While the supergranules were found to form for all accessible Rayleigh numbers, a subsequent linear stability analysis in section 3.2.1 showed that their *final* state resembles the critical mode from the onset of convection. Crucially, this critical mode is independent of the working fluid, the latter of which is characterised by the second of the two control parameters of basic Rayleigh-Bénard convection – the Prandtl number.

A subsequent numerical stability analysis of the turbulent system trajectory far beyond the onset of convection via the leading Lyapunov vector, see section 3.2.2, found that the *transient* flow develops instabilities at increasingly larger scales. Interestingly, a similar behaviour was previously reported in [118] for secondary instabilities slightly above the onset of convection. However, although the authors state that their 'results hold quite generally for all Prandtl numbers' [71] – the latter of which does not enter the analysis for symmetric mechanical boundary conditions [118] –, they simultaneously 'do not expect the theory to remain accurate for very small Pr' [118].

As the final supergranule results from the transient supergranule aggregation, clarifying this uncertainty becomes crucial especially due to the strongly varying Prandtl numbers in geo- and astrophysical convection flows – see again table 1.2. The need for this investigation is further supported by the well-known fact that the Prandtl number strongly impacts instability mechanisms slightly above the onset of convection in the complementary Dirichlet case [73, 74].

3.3.1 Diffusion of momentum and advected scalars

In fluid dynamics, diffusion represents the transfer of momentum, heat or other scalar quantities from regions of high concentration to regions of low concentration due to molecular processes. For instance, even in a simple turbulence scenario without advected scalars, the inhomogeneous motion of any viscous fluid will eventually be relaxed by molecular, viscous diffusion from fluid parcels of high momentum to adjacent ones of lower momentum. Beside the gradients of velocities, the strength of this diffusion is governed by the kinematic viscosity ν which enters the Navier-Stokes equation (1.3). As diffusion dominates smaller length scales but becomes practically irrelevant for larger ones, it dictates the smallest observable dynamical length scale – in other words, any inhomogeneous fluid motion below a certain length scale is relaxed immediately due to the effect of viscous diffusion and thus subsequently dissipated into heat.[4] Within the cascade picture of turbulence, see section 3.5.1 and in particular figure 3.15, this corresponds to the last stage and thus the dissipation range.

Dimensional considerations based on this intuition allowed Andrey N. Kolmogorov to quantify the (on average) smallest dynamical length scale in homogeneous, isotropic turbulence – the (mean) *Kolmogorov scale* [126]

$$\langle \eta_\mathrm{K} \rangle_{V,t} := \left(\frac{\nu^3}{\langle \varepsilon \rangle_{V,t}} \right)^{1/4} \equiv H \, \langle \tilde{\eta}_\mathrm{K} \rangle_{\tilde{V},\tilde{t}} \qquad \text{with } \langle \tilde{\eta}_\mathrm{K} \rangle_{\tilde{V},\tilde{t}} := \left(\frac{\mathrm{Pr}^{3/2}}{\mathrm{Ra}^{3/2} \, \langle \tilde{\varepsilon} \rangle_{\tilde{V},\tilde{t}}} \right)^{1/4}, \tag{3.18}$$

which depends in turn on the *kinetic energy dissipation rate*

$$\varepsilon := \frac{1}{2} \nu \left[(\nabla \boldsymbol{u}) + (\nabla \boldsymbol{u})^T \right]^2 \equiv \frac{U_\mathrm{f}^2}{\tau_\mathrm{f}} \, \tilde{\varepsilon} \qquad \text{with } \tilde{\varepsilon} := \frac{1}{2} \sqrt{\frac{\mathrm{Pr}}{\mathrm{Ra}}} \left[\left(\tilde{\nabla} \tilde{\boldsymbol{u}} \right) + \left(\tilde{\nabla} \tilde{\boldsymbol{u}} \right)^T \right]^2. \tag{3.19}$$

Here, the superscript Φ^T represents the transpose, whereas tildes indicate non-dimensional quantities based on the free-fall inertial balance – see again section 1.2.2.3. As diffusion dominates conceptually at the Kolmogorov scale, the characteristic Reynolds number becomes unity and thus the corresponding *Kolmogorov time scale* $\tau_\mathrm{K} = \sqrt{\nu / \langle \varepsilon \rangle_{V,t}} \equiv (\mathrm{Pr}/\mathrm{Ra})^{1/4} / \sqrt{\langle \tilde{\varepsilon} \rangle_{\tilde{V},\tilde{t}}} \, \tau_\mathrm{f}$ [126].

The presence of any scalar in the flow introduces a potentially new diffusion process which may in turn be compared to the diffusion of momentum from above. For instance, in case of molecular concentrations the mass diffusivity D can be compared to the kinematic viscosity via the *Schmidt number* $\mathrm{Sc} := \nu / D$ [127]. In terms of heat transport, the temperature represents the scalar quantity – the ratio between its thermal diffusivity κ and the kinematic viscosity yields eventually the Prandtl number Pr which was introduced in eq. (1.9) and related to diffusion time scales in the footnote on page 7. In case of $\mathrm{Pr} = 1$ (as used for the studies in sections 3.1 and 3.2), viscous diffusion is just as strong as thermal diffusion and so both fields exhibit the same level of details. In contrast, in case of $\mathrm{Pr} < 1$ ($\mathrm{Pr} > 1$) viscous diffusion is weaker (stronger) than thermal diffusion and

[4] The contribution of viscous dissipation as heat source is typically – as is also the case in the present work – neglected in the heat equation (1.4) due to its vanishing significance [56].

so the velocity (temperature) field exhibits potentially more details compared to the temperature (velocity) field.

As a complement to the Kolmogorov scale from above, this effect of thermal diffusion similarly dictates the smallest observable scale in the temperature field. Based on the work of Kolmogorov, Stanley Corrsin argued using dimensional considerations that the (on average) smallest observable scale in the temperature field is given by the (mean) *Corrsin scale* [128]

$$\langle \eta_{\mathrm{C}} \rangle_{V,t} := \left(\frac{\kappa^3}{\langle \varepsilon \rangle_{V,t}} \right)^{1/4} = \frac{\langle \eta_{\mathrm{K}} \rangle_{V,t}}{\mathrm{Pr}^{3/4}} \equiv H \, \langle \tilde{\eta}_{\mathrm{C}} \rangle_{\tilde{V},\tilde{t}} \qquad \text{with } \langle \tilde{\eta}_{\mathrm{C}} \rangle_{\tilde{V},\tilde{t}} := \frac{\langle \tilde{\eta}_{\mathrm{K}} \rangle_{\tilde{V},\tilde{t}}}{\mathrm{Pr}^{3/4}}. \tag{3.20}$$

In fact, this assumes the temperature field to be nested in the inertial sub-range of the velocity field which requires $\mathrm{Pr} \leq 1$ to hold – a detail that was clarified later by George K. Batchelor [129]. In the opposing case of $\mathrm{Pr} \geq 1$, thermal diffusion becomes important only at scales smaller than the Kolmogorov scale, so different arguments become necessary. A dimensional analysis based on the advective transport of material iso-surfaces leads in this case to the (mean) *Batchelor scale* [129]

$$\langle \eta_{\mathrm{B}} \rangle_{V,t} := \left(\frac{\nu \kappa^2}{\langle \varepsilon \rangle_{V,t}} \right)^{1/4} = \frac{\langle \eta_{\mathrm{K}} \rangle_{V,t}}{\sqrt{\mathrm{Pr}}} \equiv H \, \langle \tilde{\eta}_{\mathrm{B}} \rangle_{\tilde{V},\tilde{t}} \qquad \text{with } \langle \tilde{\eta}_{\mathrm{B}} \rangle_{\tilde{V},\tilde{t}} := \frac{\langle \tilde{\eta}_{\mathrm{K}} \rangle_{\tilde{V},\tilde{t}}}{\sqrt{\mathrm{Pr}}}. \tag{3.21}$$

Despite the different underlying arguments, both scales coincide with the Kolmogorov scale for $\mathrm{Pr} = 1$. Coming back to non-dimensional quantities in the following, tildes will again be dropped.

In a nutshell, these 3 different mean length scales deserve significance as follows. On the one hand, the Kolmogorov scale $\langle \eta_{\mathrm{K}} \rangle_{V,t}$ represents the smallest mean scale in the velocity field. On the other hand, the Corrsin scale $\langle \eta_{\mathrm{C}} \rangle_{V,t} \geq \langle \eta_{\mathrm{K}} \rangle_{V,t}$ describes the smallest mean scale in the temperature field if $\mathrm{Pr} \leq 1$, whereas this is replaced by the Batchelor scale $\langle \eta_{\mathrm{B}} \rangle_{V,t} \leq \langle \eta_{\mathrm{K}} \rangle_{V,t}$ in case of $\mathrm{Pr} \geq 1$.

As becomes further clear after this brief review, both of the dissipation scales for advected scalars[5] are conceptually and by definition related to the Kolmogorov scale. Hence, all 3 scales are linked to homogeneous, isotropic turbulence at large Re which is not exactly the case for Rayleigh-Bénard convection. However, the latter is yet similar enough to the former [56] to justify the use of these scales even in thermal convection [61, 108]. To account for variations of the kinetic energy dissipation field $\varepsilon = \varepsilon(\boldsymbol{x}, t)$ in space and time [108, 130, 131], the global definitions of the mean Kolmogorov, Corrsin and Batchelor scale may be generalised to the local ones $\eta_{\mathrm{K}} = \eta_{\mathrm{K}}(\boldsymbol{x}, t)$, $\eta_{\mathrm{C}} = \eta_{\mathrm{C}}(\boldsymbol{x}, t)$, and $\eta_{\mathrm{B}} = \eta_{\mathrm{B}}(\boldsymbol{x}, t)$, respectively [108, 132]. This supports eventually tailoring them to the inhomogeneous setup of Rayleigh-Bénard convection.

Run	Pr	N_e	N	t_r	Nu	Re	Λ_T
Nfs2_Pr001	0.01	$830^2 \times 16$	13	5,575	3.17 ± 0.01	2063.0 ± 0.7	59.65 ± 0.00
Nfs2_Pr01	0.1	$400^2 \times 8$	9	4,250	4.94 ± 0.09	433.0 ± 3.4	59.71 ± 0.01
Nfs2	1	$200^2 \times 4$	11	6,500	6.74 ± 0.10	81.4 ± 0.7	59.66 ± 0.02
Nfs2_Pr7	7	$200^2 \times 4$	7	4,000	7.21 ± 0.14	16.2 ± 0.2	59.76 ± 0.01
Nfs2_Pr10	10	$200^2 \times 4$	7	6,000	7.13 ± 0.10	11.7 ± 0.0	59.80 ± 0.01
Nfs2_Pr100	100	$200^2 \times 4$	7	14,000	7.02 ± 0.03	1.1 ± 0.0	59.78 ± 0.02

Table 3.3: Simulation parameters of the direct numerical simulations at different Prandtl numbers Pr – the Rayleigh number $\mathrm{Ra} = 203,576$, aspect ratio $\Gamma = 60$, and free-slip boundary conditions are applied for all runs. Nu and Re are determined from several thousand iterations, whereas Λ_T is based on 50 (10 for Nfs2_Pr001) snapshots within the last $5\tau_f$ in case of Nfs2_Pr001, $1000\tau_f$ in case of Nfs2_Pr100, or $500\tau_f$ in case of any other simulation run. Information on the base run Nfs2 is re-printed as reference in grey. For more information, see table 3.1.

3.3.2 Supergranules at different Prandtl numbers

In order to study the gradual supergranule aggregation for different fluids, a series of simulations at fixed Rayleigh number but varying Prandtl number is conducted. To keep the computational complexity tractable despite the large aspect ratio $\Gamma = 60$, simulation Nfs2 at $\mathrm{Ra_N} = 203,576$ is chosen as reference. Table 3.3 summarises all for this section relevant runs that cover the range $\mathrm{Pr} \in [10^{-2}, 10^2]$ centred around $\mathrm{Pr} = 1$.

3.3.2.1 Flow structures

Similar to the previous sections, every simulation is run as long as necessary to indicate a stationary pattern size with a particular focus on the temperature field. Doing so reveals two important results.

Firstly, the gradual supergranule aggregation proceeds even beyond $\mathrm{Pr} = 1$ at all accessible Prandtl numbers. Yet, the varying diffusivities affect the pace of the dynamics and thus the necessary simulation runtime t_r, see table 3.3. Although t_r is by far largest for the upper limit of Pr, one finds a similar trend towards longer necessary runtimes in the opposing lower limit. This observation itself suggests that the efficiency of the aggregation process depends on both the kinematic viscosity as well as thermal diffusivity, and thus the interplay of the velocity and temperature field. This is in line with later results from section 3.5.5 which trace the (thermal) supergranule aggregation basically back to an advective transfer of thermal variance. These runtimes do thus again not support any relation to diffusive time scales which agrees with the findings from section 3.1.3.3. Interestingly, the increase of runtime is larger in the direction $\mathrm{Pr} \to \infty$.

[5] In fact, both the Corrsin and the Batchelor scale are originally stated for temperature fields where variations are small enough to render buoyancy effects negligible [129] and so temperature represents a *passive* scalar. Hence, they can also be exploited for other scalars which brings the reader back to the Schmidt number from above.

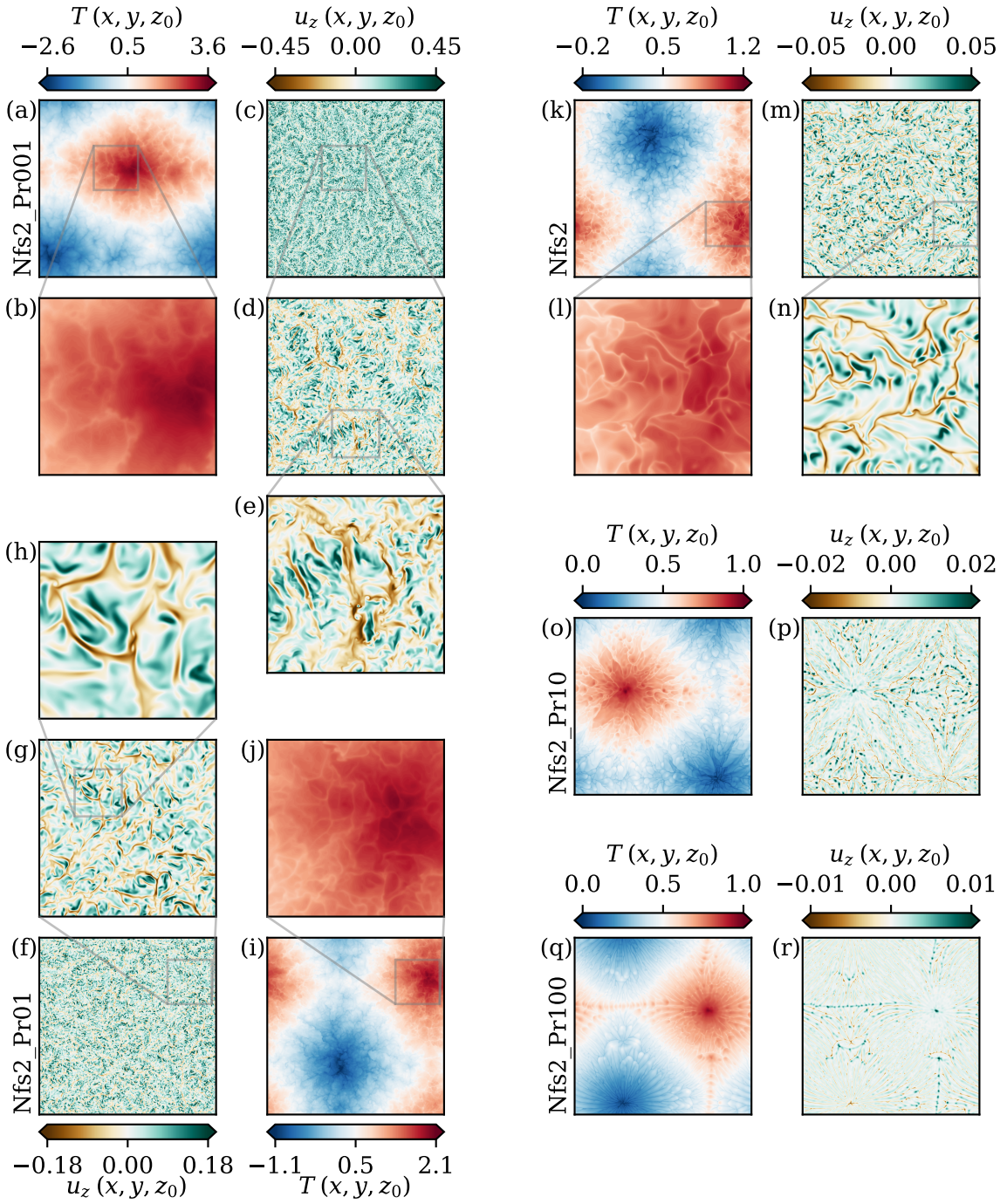

Figure 3.10: Supergranulation across 4 orders of Prandtl numbers. Although the velocity field exhibits successively smaller features for decreasing Prandtl numbers Pr, the supergranule aggregation can still easily be observed in the temperature field. Panels (a, c, f, i, k, m, o, p, q, r) visualise the entire cross-section at $z_0 = 1 - \delta_T/2$. To highlight the vast scale-separation between the temperature and (vertical) velocity field for small Pr, panels (b, d, g, j, l, m) enlarge a region of interest of size 15×15. Panels (e, h) underline this fact by additional magnifications of regions of size 4×4.

Secondly, this process ceases again only once the domain size is reached. Figure 3.10 visualises the temperature and vertical velocity field in horizontal planes within the upper thermal boundary layer for the final states of the flows. In particular, panels (a, i, k, o, q) depict the temperature fields across the entire horizontal cross-sections of the domains, whereas panels (c, f, m, p, r) exemplary contrast them to the velocity field with respect to its vertical component. This compilation underlines the enormous footprint of the supergranule aggregation in the temperature field and justifies thereby the focus on this scalar field at many places in the thesis at hand. Together with the previous paragraph, this suggests that the instability mechanism found and described in section 3.2.2 rules the pattern formation independently of Pr.

While the flows display well-ordered stems of localised up- and down-flow regions for large Pr, they become increasingly disordered for increasingly smaller Pr due to the reduced importance of molecular friction. Consequently, the ranges of observable scales or details diverge when comparing the temperature and vertical velocity field – this is highlighted by magnifications of fractions of the flows. In case of $\mathrm{Pr} = 1$, both fields offer an equivalent richness of details which is shown in panels (l, n). This changes once the Prandtl number moves off unity and the diffusivities of momentum and the scalar temperature differ. On the one hand, the temperature field becomes successively diffuse or imprecise for increasingly smaller Pr, compare thereto panels (b, j, l). On the other hand, the velocity field becomes simultaneously successively more chaotic as directly contrasted in panels (d, g, n). The tremendous scale separation between the two fields is ultimately highlighted by further magnifications of even smaller regions in panels (e, h), underlining the vast complexity of low-Pr thermal convection flows. Despite its significantly smaller Rayleigh number $\mathrm{Ra_N} \approx 2.0 \times 10^5$, simulation run Nfs2_Pr001 required more computational resources than run Nfs4 at $\mathrm{Ra_N} \approx 7.7 \times 10^7$ (see table 3.1).

The increasing local disparity of the temperature and velocity field due to the different time scales of the underlying diffusion processes suggests to investigate in the following the impact of the Prandtl number on the global transport of heat and momentum.

3.3.2.2 Global transport properties and the role of stratification

The previous section showed that the supergranule aggregation takes place across the entire range of investigated Prandtl numbers. Simultaneously, the flow structures are significantly affected by the varying relative strength of viscous and thermal diffusion processes. The incorporation of these two fields together with the Prandtl number in the global measures of heat and momentum transport, see equations (1.19b) and (1.20), suggests to analyse them in the presence of supergranules in more detail.

Figure 3.11 (a) visualises the dependence of these global transport measures on the Prandtl number for the final flow states. On the one hand, the Reynolds number as the global measure of momentum transport can be found to increase steadily when the Prandtl number is decreased. This is in accordance with the vanishing role of viscous diffusion, leading to successively more inertial flows. As this holds for the entire covered range of Prandtl numbers, it implies that the flow becomes laminar for $\mathrm{Pr} \gg 1$. On the other hand, the Nusselt number as the global measure of the importance of convective

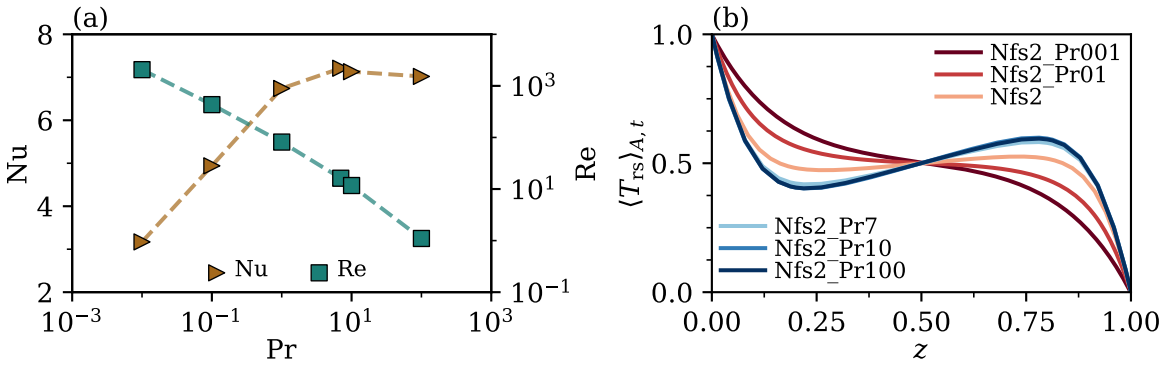

Figure 3.11: Global and local transport for different fluids. (a) While the global momentum transport increases with decreasing Pr, the convective heat transport is reduced only for Pr $\lesssim 1$. (b) A stable stratification in the bulk, previously observed in the inset of figure 3.2 (c), is no necessity for the emergence of the supergranule. The temperature field is re-scaled for this panel to allow for a direct comparability.

against diffusive heat transport shows a more complex behaviour. For decreasing Prandtl numbers in the range Pr $\lesssim 1$, thermal diffusion gains relevance as the disorder in the flow intensifies. In contrast, Nu stagnates for Pr $\gtrsim 1$ – this might be induced by the full nesting of the thermal boundary layer into the viscous one [3], so buoyancy effects get suppressed or protracted by viscous diffusion and thermal plumes detach less frequently.

These observations are in line with the effect of the Prandtl number in case of the complementary Dirichlet-type thermal boundary condition [61]. As the large-scale flow structures differ fundamentally between these two cases (see section 3.1), this underlines that diffusion processes are primarily *locally* important mechanisms.

The gradual supergranule aggregation was found in section 3.1.3.1 to be related to a slightly stable stratification of the temperature field close to the midplane for all accessible Rayleigh numbers. To answer the question if this represents a characteristic feature or necessary condition for the supergranule aggregation, the vertical temperature profiles of all for this section relevant simulations are plotted in figure 3.11 (b). Note that the temperature fields are re-scaled here to allow for a direct comparability, see again section 3.1.2. Despite the presence of supergranules for any Pr, the stratification develops qualitatively differently. While it is stable for Pr ≥ 1 and converges for Pr $\gtrsim 10$, it is increasingly unstable for successively smaller Prandtl numbers Pr < 1. These convergence properties agree with the above findings regarding the Nusselt number. Hence, the stable stratification in the bulk is no necessity for the emergence of the supergranule.

In spite of the impact of the Prandtl number on the global heat and momentum transport, as well as on the stratification in the bulk of the convection layer, the gradual supergranule aggregation emerges across the entire range of investigated Pr and ceases only when the artificially prescribed domain size is reached. This ubiquitous appearance and dominance of this large-scale flow structure raises fundamental questions on the completeness of the dynamical system and its involved physical mechanisms.

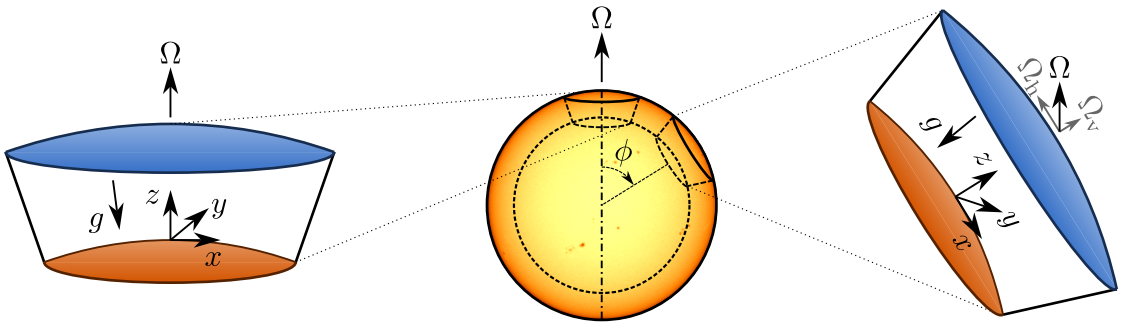

Figure 3.12: Physical interpretation of rotation around the vertical axis. The region at the geographical pole (left) of geo- and astrophysical objects can be seen as a fraction of their spherical shell (centre) – neglecting this spherical character results in the Cartesian domain depicted in figure 1.2. Regions away from the poles (right) add further complexity.

3.4 Limiting the supergranule aggregation

While it was shown in section 3.1 that the supergranule aggregation takes place for all accessible Rayleigh numbers at fixed $\mathrm{Pr} = 1$, the previous section 3.3 proved that it prevails even across all accessible Prandtl numbers at fixed $\mathrm{Ra} \approx 2.0 \times 10^5$. Assuming that (1) the qualitative results of these two series of simulations are independent of the particular fixed Ra or Pr, and (2) this pattern formation mechanism exists even beyond the numerically accessible ranges of Ra and Pr, one might hypothesise that the supergranule formation prevails throughout the entire two-dimensional Ra–Pr parameter space of any basic, heat flux-driven Rayleigh-Bénard convection flow (recall here equations (1.6) – (1.8)). As shown in section 3.1.3.3, this process ceases only when the (artificially prescribed finite) domain size is reached. Such an infinite growth is, however, in contrast to natural examples, implying in turn that this basic dynamical system needs to be extended to offer additional physical mechanisms that may eventually balance the instability.

3.4.1 Rotation as a promising candidate

While natural geo- and astrophysical flows offer a variety of extensions, they all have rotation as an additional physical mechanism in common (see also table 1.2). Figure 3.12 visualises the spherical shell of such a rotating object[6] and cuts selected fractions out of it. Although the angle between the vectors of gravity and rotation covers the entire spectrum of possibilities in case of a planet or star, a vector of rotation that is anti-parallel to the vector of gravity represents the most accentuated setting. In fact, this situation is given at the *geographical pole* of such spherical objects and can even be mimicked by Cartesian domains if the sphericity is neglected – compare for this purpose

[6]The background of the centre part of this figure 3.12 shows exemplary a photograph of the Sun with its several visible sunspots taken on 14/12/2022, 17:42:46 GMT via MicroObservatory [133].

the left part of this figure 3.12 with the basic experimental setup of Rayleigh-Bénard convection in figure 1.2.[7] This circumstance suggests to continue to work with the simple latter system and to incorporate the effect of rotation correspondingly.

In the previous sections, the behaviour of the non-rotating system at and slightly above the onset of convection has turned out to be quite insightful even for the turbulent flow. As already pointed out in section 3.2.1, additional rotation around the vertical axis generally stabilises the flow at the onset of convection. It is important to realise that this effect is more intense on large scales than on small scales – i.e., it suppresses large-scale motions –, consequently the critical mode may eventually become finite if rotation is only strong enough. Hence, rotation might turn out as a promising extension to limit the supergranule aggregation even in the fully turbulent flow.[8]

Studies in Rayleigh-Bénard convection (in particular with Dirichlet boundary conditions) report indeed that the flow patterns can be influenced under the action of rotation [30, 134] (see also [52, 63] for examples from even more complex flows). In the limit of rapid rotation, the flow structures transform towards so-called *Taylor columns* [117] with smaller horizontal scales as a consequence of the *Taylor-Proudman theorem* [45, 55, 56, 135–137]. In contrast, it might be expected that the stop of the gradual supergranule aggregation at large scales makes only *weak rotation* ($\mathrm{Ro} \gtrsim 2.5$ [30, 138]) necessary.

In the following, rotation around the vertical axis will be added as the only additional physical mechanism to the dynamical system and extend the parameter space by Ro.

3.4.2 Mathematical inclusion and involved time scales

3.4.2.1 Frames of reference

Mathematically, a measured quantity of a rotating system depends on the frame of reference, the latter of which can be either the inertial (I) or the rotating (R) frame. These frames imply that the observer is standing either outside or inside the rotating domain, respectively. Concerning the velocity field as part of the (dimensional) Navier-Stokes equation (1.3), the relation between these two frames is given by [55, 84]

$$\left(\frac{d\boldsymbol{u}_\mathrm{I}}{dt}\right)_\mathrm{I} = \left(\frac{d\boldsymbol{u}_\mathrm{R}}{dt}\right)_\mathrm{R} + 2\boldsymbol{\Omega}\times\boldsymbol{u}_\mathrm{R} + \boldsymbol{\Omega}\times(\boldsymbol{\Omega}\times\boldsymbol{x}_\mathrm{R}) \tag{3.22a}$$

$$= \left(\frac{d\boldsymbol{u}_\mathrm{R}}{dt}\right)_\mathrm{R} \underbrace{+2\boldsymbol{\Omega}\times\boldsymbol{u}_\mathrm{R}}_{\substack{\text{Coriolis}\\ \text{acceleration}}} \underbrace{-\frac{1}{2}\nabla\left(|\boldsymbol{\Omega}\times\boldsymbol{r}|^2\right)}_{\substack{\text{centrifugal}\\ \text{acceleration}}} \tag{3.22b}$$

[7] Regions away from the geographical pole add further complexity as the rotation of the spherical shell needs to be decomposed into a vertical and an additional horizontal component. The latter causes an anisotropy in the horizontal directions [100], see also the right part of figure 3.12.

[8] An analysis of the evolution equation for the temperature perturbation above the onset of convection (similar to [118]) was reportedly started in [40]. Although not finished, it might be expected that the instability mechanism (which drives the supergranule aggregation) does not disappear suddenly when rotation is added to the system. Thus, one might expect this instability to rival with the stabilising effect of rotation on large scales.

once the angular velocity and the reference point of the rotating frame are assumed to be time-independent and non-accelerated, respectively. It introduces generally both the *Coriolis acceleration* as well as the *centrifugal acceleration* term, while $\boldsymbol{r} = (r_x, r_y, r_z)$ represents here the perpendicular distance of the fluid parcel from the axis of rotation. Obviously, these two frames coincide in the non-rotating scenario – it is thus convenient to refer always to the 'rotating' frame and drop the subscript R in the following.

These above considerations point out that the Coriolis and centrifugal accelerations are *fictitious accelerations* for an observer inside a rotating frame [55]. The particular role of the Coriolis acceleration is to deflect fluid parcels perpendicular to their direction of motion.

3.4.2.2 Mathematical inclusion of rotation and its physical interpretation

It is crucial to understand the relation between the studies within a Cartesian domain and the actual physics in the motivating spherical geo- and astrophysical objects. In a spherical shell of the latter, the projection of the angular velocity or rate of rotation $\boldsymbol{\Omega}$ onto to the local unit vector along the vertical direction $\boldsymbol{e}_z$ (which is anti-parallel to the vector of gravity) depends on the latitude (lat), i.e.

$$2\boldsymbol{\Omega} \cdot \boldsymbol{e}_z = 2\Omega \cos(\phi) \underset{\substack{\text{Taylor series} \\ \text{around } \phi_0=0}}{=} 2\Omega + \text{h.o.t.} \approx 2\Omega \tag{3.23}$$

with $\phi \equiv \pi/2 - \phi_{\text{lat}}$ being measured from the geographical pole as indicated in figure 3.12. Considering now – as described above in section 3.4.1 – a region close to the geographical pole at $\phi \simeq \phi_0 = 0$, the truncation of a Taylor series after the very first term yields the expression given on the right of eq. (3.23). Neglecting the sphericity of the region close to the geographical pole, rotation is thus anti-parallel to the acceleration due to gravity as well as constant throughout the spatial domain.[9] Note that the angular velocity is, as stated above, further assumed to be constant in time. Given these considerations, the inclusion of an angular velocity $\boldsymbol{\Omega} = \Omega \boldsymbol{e}_z$ in the Cartesian domain indeed approximates the physics at the geographical pole.

Based on the characteristic angular velocity Ω, a non-dimensionalisation (further based on the free-fall inertial balance as in section 1.2.2.3) of the Coriolis and centrifugal acceleration terms from eq. (3.22b) yields

$$\frac{2\Omega H}{U_{\text{f}}}\, \boldsymbol{e}_z \times \boldsymbol{u} - \frac{\Omega^2 H^2}{2U_{\text{f}}^2}\, \nabla\left(r^2\right) \qquad \text{with } r = \sqrt{r_x^2 + r_y^2} \tag{3.24}$$

within the (non-dimensional) Navier-Stokes equation (1.7).

The centrifugal acceleration term represents basically a gradient field, and as such it can be included into a modified pressure field $p_{\text{mod}} := p - \Omega^2 H^2 / (2U_{\text{f}}^2)\, r^2$ [53, 54]. Hence,

[9] This is known as the so-called *f-plane approximation* and represents a good approximation in case of a negligible sphericity [84], i.e. $\Gamma^2 H / R_{\text{char}} \ll 1$ with a characteristic radius R_{char} of the spherical object. The β- or γ-plane approximations represent higher-order approximations [29, 84, 100, 139] but lie beyond the very general scope of this work.

the centrifugal acceleration term disappears from the governing equations although not being neglected [55, 56]. Further, there is no need to solve it numerically as a separate term as its solution is consequently part of the elliptic equation (1.18) for the pressure field. For simplicity, the pressure field will be termed p even in the rotating scenario.

3.4.2.3 Time scales associated with rotation

The inclusion of the two terms from eq. (3.24) introduces also two new time scales to the system. Firstly, the left term indicates the ratio of the free-fall time scale $\tau_\mathrm{f} = H/U_\mathrm{f}$ to the system's *rotation time scale due to Coriolis acceleration* $\tau_\Omega \equiv \tau_{\Omega u} := 1/(2\Omega)$. Secondly, the right term can be interpreted as the squared ratio of the free-fall time scale τ_f to the system's *rotation time scale due to centrifugal acceleration* $\tau_{\Omega r} := \sqrt{2}/\Omega$. Recalling the definition of the Rossby number in eq. (1.11) (which corresponds closely to the non-disappearing Coriolis term), eq. (3.24) can be re-written as

$$\frac{1}{\mathrm{Ro}}\,\boldsymbol{e}_z \times \boldsymbol{u} - \underbrace{\frac{1}{8}}_{=\tau_\Omega^2/\tau_{\Omega r}^2}\frac{1}{\mathrm{Ro}^2}\,\nabla\left(r^2\right) \qquad \text{with } \mathrm{Ro} = \frac{\tau_\Omega}{\tau_\mathrm{f}}. \tag{3.25}$$

This highlights clearly that these two rotation time scales are not independent but closely connected via $\tau_{\Omega r} \equiv 2\sqrt{2}\,\tau_\Omega$. As $\tau_{\Omega r} \gtrsim \tau_\Omega$, processes or effects caused by Coriolis acceleration may be roughly expected to dominate processes caused by centrifugal accelerations.

It might be of interest how these time scales compare with the remaining time scales – see section 1.2.2.3 and especially the footnote on page 7 – in the flow. Such a hierarchy, however, depends sensitively on the particular parameters Ra, Pr and Ro. Based on typical values of natural convection flows (see table 1.2), $\mathrm{Pr} \gg 1/\mathrm{Ra}$ and $\mathrm{Pr} \ll \mathrm{Ra}$. From this, the hierarchy establishes in the non-rotating scenario to

$$(\tau_{\Omega r}, \tau_\Omega) \gg (\tau_\nu, \tau_\kappa) \gg \tau_\mathrm{f}. \tag{3.26}$$

Presuming for the rotating scenario $\mathrm{Pr} \simeq \mathcal{O}(10^0)$, $\mathrm{Ra} \gtrsim \mathcal{O}(10^4)$ and $\mathrm{Ro} \simeq \mathcal{O}(10^1)$ instead (for the latter, see also table 3.4),

$$\tau_\nu \simeq \tau_\kappa \gg \tau_{\Omega r} \gtrsim \tau_\Omega \gg \tau_\mathrm{f} \tag{3.27}$$

holds. Thus, although buoyancy-driven processes continue to set the smallest time scale, effects caused by weak rotation may eventually dominate diffusion effects (on large length scales, as on small length scales still $\tau_\mathrm{f} \gg \tau_\mathrm{K}$) and become more important.

3.4.3 Controlling the size of supergranules

The effect of rotation as an additional physical mechanism is studied by approaching the weakly rotating regime starting from the non-rotating limit – the non-rotating simulation runs performed in section 3.1 serve thus as starting points. In terms of control parameters of the flow, this implies that the two previous ones (Ra and $\mathrm{Pr} = 1$) are kept fixed while rotation is introduced via the new parameter Ro, the latter of which will subsequently be varied. Table 3.4 summarises all simulations that are relevant for this section 3.4.

Run	Ra	Ro	N	t_r	Nu	Re	Λ_T
Dfs3	$385,014$	∞	7	$1,100$	10.21 ± 0.04	215.8 ± 0.5	5.34 ± 0.10
Dfs3_Ro10	$385,014$	10	7	625	10.22 ± 0.05	212.0 ± 0.5	5.18 ± 0.10
Nfs1	$10,432$	∞	7	$4,000$	3.93 ± 0.12	26.4 ± 0.4	59.66 ± 0.04
Nfs1_Ro5s	$10,432$	5	7	$1,250$	3.69 ± 0.05	24.4 ± 0.2	21.85 ± 3.31
Nfs2	$203,576$	∞	11	$6,500$	6.74 ± 0.10	81.4 ± 0.7	59.66 ± 0.02
Nfs2_Ro10	$203,576$	10	9	$4,500$	6.62 ± 0.09	80.3 ± 0.8	42.25 ± 0.73
Nfs2_Ro9	$203,576$	9	9	$4,500$	6.58 ± 0.09	78.7 ± 0.9	33.43 ± 1.83
Nfs2_Ro8	$203,576$	8	9	$4,500$	6.53 ± 0.09	76.3 ± 0.5	29.17 ± 0.92
Nfs2_Ro7	$203,576$	7	9	$4,500$	6.45 ± 0.07	72.8 ± 0.3	25.11 ± 0.82
Nfs2_Ro6	$203,576$	6	9	$4,500$	6.32 ± 0.07	69.1 ± 0.3	18.32 ± 0.47
Nfs2_Ro5	$203,576$	5	9	$4,500$	6.13 ± 0.05	65.1 ± 0.3	15.92 ± 1.54
Nfs3	$3,928,297$	∞	7	$10,000$	12.29 ± 0.16	229.0 ± 1.4	59.72 ± 0.02
Nfs3_Ro30	$3,928,297$	30	7	$4,500$	12.38 ± 0.13	286.0 ± 1.3	59.24 ± 0.07
Nfs3_Ro20	$3,928,297$	20	7	$4,500$	12.26 ± 0.08	231.5 ± 1.0	45.70 ± 0.21
Nfs3_Ro17	$3,928,297$	17	7	$4,500$	12.27 ± 0.13	231.4 ± 1.6	36.84 ± 2.18
Nfs3_Ro15	$3,928,297$	15	7	$4,500$	12.23 ± 0.10	224.5 ± 1.3	28.85 ± 1.49
Nfs3_Ro13	$3,928,297$	13	7	$4,500$	12.18 ± 0.09	217.4 ± 1.2	25.37 ± 0.57
Nfs3_Ro10	$3,928,297$	10	7	$4,500$	12.05 ± 0.09	205.1 ± 0.9	19.55 ± 1.11
Nfs3_Ro10s	$3,928,297$	10	7	$4,500$	12.05 ± 0.09	199.9 ± 0.7	17.73 ± 1.56
Nfs3_Ro9	$3,928,297$	9	7	$4,500$	11.97 ± 0.09	199.6 ± 1.1	15.02 ± 0.55
Nfs3_Ro8	$3,928,297$	8	7	$4,500$	11.85 ± 0.08	197.5 ± 0.7	10.98 ± 0.46
Nfs3_Ro7	$3,928,297$	7	7	$4,500$	11.71 ± 0.08	205.9 ± 0.8	9.71 ± 0.59
Nfs4	$76,887,279$	∞	7	$19,000$	23.47 ± 0.24	635.9 ± 3.1	59.68 ± 0.02
Nfs4_Ro30	$76,887,279$	30	7	$7,500$	23.44 ± 0.17	640.2 ± 3.3	27.34 ± 0.47

Table 3.4: Simulation parameters of the direct numerical simulations including rotation as an additional physical mechanism – the Prandtl number $\mathrm{Pr} = 1$, the aspect ratio $\Gamma = 60$ and free-slip boundary conditions are applied for all runs. All values correspond to the late state of the flow where the large-scale flow structures converged with respect to their mean size. Nu, Re and Λ_T are typically determined from 50 snapshots within the last $500\tau_\mathrm{f}$ of each simulation, while error bars are determined by the standard deviation. While simulation runs Nfs1_Ro5s and Nfs3_Ro10s started from scratch, all other simulations started with the final corresponding non-rotating flow as initial condition – run Nfs3_Ro10s thus proves the independence of statistical results from the specific initial condition. The total number of spectral elements N_e coincides for all runs with their corresponding non-rotating scenario. Information on these base runs are re-printed as reference in grey. For more information, see table 3.1.

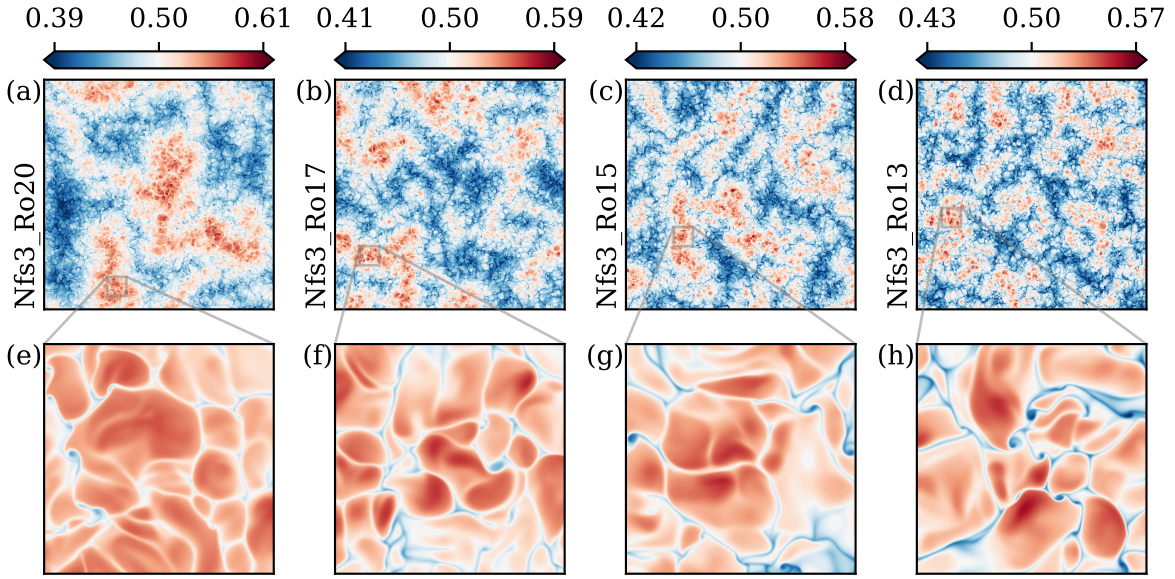

Figure 3.13: Effect of weak rotation on the flow structure hierarchy. (a – d) Weak rotation as an additional physical mechanism is capable of fragmenting the domain-sized supergranule into smaller, yet large-scale supergranule filaments. (e – h) Despite this significant transformation, the smaller-scale granular flow patterns are still preserved. While the top row visualises the temperature field $T(x, y, z_0)$ across the entire cross-section of the domain for a late state, the bottom row magnifies regions of size 5×5 at $z_0 = 1 - \delta_T/2$. Note the analogies to the granule patterns observed in the non-rotating scenario as shown in figure 3.4 (a, b) for even higher Ra.

3.4.3.1 Qualitative observations

Generally, it can be found that the global heat and momentum transfers are almost unchanged when introducing weak rotation. This can be realised when comparing simulation runs Dfs3_Ro10, Nfs1_Ro5s, Nfs2_Ro10, Nfs3_Ro20, Nfs4_Ro30 with their non-rotating counterparts. As this series shows, this holds not only for the Dirichlet case – for which this effect was already previously reported [30, 138, 140] –, but can similarly be confirmed for the Neumann case here. Increasing rotation tends to suppress convective motions [134, 138, 140], i.e. Nu and Re decrease. Although this effect is quite small, it can be confirmed for within the regime of weak rotation that is covered by the two simulation series Nfs2_Ro and Nfs3_Ro.

In the classical Dirichlet case, the large-scale flow structures – which predominantly cause the heat transport [96] – are almost unchanged. This is supported quantitatively by the integral length scale Λ_T (which is included for all simulations in the table) and might explain why the regime of weak rotation got only little attention in past studies. In contrast to these turbulent superstructures, the situation becomes very different for the supergranules.

In the Neumann case, the large-scale flow structure depends strongly on the strength of rotation even in the case of weak rotation as shown in figure 3.13 (a – d). The

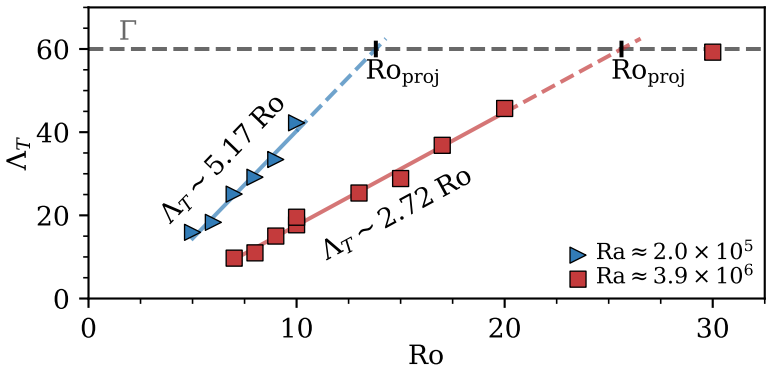

Figure 3.14: Scaling of fragmented supergranule filaments in the weakly rotating regime. The two comprehensive series of simulations at $\Gamma = 60$ indicate a linear scaling up to $\mathrm{Ro}_{\mathrm{proj}}$ as described by eq. (3.28).

gradual aggregation process can be stopped at an intermediate scale (when starting the simulation from scratch) or fragmented into smaller supergranules of intermediate scale (when rotation is suddenly introduced to an existing supergranule) once the strength of rotation is only strong enough. While simulation run Nfs3_Ro30 substantiates that latter, runs Nfs3_Ro10 and Nfs3_Ro10s prove the former by confirming the independence of statistical results from initial conditions. One might at this point extend the hypothesis from the beginning of section 3.4 and expect that there exists some transition in the three-dimensional parameter space which separates the regions of infinite and finite supergranule growth. Interestingly, the global heat and momentum transport is barely altered during this massive re-organisation of the large-scale flow. This is, in fact, in line with the behaviour of the flow during the gradual supergranule aggregation as previously shown in figure 3.5. The smaller-scale granular flow patterns, however, are not affected in an equal manner as shown in figure 3.13 (e – h).

3.4.3.2 Scaling of the fragmented supergranules

The observations from figure 3.13 suggest to quantify the resulting supergranule size as a function of the control parameter for the strength of rotation, Ro. Figure 3.14 reveals that the characteristic horizontal scale of the large-scale flow structures is in fact a *linear* function of the Rossby number which can be described by

$$\Lambda_T\,(\mathrm{Ro}) \approx f_1\,(\mathrm{Ra})\;\mathrm{Ro} + f_0\,(\mathrm{Ra}) \qquad \text{for } 2.5 \lesssim \mathrm{Ro} \lesssim \mathrm{Ro}_{\mathrm{proj}}. \tag{3.28}$$

This linear scaling can be understood by a closer look at the definition of the Rossby number in terms of time scales, see eq. (3.25). From this perspective, Ro defines basically the time scale of mechanisms induced by Coriolis accelerations. As the supergranule formation proceeds during its transient aggregation with a constant speed (see figure 3.5), a variation of this time scale via Ro might eventually set a limit to this buoyancy-driven aggregation process. Clearly, this argument relies on the independence of these two mechanisms.

Section 3.5 will highlight the responsibility of the non-linear term to the supergranule aggregation, allowing for an alternative argument for this linear scaling here. Suppose the (dimensional) non-linear term in eq. (1.3) will be constrained by the Coriolis term in magnitude, i.e. $|(\boldsymbol{u}\cdot\nabla)\,\boldsymbol{u}| \sim |2\Omega\,\boldsymbol{e}_z \times \boldsymbol{u}|$. For a characteristic dimensional flow structure of size Λ_{char} and velocity U_{f}, this translates to $U_{\mathrm{f}}^2/\Lambda_{\mathrm{char}} \sim 2\Omega U_{\mathrm{f}}$ or a Λ_{char}-based Rossby number of $\mathrm{Ro}_{\Lambda_{\mathrm{char}}} = U_{\mathrm{f}}/\left(2\Omega\Lambda_{\mathrm{char}}\right) \sim 1$. A subsequent re-translation to the original definition from eq. (1.11) results then in $\Lambda_T \equiv \tilde{\Lambda}_T = \Lambda_{\mathrm{char}}/H \sim \mathrm{Ro}$, supporting the observed linear nature of the scaling further.

From table 3.1 it is known that in the non-rotating case the supergranule aggregation proceeds slower when the strength of turbulent fluctuations – or in other words the Rayleigh number – is increased. One may thus expect that the slope f_1 depends on Ra too, which is confirmed by figure 3.14. However, further series of simulations at different Ra are required to draw a firm conclusion on this dependence.

One might wonder if it should not be possible to collapse the data onto a single line when plotting it against another rotation-based parameter such as Ta or Ek – these parameters are, however, not able to do justice to such expectations. This circumstance is just the logical result of the independence of the supergranule aggregation time from diffusive time scales as stated before in sections 3.1.3.3 and 3.3.2.1.

In eq. (3.28), $\mathrm{Ro}_{\mathrm{proj}}$ is the projected, Rayleigh number-dependent Rossby number beyond which the aggregation process becomes independent of Coriolis accelerations and thus $\Lambda_T = \Gamma$ establishes just as in the non-rotating scenario. For the two available series of simulations at varying Rossby numbers, Nfs2_Ro and Nfs3_Ro, this projection yields $\mathrm{Ro}_{\mathrm{proj}} \approx 14$ and $\mathrm{Ro}_{\mathrm{proj}} \approx 26$, respectively.

As pointed out in section 3.2.1, the critical mode at the onset of constant heat flux-driven Rayleigh-Bénard convection transitions from $k_{\mathrm{crit}} = 0$ to $k_{\mathrm{crit}} > 0$ once $\mathrm{Ta}_{\mathrm{crit}} \simeq 180.15$ is surpassed. In other words, the critical flow structure changes from infinite to finite size once the weakly rotating regime is approached sufficiently from the limit of no rotation. This critical point corresponds to critical Rossby numbers of $\mathrm{Ro}_{\mathrm{crit}} \approx 34$ and $\mathrm{Ro}_{\mathrm{crit}} \approx 148$ for the series Nfs2_Ro and Nfs3_Ro, respectively. Assuming a continuing validity of the slopes from figure 3.14 even beyond the covered range, these $\mathrm{Ro}_{\mathrm{crit}}$ correspond to critical structure sizes of $\Lambda_{T,\,\mathrm{crit}} \approx 162$ and $\Lambda_{T,\,\mathrm{crit}} \approx 392$ – a potential numerical domain might need to be even significantly larger to obtain definite results. However, one single simulation in a domain of aspect ratio, e.g., $\Gamma = 400 \approx 2.5 \times 162$ exhibits roughly $(400/60)^2 \approx 44$ times the complexity of a simulation in the current domain with $\Gamma = 60$. Keeping further in mind that the time which is necessary to form the supergranule increases with increasing aspect ratio [V1], it becomes clear that this exceeds what can be investigated with the current computational resources. Hence, it is not possible to confirm or reject this transition for the turbulent regime at this point.

Lastly, it is worth to mention that the linear nature of these results is not altered when considering another horizontal plane at a different height, vertically averaged fields [V5], or when quantifying the structure size based on different measures such as for instance the first zero-crossing of the correlation function [141]. The above findings thus clearly prove that rotation as an additional physical mechanism is able to limit the gradual supergranule aggregation at an intermediate scale $\Gamma \gg \Lambda_T \gg 1$.

Even stronger rotation than the ones listed in table 3.4 will eventually change the characteristics of the flow significantly as the weakly rotating regime will be left [30] and the flow patterns converge eventually towards Taylor columns [117]. These effects beyond the weakly rotating regime are, however, not at the focus of the present study.

3.4.4 Relating rotation to the vortex stretching term

While incompressible flows are most typically described by the evolution equation for the velocity – see the Navier-Stokes equation (1.7) –, their evolution can be formulated mathematically equivalently [57] by the use of the so-called *vorticity* $\boldsymbol{\omega} := \nabla \times \boldsymbol{u}$. This corresponding (non-dimensional) *vorticity equation* is obtained by taking the curl of the Navier-Stokes equation (1.7) and reads [52]

$$\frac{\partial \boldsymbol{\omega}}{\partial t} + (\boldsymbol{u} \cdot \nabla)\,\boldsymbol{\omega} = \underbrace{(\boldsymbol{\omega} \cdot \nabla)\,\boldsymbol{u}}_{\substack{\text{vortex} \\ \text{stretching term}}} + \underbrace{\left(\frac{1}{\mathrm{Ro}}\,\boldsymbol{e}_z \cdot \nabla\right)\boldsymbol{u}}_{\substack{\text{additional} \\ \text{Coriolis term}}} + \sqrt{\frac{\mathrm{Pr}}{\mathrm{Ra}}}\,\nabla^2\boldsymbol{\omega} + \nabla \times \boldsymbol{e}_z\,T, \tag{3.29}$$

including here only rotation around the vertical axis as an additional physical mechanism.[10] Note that $\boldsymbol{\omega} = \boldsymbol{\omega}\,(\boldsymbol{x}, t)$ with $\boldsymbol{\omega} = (\omega_x, \omega_y, \omega_z)$.

Using this representation of the dynamics of the system, it becomes clear that the shape of the first two terms on the right side of this equation – i.e. the *vortex stretching term* and the additional Coriolis term – is similar, which suggests to merge them hypothetically into one as

$$(\boldsymbol{\omega} \cdot \nabla)\,\boldsymbol{u} + \left(\frac{1}{\mathrm{Ro}}\,\boldsymbol{e}_z \cdot \nabla\right)\boldsymbol{u} = \left[\left(\boldsymbol{\omega} + \frac{1}{\mathrm{Ro}}\,\boldsymbol{e}_z\right) \cdot \nabla\right]\boldsymbol{u} \tag{3.30a}$$

$$= \left[\omega_x \frac{\partial}{\partial x} + \omega_y \frac{\partial}{\partial y} + \left(\omega_z + \frac{1}{\mathrm{Ro}}\right)\frac{\partial}{\partial z}\right]\begin{pmatrix} u_x \\ u_y \\ u_z \end{pmatrix}. \tag{3.30b}$$

This highlights that additional rotation can in fact be interpreted as a reinforcement or extension of the vortex stretching term.

Interestingly, the vortex stretching term exists only in three-dimensional turbulence but disappears in two-dimensional problems. Hence, also the governing vorticity equation (3.29) differs fundamentally, leading to qualitatively different physics [57, 142]. Two-dimensional turbulence [143–146] – or three-dimensional turbulence which is by external mechanisms, such as rapid rotation [147, 148] or suitable artificial forcing [149, 150], rendered quasi-two-dimensional – is commonly associated with the growth of flow structures up to domain size. In contrast, in three-dimensional turbulence such phenomena are typically absent [57]. For this reason, the vortex stretching term was originally suspected of being responsible for this phenomenological disparity [55, 142]. Indeed, recent research confirmed that the latter can – beside the slightly more important self-amplification of

[10] Note that although the pressure disappears in this formulation, the equation is still non-local due to the presence of $\boldsymbol{u}$ which has to be computed according to the *Biot-Savart law* [55, 57].

the strain-rate field – partly be related to the presence of the vortex stretching term in the three-dimensional case [151–153]. Roughly speaking, the vortex stretching term supports the suppression of a large-scale flow structure formation in three-dimensional turbulence.

Constant heat flux-driven Rayleigh-Bénard convection in a horizontally extended domain seems to contain characteristics from both scenarios. On the one hand, the ongoing supergranule aggregation up to domain size is accompanied by an accumulation of energy on large horizontal scales (see again figure 3.5 (h – l)) and resembles a characteristic of two-dimensional turbulence. On the other hand, even though the vortex stretching might be too weak in the non-rotating scenario to suppress this large-scale effect, additional weak rotation – which is related via eq. (3.30) – is able to limit the large-scale aggregation eventually which provides finally closer analogies to three-dimensional turbulence.

Although these considerations might help to classify the character of the flow, they lack a well-founded explanation of root-causes for the transfer of energy towards large scales in the fully three-dimensional flow. Nevertheless, the necessary direction of the scientific journey becomes clearer as these considerations suggest to analyse the (spectral) energy transfer of constant heat flux-driven Rayleigh-Bénard convection in the following.

3.5 Superganule aggregation as inverse spectral cascade process

The discovered supergranule aggregation is a transient process that proceeds over thousands of convective time units before it is limited by the finite domain size, see again figure 3.5. Albeit the underlying constant heat flux-driven convection is fully three-dimensional and naturally forced over a whole range of scales [154] – which incorporates the locally fluctuating thickness of the (detached) thermal boundary layer fragments –, it simultaneously exhibits characteristics of a two-dimensional flow. Several signs for the latter can already be found in previous parts of this work, e.g.:

1. The thermal variance in the domain increases throughout the transient process and accumulates at the largest scales, see figure 3.5. As mentioned in the discussion in section 3.4.4, such an accumulation is typically observed in two-dimensional processes.

2. The (thermal) supergranule is practically height-independent. This can be detected when comparing figure 3.3 (l) and figure 3.4 (f), which both visualise the temperature field of the same snapshot but at very different vertical coordinates – once at midplane, and once within the upper thermal boundary layer close to the top plane, respectively.

Additional rotation around the vertical axis seems to control the extension of the two-dimensional characteristics as it has been shown in section 3.4.3 to limit the growth

of the large-scale flow structures at intermediate scales. Note that this also interrupts the growth of the thermal variance [V5].

Hence, one might ask how energy is actually transported across different scales in this three-dimensional flow and what in particular causes the accumulation of kinetic energy and thermal variance on large scales. This fundamental question shall be started to be answered by a *spectral energy transfer analysis*.

3.5.1 Basics on the nature of turbulence

3.5.1.1 Richardson's cascade picture

The *cascade picture* is yet the most revealing insight into the nature of turbulence and its transfer of energy [155]. This picture goes back to Lewis F. Richardson who summarised it in his book on weather prediction in 1922 in the following famous rhyme:

> 'Big whirls have little whirls that feed on their velocity,
> and little whirls have lesser whirls and so on to viscosity.'
> – L. F. Richardson [156]

More precisely, this concept supposes the coexistence of vortices or eddies of different size in turbulent flows and consists basically of three stages [57, 142, 157].

1. Kinetic energy, which is injected to the system at a relatively large scale l_0, generates large vortices.

2. These vortices become unstable after some time and break up into smaller vortices – without the loss of energy. These new vortices exhibit the same instability and decay again and again to even smaller vortices.

3. The transfer of energy towards even smaller vortices comes finally to an end at a scale where viscous diffusion becomes important. Here, kinetic energy is dissipated into heat.

These three stages allow a statistically stationary transfer of energy – from the initial injection at larger scales over intermediate scales down to the smallest scales – if the source of energy is maintained. In this case, the rate of energy input $\langle \varepsilon_{\mathrm{in}} \rangle_V$, throughput, and dissipation $\langle \varepsilon \rangle_V$ coincides.

The general arrangement of this process in a series of stages, such that each stage – in particular the recursive second one – is driven from the preceding one, terms this process a *cascade* [158]. Its concept is visualised in figure 3.15.[11] This cascade picture of turbulence describes the energy exchange *across different length scales* (which is not to be confused with the energy flux across a certain area in physical space) [159], which immediately suggests to analyse the flow in spectral space in favour of physical space. From this spectral perspective, the three stages of the above picture are thus termed the *forcing range*, *inertial range*, and *dissipation range* [159].

[11] Note that flow structures of all available scales are superposed during this entire process, i.e. the region of a large vortex may also contain smaller vortices [142].

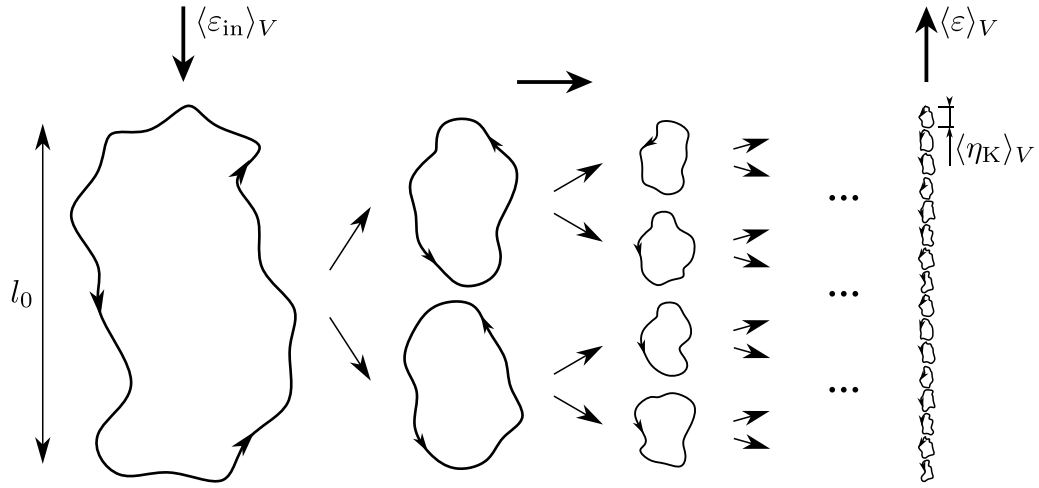

Figure 3.15: Sketch of the three-dimensional cascade of turbulence. The at large scales l_0 injected energy is transferred towards increasingly smaller scales until dissipation becomes effective at the mean Kolmogorov scale $\langle\eta_{\mathrm{K}}\rangle_V$. The three arrows at the top correspond to the transport of energy in the three stages of the cascade model. If the process is statistically stationary, all these arrows correspond to $\langle\varepsilon\rangle_V$.

3.5.1.2 Energy transfer in two- and three-dimensional turbulence

The qualitative picture of Richardson's energy cascade got quantified in 1941 by Kolmogorov for *three-dimensional* homogeneous, isotropic turbulence [126, 142, 159, 160]. Exploiting the constancy of energy flux and dimensional arguments, some of his main results were to find the scaling of the kinetic energy spectrum $E_{uu}(k) \sim k^{-5/3}$ in the inertial range and to quantify the (on average) smallest dynamical length scale in the flow, the mean Kolmogorov scale $\langle\eta_{\mathrm{K}}\rangle_{V,t}$ (see eq. (3.18)). The latter allows further to estimate the range of present dynamical length scales in a turbulent flow as $\mathrm{Re} = U_{\mathrm{char}} L_{\mathrm{char}}/\nu \sim U_0 l_0/(U_{\mathrm{K}}\eta_{\mathrm{K}}) \sim (l_0/\eta_{\mathrm{K}})^{4/3}$ – the subscripts correspond here to the first and third stage of the cascade, see figure 3.15. Assuming l_0 to be of the size of the system, this relation has important implications also for direct numerical simulations as it sets the minimum requirement on the numerical grid resolution [159].

The above picture exhibits a transfer of energy from large to small scales – this is called a *forward cascade*. However, also the opposite is possible which is termed *inverse cascade*. Which of them applies depends on the dimensionality of the flow, as well as on the quantity of interest – the following statements can be derived for conserved quantities of inviscid flows. In three-dimensional turbulence, the kinetic energy $u^2/2$ exhibits a forward cascade whereas the *kinetic helicity* $\boldsymbol{h} := \boldsymbol{u}\cdot\boldsymbol{\omega}$ [55, 159] shows an inverse cascade. In two-dimensional turbulence, the kinetic energy $u^2/2$ exhibits just the opposite, an inverse cascade, while the *enstrophy* $\omega^2/2$ offers a forward cascade [56, 159, 161].

Using these conservation laws, Robert H. Kraichnan was eventually able in 1967 to provide statements on the scaling of kinetic energy in *two-dimensional* turbulence, resulting in $E_{uu}(k) \sim k^{-5/3}$ or $\sim k^{-3}$ depending on the wave number range [56, 162].

The above considerations on two- and three-dimensional turbulence provide first valuable insights on the nature of turbulence. However, the complexity of Rayleigh-Bénard convection goes (because of its dimension and anisotropy in the vertical direction) beyond these general theories – in particular, none of them applies strictly [159]. Albeit the bulk region of Rayleigh-Bénard convection can be interpreted to be similar to three-dimensional turbulence [56], its natural forcing via the thermal boundary layer is very complex and only numerical investigations of such complex flows allow detailed insights.

3.5.2 Spectral description of the dynamical system

As outlined above in section 3.5.1.1, the study of energy transfer across scales – which allows eventually to conclude over the existence of inverse or forward cascade processes – requires a spectral description of the dynamical system. This implies that the governing equations (1.6) – (1.8) need to be translated into spectral space. The corresponding spectral expansion, however, must be performed in accordance with the boundary conditions. The focus is here, just as in the previous sections, again on the combination of free-slip and constant heat flux boundary conditions.

3.5.2.1 Spectral expansion of all fields

For this set of boundary conditions, the velocity, pressure and temperature fields can be expanded as *Fourier series* via

$$u_x\left(\boldsymbol{x},t\right) = \sum_{\boldsymbol{k}_\mathrm{h}}\sum_{k_z} \hat{u}_x(\boldsymbol{k}_\mathrm{h},k_z,t)\, e^{\imath\boldsymbol{k}_\mathrm{h}\cdot\boldsymbol{x}_\mathrm{h}}\ \cos\left(k_z z\right), \tag{3.31}$$

$$u_y\left(\boldsymbol{x},t\right) = \sum_{\boldsymbol{k}_\mathrm{h}}\sum_{k_z} \hat{u}_y(\boldsymbol{k}_\mathrm{h},k_z,t)\, e^{\imath\boldsymbol{k}_\mathrm{h}\cdot\boldsymbol{x}_\mathrm{h}}\ \cos\left(k_z z\right), \tag{3.32}$$

$$u_z\left(\boldsymbol{x},t\right) = \sum_{\boldsymbol{k}_\mathrm{h}}\sum_{k_z} \hat{u}_z(\boldsymbol{k}_\mathrm{h},k_z,t)\, e^{\imath\boldsymbol{k}_\mathrm{h}\cdot\boldsymbol{x}_\mathrm{h}}\ \imath\sin\left(k_z z\right), \tag{3.33}$$

$$p\ \left(\boldsymbol{x},t\right) = \sum_{\boldsymbol{k}_\mathrm{h}}\sum_{k_z} \hat{p}\ (\boldsymbol{k}_\mathrm{h},k_z,t)\, e^{\imath\boldsymbol{k}_\mathrm{h}\cdot\boldsymbol{x}_\mathrm{h}}\ \cos\left(k_z z\right), \tag{3.34}$$

$$\Theta\ \left(\boldsymbol{x},t\right) = \sum_{\boldsymbol{k}_\mathrm{h}}\sum_{k_z} \hat{\Theta}\ (\boldsymbol{k}_\mathrm{h},k_z,t)\, e^{\imath\boldsymbol{k}_\mathrm{h}\cdot\boldsymbol{x}_\mathrm{h}}\ \cos\left(k_z z\right). \tag{3.35}$$

In general, these expansions represent three-dimensional generalisations of the two-dimensional expansion described by eq. (3.6). The spectral *Fourier coefficients* $\hat{\Phi}$ represent thus the key elements to describe the fields in spectral space – these depend on wave numbers $\boldsymbol{k} = (\boldsymbol{k}_\mathrm{h}, k_z)$ instead of locations $\boldsymbol{x} = (\boldsymbol{x}_\mathrm{h}, z)$. Recall thereto also from section 3.1.3.3 the vectors of horizontal wave numbers $\boldsymbol{k}_\mathrm{h} = (k_x, k_y)$ and coordinates $\boldsymbol{x}_\mathrm{h} = (x, y)$, as well as the definition of the numerically discrete k_x and k_y. In the vertical direction, strictly either $k_{z,n} := 2\pi\ n/L_z$ with $n \in \mathbb{N}$ for cosine basis functions or $k_{z,m} := 2\pi\ m/L_z$ with $m \in \mathbb{N}^+$ for sine basis functions and $L_z = 2$. By defining $\hat{\Phi}\left(k_{z,m=0} = 0\right) = 0$, it follows that $k_z \equiv k_{z,n}$ for all fields. The resulting leading vertical spectral basis functions are visualised in figure 3.16.

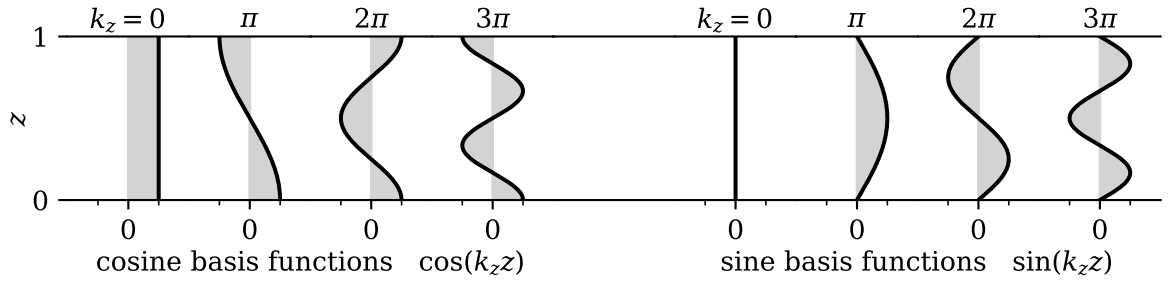

Figure 3.16: Leading vertical spectral basis functions. The particular choice – cosine or sine basis functions – depends on the boundary conditions of the spectrally expanded quantity. Amplitudes are highlighted by the shaded areas.

Note also that, due to the periodicity of the lateral boundaries, all fields support using the typical Fourier basis function $e^{\imath\Phi} = \cos(\Phi) + \imath \sin(\Phi)$ in both horizontal directions. In contrast, the basis function in the vertical direction depends on the particular quantity and is either $\cos(\Phi)$ or $\imath \sin(\Phi)$. Remark in case of the latter the usage of the coefficient $\imath$ – this allows for a direct comparability of the resulting Fourier coefficient with the one obtained for a similar but periodic quantity that is expanded through the typical basis function $e^{\imath\Phi}$.

The above spectral expansion requires (in case of both Dirichlet and Neumann boundary conditions) to describe the temperature field through the *temperature deviation field* Θ, recall thereto eq. (3.5) and find more details on this requirement in appendix B. This field will for simplicity just be termed 'temperature field' in this section. The corresponding evolution equation[12] and boundary conditions[13] in physical space are given by

$$\frac{\partial \Theta}{\partial t} + (\boldsymbol{u} \cdot \nabla)\,\Theta = \frac{1}{\sqrt{\mathrm{RaPr}}}\,\nabla^2 \Theta + u_z \tag{3.36}$$

and

$$\frac{\partial \Theta}{\partial z}\ (z \in \{0,1\}) = 0, \tag{3.37}$$

respectively.

3.5.2.2 Modal governing equations

To the knowledge of the author, a derivation of the governing equations in spectral description – which are in particular in accordance with constant heat flux boundary conditions – cannot be found in literature. Hence, a detailed derivation is included in appendix B.

[12] In contrast, the evolution equation for the velocity field – the Navier-Stokes equation (1.7) – does basically not change and can be simply adjusted by replacing T with Θ. This involves a modification of the pressure field.

[13] In case of Dirichlet boundary conditions, this reads $\Theta\,(z \in \{0,1\}) = 0$ and makes in eq. (3.35) an expansion in the vertical direction with respect to sine basis functions necessary.

The spectral governing equations read eventually

$$\imath \boldsymbol{k} \cdot \hat{\boldsymbol{u}} = 0, \tag{3.38}$$

$$\frac{\partial \hat{\boldsymbol{u}}}{\partial t} + \widehat{(\boldsymbol{u} \cdot \nabla)\, \boldsymbol{u}} + \frac{1}{\mathrm{Ro}}\, \boldsymbol{e}_z \times \hat{\boldsymbol{u}} = -\imath \boldsymbol{k}\, \hat{p} - \sqrt{\frac{\mathrm{Pr}}{\mathrm{Ra}}}\, k^2 \hat{\boldsymbol{u}} + \hat{\Theta}_{\mathrm{se}}\, \boldsymbol{e}_z, \tag{3.39}$$

$$\frac{\partial \hat{\Theta}}{\partial t} + \widehat{(\boldsymbol{u} \cdot \nabla)\, \Theta} = -\frac{1}{\sqrt{\mathrm{RaPr}}}\, k^2 \hat{\Theta} + \hat{u}_{z,\,\mathrm{ce}}. \tag{3.40}$$

These equations describe the evolution of the *modal energy* of both the velocity and temperature field, i.e. they are projected onto one particular wave number $\boldsymbol{k}$ with a magnitude given by $k := |\boldsymbol{k}|$. For this reason, $\hat{\Theta}$ needs to be described by a sine expansion (se) in eq. (3.39) and $\hat{u}_z$ by a cosine expansion (ce) in eq. (3.40) – this can be done by either projecting the Fourier coefficients obtained from sine (cosine) expansions onto cosine (sine) basis functions, or by directly transforming the corresponding field with cosine (sine) basis functions.[14] More details on this are included in appendix B – see in particular equations (B.29) and (B.30) for the definitions of $\hat{\Theta}_{\mathrm{se}}$ and $\hat{u}_{z,\,\mathrm{ce}}$, respectively. In order to keep a compact notation, the advection terms are transformed here after computing the corresponding product – see also equations (B.14) – (B.17). However, they can be expressed equivalently via convolution sums as will be shown later in section 3.5.2.4.

Note that an evaluation of these spectral equations does not require to run different numerical simulations – so, the same numerical method can be used. However, as the latter makes use of non-uniformly spaced GLL nodes, it becomes necessary to spectrally interpolate the snapshot data onto a uniformly spaced grid to subsequently compute the Fourier coefficients from equations (3.31) – (3.35).

3.5.2.3 Spectral evolution equations for kinetic energy and thermal variance

The observations from section 3.1.3.3 and especially figure 3.5 (h – l) suggest to analyse the transfer of kinetic energy E_{uu} and thermal variance $E_{\Theta\Theta}$ across scales. Recalling that in spectral space $|\hat{\Phi}|^2 = \hat{\Phi}\, \hat{\Phi}^*$ for $\hat{\Phi} \in \mathbb{C}$ – which is similar to the physical space product $|\Phi|^2$ used in, e.g., the kinetic energy density $u^2/2$ –, it becomes clear that the corresponding modal evolution equations for these two quantities can be derived from equations (3.39) and (3.40) by a multiplication with the projected complex conjugates $\hat{\boldsymbol{u}}^*$ and $\hat{\Theta}^*$, respectively, as well as subsequently taking the real part to ensure real results for all terms [159]. This yields after some re-arrangements

$$\frac{\partial E_{uu}}{\partial t}(\boldsymbol{k}, t) = -\Re\left[\widehat{(\boldsymbol{u} \cdot \nabla)\, \boldsymbol{u}} \cdot \hat{\boldsymbol{u}}^*\right] - \sqrt{\frac{\mathrm{Pr}}{\mathrm{Ra}}}\, k^2\, \hat{\boldsymbol{u}} \cdot \hat{\boldsymbol{u}}^* \; + \Re\left(\hat{\Theta}_{\mathrm{se}}\, \hat{u}_z^*\right), \tag{3.41}$$

$$\frac{\partial E_{\Theta\Theta}}{\partial t}(\boldsymbol{k}, t) = -\Re\left[\widehat{(\boldsymbol{u} \cdot \nabla)\, \Theta}\, \hat{\Theta}^*\right] \; - \frac{1}{\sqrt{\mathrm{RaPr}}}\, k^2\, \hat{\Theta}\hat{\Theta}^* + \Re\left(\hat{u}_{z,\,\mathrm{ce}}\, \hat{\Theta}^*\right) \tag{3.42}$$

[14] This implies that a forcing of, e.g., $\hat{u}_z\,(\boldsymbol{k}_{\mathrm{h}}, k_z = k_0)$ in eq. (3.39) happens not only via $\hat{\Theta}\,(\boldsymbol{k}_{\mathrm{h}}, k_z = k_0)$ but also via many different k_z.

with the kinetic energy and thermal variance defined spectrally as

$$E_{uu}\left(\boldsymbol{k},t\right) := \frac{1}{2}\hat{\boldsymbol{u}}\cdot\hat{\boldsymbol{u}}^{*} \qquad \text{and} \qquad E_{\Theta\Theta}\left(\boldsymbol{k},t\right) := \frac{1}{2}\hat{\Theta}\hat{\Theta}^{*}, \tag{3.43}$$

respectively. Note in eq. (3.41) that two terms from eq. (3.39) vanished: (1) the pressure term drops out due to incompressibility, and (2) the Coriolis term[15] drops out due to symmetry constraints as $\Re\left(\hat{\Phi}_1\hat{\Phi}_2^{*}\right) = \Re\left(\hat{\Phi}_1^{*}\hat{\Phi}_2\right)$ for $\left(\hat{\Phi}_1,\hat{\Phi}_2\right) \in \mathbb{C}$.

Both evolution equations become thus very similar as they consist basically (from left to right) of a time derivative, as well as an advection, a dissipation, and a forcing term. So, it is convenient to assign certain abbreviations for these terms [159], all of which are in the following[16]

$$A_u\left(\boldsymbol{k},t\right) := \Re\left[\widehat{\left(\boldsymbol{u}\cdot\nabla\right)\boldsymbol{u}}\cdot\hat{\boldsymbol{u}}^{*}\right], \tag{3.44}$$

$$D_u\left(\boldsymbol{k},t\right) := \sqrt{\frac{\mathrm{Pr}}{\mathrm{Ra}}}\,k^2\,\hat{\boldsymbol{u}}\cdot\hat{\boldsymbol{u}}^{*} = 2\sqrt{\frac{\mathrm{Pr}}{\mathrm{Ra}}}\,k^2\,E_{uu}, \tag{3.45}$$

$$F_u\left(\boldsymbol{k},t\right) := \Re\left(\hat{\Theta}_{\mathrm{se}}\,\hat{u}_z^{*}\right), \tag{3.46}$$

$$A_\Theta\left(\boldsymbol{k},t\right) := \Re\left[\widehat{\left(\boldsymbol{u}\cdot\nabla\right)\Theta}\,\hat{\Theta}^{*}\right], \tag{3.47}$$

$$D_\Theta\left(\boldsymbol{k},t\right) := \frac{1}{\sqrt{\mathrm{RaPr}}}\,k^2\,\hat{\Theta}\hat{\Theta}^{*} = \frac{2}{\sqrt{\mathrm{RaPr}}}\,k^2\,E_{\Theta\Theta}, \tag{3.48}$$

$$F_\Theta\left(\boldsymbol{k},t\right) := \Re\left(\hat{u}_{z,\,\mathrm{ce}}\,\hat{\Theta}^{*}\right), \tag{3.49}$$

translating equations (3.41) and (3.42) into

$$\frac{\partial E_{uu}}{\partial t}\left(\boldsymbol{k},t\right) = -A_u - D_u + F_u, \tag{3.50}$$

$$\frac{\partial E_{\Theta\Theta}}{\partial t}\left(\boldsymbol{k},t\right) = -A_\Theta - D_\Theta + F_\Theta. \tag{3.51}$$

Now that the fundamental evolution equations are derived, the exploration for the root cause of the supergranule aggregation raises two particular questions:

1. Which wave numbers $\boldsymbol{k}$ capture the observed supergranule aggregation principally?
2. Which mechanism – and thus which term in eq. (3.50) or (3.51) – is responsible?

The first question might seem trivial at first glance as one might state that large scales and thus small wave numbers should be relevant. Albeit this is not entirely wrong, the inherent anisotropy of the setup allows to deduce even more valuable statements. As explained at the beginning of section 3.5, the *temperature* field becomes practically height-independent – in the spectral description, this corresponds to the $k_z = 0$ plane, see

[15] Physically, the Coriolis acceleration is a fictitious acceleration and acts only perpendicular to the velocity field, thus $(2\boldsymbol{\Omega}\times\boldsymbol{u})\cdot\boldsymbol{u} = 0$ and so there is no contribution to the kinetic energy [55].

[16] Some works, such as [55, 159], may also define the *spectral transfer function* $T_\Phi := -A_\Phi$ instead.

again figure 3.16. However, this plane does not capture the convectively heat transporting *velocity* structures. Convection rolls fundamentally require up- and downflow regions. The vertical velocity – which is expanded as a sine function, see eq. (3.33) – does, however, not participate in this plane and so the main velocity structures of the supergranules are only captured by higher vertical modes. As ideal convection rolls correspond to the $k_z = \pi$ plane, see also figure B.1, one may expect most of the kinetic energy there. In a nutshell, the vertical mode k_z to focus on depends on the particular quantity of interest. In any case, large horizontal scales are of importance which correspond to small horizontal wave numbers $\boldsymbol{k}_\mathrm{h}$.

To answer the second question it becomes helpful to contemplate the general effect of the different terms in these equations. The dissipation terms D_Φ are mathematically positive definite and (because of the negative sign) thus always reduce the amount of energy in these modes – this dissipated energy is provided by the forcing terms F_Φ. In the Dirichlet case $F_u = F_\Theta$, whereas in the Neumann case $F_u \neq F_\Theta$ due to the projection onto complementary basis functions. Albeit the forcing becomes thus more complex in the Neumann case, the nature of these dissipation and forcing terms is still rather simple. In contrast, the advection terms A_Φ couple (as will be shown below in equations (3.53) and (3.54)) three different wave number vectors, and re-distribute thereby energy across scales while keeping the total amount of energy constant, i.e. $\sum_{\boldsymbol{k}} A_\Phi = 0$ [55, 159]. It seems thus conclusive to suspect that the advection terms are responsible for the gradual transfer of energy across scales. As will be proven later in section 3.5.5, it is indeed a subset of the advection term that can be identified to be responsible for the (thermal) supergranule aggregation.

3.5.2.4 The advection terms revisited

Most terms in equations (3.50) and (3.51) consist of 'pure' expansions of either the velocity or temperature field – this is not (yet) the case for the advection terms. These terms contain still expansions of the product $(\boldsymbol{u} \cdot \nabla)\,\boldsymbol{u}$ or $(\boldsymbol{u} \cdot \nabla)\,\Theta$, respectively. However, due to the particular choice of trigonometrical basis functions in equations (3.31) – (3.35) (which leads in combination with the coefficient $\imath$ to typical Fourier coefficients), these products can be expressed and evaluated as well-known convolution [159]

$$\widehat{\boldsymbol{u}\boldsymbol{\Phi}}\,(\boldsymbol{k},t) = \sum_{\boldsymbol{p},\boldsymbol{q}} \hat{\boldsymbol{u}}\,(\boldsymbol{q},t)\;\hat{\boldsymbol{\Phi}}\,(\boldsymbol{p},t) \qquad \text{with } \boldsymbol{q} = \boldsymbol{k} - \boldsymbol{p} \tag{3.52}$$

as in case of incompressibility $(\boldsymbol{u} \cdot \nabla)\,\boldsymbol{\Phi} = \nabla \cdot (\boldsymbol{u}\boldsymbol{\Phi})$. Further, the above-mentioned projection onto a particular wave number vector $\boldsymbol{k}$ requires $\boldsymbol{q} = \boldsymbol{k} - \boldsymbol{p}$ to hold. In other words, the three wave number vectors $\boldsymbol{k}$, $\boldsymbol{q}$, $\boldsymbol{p}$ must form a closed triangle – this basic unit of interaction is often called a *triad* [159]. With this convolution in mind, it is hence

possible to re-formulate eq. (3.44) and (3.47) to

$$A_u(\boldsymbol{k},t) = \Re\left\{\imath \sum_{\boldsymbol{p},\boldsymbol{q}} \left[\boldsymbol{k}\cdot\hat{\boldsymbol{u}}(\boldsymbol{q},t)\right]\hat{\boldsymbol{u}}(\boldsymbol{p},t)\cdot\hat{\boldsymbol{u}}^*(\boldsymbol{k},t)\right\} \tag{3.53a}$$

$$= -\sum_{\boldsymbol{p},\boldsymbol{q}} \underbrace{\Im\left\{\left[\boldsymbol{k}\cdot\hat{\boldsymbol{u}}(\boldsymbol{q},t)\right]\hat{\boldsymbol{u}}(\boldsymbol{p},t)\cdot\hat{\boldsymbol{u}}^*(\boldsymbol{k},t)\right\}}_{=:S_u(\boldsymbol{k}|\boldsymbol{p}|\boldsymbol{q},t)}, \tag{3.53b}$$

$$A_\Theta(\boldsymbol{k},t) = \Re\left\{\imath \sum_{\boldsymbol{p},\boldsymbol{q}} \left[\boldsymbol{k}\cdot\hat{\boldsymbol{u}}(\boldsymbol{q},t)\right]\hat{\Theta}(\boldsymbol{p},t)\ \hat{\Theta}^*(\boldsymbol{k},t)\right\} \tag{3.54a}$$

$$= -\sum_{\boldsymbol{p},\boldsymbol{q}} \underbrace{\Im\left\{\left[\boldsymbol{k}\cdot\hat{\boldsymbol{u}}(\boldsymbol{q},t)\right]\hat{\Theta}(\boldsymbol{p},t)\ \hat{\Theta}^*(\boldsymbol{k},t)\right\}}_{=:S_\Theta(\boldsymbol{k}|\boldsymbol{p}|\boldsymbol{q},t)} \tag{3.54b}$$

with the imaginary part $\Im$. The second line of each above equation defines the so-called (rate of) *mode-to-mode energy transfer* $S_\Phi(\boldsymbol{k}|\boldsymbol{p}|\boldsymbol{q},t)$. This quantity describes the transfer of energy from mode $\boldsymbol{p}$ (giver) to mode $\boldsymbol{k}$ (receiver) with $\boldsymbol{q}$ acting as mediator [159].

3.5.3 Fluxes of spectral energy

3.5.3.1 An intuitive introduction

The *net budget* of spectral energy $E_{\Phi\Phi}$ within certain ranges of wave numbers k can be obtained by accumulating the energy in all modes up to a *threshold wave number* k'. This concept thus helps answering why kinetic energy or thermal variance grows over time on large scales. The question is now: how is a sum like $\sum_{k\le k'}$ over equations (3.50) and (3.51) related to the direction of the cascade?

This can be answered by defining the *spectral energy flux* terms (just as required by the above concept) [55, 159]

$$\Pi_u(k',t) := \sum_{k\le k'} A_u(\boldsymbol{k},t) \qquad \text{as well as} \qquad \Pi_\Theta(k',t) := \sum_{k\le k'} A_\Theta(\boldsymbol{k},t)\,, \tag{3.55}$$

and relating them to the mode-to-mode energy transfer $S_\Phi(\boldsymbol{k}|\boldsymbol{p}|\boldsymbol{q},t)$ from equations (3.53) and (3.54). Together with $p = |\boldsymbol{p}|$, this yields [159]

$$\Pi_\Phi(k',t) := \sum_{k\le k'} A_\Phi \tag{3.56a}$$

$$= -\sum_{k\le k'}\sum_{\boldsymbol{p},\boldsymbol{q}} S_\Phi(\boldsymbol{k}|\boldsymbol{p}|\boldsymbol{q},t) \tag{3.56b}$$

$$= -\sum_{k\le k'}\sum_{p>k'} S_\Phi(\boldsymbol{k}|\boldsymbol{p}|\boldsymbol{q},t) - \underbrace{\sum_{k\le k'}\sum_{p\le k'} S_\Phi(\boldsymbol{k}|\boldsymbol{p}|\boldsymbol{q},t)}_{=0} \tag{3.56c}$$

$$= \sum_{k>k'}\sum_{p\le k'} S_\Phi(\boldsymbol{k}|\boldsymbol{p}|\boldsymbol{q},t)\,. \tag{3.56d}$$

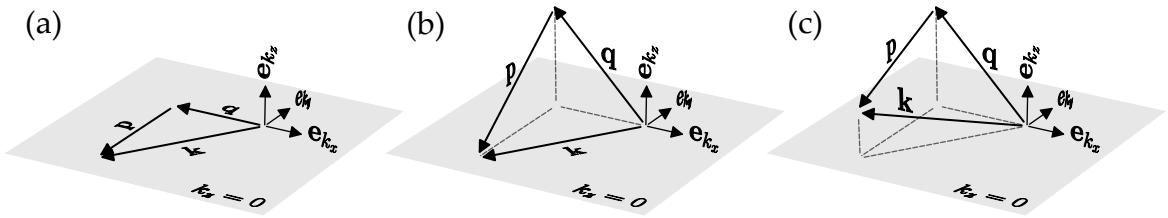

Figure 3.17: Subsets of triads. All possible triads are disentangled based on the dimensionality of the involved wave number vectors. (a) Purely two-dimensional triads with $k_z = p_z = q_z = 0$. (b) Triads ending up in the $k_z = 0$ plane that interact with three-dimensional modes $p_z = -q_z \neq 0$. (c) Fully three-dimensional triad interactions.

In other words, the sum of A_Φ over all $\boldsymbol{k}$ within a sphere of radius k' equals the total transfer of energy from modes $\boldsymbol{p}$ inside of this sphere to modes $\boldsymbol{k}$ outside of this sphere.

This allows eventually to define mathematically the ranges of existence of inverse or forward cascades [56], i.e. the types of cascades that were already introduced conceptually in section 3.5.1.2. An *inverse cascade* exists in the range of wave numbers where

$$\Pi_\Phi\left(k',t\right) = \sum_{k>k'} \sum_{p\leq k'} S_\Phi\left(\boldsymbol{k}|\boldsymbol{p}|\boldsymbol{q},t\right) \leq 0, \tag{3.57}$$

whereas a *forward cascade* exists where

$$\Pi_\Phi\left(k',t\right) = \sum_{k>k'} \sum_{p\leq k'} S_\Phi\left(\boldsymbol{k}|\boldsymbol{p}|\boldsymbol{q},t\right) > 0. \tag{3.58}$$

The above explanations and their relation to spectral spheres cohere with isotropic flows. This is in contrast to Rayleigh-Bénard convection, the latter of which exhibits anisotropic physics already due to the action of gravity in the vertical direction. As, however, the above argument from equation (3.56) can be interpreted as Gauss's theorem, one may equivalently re-formulate the initial sum $\sum_{k\leq k'}$ to another one that describes the quantity of interest in a better way (and simply changes the volume or surface over which is being integrated).

3.5.3.2 Disentangling the energy flux

As elaborated at the beginning of section 3.5, the supergranule aggregation leaves a practically height-independent footprint in the temperature field. It was further explained in section 3.5.2.3 that this is in contrast to the complementary velocity field – its situation becomes more advanced, which suggests to give the scalar field imprint priority.

The observations thus suggest, on the one hand, to focus the spectral energy flux on the two-dimensional receiving modes at $k_z = 0$, and, on the other hand, to disentangle all the possible triads based on the dimensionality of the involved modes. Three different subsets of spectral interactions can be derived from these considerations, all of which are visualised in figure 3.17. Interactions of the first subset – visualised in panel (a) – capture all those interactions that are made up of purely two-dimensional modes, thus

$k_z = p_z = q_z = 0$ and one may define the corresponding energy flux due to purely horizontal interactions as

$$\Pi_\Phi^{\mathrm{h}}\left(k_{\mathrm{h}}', t\right) := -\sum_{k_{\mathrm{h}} \leq k_{\mathrm{h}}'} \sum_{\boldsymbol{p},\boldsymbol{q}} S_\Phi\left(\boldsymbol{k}|\boldsymbol{p}|\boldsymbol{q}, t\right)\Big|_{\substack{k_z=0,\\ p_z=q_z=0}} . \tag{3.59}$$

In contrast, the second subset – which is visualised in panel (b) – contains all those triads that still end up in the $k_z = 0$ plane but which result from interactions with vertically non-homogeneous modes. The corresponding energy flux is given by

$$\Pi_\Phi^{\mathrm{v}}\left(k_{\mathrm{h}}', t\right) := -\sum_{k_{\mathrm{h}} \leq k_{\mathrm{h}}'} \sum_{\boldsymbol{p},\boldsymbol{q}} S_\Phi\left(\boldsymbol{k}|\boldsymbol{p}|\boldsymbol{q}, t\right)\Big|_{\substack{k_z=0,\\ p_z=-q_z\neq 0}} . \tag{3.60}$$

All the remaining, fully three-dimensional interactions – see panel (c) – do not contribute to the $k_z = 0$ plane and are thus not of particular interest here.

These above definitions and explanations will be used in the following to evaluate the spectral energy transfer of the dynamical system at hand.

3.5.4 Spectral energy transfer analysis

The preceding sections 3.5.2 and 3.5.3 introduced the formalism that allows to study the spectral energy transfer in three-dimensional, constant heat flux-driven Rayleigh-Bénard convection. In a nutshell, this enables to identify inverse and forward cascade mechanisms by evaluating the net budget of the spectral energy flux, the latter of which is caused by the advection term. The phenomenon of interest – the supergranule aggregation – is most prominent in the temperature field where it leads to a significant increase of thermal variance over time and leaves a clear footprint in the $k_z = 0$ plane. To this end it becomes necessary to study how energy is exchanged with this particular plane. Equations (3.59) and (3.60) provide eventually corresponding definitions of energy fluxes for two different subsets based on arguments on the dimensionality of the involved modes.

3.5.4.1 The non-rotating system

The spectral energy transfer analysis is shown exemplary for the non-rotating simulation run Nfs1, see also table 3.1. The absence of rotation is important as rotation increases the complexity while simultaneously not appearing explicitly in the evolution equations for kinetic energy and thermal variance, see section 3.5.2.3. Furthermore, this simulation run is the same as the one used in figure 3.5. This run at lower Ra offers a large number of snapshots which allows in turn to compute averages over a few subsequent snapshots without being significantly biased by the slow evolution. Figure 3.18 captures all important quantities for this analysis.

Panels (a1 – a4) visualise the instantaneous temperature fields Θ of the entire horizontal cross-section during and after the transient supergranule aggregation. Note that these depict the $k_z = 0$ plane which correspond to a vertical average of the numerical domain. A comparison of some of these panels with the ones contained in figure 3.5 (a – e) confirms

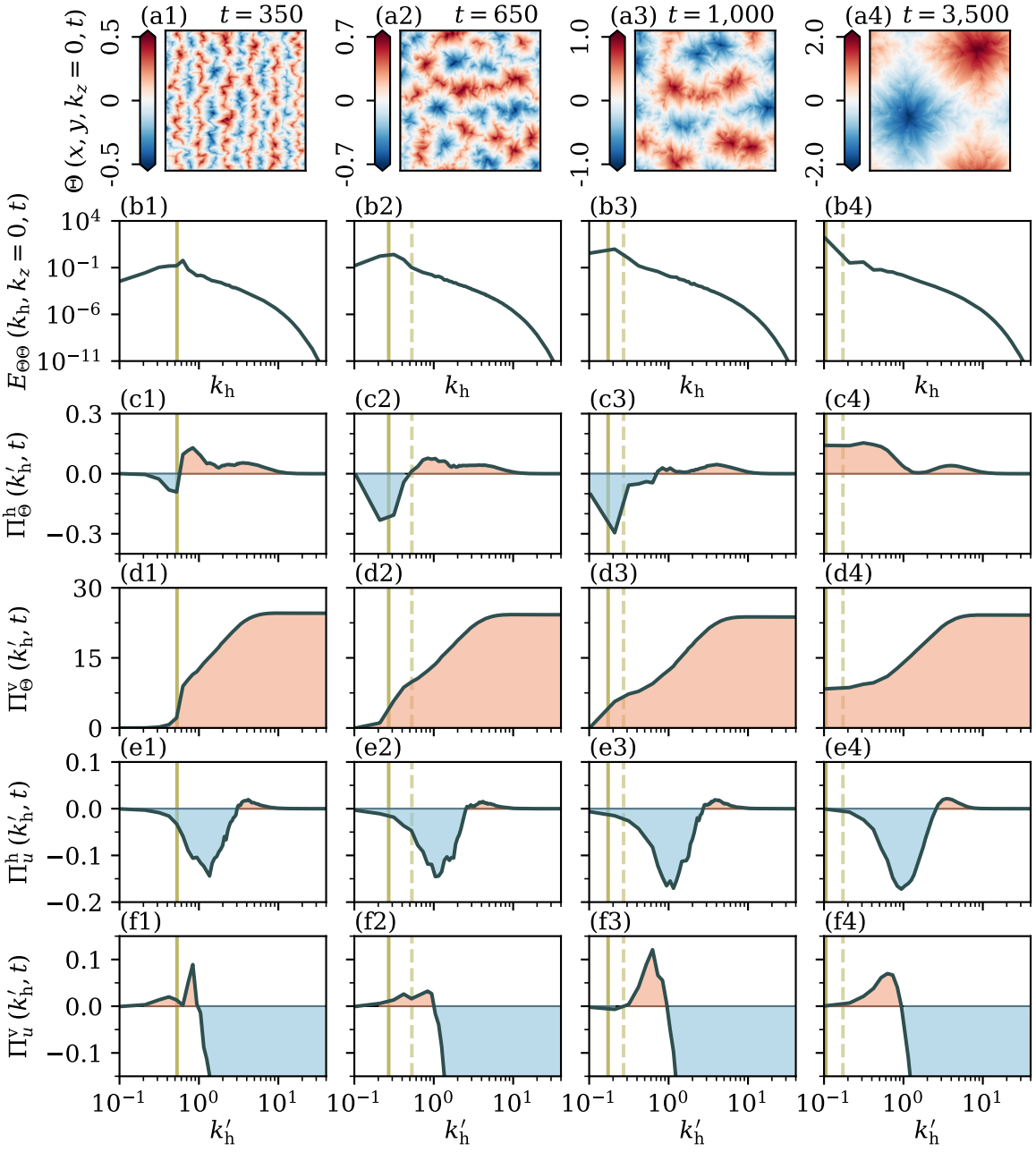

Figure 3.18: Spectral energy transfer analysis. The supergranule aggregation of the non-rotating simulation Nfs1 is captured by (a) the $k_z = 0$ plane of the instantaneous temperature field Θ, as well as (b) the corresponding azimuthally averaged spectrum $E_{\Theta\Theta}$. (c – f) The disentangled spectral thermal variance or kinetic energy fluxes $\Pi^{\mathrm{h,\,v}}_{\Theta,u}$ exhibit both inverse and forward cascades which are shaded here in blue and red, respectively. The solid and dashed khaki vertical lines quantify the current and preceding pattern size, respectively, based on the integral length scale of the above $E_{\Theta\Theta}$. The data in (b4 – f4) corresponds to the statistically stationary state and is thus time-averaged over $10^3\tau_\mathrm{f}$ centred around the indicated time.

that this plane captures indeed the (growing and final) supergranules. All subsequent rows in this figure will correspond to the times given above these top panels. Note that the subsequent panels (b1 – f3) contain (almost) instantaneous data that corresponds to the transient growth of the supergranule. In contrast, the data in the right-most panels (b4 – f4) corresponds to the statistically stationary state where the supergranule growth finished. Hence, this data is time-averaged over $10^3\tau_\mathrm{f}$ centred around the indicated time.

Panels (b1 – b4) plot the respective azimuthally averaged thermal variance spectrum $E_{\Theta\Theta}(k_\mathrm{h}, k_z = 0, t)$. In agreement with figure 3.5 (h – l), these spectra capture the aggregation of thermal variance in the smallest horizontal wave numbers. The size of the temperature patterns is evaluated based on the integral length scale corresponding to this $k_z = 0$ plane, see also eq. (3.4). The current values are included in these and all subsequent panels as solid khaki vertical lines – the dashed lines re-plot this quantity from the previous column to highlight the gradual growth.

In accordance with these previous panels, the study of spectral energy flux is started with a focus on the thermal variance. Panels (c1 – c4) show how purely two-dimensional mode interactions contribute to the thermal variance in the $k_z = 0$ plane. Indeed, throughout the transient period an inverse cascade with $\Pi^\mathrm{h}_\Theta \leq 0$ can be discovered acting at large scales. Moving towards larger wave numbers k'_h, Π^h_Θ changes its sign and thus a forward cascade can be found at smaller scales. The region of an inverse (forward) cascade is filled with blue (red) colour. This qualitative picture persists throughout the transient times albeit the gradual supergranule aggregation leaves a clear footprint in the spectrum of Π^h_Θ. Once the statistically stationary state is reached, this changes and the inverse cascade vanishes – a forward cascade establishes then throughout the spectrum.

This analysis is repeated in panels (d1 – d4) for the spectral thermal variance flux into the $k_z = 0$ plane but due to three-dimensional interactions. Despite a footprint of the supergranule aggregation, $\Pi^\mathrm{v}_\Theta > 0$ throughout the spectrum which thus exhibits a forward cascade only. It can be found that this behaviour is predominantly caused by interactions with the high-energetic $p_z = -q_z = \pm\pi$ modes.

As $\Pi^\mathrm{v}_\Theta > 0$ throughout the spectrum, interactions between purely two-dimensional modes – captured by the spectral flux Π^h_Θ – can be identified as the only interactions causing an inverse cascade of thermal variance at large scales. The involved triads comprise (beside the temperature) also velocities from the $k_z = 0$ plane, see again equations (3.59) and (3.54b). However, a closer look at the governing kinetic energy equation (3.50) and in particular its forcing term from eq. (3.46) reveals that $F_u(\boldsymbol{k}_\mathrm{h}, k_z = 0, t) = 0$, i.e. there is no forcing in this spectral plane. In other words, the advection term is the only source for kinetic energy in this $k_z = 0$ plane. For this reason, the above spectral flux analysis is repeated for the kinetic energy fluxes Π^h_u and Π^v_u in the following.

As shown in panels (e1 – e4), one can identify a pronounced inverse cascade of spectral kinetic energy at scales $k'_\mathrm{h} \lesssim 3$ caused by purely two-dimensional modes – this corresponds to large-scale structures of horizontal extension larger than $2H$. For smaller scales, a forward cascade establishes. Interestingly, this picture is quite time-independent.

Further, it is in contrast to the contribution of three-dimensional interactions to the kinetic energy in the $k_z = 0$ plane, see panels (f1 – f4). These interactions cause an inverse cascade on small scales with $k'_\mathrm{h} \gtrsim 1$ only which corresponds to structures up to a

horizontal extension of about $6H$. For larger scales, a relatively weak forward cascade can be found. Similarly to the analysis of Π_u^{h}, this picture is again quite time-independent.

The scale separation of the two identified inverse cascade processes in the kinetic energy field suggests to attribute them to either the supergranule or granule patterns. Moreover, the overlap allows the emergence of velocity structures of arbitrary horizontal extension in the $k_z = 0$ plane which enter subsequently the thermal variance flux Π_Θ^{h}.

The above analysis of the spectral flux of thermal variance $\Pi_\Theta^{\mathrm{h,\,v}}$ and kinetic energy $\Pi_u^{\mathrm{h,\,v}}$ proves that interactions between purely two-dimensional modes cause inverse cascades in both the temperature, as well as the velocity field on large scales. As shown in [V5], the situation is similar for simulations at higher Rayleigh numbers. Thus, one might eventually be able to attribute the gradual supergranule aggregation to these purely two-dimensional mode interactions.

3.5.4.2 The weakly rotating system

The above analysis has proven the existence of inverse cascades in the case of *non-rotating* constant heat flux-driven Rayleigh-Bénard convection. The inverse cascade in the temperature variance vanished once the supergranule size reached the horizontal extent of the numerical domain. However, as shown in section 3.4, additional rotation around the vertical axis may stop the growth of the supergranules at intermediate scales $\Gamma \gg \Lambda_T \gg 1$. This suggests to repeat the analysis for the corresponding weakly rotating run Nfs1_Ro5s – see also table 3.4 – to study the effect of such rotation on the inverse cascades.

As shown in more detail in [V5], the cascade pictures are not altered qualitatively during the transient supergranule growth even in the weakly rotating scenario. This holds even in the statistically stationary regime for the observed cascades of kinetic energy. However, the situation changes at these late times to some extent for the cascades in Π_Θ^{h}. Despite its initial appearance during the transient supergranule growth, the inverse cascade is interrupted once the statistically stationary pattern size and thus also thermal variance in the system is reached. As eventually $\Pi_\Theta^{\mathrm{h}} \approx 0$ at scales larger than this final pattern size, $\Pi_\Theta^{\mathrm{h}} \geq 0$ throughout the entire spectrum and the complex Coriolis acceleration becomes dominant at the given horizontal extension.

3.5.5 Is the advective transfer the root cause of the thermal variance aggregation?

The spectral energy transfer analyses above identified time-dependent inverse and forward cascade regions of horizontal wave numbers k_{h}' in the spectral thermal variance fluxes $\Pi_\Theta^{\mathrm{h,\,v}}$ – the particular existence of an inverse cascade on large scales during transient times implies that energy is re-distributed from small to large scales. However, as shown and explained in section 3.5.2.3, a growth of thermal variance over time could – beside the advection term A_Θ – also be caused by the forcing term F_Θ. So the final question to answer in this section 3.5 becomes eventually: Is the advective transfer really the root cause of the thermal variance aggregation?

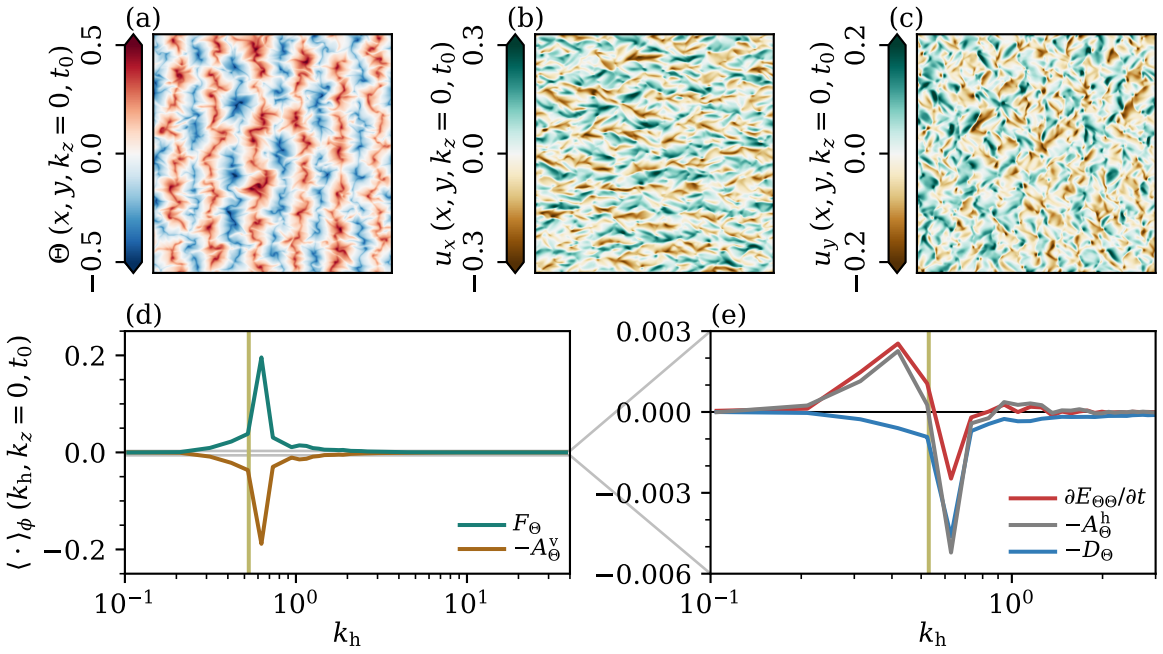

Figure 3.19: Root cause identification. (a – c) Temperature can be advected via height-independent velocity components. All panels visualise the entire horizontal cross-section. (d, e) A comparison of azimuthally averaged terms that participate in the thermal variance equation (3.51) allows to identify such an advective transfer as the root cause of the supergranule aggregation. Here, the advection term is split and each term is plotted in accordance with its corresponding sign in this equation. All data corresponds to simulation run Nfs1 at time $t_0 = 350$, see also figure 3.18.

If there is one single term that is responsible for the observed (thermal) supergranule aggregation, its spectrum should coincide with the spectrum of the time derivative $\partial E_{\Theta\Theta}/\partial t$ at the spectral plane $k_z = 0$ for transient times. So to conquer the above question, the azimuthally averaged spectra of all terms from the thermal variance equation (3.51) will be compared. Figure 3.19 captures the corresponding data for one snapshot of the early transient of simulation run Nfs1 – this is the same run as analysed above in the non-rotating case. The time $t_0 = 350$ coincides with the time in the first column of figure 3.18, allowing a direct comparability.

Panels (a – c) visualise all important physical space fields. Note that the depicted horizontal velocity fields represent constant translations of fluid across the entire domain height. Further, their structure already appears to be related to the early superganules.

Panels (d) and (e) compare the azimuthally averaged spectra. In accordance with the above disentangling of involved triads, see figure 3.17, the advection term is split into A_Θ^h and A_Θ^v with $A_\Theta(\boldsymbol{k}_\mathrm{h}, k_z = 0, t) = A_\Theta^\mathrm{h}(\boldsymbol{k}_\mathrm{h}, t) + A_\Theta^\mathrm{v}(\boldsymbol{k}_\mathrm{h}, t)$. These subsets of the advection term are thus directly related to Π_Θ^h and Π_Θ^v, respectively. Each of these two panels captures an important point. Firstly, panel (d) shows that while the forcing F_Θ supplies thermal variance, a similar amount is immediately compensated by

three-dimensional interactions A_Θ^{v} and thus transferred to three-dimensional structures. Secondly, a comparison of the time derivative of the thermal variance with the advection A_Θ^{h} due to purely horizontal mode interactions in panel (e) confirms that these two terms agree almost perfectly on horizontal scales where $\partial E_{\Theta\Theta}/\partial t > 0$.[17] This comparison allows to conclude eventually two important points:

1. The growth of thermal variance and thus the gradual (thermal) supergranule aggregation can indeed be associated with inverse cascades between purely two-dimensional modes at large scales. The responsible inverse cascade can be found in the non-rotating, as well as in the weakly rotating dynamical system.

2. In case of the latter, the final balance between the non-linear term on the one hand, and the Coriolis term on the other hand allows for scaling arguments as exploited in section 3.4.3.2.

These points prove that even the three-dimensional dynamics of a system can be significantly affected by two-dimensional characteristics of the flow. This becomes even more striking considering that three-dimensional modes outnumber the two-dimensional ones.

Crucially, not all convection flows allow for the above identified inverse cascades mechanisms. In particular, the complementary constant temperature boundary conditions require Θ to be expanded with respect to sine basis functions along the vertical direction in eq. (3.35). Hence, the corresponding dynamical system exhibits fewer spectral degrees of freedom and does generally not allow for the spectral thermal variance fluxes $\Pi_\Theta^{\mathrm{h,\,v}}$. This explains eventually the different characteristics of large-scale flow structures for these two scenarios as discovered in section 3.1.

3.6 Summary

As elaborated in chapter 1, geo- and astrophysical convection systems exhibit a variety of different combinations of boundary conditions and sometimes even particular hierarchies of flow structures. This observational fact motivated the first objective of the thesis at hand.

This chapter 3 aimed at understanding how large-scale flow structures are altered by different boundary conditions. To this end, sets of combinations of idealised thermal and mechanical boundary conditions were deduced and studied in an explorative approach. In order to minimise the influence of the lateral boundaries of the flow domain on this systematic comparison, an extraordinary large aspect ratio combined with periodic boundary conditions in the horizontal directions was chosen.

From a perspective of global statistical values it was found that the heat transport across the fluid layer scales differently for different combinations of boundary conditions in

[17] Note that the time derivative $\partial E_{\Theta\Theta}/\partial t$ needs to be reconstructed from the other terms A_Θ, D_Θ, and F_Θ. However, the determination of the advection term A_Θ^{h} represents an independent computation and does thus not alter this time derivative.

the Ra-range under consideration. Even more strikingly, it was discovered that the large-scale flow structures changed fundamentally once the classical constant temperature boundary conditions were substituted by the opposing constant heat flux boundary conditions. Albeit large-scale skeletons emerge in both scenarios as backbone of turbulent heat transport, they are extraordinarily different in nature.

For constant heat flux-driven convection layers, a large-scale flow structure grew gradually until the domain size was reached while being superposed to smaller (but still large-scale) flow structures. This exemplified that hierarchies of different large-scale flow structures are achievable even in simple Rayleigh-Bénard convection flows. In reminiscence to the astrophysical motivation, this interesting structure was termed *supergranule*. Albeit the common global measures of heat and momentum transport, Nu and Re, were mostly unaffected by the slow transient growth of the supergranule, several alternative observables – e.g. the standard deviation of the temperature deviation field – were able to capture it and to mark reaching the statistically stationary state of pattern formation. This effect of a gradual supergranule aggregation was not observed in previous studies and hence asked for more detailed investigations. Subsequent sections of this chapter thus aimed at improving our understanding of this new mechanism of *self-organisation* of the flow.

It was found that, in addition to the thermal driving, this mechanism seems to continue to exist for all accessible working fluids. This is in particular because of the astrophysical motivation remarkable. Given the reachable limits, one might hypothesise that this supergranule aggregation mechanism prevails throughout the entire two-dimensional Ra–Pr parameter space of any basic, heat flux-driven Rayleigh-Bénard convection flow.

This quasi-unlimited growth is in contrast to the observed flow structures in geo- and astrophysical examples. Rotation as one promising candidate was thus added around the vertical axis as an additional physical mechanism to the dynamical system. It was shown that weak rotation allowed indeed to control the final size of the supergranules or large-scale flow structures, whereas the granules or smaller structures remained mostly unaffected.

The computational costs of simulations at the given aspect ratio did not allow to study a hypothesised separating transition between unlimited and limited supergranule growth in the three-dimensional Ra–Pr–Ro parameter space. Instead, its dynamical origin and formation were studied by two different methods.

On the one hand, a leading Lyapunov vector analysis was performed. This dynamical system approach evaluated the susceptibility of the high-dimensional system trajectory to linear instabilities. From this, the turbulent flow was found to develop instabilities at increasingly larger wavelengths. Interestingly, the same behaviour can be found analytically for secondary instabilities slightly above the onset of convection. One may thus conclude that the dynamical system has not forgotten its origin although being fully turbulent where non-linearity plays typically a crucial role.

On the other hand, a spectral energy transfer analysis was performed to classify the supergranule formation into the picture of energy cascades. In contrast to the Lyapunov vector analysis, which represents a Lagrangian ansatz, this approach evaluates the governing equations in spectral space for (discrete) wave numbers and represents thus

an Eulerian ansatz. The transfer of thermal variance due to the advection term was at the focus of this investigation. The observations suggested to pay particular attention to the $k_z = 0$ plane, i.e. two-dimensional height-independent structures. Disentangling the transfer contributions correspondingly allowed to identify inverse cascades in the subsets of purely two-dimensional mode interactions for the thermal variance (as well as kinetic energy) at large scales during the transient supergranule growth. This analysis proved eventually the inverse cascade as the root cause for the growth of thermal variance, underlining the importance of two-dimensional characteristics even for three-dimensional flows.

The initial explorative study of the impact of different boundary conditions on large-scale flow structures provides in its essence information about what kind of large-scale flow structures can emerge from Rayleigh-Bénard convection as the paradigm of natural thermal convection – this fundamental insight should turn out to be really insightful for several geo- and astrophysical convection flows. Especially the gained understanding of the dynamical origin and transient formation of the gradual supergranule aggregation might help building or significantly improving reduced order convection models, the latter of which simultaneously avoid the vast complexity of direct numerical simulations while still capturing the essential key dynamics. *Galerkin projections* [159, 163] that make use of the identified spectral inverse cascade mechanisms might represent one particularly promising extension of the reported discoveries.

Chapter 4

Large-scale flow structures from a material transport perspective

Nature offers a variety of different flows that are of particular interest for scientists, see again table 1.2 for examples of corresponding thermal convection flows. Albeit chapter 3 has contrasted such flows numerically for various boundary conditions and subsequently described and analysed their large-scale flow structures, comparably detailed velocity and scalar field data can most typically not be collected from any natural flow – even not at a single time. The observation techniques do simply not allow to do so.

Instead of measuring a dense Eulerian grid, one may track (coherent) structures or point-like objects – as for instance sunspots [164], the great red spot [165], ocean surface drifters [166], or (weather) balloons in the atmospheres of geo- [167] and astrophysical [168] objects – that are drifted by the surrounding flow and eventually provide some sparse data. Beside inferring properties of this surrounding flow from the gathered data, it can also be desired to know how such structures interact or mix with their vicinity. This latter aspect in particular would not just improve our understanding of natural convection flows in general, but becomes crucial when considering, e.g., the anthropogenic release of radioactive material into the ocean or atmosphere [169–172].

This chapter bridges the gap between observations from the Lagrangian (i.e. material [173]) perspective and the turbulent superstructures, the latter of which are known from the Eulerian framework. To this end, coherent flow structures will be identified based on particle data by unsupervised machine learning techniques in section 4.3 – the extracted coherent regions of the turbulent flows will be related to spatial regions of the large-scale flow structures described in the previous chapter 3. It follows eventually that these coherent flow regions interact only weakly with their spatial complement as they reduce the heat transport significantly across different fluids. To allow for an investigation of the gradual supergranule aggregation via Lagrangian techniques, a new evolutionary clustering method will be developed and applied to turbulent superstructures in section 4.4. Its application to the supergranule aggregation remains open for future studies.

Many parts of this chapter have already been published [V2, V3] or extended [V7], which may again provide additional information beyond this chapter's content.

4.1 The Lagrangian framework and particles

4.1.1 Lagrangian coherent features

As pointed out for several examples in this chapter's introduction, natural flows are often inferred from observations of *coherent features*, i.e. parts of the flow that mix or interact only weakly with their surroundings [174, 175]. This perspective is inherently linked to *material transport* as those features consist of particles which in turn may exhibit certain scalar properties – they can, for instance, describe the advective transport of concentrations or heat. This role of Lagrangian coherent features in classical Rayleigh-Bénard convection on the global heat transport will be studied later in section 4.3.4.

Coherent features of the flow can basically be extracted from two different categories of approaches [176, 177]. *Lagrangian coherent structures* are interested in finding material surfaces based on the deformation of nearby material elements and thereto rely on detailed local gradients of the flow field [173]. In contrast to this 'dense' method, *Lagrangian coherent sets* use 'sparse' particle data to detect coherent behaviour between different trajectories [178]. Albeit these two categories are quite different, the extracted coherent features may coincide as the Lagrangian coherent sets represent the interior spatial regions that are bounded by the Lagrangian coherent structures [173, 176, 177].

In accordance with the motivation of this chapter, Lagrangian coherent sets will be used in the following to extract coherent sets from numerically obtained particle trajectories.

4.1.2 Properties and advection of particles

Placing particles in fluid flows is not trivial – they can be, e.g., light or heavy, small or big, spherical or non-spherical. The situation is similarly complex when describing the corresponding effects of the flow on the particles, as well as their feedback on the flow.

To narrow down this vast complexity, it is common to study point-like particles – i.e. the particles' radii $r_\mathrm{p} \ll \eta_\mathrm{K}$ [179] – that do not support particle-particle interactions [180]. Presuming them further to exhibit the same density as the fluid, i.e. $\rho_\mathrm{p} = \rho_\mathrm{ref}$, the (dimensional) equation of motion for any particle can be written as [180]

$$\boldsymbol{u}_\mathrm{p} = (\boldsymbol{u}_\mathrm{p} - \boldsymbol{u})|_{t=0}\, e^{-t/\tau_\mathrm{r}} + \boldsymbol{u} \qquad \text{with } \tau_\mathrm{r} = \frac{r_\mathrm{p}^2}{3\nu} \equiv \sqrt{\frac{\mathrm{Ra}}{\mathrm{Pr}}}\,\frac{\tilde{r}_\mathrm{p}^2}{3}\,\tau_\mathrm{f} \tag{4.1}$$

where τ_r represents the *inertial response time scale*. In the ultimate limit of vanishing radii with $r_\mathrm{p} \to 0$, the particles will follow the flow without any delay and one arrives at the concept of *Lagrangian particles*, the latter of which represent the simplest conceivable sort of point-like particles. Conceptually, they can be seen as individual particles of the original (continuum of) fluid. They introduce no additional parameters, and as being massless they do not provide any feedback on the fluid flow. Note that these particles correspond to a *Stokes number* $\mathrm{St} := \tau_\mathrm{r}/\tau_\mathrm{K} \to 0$ [180].

The evolution of any Lagrangian particle is eventually given by [181]

$$\frac{d\boldsymbol{x}_\mathrm{Lp}(t)}{dt} = \boldsymbol{u}_\mathrm{Lp}(t) \qquad \text{and} \qquad \boldsymbol{u}_\mathrm{Lp}(t) = \boldsymbol{u}\left[\boldsymbol{x} = \boldsymbol{x}_\mathrm{Lp}(t), t\right] \tag{4.2}$$

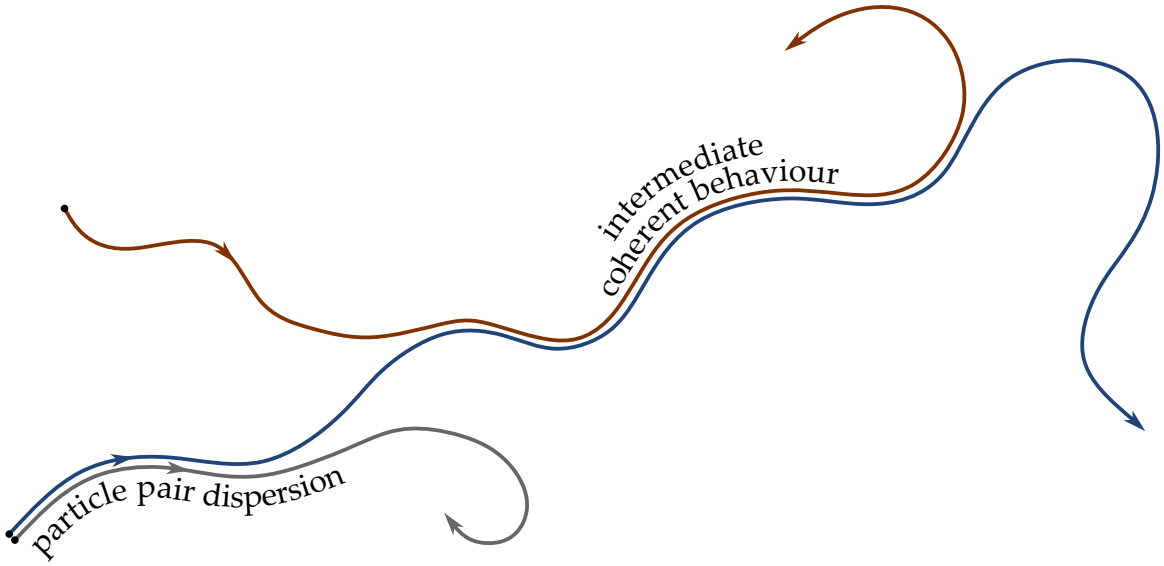

Figure 4.1: Lagrangian particle pair dispersion and coherence. Suppose the blue particle trajectory to represent a reference in a turbulent flow. Any initially extremely close particle (grey trajectory) will eventually be separated – hence, coherent behaviour is always limited to intermediate time intervals (red trajectory).

with the particle's (non-dimensional) trajectory $\boldsymbol{x}_{\mathrm{Lp}}$ and velocity $\boldsymbol{u}_{\mathrm{Lp}}$. Scalar properties of the Lagrangian particles, such as the temperature, can be similarly obtained via $\Phi_{\mathrm{Lp}}(t) = \Phi[\boldsymbol{x} = \boldsymbol{x}_{\mathrm{Lp}}(t), t]$. In the following, these Lagrangian particles will be used to extract material transport behaviour that is inherent to the turbulent flow.

4.1.3 The obstacle to Lagrangian coherent sets: pair dispersion

The previous sections introduced concepts for Lagrangian coherent feature detection as well as particles – Lagrangian coherent sets and Lagrangian particles got selected because of their applicability to sparse trajectory data and paradigmatic simplicity as the methods of choice for the subsequent analysis of large-scale flow structures from a material transport perspective. One might expect now that it should be easily possible to detect coherent features in the convection flow from comparing Lagrangian particles' trajectories, and – given the access to long corresponding histories – to track these coherent spatial regions' evolutions over time. Unfortunately, meeting this expectation is not trivial due to one fundamental obstacle: *Lagrangian particle pair dispersion*.

Section 3.2.2.1 introduced the concept of chaoticity of a dynamical system's trajectory in the high-dimensional state space and illustrated that any two initially close system trajectories will eventually diverge in case of turbulent flows. Such a sensitivity on the initial conditions can be found equivalently for Lagrangian particles that participate in these flows, see figure 4.1. Suppose two initially adjacent particles as shown at the bottom left of the figure – as long as their initial position does not coincide, their trajectories will be separated once advected only long enough by the turbulent flow.

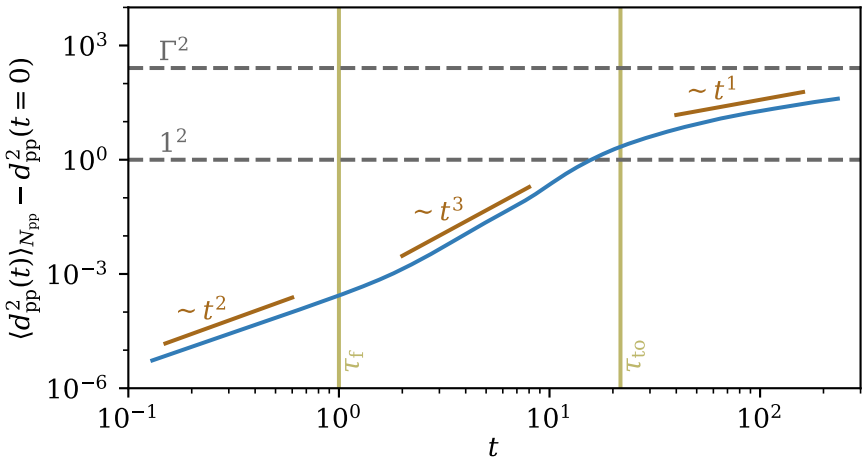

Figure 4.2: Regimes of Lagrangian particle pair dispersion. The tiny initial displacement of partner particles grows over time while going through the Batchelor, Richardson and Taylor sub-regimes. In the end, the particles will be de-correlated and correspond to substantially different regions of the turbulent flow. This statistics is based on the entire particle ensemble of simulation run L2, see also table 4.1.

The effect of Lagrangian particle pair dispersion can easily be quantified for actual trajectory data. To show this numerically, the trajectory data from simulation run L2 (which will be reported in more detail in section 4.2.1, see also table 4.1) is analysed. In a nutshell, two sets of 512^2 particles each are seeded once the turbulent superstructures have formed – the difference between the two sets is an initial vertical displacement of $d_{pp}(t=0) = 5 \times 10^{-3}$. In other words, there are $N_{pp} = 512^2$ pairs of particles and every single particle from one set exhibits a 'partner' particle (pp) which is initially highly nearby. After seeding the particles, they are advected in the time-dependent flow in accordance with eq. (4.2) while the distance d_{pp} between the partner particles is quantified via

$$d_{pp}(t) = |\boldsymbol{x}_{Lp,1}(t) - \boldsymbol{x}_{Lp,2}(t)| . \tag{4.3}$$

The subscripts 1 and 2 refer to the corresponding particle from set 1 and 2, respectively. The average increase of squared displacement over time due to Lagrangian particle pair dispersion, $\langle \Delta d_{pp}^2 \rangle_{N_{pp}}(t) := \langle d_{pp}^2(t) \rangle_{N_{pp}} - d_{pp}^2(t=0)$ [182–184], is obtained from the statistics over all N_{pp} particle pairs and quantified in figure 4.2.

Three different sub-regimes of pair dispersion can be identified from this dataset. At early times $t \lesssim \tau_f$, the particles remember still their initial velocity difference Δu. Hence, as the separation $\Delta x \sim \Delta u\, t$, the mean increase of displacement $\langle \Delta d_{pp}^2 \rangle_{N_{pp}} \sim t^2$. This sub-regime is called *Batchelor* or *ballistic regime* [182–184]. Once the displacement is large enough, the partner particles will be swept by different larger eddies in the second sub-regime, which in turn increases their speed of separation. A dimensional analysis motivated by the inertial range of the Richardson cascade – see section 3.5.1.1 – yields $\langle \Delta d_{pp}^2 \rangle_{N_{pp}} \sim \varepsilon\, t^3$ [159, 184], so this sub-regime at $\tau_f \lesssim t \lesssim \tau_{to}$ (with the Lagrangian turnover time scale τ_{to}, see section 4.2.2) is typically referred to as *Richardson regime*

[182–184] (even if it might also just be a transition region between the surrounding sub-regimes [184]). In the third sub-regime, the average vertical displacement has reached its limits given the vertical confinement of the domain [183] and the continued displacement of the particle pairs proceeds due to an increasing horizontal separation. The motions are now completely de-correlated as the different particles participate now in different turbulent superstructure rolls. This de-correlation resembles Brownian motion and one finds accordingly $\langle \Delta d_{\mathrm{pp}}^2 \rangle_{N_{\mathrm{pp}}} \sim t^1$ for $\tau_{\mathrm{to}} \lesssim t$. Therefore, this sub-regime is called *Taylor* or *diffusive regime* [182–184]. For even longer evolutions of the trajectories, the finite horizontal extent of the domain will become significant and the displacement will eventually converge.

These vivid interactions of particle pairs with different scales of the flow represent a fundamental obstacle for all Lagrangian coherent set detection methods. Undoubtedly, in the course of the evolution of a single particle its trajectory might be swept into the vicinity of another particle, see again figure 4.1. Both of them might then exhibit some coherent behaviour over intermediate times, but will definitely diverge again eventually. Hence, any (coherent) set of particles will vanish once just enough time has passed.

The remaining parts of this chapter will infer properties of coherent features of the flow over longer times via different approaches such as independent time windows, see section 4.3, or advanced evolutionary clustering methods, see section 4.4.

4.2 Lagrangian trajectories in Rayleigh-Bénard convection

4.2.1 Generation of Lagrangian datasets

As indicated in the previous section 4.1.3, large-scale flow structures in Rayleigh-Bénard convection seem to play a crucial role concerning the longer-term particle advection. The nature of these structures is, however, governed by the thermal boundary conditions as shown previously in chapter 3. In essence, in the (Neumann) case of an applied constant heat flux a hierarchy of different large-scale flow structures – termed granules and supergranules – can be observed, whereas turbulent superstructures emerge in the opposing (Dirichlet) case of applied constant temperatures.

The dynamical character of these structures, i.e. their alteration over time, adds beside pair dispersion another challenge to the detection of Lagrangian coherent sets. On the one hand, turbulent superstructures re-organise extremely slowly over time while showing a practically constant pattern size [185, 186]. On the other hand, supergranules re-organise fundamentally during their gradual aggregation process. For this reason, Lagrangian coherent features will be extracted in the following from turbulent superstructures in Rayleigh-Bénard convection.

To account partly for the enormous variety of different fluids in natural convection flows, a set of three simulations with varying Prandtl numbers is generated[1] – table 4.1

[1] The raw data of simulation run L2 is acquired from [183].

Run	Pr	N_e	N	t_r	Nu	Re	Λ_T	...
L1	0.1	$178^2 \times 14$	5	368	3.50 ± 0.04	409.0 ± 2.3	3.50 ± 0.04	...
L2	0.7	$166^2 \times 16$	5	469	4.13 ± 0.05	91.1 ± 0.5	4.13 ± 0.05	...
L3	7	$178^2 \times 14$	5	1,400	4.18 ± 0.03	10.7 ± 0.0	4.18 ± 0.03	...

...	t_Lr	Λ_to	τ_to	Δt_ow	ε_ks	$\langle n_\mathrm{cf} \rangle_{t_\mathrm{Lr}}$	$\langle \mathrm{Nu_{cf}} \rangle$
...	133	3.66 ± 2.13	13.7 ± 8.7	3.25	49/800	75.9 ± 1.2	2.90 ± 6.65
...	234	3.58 ± 2.08	21.7 ± 14.5	5.5	9/200	79.8 ± 1.6	2.74 ± 9.98
...	700	4.98 ± 2.43	68.6 ± 51.1	17	9/200	39.5 ± 1.0	2.87 ± 11.08

Table 4.1: Simulation parameters of the direct numerical simulations performing Lagrangian particle advection – the Rayleigh number $\mathrm{Ra_D} = 10^5$, the aspect ratio $\Gamma = 16$, the total number of advected Lagrangian particles $N_\mathrm{p} = 2 \times 512^2$, and no-slip boundary conditions are applied for all runs. Besides values known from table 3.1, the table includes the total Lagrangian runtime t_Lr (which is a fraction of t_r), the characteristic turnover wavelength Λ_to and time τ_to, the temporal width of the observation windows Δt_ow, the Gaussian kernel scale ε_ks, the observed number of coherent features $\langle n_\mathrm{cf} \rangle_{t_\mathrm{Lr}}$, and the Lagrangian Nusselt number of the extracted coherent features $\langle \mathrm{Nu_{cf}} \rangle$. All statistical values correspond to the time window captured by t_Lr where the turbulent superstructures are fully established.

summarises the important parameters for all of them. The Prandtl numbers $\mathrm{Pr} = 7$ and 0.7 correspond to water and air, respectively, whereas $\mathrm{Pr} = 0.1$ addresses the transition to fluids as found in the Earth's outer core. All simulations take place in non-rotating closed domains of aspect ratio $\Gamma = 16$ which exhibit no-slip boundary conditions at every boundary. In addition to the fixed temperatures at the top and bottom planes, the lateral walls are set adiabatic. With a fixed Rayleigh number of $\mathrm{Ra_D} = 10^5$, this setup resembles laboratory experiments and ensures that the complexity is still tractable.

Once the turbulent superstructures have formed after the initial transient of each dynamical system, a total of $N_\mathrm{p} = 2 \times 512^2$ Lagrangian tracer particles is seeded on two regular horizontal grids at $z_0 = 3 \times 10^{-2}$ and $z_1 = z_0 + 5 \times 10^{-3}$. Every particle is advected at each numerical iteration in accordance with eq. (4.2) using a third-order Adams-Bashforth scheme [187] while its velocities and temperature are interpolated with spectral accuracy to its time-dependent position – this advection procedure is performed for a total Lagrangian runtime of t_Lr.

4.2.2 Lagrangian characteristics of turbulent superstructures

Lagrangian particles follow the time-dependent streamlines of the turbulent flows perfectly [188], so one might expect that their trajectories can be related to the turbulent superstructures which are known from the Eulerian perspective. To address this thought and to obtain a better understanding of the Lagrangian properties of turbulent superstructures, two objective Lagrangian measures [183] will be derived in this section.

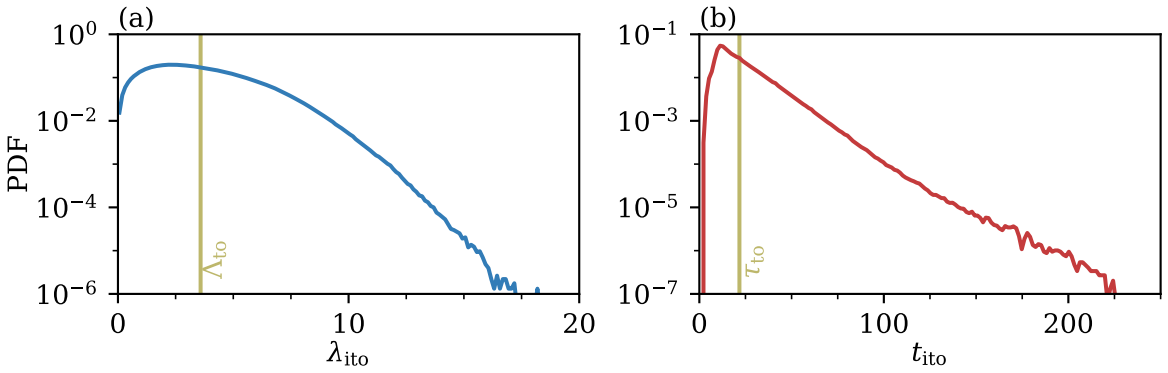

Figure 4.3: Distribution of Lagrangian turnover scales. Both the individual turnover wavelengths (a) and times (b) are spread over extended ranges. The data is based on the entire particle ensemble from simulation run L2.

The first measure, the characteristic *turnover wavelength* Λ_{to}, is a horizontal length scale that can be associated with the counter-rotating double roll-like movement of the particles. This characteristic is determined via

$$\Lambda_{\mathrm{to}} := \langle \lambda_{\mathrm{ito}} \rangle_{N_{\mathrm{p}}} \qquad \text{with } \lambda_{\mathrm{ito}} := 4\, l_{\mathrm{ht}}, \tag{4.4}$$

where λ_{ito} is the distribution of individual turnover wavelengths and l_{ht} captures the particles' horizontal travel distances between two successive intersections of the midplane. The coefficient 4 is supposed to approximately convert the latter to a wavelength (which is the well-known measure known from the Eulerian framework).

The second measure is the characteristic *turnover time* τ_{to}. This time scale is quantified as the average time necessary for each particle to complete an entire turnover, the latter of which is probed by passing the heights $z_1 = 0.2$ and $z_2 = 0.8$. An example helps understanding how this is evaluated: suppose a particle is initially at $z_{\mathrm{Lp}} < z_1$ and passes at time t_1 the horizontal plane at z_1. To finish an entire turnover, it is required to continue moving upwards, pass z_2, start moving downwards, pass z_2 and z_1 again, start once more moving upwards and pass z_1 at t_2. The time difference $t_2 - t_1$ yields subsequently the corresponding turnover time. The characteristic turnover time

$$\tau_{\mathrm{to}} := \langle t_{\mathrm{ito}} \rangle_{N_{\mathrm{p}}} \tag{4.5}$$

is eventually determined from the distribution t_{ito} of these above described individual turnover times.

Figure 4.3 provides the distribution of the individual turnover wavelengths λ_{ito} and times t_{ito} exemplary for simulation run L2 via their probability density functions (PDFs). Both distributions are characterised by extended tails, underlining the high probability of long excursions of the particles in either a boundary layer or the bulk. The corresponding characteristic turnover wavelengths and times are included for all simulations in table 4.1 – as the characteristic turnover wavelengths can be found to be in good accordance with the integral length scale of the temperature field, $\Lambda_{\mathrm{to}} \simeq \Lambda_T$, the consistency of the Lagrangian with the Eulerian framework is confirmed.

4.3 Lagrangian coherent features and their impact on the global heat transport

Albeit Lagrangian coherent features mix or interact only weakly with their surroundings [174, 175], pair dispersion introduces chaoticity and prohibits any efficient manual extraction of coherent sets. Instead, *unsupervised machine learning* – i.e. learning from a dataset that is not biased by labels provided by a human – is the key to automated, objective, and data-driven feature recognition [189, 190]. For this reason, previous studies [174, 177, 178, 183, 191, 192] developed and applied corresponding approaches to successfully detect coherent sets for simple flows or structures.

In this section, the knowledge on *spectral clustering* – i.e. the sub-division of data into different groups by exploiting spectral properties – gained from these previous studies will be combined with a recently developed feature separation technique [193] to objectively extract a large number of individual coherent sets in three-dimensional Rayleigh-Bénard convection. To subsequently quantify the interaction of these sets with their surroundings, their transport of temperature as an advected scalar will be compared with their complement.

4.3.1 Feature extraction procedure

The feature extraction procedure consists of several distinct steps [183, 191, 192] and will be described in the following.

4.3.1.1 Generation of Lagrangian data

Lagrangian data is generated for 3 different flows as pointed out in section 4.2. In every run, a vast number of Lagrangian particles is advected for about 10 characteristic Lagrangian turnover times τ_{to} while position, velocity, and temperature are recorded throughout. Although being seeded on regular grids, the particles are randomly distributed across the domain after approximately $3\tau_{\mathrm{to}}$.

4.3.1.2 Graph construction using some (dis-)similarity measure

Coherent features are represented by trajectories that remain in close proximity throughout the time interval of observation [176]. As pair dispersion destroys any coherence for too long observation times, see again figure 4.1, coherent sets are extracted from several distinct observation windows of length $\Delta t_{\mathrm{ow}} \ll t_{\mathrm{Lr}}$. In accordance with the intuition, the (dis-)similarity of trajectories is evaluated within each window by the time-averaged distance between the trajectories fragments [178, 191]

$$d_{ij}\left(t_0\right) = \left\langle \left| \boldsymbol{x}_i - \boldsymbol{x}_j \right| \right\rangle_{\Delta t_{\mathrm{ow}}}. \tag{4.6}$$

Here, t_0 indicates the centre of the observation window – i.e. the average is computed for the time interval $t_0 - \Delta t_{\mathrm{ow}}/2 \leq t < t_0 + \Delta t_{\mathrm{ow}}/2$ –, and the subscripts i and j denote the particle indices with $(i, j) = 1 \ldots n_{\mathrm{ep}}$ where $n_{\mathrm{ep}} \leq N_{\mathrm{p}}$ is the number of evaluated particles.

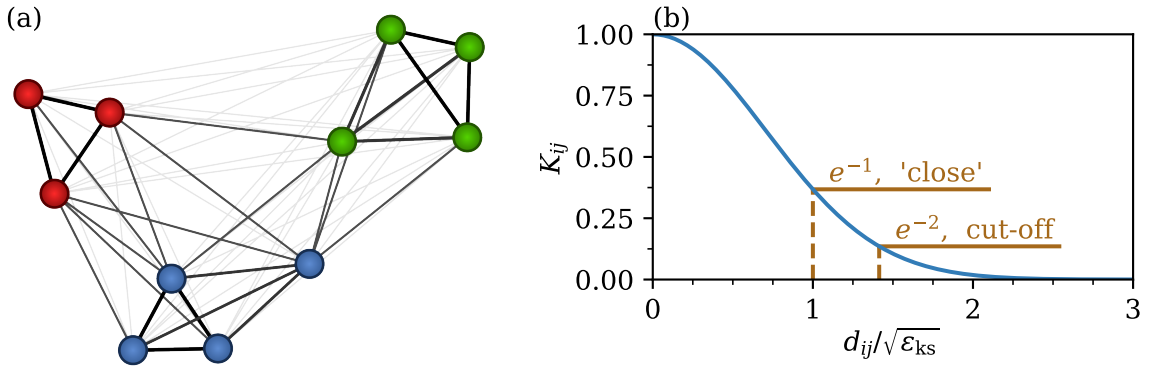

Figure 4.4: Graph construction. (a) Different data points (here trajectory fragments) are represented in graphs by different nodes. The relation between different nodes is described by the edges (drawn thinner and less dark for weaker relations) and can be used to extract features of the graph. (b) A Gaussian kernel adjusts the edges based on the kernel scale $\varepsilon_{\mathrm{ks}}$ and helps deciding which to cut off.

This measure relates any such particle to every other particle and thereby constructs a *graph* or network amongst them, see figure 4.4 (a). In such a graph, different data points are represented by different nodes and the relations between these different nodes are characterised by the edges. As the time-averaged distance between the particles is symmetric, the graph is undirected.

4.3.1.3 Adjustment of edge weights and sparsification of the graph

The constructed graph is an alternative representation of the high-dimensional dynamical system. However, the measured data is often embedded on a lower-dimensional manifold which might not be captured properly by the chosen (dis-)similarity measure. In contrast, a diffusion process on this manifold would optimally feel its intrinsic geometry [194]. To resemble such a diffusion process, the edge weights of the graph need to be adjusted.

In a first sub-step, a Gaussian (or diffusion) kernel [195, 196]

$$K_{ij} = \begin{cases} e^{-d_{ij}^2/\varepsilon_{\mathrm{ks}}} & \text{if } d_{ij} \leq d_{\mathrm{cut}}, \\ 0 & \text{if } d_{ij} > d_{\mathrm{cut}}, \end{cases} \tag{4.7}$$

with the kernel scale $\varepsilon_{\mathrm{ks}}$, see also figure 4.4 (b), is applied to the graph. The resulting edge weights are now bounded between 0 and 1, include non-linearity (just as the dynamical system), and can be interpreted in terms of similarity. Weak connections between different nodes are hardly relevant for the global manifold, so these edges can be cut off and the graph sparsified without loss of accuracy [196] – this is implemented in the above equation by the cut-off distance d_{cut}.

In a second sub-step, the graph Laplacian $\boldsymbol{L}$ is obtained via [196]

$$L_{ij} = \frac{1}{\varepsilon_{\mathrm{ks}}}\left(P_{ij} - \delta_{ij}\right) \quad \text{with } P_{ij} = \frac{\hat{K}_{ij}}{\sum_{j=1}^{n_{\mathrm{ep}}} \hat{K}_{ij}}, \quad \hat{K}_{ij} = \frac{K_{ij}}{k_i^{\alpha} k_j^{\alpha}}, \text{ and } \quad k_i = \sum_{i=1}^{n_{\mathrm{ep}}} K_{ij}. \tag{4.8}$$

Therefore, the kernel matrix $\boldsymbol{K}$ can be pre-normalised to account for density variations on the manifold, and the edge weights are translated in the stochastic transition matrix $\boldsymbol{P}$ to transition probabilities between different states of a Markov chain [197]. With $\alpha = 1$ (as used in this work), a random walk generated by $\boldsymbol{P}$ on the data points may converge to Brownian motion on the manifold and the resulting graph Laplacian $\boldsymbol{L}$ may be related to the Laplace-Beltrami operator [196, 198, 199]. In more detail, the entries of this Laplacian rate matrix are related to the expected holding time of state i (for $i = j$) and the transition probability from state i to j (for $i \neq j$) of the Markov chain [192].

Hence, after these two sub-steps, the Laplacian $\boldsymbol{L} \in \mathbb{R}^{n_{\mathrm{ep}} \times n_{\mathrm{ep}}}$ describes eventually the different data points or trajectory fragments effectively on the underlying manifold.

4.3.1.4 Translation of the graph data into eigenspace

To detect coherent features, the graph needs to be sub-divided such that the within-cluster similarity is maximised whereas the between-cluster similarity is simultaneously minimised [191], see again figure 4.4 (a). This aim requires a similarity graph and could thus already be applied after the first sub-step from above. However, to avoid the separation of a single node from the rest, a balanced or normalised cut is necessary [191] – unfortunately, this is practically not solvable for large datasets [200]. Fortunately, the solution of the eigenvalue problem

$$\boldsymbol{L}\boldsymbol{\Xi}_n = \xi_n \boldsymbol{\Xi}_n \tag{4.9}$$

approximates the solution of this cut problem [201] and serves as an indicator for the sub-division of the graph [183, 191]. The subscript $n = 1 \ldots n_{\mathrm{ep}}$, and by construction of the graph Laplacian the ordered eigenvalues ξ_n satisfy $0 = \xi_1 \geq \xi_2 \geq \cdots \geq \xi_{n_{\mathrm{ep}}}$ [192] – as these represent the spectrum of the Laplacian, the clustering derived from such eigenvalue problems is termed *spectral*. Jumps in this spectrum, so-called *spectral gaps*, provide information on the intrinsic connectivity of the graph [196] and thus potential numbers of coherent features n_{cf} [V3]. In contrast, the eigenvectors $\boldsymbol{\Xi}_n \in \mathbb{R}^{n_{\mathrm{ep}}}$ encode the inherent (diffusion) coordinates of the data points on the manifold [194, 197]. They can eventually be used to extract the desired features.

4.3.1.5 Feature separation and extraction

Different eigenvectors contain the coordinates of all the n_{ep} data points along different axes in eigenspace. This implies in turn that individual features may be spread over several different coordinates. This becomes unintuitive and an obstacle to feature extraction – for instance via the k-means algorithm [177, 178, 183, 191] – once the number of features becomes large (say, $\gtrsim 10$). For these reasons, the recently developed *sparse eigenbasis approximation* algorithm [193] is utilised subsequently to the spectral procedure from above. In a nutshell, its key idea is to iteratively apply a rotation to the coordinates in eigenspace such that the set of eigenvectors $\{\boldsymbol{\Xi}_n\}_{n=1\ldots n_{\mathrm{cf}}}$ is transformed to a new set of vectors $\{\boldsymbol{\Psi}_n\}_{n=1\ldots n_{\mathrm{cf}}}$ which span approximately the same sub-space but are significantly sparser.

In more detail, this is realised as follows. First, let the sub-space that is spanned by the set of original orthonormal eigenvectors $\{\boldsymbol{\Xi}_n\}_{n=1\ldots n_{\mathrm{cf}}}$ be $\mathcal{V} \subset \mathbb{R}^{n_{\mathrm{ep}}}$. As the individual features are spread over different coordinates, every entry of these eigenvectors is most probably non-zero and so these eigenvectors are *dense*. One aims now at transforming this set of eigenvectors to a new set of vectors $\{\boldsymbol{\Psi}_n\}_{n=1\ldots n_{\mathrm{cf}}}$ which (1) spans a sub-space $\mathcal{S} \subset \mathbb{R}^{n_{\mathrm{ep}}}$ such that $\mathcal{S} \approx \mathcal{V}$, and (2) contains mostly *sparse* vectors. Considering the matrices $\boldsymbol{V} := [\boldsymbol{\Xi}_1 | \ldots | \boldsymbol{\Xi}_{n_{\mathrm{cf}}}]$ and $\boldsymbol{S} := [\boldsymbol{\Psi}_1 | \ldots | \boldsymbol{\Psi}_{n_{\mathrm{cf}}}]$ with $(\boldsymbol{V}, \boldsymbol{S}) \in \mathbb{R}^{n_{\mathrm{ep}} \times n_{\mathrm{cf}}}$, as well as some rotation matrix $\boldsymbol{R} \in \mathbb{R}^{n_{\mathrm{cf}} \times n_{\mathrm{cf}}}$, such an optimisation problem can mathematically be expressed as [193]

$$\underset{\substack{\boldsymbol{R} \in \mathfrak{S}^{n_{\mathrm{cf}}} \\ \boldsymbol{S} \in \mathfrak{U}^{n_{\mathrm{ep}}, n_{\mathrm{cf}}}}}{\arg\min} \underbrace{\frac{1}{2} \| \boldsymbol{V} - \boldsymbol{S}\boldsymbol{R} \|_{\mathrm{F}}^2}_{\substack{\text{sub-space} \\ \text{preservation}}} + \underbrace{\mu \| \boldsymbol{S} \|_{1,1}}_{\substack{\text{sparsity} \\ \text{induction}}} . \tag{4.10}$$

Here, $\mathfrak{S}^{n_{\mathrm{cf}}} = \{\boldsymbol{\Phi} \in \mathbb{R}^{n_{\mathrm{cf}} \times n_{\mathrm{cf}}} : \boldsymbol{\Phi}^T \boldsymbol{\Phi} = \boldsymbol{I}_{n_{\mathrm{cf}}}\}$ is the Stiefel manifold with the identity matrix $\boldsymbol{I}_{n_{\mathrm{cf}}}$, and $\mathfrak{U}^{n_{\mathrm{ep}}, n_{\mathrm{cf}}} = \{\boldsymbol{\Phi} \in \mathbb{R}^{n_{\mathrm{ep}} \times n_{\mathrm{cf}}} : \text{each column of } \boldsymbol{\Phi} \text{ has an } l_2 \text{ norm } 1\}$. Furthermore, $\mu = 0.99/\sqrt{n_{\mathrm{ep}}}$ is a small positive sparsity parameter, whereas $\| \boldsymbol{\Phi} \|_{\mathrm{F}} := \sqrt{\sum_{i,j} \Phi_{ij}^2}$ and $\| \boldsymbol{\Phi} \|_{1,1} := \sum_{i,j} |\Phi_{ij}|$ represent the Frobenius and $l_{1,1}$ matrix norm, respectively. In contrast, the l_2 or Euclidean norm of a vector is given by $\| \boldsymbol{\Phi} \|_2 := \sqrt{\sum_i \Phi_i^2}$. Thus, the optimisation in eq. (4.10) considers the two conditions from above just as indicated below the two individual terms. Unfortunately, finding a *global* minimum of $(\boldsymbol{R}, \boldsymbol{S}) \in \mathfrak{S}^{n_{\mathrm{cf}}} \times \mathfrak{U}^{n_{\mathrm{ep}}, n_{\mathrm{cf}}}$ is non-trivial due to non-convexity.

It is therefore proposed to find a *local* minimum by alternately fixing the rotation matrix $\boldsymbol{R}$ and optimising the sparse vector matrix $\boldsymbol{S}$, and vice versa. Both of these steps can be solved fast and exactly. First, suppose the case that $\boldsymbol{R}$ is fixed. The sparsification of $\boldsymbol{S}$ can be performed by a thresholding transformation such that $\boldsymbol{\Psi}_n = f_\mu \left[\left(\boldsymbol{V}\boldsymbol{R}^T \right)_n \right] / \left\| f_\mu \left[\left(\boldsymbol{V}\boldsymbol{R}^T \right)_n \right] \right\|_2$ yields the n-th column of $\boldsymbol{S}$ where $f_\mu(\Phi) = \mathrm{sgn}(\Phi) \max\{|\Phi| - \mu, 0\}$ is an element-wise thresholding function. Second, suppose the case that $\boldsymbol{S}$ is fixed. In order to find $\boldsymbol{R}$, the Procrustes problem $\min_{\boldsymbol{R} \in \mathfrak{S}^{n_{\mathrm{cf}}}} \frac{1}{2} \| \boldsymbol{V} - \boldsymbol{S}\boldsymbol{R} \|_{\mathrm{F}}^2$ has to be solved by a polar decomposition. If the singular value decomposition of $\boldsymbol{S}^T\boldsymbol{V}$ is denoted as $\boldsymbol{S}^T\boldsymbol{V} = \boldsymbol{M}\boldsymbol{\Sigma}\boldsymbol{N}^T$, then $\boldsymbol{R} = \boldsymbol{M}\boldsymbol{N}^T$.

After an initialisation with $\boldsymbol{R} = \boldsymbol{I}_{n_{\mathrm{cf}}}$, a loop of these two steps can iteratively be applied until the rotation matrix has converged. Finally, $\boldsymbol{S}$ is re-scaled to allow for an interpretation in terms of likelihoods – i.e., its columns $\boldsymbol{\Psi}_n$ exhibit maximum values of 1 –, and its columns get re-ordered based on their minimum values [193].

The central result of this algorithm is revealed when recalling that the columns of $\boldsymbol{S}$ are composed of the new set of sparse vectors $\{\boldsymbol{\Psi}_n\}_{n=1\ldots n_{\mathrm{cf}}}$ with $\boldsymbol{\Psi}_n \in \mathbb{R}^{n_{\mathrm{ep}}}$: different features are now separated into different vectors, because the many data points that do *not* belong to a particular feature cause a high sparsity in the corresponding vector. As the individual (non-negative) entries within each vector encode the likelihoods of the n_{ep} data points to belong to this particular feature, these feature vectors $\boldsymbol{\Psi}_n$ are extraordinarily intuitive and useful.

Ultimately, there are two particularly interesting things one can do with these sparse vectors. Firstly, one may combine the information captured in the n_{cf} sparse vectors

into a single vector $\boldsymbol{\Psi}_{\max}$ with $\Psi_{\max,\,i} = \max_{n=1\ldots n_{\mathrm{cf}}} \Psi_{i,\,n}$ which captures the maximum likelihood of feature affiliation of every data point to any feature. Secondly, one may threshold the sparse feature vectors using some threshold value ζ to extract distinct clusters, i.e., to assign every data point either to exactly one feature or to the incoherent background (in case no feature is assigned to the data point).

4.3.2 Algorithmic parameters and details

The above steps for Lagrangian coherent set extraction introduce several parameters. Although this allows algorithms to be flexible, physical or data-driven arguments help deciding for particular values which makes the process much more objective and automatable.

The number of evaluated particles n_{ep} – for which the pair-wise time-averaged distances are evaluated in eq. (4.6) – represents a spatial resolution parameter. Here, $n_{\mathrm{ep}} = N_{\mathrm{p}}$ to allow for the most detailed feature detection.

The temporal width of the observation window Δt_{ow} acts as a temporal coherence filter – patterns that exist only for significantly shorter times do not offer coherence on this time scale and thus cannot be detected. Physical arguments based on particle pair dispersion, see section 4.1.3, suggest $\tau_{\mathrm{f}} \lesssim \Delta t_{\mathrm{ow}} \lesssim \tau_{\mathrm{to}}$. For these reasons, $\Delta t_{\mathrm{ow}} \simeq \tau_{\mathrm{to}}/4$ is chosen for all flows.

The Gaussian kernel scale $\varepsilon_{\mathrm{ks}}$, see again figure 4.4 (b), represents in the present context predominantly a spatial coherence filter – as it defines which time-averaged distances are evaluated as 'close', patterns of size $d_{ij} \lesssim \sqrt{\varepsilon_{\mathrm{ks}}}$ can (roughly speaking) not be disentangled or extracted [197, 202]. So, while small values are desirable, this affects the connectivity of the graph and the lower limit of this parameter is thus clearly influenced by n_{ep} and Δt_{ow}. Given their previous choices, $\varepsilon_{\mathrm{ks}}$ is decided to be as small as the connectivity of the graph permits.

The previous section has only briefly justified a sparsification of the graph via the cut-off distance d_{cut}. However, this is actually crucial for the evaluation of larger datasets – why? Already the matrix $\boldsymbol{D}$, collecting the pair-wise distances d_{ij}, scales with the number of evaluated particles by $\boldsymbol{D} \in \mathbb{R}^{n_{\mathrm{ep}} \times n_{\mathrm{ep}}}$. For $n_{\mathrm{ep}} = N_{\mathrm{p}}$ as chosen above, this implies that $\boldsymbol{D}$ requires 2 TB of memory – beside its storage itself, its determination becomes extremely expensive. Considering the properties of the Gaussian kernel, this effort bears above some threshold no relation to its advantages. For this reason, already the instantaneous pair-wise distances are efficiently computed using k-d tree data structures (via `scipy.spatial.KDTree`) together with an intermediate threshold $d_{\mathrm{icut}} > d_{\mathrm{cut}}$. The final cut-off d_{cut} is eventually applied after the time-averaging. The resulting sparse matrices can be stored using sparse array formats (see `scipy.sparse`). Setting the sparsification parameter $d_{\mathrm{cut}} = \sqrt{2\varepsilon_{\mathrm{ks}}}$ directly relates it to the kernel scale – avoiding thus another independent parameter –, and simultaneously ensures that disregarded edges of the graph do not affect its accuracy [192, 196].

The number of coherent features n_{cf} depends on what one is searching for – in the present context, this could be for instance entire double-roll related regions of turbulent superstructures [183] or fractions of them [192]. Expecting coherent sets to be related to

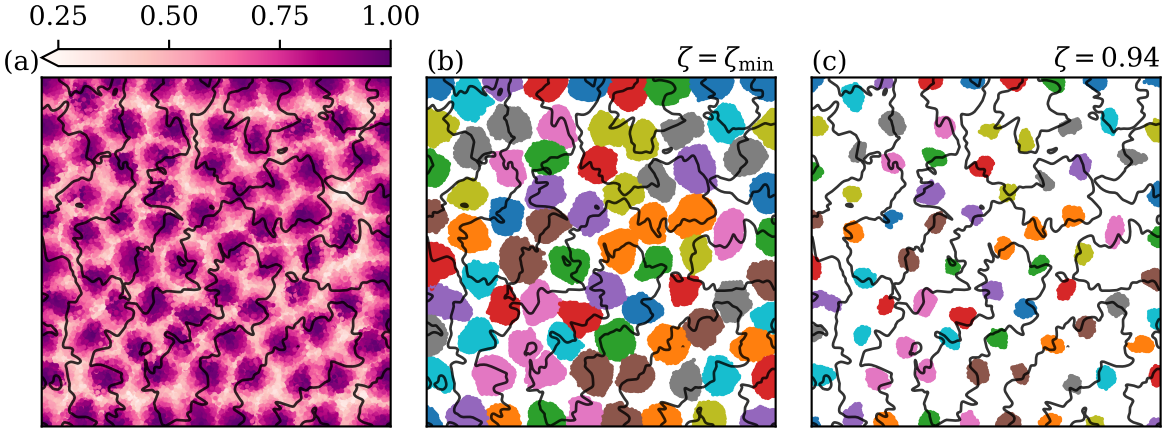

Figure 4.5: Locating Lagrangian coherent features. (a) The entire horizontal cross-section is covered by high maximum likelihoods of feature affiliation $\boldsymbol{\Psi}_{\mathrm{max}}$ of the particles $\boldsymbol{x}_i\,(t_0)$. From this, (b, c) Lagrangian coherent features can be extracted and further segregated from each other for different thresholds ζ. Different colours indicate different features, whereas the isotherm $\langle T\,(x, y, z = 0.5, t)\rangle_{\Delta t_{\mathrm{ow}}} = 0.5$ is superposed via black solid lines. The data corresponds to simulation L2 at $t_0 = 303.75$.

individual convection rolls (which are not continuously disrupted by thermal plumes), one may estimate the number of coherent features by $n_{\mathrm{cf,\,est}} \approx [\Gamma/\,(\Lambda_{\mathrm{to}}/2)]^2$. The precise number of coherent features per time window is eventually determined based on a data-driven spectral gap criterion with $n_{\mathrm{cf}} \approx n_{\mathrm{cf,\,est}}$ as described in [V2]. Furthermore, this allows to efficiently compute only the leading n_{lep} eigenpairs in eq. (4.9) with $n_{\mathrm{cf}} \lesssim n_{\mathrm{lep}} \ll n_{\mathrm{ep}}$ (via `scipy.sparse.linalg.eigs`).

Finally, the threshold ζ applies the final clustering by prescribing a particular certainty of cluster affiliation. In principle, this divides the data points into two different groups depending on if they are part of some feature or not. While ζ_{min} represents the minimum threshold necessary to isolate the individual features, higher thresholds $\zeta > \zeta_{\mathrm{min}}$ can be used to focus even stronger on the core elements. For the flow data at hand, $\zeta_{\mathrm{min}} \approx 0.7$ and the final clustering is performed using $\zeta = 0.94$ for all cases.

Hence, after these above considerations, Δt_{ow} and $\varepsilon_{\mathrm{ks}}$ represent the only simulation run-dependent parameters, and so they are included in table 4.1.

4.3.3 Relating coherent features to large-scale flow structures

The previous sections outlined how unsupervised machine learning can be used to reorganise the data in useful ways [190] by exploiting its spectral properties. This algorithm is now applied to detect Lagrangian coherent features from the three simulation runs introduced in section 4.2.

The first observation window – at $t_0 = 303.75$ – of simulation run L2 is used to obtain first insights on the relation between Lagrangian coherent features and the turbulent superstructures. For this time, the data suggests $n_{\mathrm{cf}}\,(t_0) = 80$ coherent features.

After employing the algorithm, high maximum likelihoods of feature affiliation $\mathbf{\Psi}_{\max}(t_0)$ – see again section 4.3.1.5 for their definition – can be attributed to all data points. As every such data point corresponds to a particular trajectory fragment, it is possible to relate $\mathbf{\Psi}_{\max}$ spatially to the simulation domain. Figure 4.5 (a) plots the horizontal position of all Lagrangian particles at time t_0 and colours them according to $\mathbf{\Psi}_{\max}$. It can be found that the entire simulation domain is covered by pronounced spots of extraordinarily high maximum likelihoods. To relate those regions to the present turbulent superstructures, the isotherm $\langle T(x, y, z = 0.5, t)\rangle_{\Delta t_{\mathrm{ow}}} = 0.5$ is superposed via black solid lines. Note that these lines correspond to the presence of the global mean temperature, so they should typically indicate the cores of convection rolls where the fluid is well mixed. As the isotherms intersect most of the pronounced maximum likelihood spots, a relation to the turbulent superstructures can be confirmed.

To isolate different features from each other, a minimum threshold $\zeta_{\min}$ has to be applied to the feature vectors $\mathbf{\Psi}_n$ [193] – after doing so, every trajectory fragment corresponds either to one particular feature or to the incoherent background instead. To focus on the former, figure 4.5 (b) re-plots only their corresponding particles. As different features are indicated here by different colours, their proper separation can be clearly verified.

In the following, only the very certain aspects of Lagrangian coherent features shall be used to draw conclusions on their character and properties. For this reason, a significantly higher threshold (see section 4.3.2) is applied. As visualised by figure 4.5 (c), this promotes the segregation of the individual features significantly without the extinction of any of them.

These general insights into the relation between Lagrangian coherent features and turbulent superstructures can also be drawn for other times, as well as the other simulation runs. Furthermore, a statistical analysis of the corresponding particles shows that these are located more likely outside of the boundary layers and exhibit more often close-to-mean temperatures [V2]. These trends are in accordance with the expectation of finding coherent sets at the centres of convection rolls.

Figure 4.6 visualises one Lagrangian coherent set for every simulation by evaluating vertical slabs of the domains. Every particle that is part of the focussed feature and located within the slab is drawn as a black dot for some time t_0, whereas the background shows the temperature field that is averaged over Δt_{ow} – grey arrows indicate the instantaneous surrounding flow field of the incoherent background. Firstly, this figure shows nicely how different Prandtl numbers affect the flows – thermal stems become thinner and the flow more organised for successively larger Pr. The increased spacing between the stems indicates further the slight trend towards larger patterns [75]. Secondly, it proves eventually that Lagrangian coherent features can indeed typically be related to the centres of convection rolls and so to the large-scale flow structures independently of the Prandtl number. Albeit the sets are located between regions that are more frequently disrupted by up- or down-welling thermal plumes, they are not completely decoupled from the background flow as can be expected for a continuum of fluid. Finally, Lagrangian coherent structures, see section 4.1.1, might be expected to be related to the quite regular shape of these Lagrangian coherent sets.

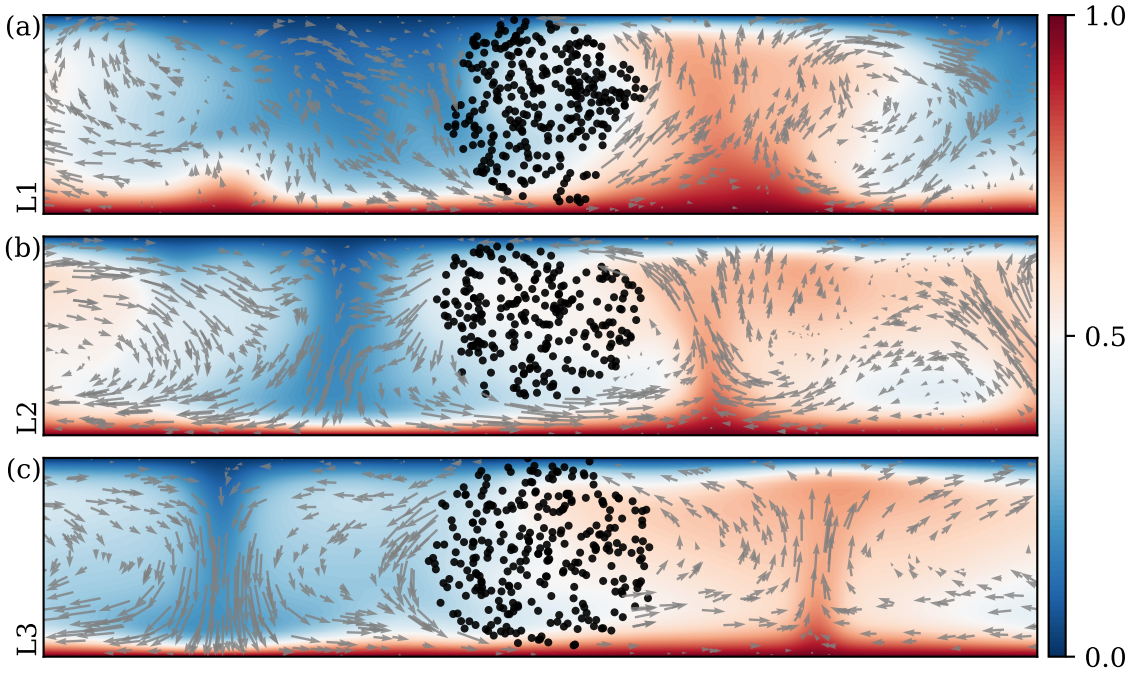

Figure 4.6: Lagrangian coherent sets at focus. Vertical slabs in the xz-plane of the domains reveal detailed information on the fundamental character of coherent features across the different Prandtl numbers. Particles that correspond to the coherent set at focus are shown as black dots for some time t_0 if located within the slab, whereas the coloured background encodes the time-averaged temperature field $\langle T \rangle_{\Delta t_{\mathrm{ow}}}$ within the slab. The grey arrows indicate the instantaneous surrounding flow field. The slabs' thickness is 0.2 and placed around the centre of the coherent sets.

4.3.4 Heat transport of Lagrangian coherent features

Coherent sets or features are represented by trajectory fragments that remain in close proximity throughout some intermediate time interval [176] and can thus be expected to mix or interact only weakly with their surroundings [174, 175]. However, the above detected coherent features in Rayleigh-Bénard convection are shown to be clearly embedded into the surrounding flow – in other words, they are not fully decoupled from the incoherent background. This suggests to analyse the participation of those sets in the heat transfer across the fluid layer, which should eventually allow to conclude on their interaction with the surrounding flow.

In order to evaluate the heat transfer of individual Lagrangian particles, one may start by defining a *local* Nusselt number

$$\mathrm{Nu}_{\mathrm{loc},\,i}\ \left[\boldsymbol{x}_i\left(t\right),t\right] := -\left.\frac{\partial T}{\partial z}\right|_{\boldsymbol{x}_i(t)} + \sqrt{\mathrm{RaPr}}\ \left.u_z T\right|_{\boldsymbol{x}_i(t)} \tag{4.11}$$

that is proportional to the vertical component of the heat current vector and corresponds

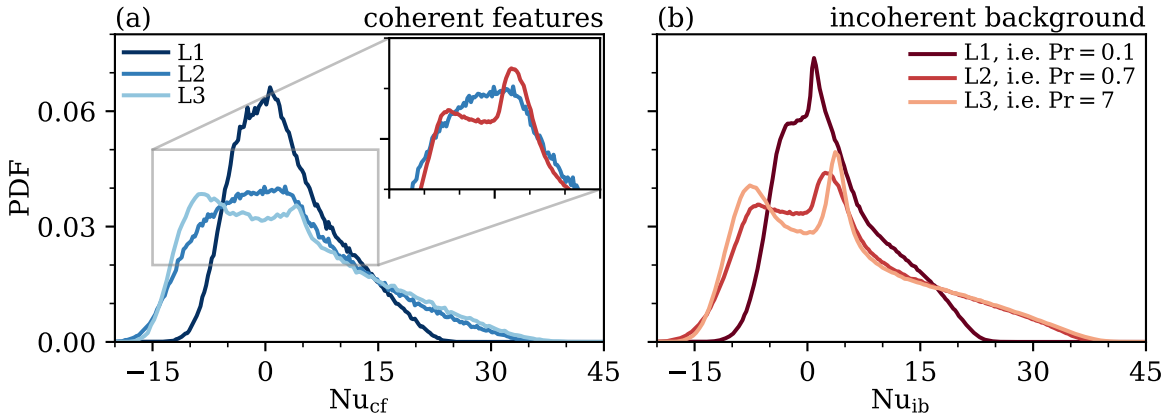

Figure 4.7: Lagrangian heat transport statistics. The Lagrangian Nusselt numbers are disentangled for all three simulation runs depending on the affiliation of the trajectory fragments to either (a) coherent features or (b) the incoherent background. The inset in panel (a) contrasts the statistics close to the peak for simulation L2.

to the instantaneous position of any particle.[2] As entire trajectory fragments – which are generated by the individual particles during the various distinct observation windows Δt_{ow} – are evaluated in the feature extraction procedure, it is possible to subsequently associate a Lagrangian Nusselt number $\mathrm{Nu}_{\mathrm{L},\,i}\ (t_0) = \langle \mathrm{Nu}_{\mathrm{loc},\,i}\ [\boldsymbol{x}_i\,(t)\,, t] \rangle_{\Delta t_{\mathrm{ow}}}$ to any of these fragments.

In the following, the Lagrangian heat transport of the trajectory fragments will be disentangled depending on the affiliation of these fragments to any coherent feature (cf) – or to the incoherent background (ib) otherwise – within the different observation windows. More specifically, two statistics are generated for each such window: one for trajectory fragments that correspond to coherent features and another one for the remaining fragments, $\mathrm{Nu}_{\mathrm{L},\,\mathrm{cf}}\ (t_0)$ and $\mathrm{Nu}_{\mathrm{L},\,\mathrm{ib}}\ (t_0)$, respectively. Incorporating information from all the different times t_0 across the total Lagrangian runtime t_{Lr} allows eventually to obtain more robust statistics and yields $\mathrm{Nu}_{\mathrm{cf}} = \langle \mathrm{Nu}_{\mathrm{L},\,\mathrm{cf}} \rangle_{t_{\mathrm{Lr}}}$ as well as $\mathrm{Nu}_{\mathrm{ib}} = \langle \mathrm{Nu}_{\mathrm{L},\,\mathrm{ib}} \rangle_{t_{\mathrm{Lr}}}$. The results of this statistical analysis are displayed for all three investigated Prandtl numbers in figure 4.7.

On the one hand, by comparing the statistics between different Prandtl numbers it is observed that both PDFs are most narrow for the smallest Prandtl number $\mathrm{Pr} = 0.1$. This observation is in line with the less efficient global convective heat transport across the fluid layer and the coarse thermal stems[3] shown in figure 4.6 (a). In contrast, the PDFs corresponding to the largest investigated Prandtl number $\mathrm{Pr} = 7$ exhibit pronounced bi-modal shapes. While the peak on the positive side of the abscissa originates in strong plume detachments from the bottom and top boundary layer, the peak on the negative side is related to plume reversals – this effect is strongest for the largest Pr due to its

[2] This local definition can be obtained similar to eq. (1.19) but without taking any average.

[3] See also section 3.3 for similar effects of the Prandtl number on the global heat transport and thermal stems in case of complementary thermal boundary conditions.

smallest thermal diffusion and Reynolds number, i.e., the plumes do not lose as much thermal energy on their way up or down due to thermal diffusion and turbulent mixing.

On the other hand, the two different statistics within each simulation run indicate a significant separation of the coherent features from the incoherent background. For instance, the peaks in $\mathrm{Nu}_{\mathrm{ib}}$ due to the thermal plume dynamics (described above) are less pronounced or even excluded in $\mathrm{Nu}_{\mathrm{cf}}$ – the inset in panel (a) highlights this by a direct comparison of the two statistics for run L2. The differences between the distributions become even more prominent by their mean values. While these are close to the global Nusselt numbers for the incoherent backgrounds, $\langle \mathrm{Nu}_{\mathrm{ib}} \rangle \approx \mathrm{Nu}$ [V2], the heat transfer of the coherent features is substantially reduced. Table 4.1 includes these latter values for all three simulations, highlighting eventually that $\langle \mathrm{Nu}_{\mathrm{cf}} \rangle \approx 2/3\ \mathrm{Nu}$.

This locally refined analysis of the heat transport demonstrates unambiguously that coherent features – which are typically trapped for intermediate times at the centres of convection rolls, see again figure 4.6 – contribute considerably less to the global heat transport across the fluid layers than the incoherent background. Hence, the spatial regions that are represented by the former are proven to interact or mix only weakly with their surroundings.

It is clear that the individual particles are not trapped for arbitrary long times inside the Lagrangian coherent features. Instead, some particles from the incoherent background will join the coherent features whereas others will leave them – this is the effect of Lagrangian particle pair dispersion, see again section 4.1.3. In turn, this suggests to incorporate a memory in time into the clustering analysis such that the coherent features can be treated as abstract entities.

4.4 Evolutionary clustering of Lagrangian trajectories

The previous section showed that a large number of Lagrangian coherent sets can be extracted by the use of unsupervised machine learning from complex three-dimensional, turbulent flows and related these sets to turbulent superstructures. On the one hand, the spatial regions that correspond to the former are shown to interact only weakly with the surrounding flow due to their coherent nature. On the other hand, however, such observations are limited to finite intermediate time windows. With increasingly extended observation, particle pair dispersion destroys any coherence and the underlying similarity measure – see eq. (4.6) – becomes meaningless.

This circumstance might seem contradicting at first glance. How can coherent sets vanish for times $\Delta t_{\mathrm{ow}} \gtrsim \tau_{\mathrm{to}}$ while turbulent superstructures survive over $t \gg \tau_{\mathrm{to}}$? Actually, this question leads astray as it misses the point – it compares, casually speaking, apples and oranges. In fact, even turbulent superstructures vanish once the flow field is averaged over excessively long times [75] instead of being observed for shorter windows.

This comparison suggests that even coherent spatial flow regions – that are inferred from (finite-time) Lagrangian coherent sets – do not need to disappear if evaluated in the right way. Instead, they could be seen as abstract entities that may consist of *different* particles or trajectory fragments over time. Some particles from outside of a

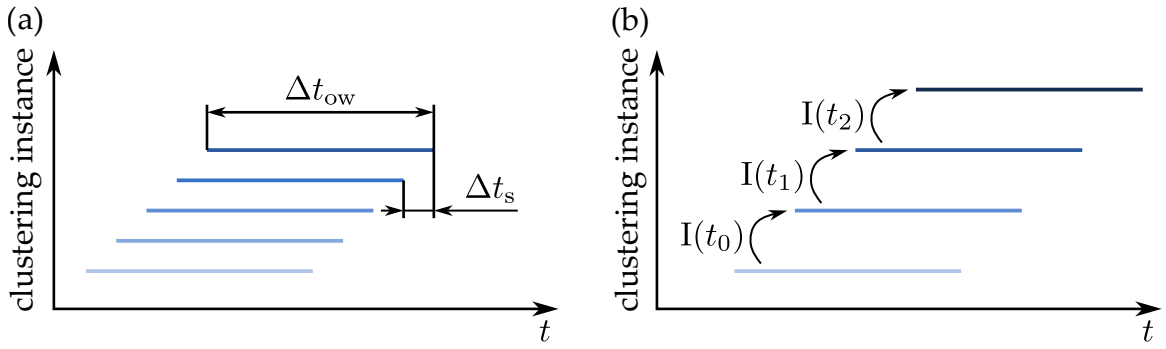

Figure 4.8: Concepts of information blending. (a) Albeit different observation windows Δt_{ow} are technically independent, they may share significant historical information if $\Delta t_{\mathrm{s}} \ll \Delta t_{\mathrm{ow}}$. (b) The active transfer of information $\mathrm{I} \geq 0$ from one instance to the subsequent one allows to manipulate the results based on historical information.

coherent feature may join it, while others from inside may leave it. What matters is not the particular sets of trajectories, but the ongoing existence of certain coherent flow regions that trap sufficiently many particles. As the contributing trajectories may alter, this concept can be termed *leaking Lagrangian coherent sets*. To keep identifying these evolving sets, this makes necessary to remember their origins.

4.4.1 Concepts of incorporating historical information

In order to overcome the constraints of particle pair dispersion, the clustering procedure should blend information from a given time with information from some previous time. This concept of *evolutionary spectral clustering* [203] should eventually allow to study the coherent features' long-term evolution. Two possible approaches are outlined in the following.

4.4.1.1 Technically independent temporal overlaps

Suppose the spectral clustering is performed for one observation window at t_0. The subsequent clustering at time t_1 can be seen as shifting the observation window Δt_{ow} in time by Δt_{s} such that $t_1 = t_0 + \Delta t_{\mathrm{s}}$. This concept is visualised in figure 4.8 (a).[4]

Clearly, if $\Delta t_{\mathrm{s}} \ll \Delta t_{\mathrm{ow}}$, the subsequent clustering incorporates a significant amount of previously seen information, drops some historical information, and adds new future information. As most of the information is shared, one can expect a smooth variation of the different clustering results over time. This sliding window approach is the easiest way to blend current information with some historical information, and an evaluation at time t_1 is technically independent of the clustering performed at t_0.

[4] In section 4.3, this time lag $\Delta t_{\mathrm{s}} \simeq \tau_{\mathrm{to}}/2 \simeq 2\ \Delta t_{\mathrm{ow}}$, yielding thus fully separated observation windows.

4.4.1.2 Active short-term memory about past coherent features

The inclusion of historical information through independent overlapping windows works well when spectral gaps are sufficiently strong [V3], i.e., when the current intrinsic connectivity of the graph deviates only slightly from the preceding time. However, in the presence of a large number of coherent features that are subjected to a turbulent flow, the induced noise in the graph can become a serious obstacle.

To overcome this issue, a *short-term memory* about the previously extracted subdominant features can be added to the present evaluation. Mathematically, this can be done in the form of a linear combination

$$\hat{\boldsymbol{K}}_{\mathrm{evo}}\left(t_0\right) = \underbrace{\mu_{\mathrm{op}}\hat{\boldsymbol{K}}\left(t_0\right)}_{\text{current situation}} + \underbrace{\left(1-\mu_{\mathrm{op}}\right)\ F\left[\hat{\boldsymbol{K}}_{\mathrm{evo}}\left(t_0-\Delta t_s\right)\right]}_{\text{short-term memory}} \tag{4.12}$$

and implemented into eq. (4.8) – thus, evolutionary techniques can be combined with the feature extraction procedure developed in section 4.3.1. Here, $0 \leq \mu_{\mathrm{op}} \leq 1$ is an obliviousness parameter, whereas the operator F extracts information about the coherent features from the past kernel matrix. Figure 4.8 (b) visualises this concept of adding an active short-term memory about past coherent features to the current evaluation.

In the case of $\mu_{\mathrm{op}} = 1$, this approach ignores historical information but coincides instead with the technically independent overlaps described above. In contrast, information about the historical coherent features is incorporated for $\mu_{\mathrm{op}} < 1$ and weighted stronger for smaller μ_{op}. This implies that once $\mu_{\mathrm{op}} < 1$, the evolutionary clustering result at time t_0 depends on the extracted features at time $t_0 - \Delta t_s$. Hence, it is not independent any more, but actively manipulated by the previously extracted features.

4.4.2 Evolving coherent features in Rayleigh-Bénard convection

Both of the above introduced concepts are suitable for extracting evolving coherent features from turbulent Rayleigh-Bénard convection flows. First, the concept of technically independent overlapping windows can successfully be applied to a two-dimensional flow at $\mathrm{Pr} = 7$, $\mathrm{Ra} = 10^8$, $\Gamma = 8$ with $6 \leq n_{\mathrm{cf}} \leq 8$ coherent features. Beside the successful evolutionary clustering, this example proves the accordance of the (time-dependent) number of coherent features in the flow with their stronger intrinsic connectivity in the graph via pronounced spectral gaps. More information on this particular analysis can be found in [V3]. In contrast, the increased complexity of three-dimensional simulations suggests and requires the extraction of evolving coherent features by the use of the more advanced active short-term memory. Here, the Lagrangian data from simulation run L2 is re-used, see again table 4.1.

Compared to section 4.3, the graph construction is slightly simplified for the following as the evolutionary feature extraction code has leadingly been written by Christiane Schneide during our collaboration. Amongst smaller modifications, the time-averaged distance d_{ij} is replaced by the number of d_{icut}-close encounters between the different particles and the Gaussian kernel is thus omitted. Here, the features are extracted from $n_{\mathrm{ep}} = 256^2$ particles with $\Delta t_{\mathrm{ow}} \simeq \tau_{\mathrm{to}}$, $d_{\mathrm{icut}} = 14/100$, $\Delta t_{\mathrm{s}} = \Delta t_{\mathrm{ow}}/10$, and $\zeta = 0.7$.

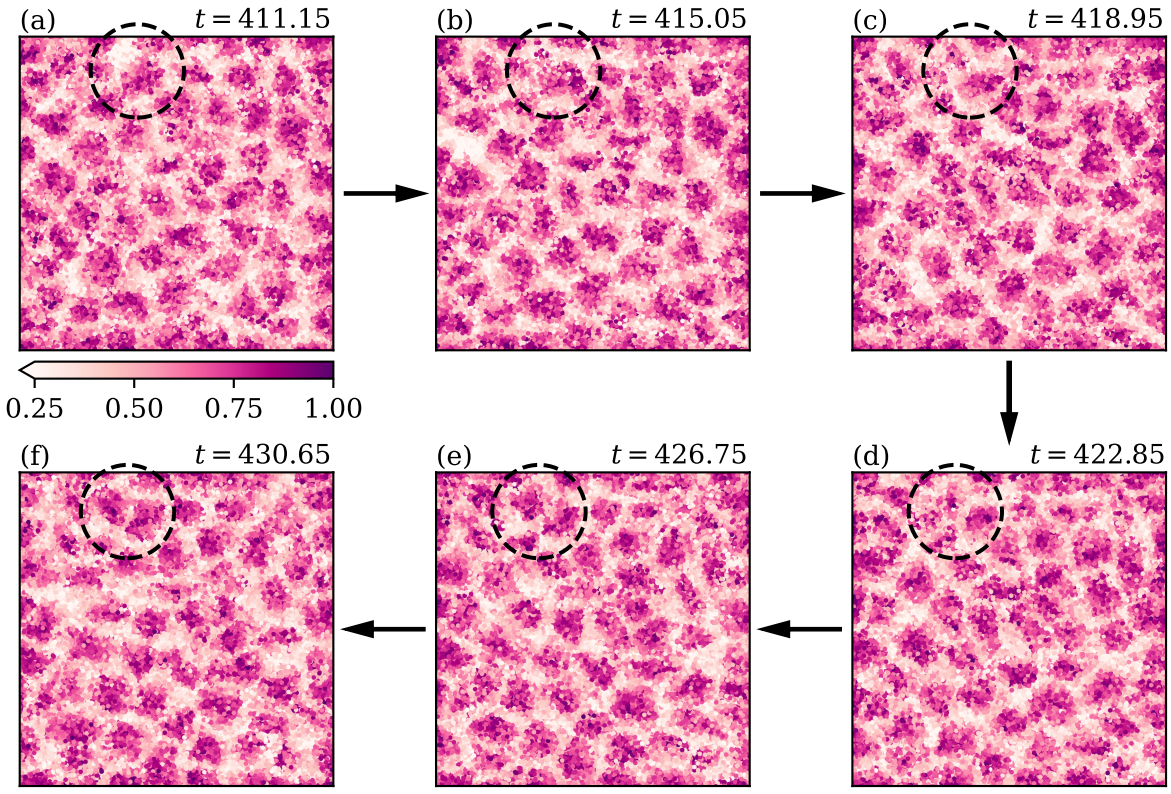

Figure 4.9: Evolving Lagrangian coherent features. The maximum likelihood of feature affiliation $\mathbf{\Psi}_{\max}(t)$ indicates rare dynamic events during the evolution of leaking Lagrangian coherent sets. (a – c) An existing feature splits a new one off. (d, e) This young feature merges shortly after its birth with another one, just before (f) the situation relaxes. All panels visualise the entire horizontal cross-section from simulation L2 and highlight the regions of interest by dashed circles.

Despite these different parameters, the first investigated observation window suggests through its spectrum a roughly similar number of coherent features compared to the previous analysis in section 4.3. All subsequent evaluations are biased to some extend by the choice of this initial number of coherent features as historical information is included from now on with $\mu_{\text{op}} = 0.9$. To support the dynamical evolution of the coherent features, their number is allowed to vary within 10% between subsequent observation windows. Hence, the extraction of evolving Lagrangian coherent sets across the Lagrangian runtime t_{Lr} can again be automated to a large extent.

This new method of evolving coherent feature detection allows to track a large number of coherent features over long time spans. As the trajectory fragments within these features exhibit still reduced heat transport properties, features extracted from this evolutionary approach can be found to be in accordance with the previously extracted features from section 4.3. Throughout their slow dynamical evolution, some features might emerge while others might vanish or even join. Albeit these events of the birth or death of coherent features can be presumed to be rare (due to the slow re-organisation

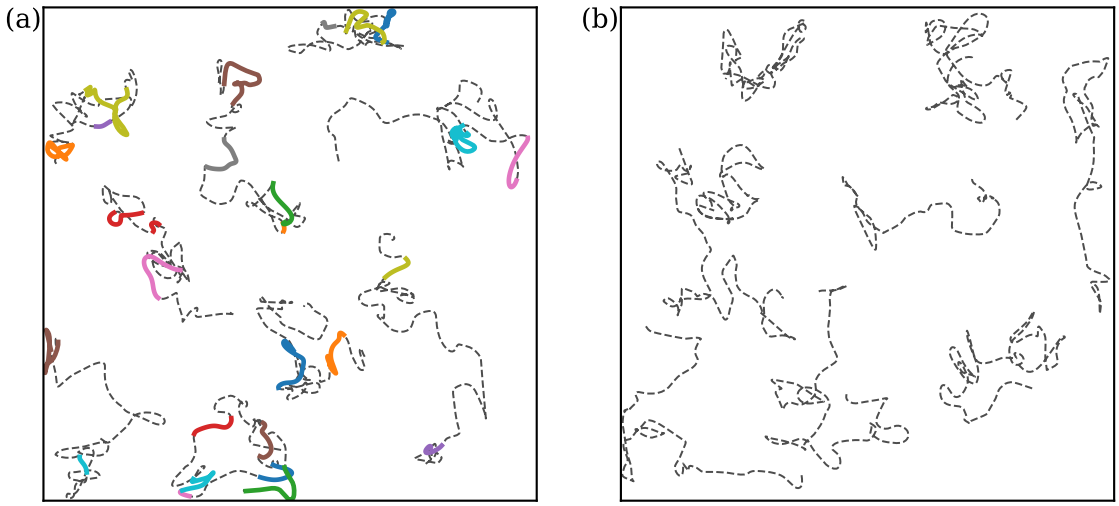

Figure 4.10: Alternating coherent feature affiliation. (a) Some trajectories participate in one or more evolving features throughout their evolution, whereas (b) some other trajectories cannot be associated to any feature during the entire Lagrangian runtime. Trajectory fragments with feature affiliations are plotted using solid lines, whereas the remaining fragments are dashed. Different colours indicate different features. Both panels visualise the entire horizontal cross-section from simulation L2.

of turbulent superstructures), a few of them can be detected during the Lagrangian runtime. Figure 4.9 visualises thereto a time series of the maximum likelihood of feature affiliation $\mathbf{\Psi}_{\max}(t)$ of all evaluated particles. As highlighted by the dashed circles, the split of a feature creates a new one which merges shortly afterwards with another feature. Interestingly, such highly dynamic events leave again a clear trace in the spectrum of the graph [V3].

Bearing this slow eternal evolution of Lagrangian coherent features in mind, it is eventually time to return to the concept of leaking Lagrangian coherent sets. As raised in the introduction of this section 4.4, different particles are expected to participate in numerous evolving coherent features by joining or leaving them. This expectation is confirmed by figure 4.10, the latter of which projects a few selected trajectories onto a horizontal plane. Here, trajectory fragments are plotted as solid lines if the corresponding particle can be associated at that time with some feature – different features are again indicated by different colours. In contrast, the remaining trajectory fragments – corresponding to times at which the particles cannot be associated with any evolving feature – are plotted as dashed lines. As shown by panel (a), several trajectories switch indeed between different evolving coherent features as time passes.

However, not every particle participates during the finite Lagrangian runtime in some feature. This circumstance is underlined by panel (b), which plots only trajectories that do not contribute to any feature throughout their entire evolution. Undoubtedly, the number of such trajectories will decrease for an increasingly extended Lagrangian runtime.

The fact that dynamically evolving Lagrangian coherent features are constructed by alternating trajectory fragments proves their independence from a particular set of particles. Clearly, not every particle can participate in such a feature at once, and not every particle will do so due to the limited lifetime of the evolving features. As turbulent superstructures change over time, so do these coherent spatial regions of fluid. Hence, these persistent features of turbulent natural thermal convection flows are excellent candidates to serve as the Lagrangian counterpart of the large-scale flow structures in the Eulerian frame of reference.

4.5 Summary

The vast complexity of geo- and astrophysical convection systems, such as the ones outlined in chapter 1, exceeds by far what can be captured through measurements. Instead, many aspects of their dynamics need to be inferred from sparse observational data. This circumstance motivated the second objective of the thesis at hand.

This chapter 4 aimed at bridging the gap between such sparse observations of coherent or point-like objects and the large-scale flow structures of natural thermal convection. To this end, the dynamic evolution of massless Lagrangian (material) particles that are advected in classical Rayleigh-Bénard convection flows was studied. As the chaoticity of turbulent flows manifests in particle pair dispersion, automated feature extraction techniques are vital to finding persistent coherent features in this framework. Here, unsupervised machine learning was used to extract and learn from these coherent features.

In a first approach, spectral clustering was combined with a recently developed feature separation algorithm to extract an immense number of coherent subsets of trajectory fragments on the underlying manifold of the flow. Equipped with these tools it was subsequently possible to relate these features to the large-scale flow structures. It was found that Lagrangian coherent sets or features can be associated with the centres of convection rolls, the latter of which are essential concepts of turbulent superstructures. However, although these spatial regions offer an increased coherence, they are still continuously embedded into the surrounding flow.

The mixing or interaction of coherent sets with their surroundings was studied by means of an analysis of their heat transport across the fluid layer. As Lagrangian coherent features mark spatial regions that are less frequently disrupted by up- or down-welling thermal plumes, they contribute less to the global heat transport compared to the incoherent background flow. A Lagrangian evaluation of the Nusselt number revealed that Lagrangian coherent features transfer about one third less heat across the fluid layer relative to the global average. Hence, albeit being a necessary skeleton for turbulent superstructures, they reduce the overall heat transfer significantly across different fluids.

As the observation window is extended, increasingly more particles will leave the spatial regions at which the coherent sets have been located – instead, other particles will join them and so these regions will consist over time of alternating particles. This idea of leaking Lagrangian coherent sets gave rise to study coherent features as abstract entities. In a second approach, historical information was incorporated to the previous procedure.

This allowed finally to study the evolution of Lagrangian coherent features – together with their possible birth and death – successfully throughout the entire Lagrangian runtime. It remains open for future studies to apply this new evolving feature extraction technique to the gradual supergranule aggregation discovered in chapter 3.

These results from the material transport perspective connect Lagrangian observations with the complementary Eulerian framework. The trapping of trajectories at some spatial regions for an intermediate time allows thus to infer properties of the surrounding flow – vice versa, this identifies the role of the large-scale flow structures on material transport. This is not just useful for sparse particle tracking data obtained from long laboratory experiment runs [185, 204], but also to cannibalise the previously collected data from geo- and astrophysical flows even more. Moreover, the birth and death of such coherent spatial regions might be used to extract a time scale that is characteristic to the lifetime of large-scale flow structures such as turbulent superstructures. This access to more data via inferred properties might ultimately pave the way for an improved understanding of flow hierarchies in natural thermal convection flows.

Chapter 5

Concluding remarks and perspectives

In this thesis, turbulent Rayleigh-Bénard convection as the paradigm of natural thermal convection flows was studied from both Eulerian and Lagrangian perspectives. In a nutshell, the results can be summarised as follows:

- The thermal boundary conditions rule the large-scale pattern formation. In case of an applied constant heat flux, a new mechanism of self-organisation was discovered, termed gradual supergranule aggregation in accordance with the astrophysical motivation, and studied across the Ra–Pr–Ro parameter space. On the one hand, a leading Lyapunov vector analysis allowed to relate this transient mechanism's dynamical origin to secondary instabilities. On the other hand, a spectral energy transfer analysis revealed that purely two-dimensional advective mode interactions exhibit an inverse cascade on large scales and can be accounted for the growth of thermal variance during this transient process of large-scale pattern formation.

- Unsupervised machine learning methods to successfully relate sparse observational Lagrangian data to (evolving) turbulent superstructures – i.e., the large-scale flow structures that form in the complementary case of applied constant temperatures – were established. The role of these structures for the material transport was identified as to trap particles for intermediate times in coherent regions close to the centres of convection rolls, the latter of which interact only weakly with the surrounding flow and thus offer a reduced heat transport across the fluid layer.

Due to the simplicity of the underlying dynamical system, it applies to various natural flows (see again table 1.2) and so these results allow to interpret these flows' extremely complex nature more successfully.

Fluid dynamics is typically about looking at things from a far distance [205] – thus, the fundamental governing equations (1.2) – (1.4) exploit continuum mechanics instead of particle-particle interactions (see e.g. [206] for a corresponding study of constant heat flux-driven Rayleigh-Bénard convection). The underlying physics of the latter is consequently

captured in the fluid properties ρ, ν, λ_t, and so on, assuming further a Newtonian fluid. These first simplifications are in this work complemented by the Oberbeck-Boussinesq approximation. However, even after these steps, the main ingredients for thermal convection are still included which allows eventually to study it numerically in a horizontally extraordinarily extended domain with nowadays' computational capabilities.

In the long run, these simplifications or approximations may be less restrictive than they seem at first glance. For instance, Newtonian properties hold definitely not for all fluids but even complex (e.g. colloidal [207]) ones may behave within certain ranges of shear rates just like classical Newtonian fluids. The situation is quite similar for the extension of the dynamical system by rotation around the vertical axis. Although this is a first approximation to the behaviour close to the geographical pole, one can nevertheless learn from it how geo- and astrophysical objects are influenced even farer away from it if anisotropies due to horizontal rotation are disregarded.

The insights obtained in this thesis found on computationally expensive direct numerical simulations which do not involve any additional, tailored modelling of physics. Hence, the obtained understanding and collected data could be used to subsequently derive and enhance models for LES and RANS simulations or to evaluate the quality of GQL approximations. This is not only useful to allow for cheaper simulations in the field of engineering – all our geo- and astrophysical observations collect sparse data (if at all) on a coarse grid only. These measurements' dynamics are thus inherently governed by (filtered) equations for large-scale quantities.

This observational restriction is accompanied by our limited computational capabilities. Albeit seemingly endless, there is currently no way to solve the governing equations for an entire geo- or astrophysical object numerically [8, 208, 209]. For instance, a full simulation of the Sun would require approximately 10^{22} W – as this represents the entire energy produced by an M9V main sequence red dwarf [210], it becomes ultimately clear that one will rely forever on simplified setups and approximations to project their behaviour into future.

Fortunately, this inevitable circumstance can be conquered by our knowledge on the present fundamental equations from which one may derive models for analytical and numerical studies [8]. It can be conceptually helpful to think of such flows as multiple loosely connected layers that allow for a separation of flow features into ones that penetrate most of the fluid layer, and ones that become important just at the boundaries [8, 211]. For instance, in the solar case the *outer shallow layer* (which makes basically up the outer-most 1% of the convection zone) sets itself apart from the rest of the convection zone due to its extreme gradients and supersonic flow velocities [8]. Large-scale flow structures – such as those discovered and studied in the thesis at hand – correspond in this context to the depth-penetrating layer. Some basic assumptions or simplifications are thus not just allowed but key to a successful tailoring of such models.

The interplay of magnetic fields – as often part of geo- and astrophysical objects – with these large-scale turbulent structures is yet almost unknown and even less is known about the feedback of their induced magnetic field on the external magnetic field. Answering a scientific question raises not rarely again several new ones, and so will it be the work of future studies to address these interesting and exciting questions of physics.

Appendix

A Linear stability analysis

In this appendix A, the linear stability of rotating Rayleigh-Bénard convection – see equations (3.8) and (3.9) in the main text – will be derived. While taking care of both idealised thermal boundary conditions, the free-slip scenario is assumed throughout.

Governing equations

At the onset of convection, heat conduction is starting to be supported by convective heat transfer across the fluid layer – consequently, the temperature profile changes from the horizontally homogeneous linear conduction profile towards another profile. This suggests to express the governing equations based on the temperature deviation field Θ – see also eq. (3.5) –, the latter of which is zero below the onset and becomes non-zero above. For simplicity, this temperature deviation field will be called just temperature field in the following. These governing equations read in the dimensional form

$$\nabla \cdot \boldsymbol{u} = 0, \tag{A.1}$$

$$\frac{\partial \boldsymbol{u}}{\partial t} + (\boldsymbol{u} \cdot \nabla)\, \boldsymbol{u} + 2\Omega\, \boldsymbol{e}_z \times \boldsymbol{u} = -\frac{1}{\rho_{\mathrm{ref}}} \nabla p + \nu\, \nabla^2 \boldsymbol{u} + \alpha g \Theta \boldsymbol{e}_z, \tag{A.2}$$

$$\frac{\partial \Theta}{\partial t} + (\boldsymbol{u} \cdot \nabla)\, \Theta = \kappa\, \nabla^2 \Theta + \beta u_z \tag{A.3}$$

with

$$\Theta\,(\boldsymbol{x}, t) := T\,(\boldsymbol{x}, t) - T_{\mathrm{lin}}\,(z)\,, \qquad T_{\mathrm{lin}}\,(z) := T_{\mathrm{bot}} - \beta\,(z - z_{\mathrm{bot}})\,, \tag{A.4}$$

and can be derived from equations (1.2) – (1.4) by inserting eq. (A.4). β represents the applied vertical temperature gradient across the fluid layer – in the Dirichlet case, this can be substituted by $\Delta T/H$. Section 3.5 (and in particular section 3.5.2.1) made use of these equations in the non-dimensional form based on the free-fall inertial balance, for the latter see again section 1.2.2.3. This inertia-based scaling is not appropriate for describing the situation at the onset of convection. Instead, diffusion is the important mechanism to balance the buoyancy – recall here also the vivid explanations in section 1.2.1. Presuming that viscous diffusion balances the buoyancy, the equations can be non-dimensionalised by

$$\boldsymbol{x} = H\, \tilde{\boldsymbol{x}}, \qquad \boldsymbol{u} = \frac{\nu}{H}\, \tilde{\boldsymbol{u}}, \qquad \Theta = \beta H\, \mathrm{Pr}\, \tilde{\Theta}, \qquad t = \frac{H^2}{\nu}\, \tilde{t}, \qquad p = \frac{\rho_{\mathrm{ref}} \nu^2}{H^2}\, \tilde{p}, \tag{A.5}$$

with variables exhibiting tildes being non-dimensional. Note that here the vertical viscous diffusion time scale τ_ν, which is known from the footnote on page 7, emerges. The tildes are, as is common, dropped in the following.

The non-dimensional governing equations read eventually

$$\nabla \cdot \boldsymbol{u} = 0, \tag{A.6}$$

$$\frac{\partial \boldsymbol{u}}{\partial t} + (\boldsymbol{u} \cdot \nabla)\, \boldsymbol{u} + \sqrt{\mathrm{Ta}}\, \boldsymbol{e}_z \times \boldsymbol{u} = -\nabla p + \nabla^2 \boldsymbol{u} + \mathrm{Ra}\, \Theta \boldsymbol{e}_z, \tag{A.7}$$

$$\mathrm{Pr}\, \frac{\partial \Theta}{\partial t} + \mathrm{Pr}\ (\boldsymbol{u} \cdot \nabla)\, \Theta = \nabla^2 \Theta + u_z, \tag{A.8}$$

revealing the Prandtl number Pr, Rayleigh number Ra, and Taylor number Ta – see equations (1.9), (1.10), and (3.10), respectively – as control parameters. To eliminate the pressure from the Navier-Stokes equation, one may want to work with the vorticity equation (see again section 3.4.4) as well as its curl, both of which read with this scaling

$$\frac{\partial \boldsymbol{\omega}}{\partial t} + \nabla \times [(\boldsymbol{u} \cdot \nabla)\, \boldsymbol{u}] - \sqrt{\mathrm{Ta}}\, \frac{\partial \boldsymbol{u}}{\partial z} = \nabla^2 \boldsymbol{\omega} + \mathrm{Ra}\, \nabla \times \boldsymbol{e}_z\, \Theta, \tag{A.9}$$

$$\begin{aligned} \frac{\partial \left(\nabla^2 \boldsymbol{u}\right)}{\partial t} - \nabla \times \nabla \times [(\boldsymbol{u} \cdot \nabla)\, \boldsymbol{u}] + \sqrt{\mathrm{Ta}}\, \frac{\partial \boldsymbol{\omega}}{\partial z} = \\ = \left(\nabla^2\right)^2 \boldsymbol{u} + \mathrm{Ra}\, \left[\nabla^2 \Theta \boldsymbol{e}_z - \nabla \left(\frac{\partial \Theta}{\partial z}\right)\right]. \end{aligned} \tag{A.10}$$

Boundary conditions

The set of boundary conditions reads in the non-dimensional form

$$\frac{\partial u_{x,y}}{\partial z}\ (z \in \{z_{\mathrm{bot}}, z_{\mathrm{top}}\}) = 0, \tag{A.11}$$

$$u_z\ (z \in \{z_{\mathrm{bot}}, z_{\mathrm{top}}\}) = 0, \tag{A.12}$$

$$\Theta\ (z \in \{z_{\mathrm{bot}}, z_{\mathrm{top}}\}) = 0, \qquad \text{or} \qquad \frac{\partial \Theta}{\partial z}\ (z \in \{z_{\mathrm{bot}}, z_{\mathrm{top}}\}) = 0, \tag{A.13}$$

recall also equations (1.14), (3.37), and the footnote on page 59. There are two additional boundary conditions that emerge from this set of equations and conditions. First, the continuity equation (A.6) yields together with the free-slip boundary conditions (A.11)

$$\frac{\partial^2 u_z}{\partial z^2}\ (z \in \{z_{\mathrm{bot}}, z_{\mathrm{top}}\}) = 0. \tag{A.14}$$

Second, the definition of the vorticity gives together with these free-slip boundary conditions

$$\frac{\partial \omega_z}{\partial z}\ (z \in \{z_{\mathrm{bot}}, z_{\mathrm{top}}\}) = 0. \tag{A.15}$$

This extended set of boundary conditions will be used in the following to analyse the linear stability of Rayleigh-Bénard convection in a horizontally infinitely extended domain.

Basic idea of a linear stability analysis

The basic idea of a linear stability analysis is to apply a small perturbation (indicated in the following by a dash Φ') onto a base state (indicated by a bar $\bar{\Phi}$) such that

$$\boldsymbol{\Phi} = \bar{\boldsymbol{\Phi}} + \varepsilon_{\mathrm{p}} \boldsymbol{\Phi}'. \tag{A.16}$$

Here, $\varepsilon_\mathrm{p} \ll 1$ is a tiny perturbation parameter. For the set of variables present, this yields

$$\boldsymbol{u} = \bar{\boldsymbol{u}} + \varepsilon_\mathrm{p}\boldsymbol{u}', \tag{A.17}$$
$$p = \bar{p} \ + \varepsilon_\mathrm{p}p', \tag{A.18}$$
$$\Theta = \bar{\Theta} + \varepsilon_\mathrm{p}\Theta', \tag{A.19}$$
$$\boldsymbol{\omega} = \bar{\boldsymbol{\omega}} + \varepsilon_\mathrm{p}\boldsymbol{\omega}'. \tag{A.20}$$

After defining the base state (in case of which $\varepsilon_\mathrm{p} = 0$), these perturbations will be introduced and their growth or decay will be studied subsequently – if they grow, the base state becomes unstable. Hence, this switching point between growth and decay marks the neutral or marginal stability of the system.

Definition of the base state

The non-convective state does not offer any motion and a linear conductive temperature profile only – the base state of the dynamical system is thus given by

$$\bar{\boldsymbol{u}} = \bar{\boldsymbol{\omega}} = \bar{\Theta} = 0. \tag{A.21}$$

Together with eq. (A.7), the base pressure can be found to be constant and is arbitrarily set to zero, i.e., $\bar{p} = 0$.

In contrast, the boundary conditions (A.11) – (A.15) set the following constraints on this base state

$$\frac{\partial \bar{u}_{x,y}}{\partial z} \ (z \in \{z_\mathrm{bot}, z_\mathrm{top}\}) = 0, \tag{A.22}$$
$$\bar{u}_z \ (z \in \{z_\mathrm{bot}, z_\mathrm{top}\}) = 0, \tag{A.23}$$
$$\bar{\Theta} \ (z \in \{z_\mathrm{bot}, z_\mathrm{top}\}) = 0, \qquad \text{or} \qquad \frac{\partial \bar{\Theta}}{\partial z} \ (z \in \{z_\mathrm{bot}, z_\mathrm{top}\}) = 0, \tag{A.24}$$
$$\frac{\partial^2 \bar{u}_z}{\partial z^2} \ (z \in \{z_\mathrm{bot}, z_\mathrm{top}\}) = 0, \tag{A.25}$$
$$\frac{\partial \bar{\omega}_z}{\partial z} \ (z \in \{z_\mathrm{bot}, z_\mathrm{top}\}) = 0. \tag{A.26}$$

Introduction of tiny perturbations

As a next step, the perturbations from equations (A.17) – (A.20) with $\varepsilon_\mathrm{p} \neq 0$ are introduced into the governing equations (A.6) – (A.10). Results from the base state are simultaneously incorporated. As the perturbation parameter $\varepsilon_\mathrm{p} \ll 1$ is tiny, only terms of order $\mathcal{O}\left(\varepsilon_\mathrm{p}^1\right)$ are kept while higher-order terms are disregarded in the following – this

terms this method a *linear* stability analysis. After dividing by ε_p,

$$\frac{\partial u'_x}{\partial x} + \frac{\partial u'_y}{\partial y} + \frac{\partial u'_z}{\partial z} = 0, \tag{A.27}$$

$$\frac{\partial \boldsymbol{u}'}{\partial t} + \sqrt{\mathrm{Ta}}\, \boldsymbol{e}_z \times \boldsymbol{u}' = -\nabla p' + \nabla^2 \boldsymbol{u}' + \mathrm{Ra}\, \Theta' \boldsymbol{e}_z, \tag{A.28}$$

$$\mathrm{Pr}\, \frac{\partial \Theta'}{\partial t} = \nabla^2 \Theta' + u'_z, \tag{A.29}$$

$$\frac{\partial \boldsymbol{\omega}'}{\partial t} - \sqrt{\mathrm{Ta}}\, \frac{\partial \boldsymbol{u}'}{\partial z} = \nabla^2 \boldsymbol{\omega}' + \mathrm{Ra}\, \nabla \times \boldsymbol{e}_z\, \Theta', \tag{A.30}$$

$$\frac{\partial \left(\nabla^2 \boldsymbol{u}'\right)}{\partial t} + \sqrt{\mathrm{Ta}}\, \frac{\partial \boldsymbol{\omega}'}{\partial z} = \left(\nabla^2\right)^2 \boldsymbol{u}' + \mathrm{Ra}\, \left[\nabla^2 \Theta' \boldsymbol{e}_z - \nabla \left(\frac{\partial \Theta'}{\partial z}\right)\right] \tag{A.31}$$

follows. Hence, the advection terms and their descendants drop out. Moreover, only perturbations remain in these equations as the base state drops out completely.

Similarly, the ansatz is introduced into the boundary conditions (A.11) – (A.15), the results from the base state are kept in mind, and

$$\frac{\partial u'_{x,y}}{\partial z}\ \left(z \in \{z_\mathrm{bot}, z_\mathrm{top}\}\right) = 0, \tag{A.32}$$

$$u'_z\ \left(z \in \{z_\mathrm{bot}, z_\mathrm{top}\}\right) = 0, \tag{A.33}$$

$$\Theta'\ \left(z \in \{z_\mathrm{bot}, z_\mathrm{top}\}\right) = 0, \qquad \text{or} \qquad \frac{\partial \Theta'}{\partial z}\ \left(z \in \{z_\mathrm{bot}, z_\mathrm{top}\}\right) = 0, \tag{A.34}$$

$$\frac{\partial^2 u'_z}{\partial z^2}\ \left(z \in \{z_\mathrm{bot}, z_\mathrm{top}\}\right) = 0, \tag{A.35}$$

$$\frac{\partial \omega'_z}{\partial z}\ \left(z \in \{z_\mathrm{bot}, z_\mathrm{top}\}\right) = 0 \tag{A.36}$$

emerges as set of constraints for the perturbations.

Applying a normal mode ansatz

The equations (A.27) – (A.31) are linear and the system is presumed to be infinitely extended in the horizontal directions. One can thus study its stability using a so-called normal mode ansatz of the form

$$\Phi'\left(\boldsymbol{x}, t\right) = \Phi\left(z\right)\ e^{\imath \boldsymbol{k}_\mathrm{h} \cdot \boldsymbol{x}_\mathrm{h}}\ e^{\sigma t} \qquad \text{with } \Phi\left(z\right) \equiv \hat{\Phi}'\left(\boldsymbol{k}_\mathrm{h}, z, t\right). \tag{A.37}$$

Note that this can be seen as a particular variation of the two-dimensional spectral expansion in eq. (3.6). Here, the hat of the Fourier coefficient is skipped for simplicity – the same is done with the dash as only perturbations remained in the equations. Moreover, $\sigma = \sigma_\mathrm{r} + \imath\sigma_\mathrm{i} \in \mathbb{C}$ is the so-called growth rate – its sign will be used in the following to determine the stability of the system. In particular, the extracted modes are either termed stationary if $\sigma = 0$, or termed oscillatory if $\sigma_\mathrm{r} = 0$ but $\sigma_\mathrm{i} \neq 0$. As oscillatory modes do not allow for a steady growth over time, the focus is here on stationary modes.

With this normal mode ansatz, the computation of horizontal or temporal derivatives becomes simple as they translate to a multiplication with $\imath k_{x,y}$ or σ, respectively. Vertical derivatives will in the following, as is common when studying the linear stability, be represented by $\partial\Phi/\partial z \equiv D\Phi$.

The insertion of the normal mode ansatz into equations (A.27) – (A.31) yields

$$\imath k_x U + \imath k_y V + DW = 0, \tag{A.38}$$

$$\sigma U - \sqrt{\mathrm{Ta}}\, V = -\imath k_x P + \left(D^2 - k_\mathrm{h}^2\right) U, \tag{A.39}$$

$$\sigma V + \sqrt{\mathrm{Ta}}\, U = -\imath k_y P + \left(D^2 - k_\mathrm{h}^2\right) V, \tag{A.40}$$

$$\sigma W = -DP + \left(D^2 - k_\mathrm{h}^2\right) W + \mathrm{Ra}\, C, \tag{A.41}$$

$$\mathrm{Pr}\,\sigma C = \left(D^2 - k_\mathrm{h}^2\right) C + W, \tag{A.42}$$

$$\sigma Z - \sqrt{\mathrm{Ta}}\, DW = \left(D^2 - k_\mathrm{h}^2\right) Z, \tag{A.43}$$

$$\left(D^2 - k_\mathrm{h}^2\right)\sigma W + \sqrt{\mathrm{Ta}}\, DZ = \left(D^2 - k_\mathrm{h}^2\right)^2 W - \mathrm{Ra}\, k_\mathrm{h}^2\, C \tag{A.44}$$

after a division by the common factor $e^{\imath \boldsymbol{k}_\mathrm{h}\cdot\boldsymbol{x}_\mathrm{h}}\, e^{\sigma t}$. The capital letters correspond to the perturbation variables via

$$u_x' \sim U, \quad u_y' \sim V, \quad u_z' \sim W, \quad p' \sim P, \quad \Theta' \sim C, \quad \omega_z' \sim Z. \tag{A.45}$$

Note that only the z-components of equations (A.30) and (A.31) are exploited as no boundary conditions are available for other components of $\boldsymbol{\omega'}$.

The occurrence of individual horizontal velocities and the pressure field in equations (A.38) – (A.41) makes them less useful compared to the remaining equations. The following analysis will thus be restricted to equations (A.42) – (A.44) which can be re-arranged to

$$\left(D^2 - k_\mathrm{h}^2 - \mathrm{Pr}\,\sigma\right) C = -W, \tag{A.46}$$

$$\left(D^2 - k_\mathrm{h}^2 - \sigma\right) Z = -\sqrt{\mathrm{Ta}}\, DW, \tag{A.47}$$

$$\left(D^2 - k_\mathrm{h}^2\right)\left(D^2 - k_\mathrm{h}^2 - \sigma\right) W = \sqrt{\mathrm{Ta}}\, DZ + \mathrm{Ra}\, k_\mathrm{h}^2\, C. \tag{A.48}$$

As horizontal velocities are not of interest any more, so is boundary condition (A.32). The remaining conditions transform to

$$W\ (z \in \{z_\mathrm{bot}, z_\mathrm{top}\}) = 0, \tag{A.49}$$

$$C\ (z \in \{z_\mathrm{bot}, z_\mathrm{top}\}) = 0, \qquad \text{or} \qquad \frac{\partial C}{\partial z}\ (z \in \{z_\mathrm{bot}, z_\mathrm{top}\}) = 0, \tag{A.50}$$

$$\frac{\partial^2 W}{\partial z^2}\ (z \in \{z_\mathrm{bot}, z_\mathrm{top}\}) = 0, \tag{A.51}$$

$$\frac{\partial Z}{\partial z}\ (z \in \{z_\mathrm{bot}, z_\mathrm{top}\}) = 0. \tag{A.52}$$

These sets of equations and boundary conditions will be used in the following to derive the particular neutral stability curves for the case of either Dirichlet or Neumann thermal boundary conditions.

Marginal stability of the Dirichlet case

In case of the classical constant temperature boundary conditions, $C\ (z \in \{z_{\mathrm{bot}}, z_{\mathrm{top}}\}) = 0$ in condition (A.50). The set of equations transforms for marginal stability with $\sigma = 0$ to

$$\left(D^2 - k_{\mathrm{h}}^2\right) C = - W, \tag{A.53}$$

$$\left(D^2 - k_{\mathrm{h}}^2\right) Z = -\sqrt{\mathrm{Ta}}\, DW, \tag{A.54}$$

$$\left(D^2 - k_{\mathrm{h}}^2\right)\left(D^2 - k_{\mathrm{h}}^2\right) W = \sqrt{\mathrm{Ta}}\, DZ + \mathrm{Ra}\, k_{\mathrm{h}}^2\, C. \tag{A.55}$$

After multiplying $(D^2 - k_{\mathrm{h}}^2)$ to eq. (A.55) and inserting equations (A.53) as well as (A.54) to eliminate C as well as Z,

$$\left[\left(D^2 - k_{\mathrm{h}}^2\right)^3 + \mathrm{Ta}\, D^2 + \mathrm{Ra}\, k_{\mathrm{h}}^2\right] W = 0 \tag{A.56}$$

can be obtained after some re-arrangements. To solve this equation, a trial function that satisfies the boundary condition (A.49) needs to be found. In accordance with eq. (3.33),

$$W(z) = \sin(m\pi z) \qquad \text{with } m \in \mathbb{N}^+ \tag{A.57}$$

for $z \in [z_{\mathrm{bot}}, z_{\mathrm{top}}] = [0, 1]$ is used. The boundary condition is thus already met by the choice of this trial function – in order to satisfy also the situation within the fluid layer, this function is subsequently inserted into eq. (A.56). The vertical derivative $D^2 W = -m^2\pi^2 W$ and so

$$\left(-m^2\pi^2 - k_{\mathrm{h}}^2\right)^3 - \mathrm{Ta}\, m^2\pi^2 + \mathrm{Ra}\, k_{\mathrm{h}}^2 = 0 \tag{A.58}$$

follows. Solving for the Rayleigh number, one obtains eventually [39]

$$\mathrm{Ra}_{\mathrm{D,\,marg}} = \frac{1}{k_{\mathrm{h}}^2}\left[\left(k_{\mathrm{h}}^2 + m^2\pi^2\right)^3 + \mathrm{Ta}\, m^2\pi^2\right]. \tag{A.59}$$

This describes finally the neutral stability for the Dirichlet case. The lowest characteristic occurs for $m = 1$ – i.e. the smallest admissible vertical wave number – and is provided in the main text in eq. (3.8), as well as visualised in figure 3.6 (a).

One might expect at first thought that the trial function should also hold for the Neumann case, and that the solution of the linear stability thus coincides. However, this is not the case. To understand this in more detail, all trial functions for the different variables are listed in their general form. These are given by

$$W(z) = \sum_m W_m \sin(m\pi z) \qquad \text{with } m \in \mathbb{N}^+, \tag{A.60}$$

$$C(z) = \sum_m C_m \sin(m\pi z) \qquad \text{with } m \in \mathbb{N}^+, \tag{A.61}$$

$$Z(z) = \sum_n Z_n \cos(n\pi z) \qquad \text{with } n \in \mathbb{N} \tag{A.62}$$

where $\Phi_{m \text{ or } n} \equiv \Phi(m \text{ or } n)$. Albeit different basis functions are necessary in the vertical direction, only one of them remains after placing them into equations (A.53) – (A.55). Hence, the latter can be easily projected onto one particular vertical wave number (see below) and are thus solvable mode-by-mode. This changes in the Neumann scenario.

Marginal stability of the Neumann case

In the opposing scenario of the Neumann-type constant heat flux boundary conditions, $\partial C/\partial z \;\; (z \in \{z_{\mathrm{bot}}, z_{\mathrm{top}}\}) = 0$ in condition (A.50). Consequently, the necessary trial functions are expressed for $z \in [0,1]$ via

$$W(z) = \sum_m W_m \sin(m\pi z) \qquad \text{with } m \in \mathbb{N}^+, \tag{A.63}$$

$$C(z) = \sum_n C_n \;\cos(n\pi z) \qquad \text{with } \; n \in \mathbb{N}, \tag{A.64}$$

$$Z(z) = \sum_n Z_n \;\cos(n\pi z) \qquad \text{with } \; n \in \mathbb{N} \tag{A.65}$$

as infinite trigonometrical Fourier series. An insertion of them into equations (A.53) – (A.55) leads thus to mixed sine and cosine functions.

The general approach to solve for the stability of the system requires inserting these trial functions into the set of equations (A.46) – (A.48). After doing so, every equation contains sums over the infinite vertical wave numbers captured by m and n. To translate these equations into evolution equations for one particular wave number, they need to be projected onto the latter while exploiting the orthogonality of the basis functions. The scalar product $\langle \cdot, \cdot \rangle$ between two complex, one-dimensional functions (f, g) is given by

$$\langle f, g \rangle = \int_z f(z)\; g^*(z)\; dz. \tag{A.66}$$

In the present case, this projection needs to be performed onto particular vertical wave numbers (indicated in the following by a dash) of the basis function that corresponds to the growth rate σ – in more detail, one applies $\int_0^1$ (A.46) $\cos(n'\pi z)\, dz$, $\int_0^1$ (A.47) $\cos(n'\pi z)\, dz$, as well as $\int_0^1$ (A.48) $\sin(m'\pi z)\, dz$. This yields for instance

$$\int_0^1 \sum_m \Phi(m) \;\sin(m\pi z) \;\cos(n'\pi z)\, dz = \sum_m \Phi(m) \underbrace{\int_0^1 \sin(m\pi z) \;\cos(n'\pi z)\, dz}_{=:\langle \mathrm{S}_m, \mathrm{C}_{n'} \rangle} \tag{A.67a}$$

$$= \sum_m \Phi(m) \;\langle \mathrm{S}_m, \mathrm{C}_{n'} \rangle, \tag{A.67b}$$

where the scalar product between the sine (S) or cosine (C) functions at the wave number provided as subscript is defined. The results of these scalar products between trigonometrical functions depend on the particular wave numbers as well as functions, and compute as follows

$$\langle \mathrm{S}_i, \mathrm{S}_j \rangle = \begin{cases} \frac{\pi}{2} & \text{if } i = j \text{ and } \; (i,j) > 0, \\ 0 & \text{if } i \neq j \text{ and } \; (i,j) \geq 0 \text{ or just } i = j = 0, \end{cases} \tag{A.68}$$

$$\langle \mathrm{C}_i, \mathrm{C}_j \rangle = \begin{cases} \pi & \text{if } i = j = 0, \\ \frac{\pi}{2} & \text{if } i = j > 0, \\ 0 & \text{if } i \neq j \text{ and } \; (i,j) \geq 0, \end{cases} \tag{A.69}$$

$$\langle \mathrm{S}_i, \mathrm{C}_j \rangle = \begin{cases} \frac{1-(-1)^i}{i} & \text{if } j = 0 \text{ and } i > 0, \\ 0 & \text{if } i = j \text{ and } (i,j) > 0 \text{ or just } i = 0, \\ \frac{2i}{(i+j)(i-j)} & \text{if } i \neq j \text{ and } (i,j) > 0 \text{ and } (i+j) \text{ is odd}, \\ 0 & \text{if } i \neq j \text{ and } (i,j) > 0 \text{ and } (i+j) \text{ is even}, \end{cases} \tag{A.70}$$

for $(i, j) \in \mathbb{N}$. As can be realised, the infinite sums vanish due to orthogonality if the original and target basis functions are of the same kind,

$$\sum_m \Phi_m \langle \mathrm{S}_m, \mathrm{S}_{m'} \rangle = \Phi_{m'} \langle \mathrm{S}_{m'}, \mathrm{S}_{m'} \rangle \quad \text{and} \quad \sum_n \Phi_n \langle \mathrm{C}_n, \mathrm{C}_{n'} \rangle = \Phi_{n'} \langle \mathrm{C}_{n'}, \mathrm{C}_{n'} \rangle. \tag{A.71}$$

This is not the case for mixed trigonometrical functions.

Making use of these insights, the projection of equations (A.46) – (A.48) onto particular vertical wave numbers translates them after some re-arrangements into

$$\sigma C_{n'} = -\frac{1}{\mathrm{Pr}} k_{n'}^2 C_{n'} + \frac{1}{\mathrm{Pr}} \sum_m W_m \frac{\langle \mathrm{S}_m, \mathrm{C}_{n'} \rangle}{\langle \mathrm{C}_{n'}, \mathrm{C}_{n'} \rangle}, \tag{A.72}$$

$$\sigma Z_{n'} = - k_{n'}^2 Z_{n'} + \sqrt{\mathrm{Ta}} \sum_m m\pi W_m \delta_{mn'}, \tag{A.73}$$

$$\sigma W_{m'} = - k_{m'}^2 W_{m'} + \mathrm{Ra} \sum_n \frac{k_\mathrm{h}^2}{k_{m'}^2} C_n \frac{\langle \mathrm{C}_n, \mathrm{S}_{m'} \rangle}{\langle \mathrm{S}_{m'}, \mathrm{S}_{m'} \rangle} - \sqrt{\mathrm{Ta}} \frac{m'\pi}{k_{m'}^2} Z_{m'} \tag{A.74}$$

where $k_\Phi^2 := k_\mathrm{h}^2 + (\Phi\pi)^2$. The resulting equations represent eventually the temporal evolutions of the perturbations at one particular vertical wave number. This linear system of equations can now be solved to find the (finite number of) Fourier coefficients $C_{n'}$, $Z_{n'}$, and $W_{m'}$. As it has the form of an eigenvalue problem, established methods can be used to solve it for a larger number of vertical wave numbers.

In order to make an analytical solution accessible, the system is truncated after one complete wave in the vertical direction. Realising that $\sigma C_1 = -(1/\mathrm{Pr})\, k_1^2 C_1$ and $\sigma Z_0 = -k_\mathrm{h}^2 Z_0$ are independent, one obtains

$$\sigma \begin{pmatrix} C_0 \\ Z_1 \\ W_1 \end{pmatrix} = \begin{pmatrix} -\frac{1}{\mathrm{Pr}} k_\mathrm{h}^2 & 0 & \frac{1}{\mathrm{Pr}} \frac{2}{\pi} \\ 0 & -k_1^2 & \sqrt{\mathrm{Ta}}\, \pi \\ \mathrm{Ra}\, \frac{k_\mathrm{h}^2}{k_1^2} \frac{4}{\pi} & -\sqrt{\mathrm{Ta}}\, \frac{\pi}{k_1^2} & -k_1^2 \end{pmatrix} \begin{pmatrix} C_0 \\ Z_1 \\ W_1 \end{pmatrix}. \tag{A.75}$$

In the case of marginal stability with $\sigma = 0$, the determinant of this eq. (A.75) yields its solution. Re-arranging for the Rayleigh number gives eventually [29]

$$\mathrm{Ra}_{\mathrm{N,\,marg}} = \frac{\pi^2}{8} \left[\left(k_\mathrm{h}^2 + \pi^2 \right)^2 + \frac{\mathrm{Ta}\, \pi^2}{k_\mathrm{h}^2 + \pi^2} \right]. \tag{A.76}$$

This describes finally the neutral stability for the Neumann case, which is provided in the main text in eq. (3.9) and visualised in figure 3.6 (b). For the non-rotating case with $\mathrm{Ta} = 0$, this equation yields $\mathrm{Ra}_\mathrm{crit} = \pi^6/8 \approx 120.17$ – thus, it is very close to the analytical result $\mathrm{Ra}_\mathrm{crit} = 5! = 120$ from [38] that was derived much earlier but using another approach which did not include rotation.

B Derivation of the spectral governing equations for the Neumann scenario

In this appedix B, the spectral governing equations (3.38) – (3.40) from the main text will be derived. Here, free-slip and constant heat flux boundary conditions are applied.

Physical space governing equations

The derivation starts with the non-dimensional governing equations in physical space

$$\nabla \cdot \boldsymbol{u} = 0, \tag{B.1}$$

$$\frac{\partial \boldsymbol{u}}{\partial t} + (\boldsymbol{u} \cdot \nabla)\, \boldsymbol{u} + \frac{1}{\mathrm{Ro}}\, \boldsymbol{e}_z \times \boldsymbol{u} = -\nabla p + \sqrt{\frac{\mathrm{Pr}}{\mathrm{Ra}}}\, \nabla^2 \boldsymbol{u} + \Theta \boldsymbol{e}_z, \tag{B.2}$$

$$\frac{\partial \Theta}{\partial t} + (\boldsymbol{u} \cdot \nabla)\, \Theta = \frac{1}{\sqrt{\mathrm{RaPr}}}\, \nabla^2 \Theta + u_z, \tag{B.3}$$

based on the free-fall inertial balance and exploiting the description based on the temperature deviation field Θ. The latter has been defined in eq. (3.5) and will be termed just temperature field in the following for simplicity. The dimensional variants of these equations are provided in equations (A.1) – (A.3) in appendix A. In contrast to the description based on the standard temperature field T, see equations (1.6) – (1.8) in the main text, the continuity equation is unchanged. However, the Navier-Stokes equation changes as described in the footnote on page 59 and the corresponding energy equation has already been introduced in eq. (3.36).

Boundary conditions

The corresponding set of boundary conditions in the non-dimensional form is given by

$$\frac{\partial u_{x,y}}{\partial z}\ (z \in \{0, 1\}) = 0, \tag{B.4}$$

$$u_z\ (z \in \{0, 1\}) = 0, \tag{B.5}$$

$$\frac{\partial \Theta}{\partial z}\ (z \in \{0, 1\}) = 0, \tag{B.6}$$

which are provided in the main text in equations (1.14b) and (3.37). In addition, the domain is horizontally periodic, see eq. (1.17b), so

$$\Phi\ (\boldsymbol{x}) = \Phi\ (\boldsymbol{x} + i_x \Gamma_x \boldsymbol{e}_x + i_y \Gamma_y \boldsymbol{e}_y) \tag{B.7}$$

holds for every field and arbitrary integers $i \in \mathbb{Z}$.

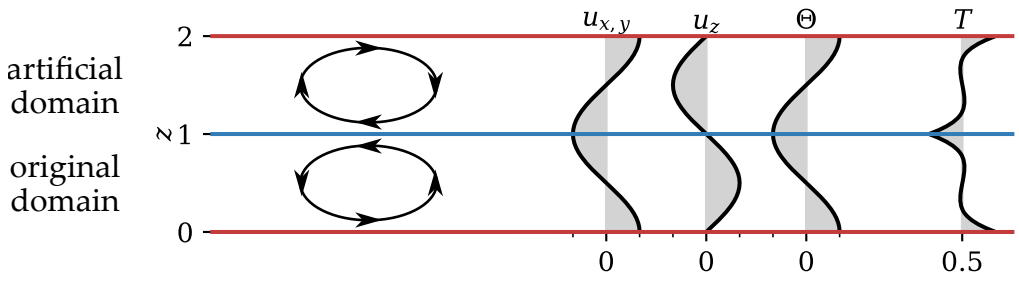

Figure B.1: Periodicity of the domain. The domain can be made periodic in the vertical direction when the fields are mirrored at the top plane. This is exemplified by means of a convection roll (left) and the $k_z = \pi$ modes of the basis functions along the vertical direction (centre) as provided by equations (B.8) – (B.11). The standard temperature field (right), here taken from simulation run Nfs1, does not allow for an expansion via trigonometrical functions. The red and blue lines spanning across the entire width of the figure indicate the hot and cold planes, respectively.

Selection of appropriate basis functions

A spectral expansions requires to decide for the particular basis functions along the different coordinates.

As all fields are horizontally periodic, they can be expanded as typical Fourier series with the basis functions $e^{\imath \boldsymbol{k}_\mathrm{h} \cdot \boldsymbol{x}_\mathrm{h}}$ in these directions. This basis is due to Euler's formula $e^{\imath\Phi} = \cos(\Phi) + \imath \sin(\Phi)$ directly related to both trigonometrical functions. Due to the periodicity, the wave numbers $k_{x,y} := 2\pi\ n/L_{x,y}$ are discrete in these horizontal directions with the number of complete waves $n \in \mathbb{N}$ over the periodic length $L_{x,y} = \Gamma_{x,y}$.

In the vertical direction, the domain is confined between the two different horizontal planes and thus the fields are not periodic in $z \in [0, 1]$. However, the domain can (hypothetically) be mirrored at the top plane with $z = 1$ – see figure B.1 – to obtain vertically periodic fields in $z \in [0, 2]$. In particular, the fields of the horizontal velocities and the temperature need to be stacked on top in reversed order, whereas the vertical velocity requires an additional change of its sign. Note here that although the standard temperature field T is periodic in this extended domain, its boundary conditions at the planes are not unique (in the Neumann case, and can also not be satisfied by trigonometrical basis functions in the Dirichlet case as, e.g., a cosine expansion comes with vanishing derivatives) – for this particular reason, one needs to work instead with the temperature deviation field Θ.

Despite this periodicity, the boundary conditions (B.4) – (B.6) are (when continuing to work with trigonometrical functions) only properly satisfied by the use of either sine or cosine functions. In accordance with these conditions, $u_{x,y} \sim \cos(k_z z)$, $u_z \sim \sin(k_z z)$, and $\Theta \sim \cos(k_z z)$ with the vertical wave number $k_z := 2\pi\ n/L_z$ and $L_z = 2$. Defining the Fourier coefficients in case of sine basis functions at $k_z = 0$ to be zero allows to use the before-mentioned definition of k_z independently of the particular trigonometrical function.

The three-dimensional spectral expansions of the fields result eventually in

$$u_x(\boldsymbol{x},t) = \sum_{\boldsymbol{k}_\mathrm{h}} \sum_{k_z} \hat{u}_x(\boldsymbol{k}_\mathrm{h},k_z,t)\, e^{\imath \boldsymbol{k}_\mathrm{h}\cdot\boldsymbol{x}_\mathrm{h}}\ \cos(k_z z), \tag{B.8}$$

$$u_y(\boldsymbol{x},t) = \sum_{\boldsymbol{k}_\mathrm{h}} \sum_{k_z} \hat{u}_y(\boldsymbol{k}_\mathrm{h},k_z,t)\, e^{\imath \boldsymbol{k}_\mathrm{h}\cdot\boldsymbol{x}_\mathrm{h}}\ \cos(k_z z), \tag{B.9}$$

$$u_z(\boldsymbol{x},t) = \sum_{\boldsymbol{k}_\mathrm{h}} \sum_{k_z} \hat{u}_z(\boldsymbol{k}_\mathrm{h},k_z,t)\, e^{\imath \boldsymbol{k}_\mathrm{h}\cdot\boldsymbol{x}_\mathrm{h}}\ \imath \sin(k_z z), \tag{B.10}$$

$$\Theta(\boldsymbol{x},t) = \sum_{\boldsymbol{k}_\mathrm{h}} \sum_{k_z} \hat{\Theta}(\boldsymbol{k}_\mathrm{h},k_z,t)\, e^{\imath \boldsymbol{k}_\mathrm{h}\cdot\boldsymbol{x}_\mathrm{h}}\ \cos(k_z z), \tag{B.11}$$

see also equations (3.31) – (3.35) in the main text.

The spectral expansion of the pressure field (along the vertical direction) is not clear *a priori*. However, the pressure is related to velocity motion which is non-zero only for horizontal velocities at the planes. This suggests to expand the pressure field similar to those horizontal velocities using cosine functions. The entire expansion of the pressure field is thus given by

$$p\ (\boldsymbol{x},t) = \sum_{\boldsymbol{k}_\mathrm{h}} \sum_{k_z} \hat{p}\,(\boldsymbol{k}_\mathrm{h},k_z,t)\, e^{\imath \boldsymbol{k}_\mathrm{h}\cdot\boldsymbol{x}_\mathrm{h}} \cos(k_z z). \tag{B.12}$$

Finally, the advection terms need to be expanded and the proper basis functions along the vertical direction need to be found. Here, symmetry properties can be exploited to conclude which trigonometrical function to use. In more detail, the product of two even functions is again an even function – similarly, the product of two odd functions yields also an even function. Only the product of an even with an odd function results in an odd function. Together with $(\boldsymbol{u}\cdot\nabla)\,\boldsymbol{\Phi} = \nabla\cdot(\boldsymbol{u}\boldsymbol{\Phi})$ in the case of incompressibility (see also sections 3.5.2.2 and 3.5.2.4), this can be used to determine the necessary basis function along the vertical direction. Let Φ exemplary be even (as, e.g., u_x) – then

$$(\boldsymbol{u}\cdot\nabla)\,\Phi = \nabla\cdot(\boldsymbol{u}\Phi) = \frac{\partial}{\partial x}(u_x\Phi) + \frac{\partial}{\partial y}(u_y\Phi) + \frac{\partial}{\partial z}(u_z\Phi) = \tag{B.13a}$$

$$= \frac{\partial}{\partial x} \sum_{\boldsymbol{k}_\mathrm{h}} \sum_{k_z} \widehat{u_x\Phi}\,(\boldsymbol{k}_\mathrm{h},k_z,t)\ e^{\imath \boldsymbol{k}_\mathrm{h}\cdot\boldsymbol{x}_\mathrm{h}}\ \cos(k_z z) +$$

$$+ \frac{\partial}{\partial y} \sum_{\boldsymbol{k}_\mathrm{h}} \sum_{k_z} \widehat{u_y\Phi}\,(\boldsymbol{k}_\mathrm{h},k_z,t)\ e^{\imath \boldsymbol{k}_\mathrm{h}\cdot\boldsymbol{x}_\mathrm{h}}\ \cos(k_z z) + \tag{B.13b}$$

$$+ \frac{\partial}{\partial z} \sum_{\boldsymbol{k}_\mathrm{h}} \sum_{k_z} \widehat{u_z\Phi}\,(\boldsymbol{k}_\mathrm{h},k_z,t)\ e^{\imath \boldsymbol{k}_\mathrm{h}\cdot\boldsymbol{x}_\mathrm{h}}\ \imath \sin(k_z z) =$$

$$= \sum_{\boldsymbol{k}_\mathrm{h}} \sum_{k_z} \imath k_x\ \widehat{u_x\Phi}\,(\boldsymbol{k}_\mathrm{h},k_z,t)\ e^{\imath \boldsymbol{k}_\mathrm{h}\cdot\boldsymbol{x}_\mathrm{h}}\ \cos(k_z z) +$$

$$+ \sum_{\boldsymbol{k}_\mathrm{h}} \sum_{k_z} \imath k_y\ \widehat{u_y\Phi}\,(\boldsymbol{k}_\mathrm{h},k_z,t)\ e^{\imath \boldsymbol{k}_\mathrm{h}\cdot\boldsymbol{x}_\mathrm{h}}\ \cos(k_z z) + \tag{B.13c}$$

$$+ \sum_{\boldsymbol{k}_\mathrm{h}} \sum_{k_z} \imath k_z\ \widehat{u_z\Phi}\,(\boldsymbol{k}_\mathrm{h},k_z,t)\ e^{\imath \boldsymbol{k}_\mathrm{h}\cdot\boldsymbol{x}_\mathrm{h}}\ \cos(k_z z)\,.$$

Hence, the resulting basis function along the vertical direction is in accordance with the basis function of the variable Φ for which the equation describes its evolution – this is identical when Φ is odd (as, e.g., u_z). Note in this example that $\widehat{u_x\Phi}$ and $\widehat{u_y\Phi}$ are Fourier coefficients obtained from a cosine expansion, whereas $\widehat{u_z\Phi}$ – as indicated in eq. (B.13b) – still needs to be obtained from a sine expansion. If this is respected, $\imath\boldsymbol{k}\cdot\widehat{\boldsymbol{u}\Phi}$ coincides correctly with the coefficients from below.

Combining the equivalence $(\boldsymbol{u}\cdot\nabla)\,\boldsymbol{\Phi} = \nabla\cdot(\boldsymbol{u}\boldsymbol{\Phi})$ and the above insights based on symmetry arguments, the advection terms can alternatively be expanded via

$$(\boldsymbol{u}\cdot\nabla)\,u_x\,(\boldsymbol{x},t) = \sum_{\boldsymbol{k}_\mathrm{h}}\sum_{k_z} \widehat{(\boldsymbol{u}\cdot\nabla)\,u_x}(\boldsymbol{k}_\mathrm{h},k_z,t)\;e^{\imath\boldsymbol{k}_\mathrm{h}\cdot\boldsymbol{x}_\mathrm{h}}\;\cos(k_z z), \tag{B.14}$$

$$(\boldsymbol{u}\cdot\nabla)\,u_y\,(\boldsymbol{x},t) = \sum_{\boldsymbol{k}_\mathrm{h}}\sum_{k_z} \widehat{(\boldsymbol{u}\cdot\nabla)\,u_y}(\boldsymbol{k}_\mathrm{h},k_z,t)\;e^{\imath\boldsymbol{k}_\mathrm{h}\cdot\boldsymbol{x}_\mathrm{h}}\;\cos(k_z z), \tag{B.15}$$

$$(\boldsymbol{u}\cdot\nabla)\,u_z\,(\boldsymbol{x},t) = \sum_{\boldsymbol{k}_\mathrm{h}}\sum_{k_z} \widehat{(\boldsymbol{u}\cdot\nabla)\,u_z}(\boldsymbol{k}_\mathrm{h},k_z,t)\;e^{\imath\boldsymbol{k}_\mathrm{h}\cdot\boldsymbol{x}_\mathrm{h}}\;\imath\sin(k_z z), \tag{B.16}$$

$$(\boldsymbol{u}\cdot\nabla)\,\Theta\,(\boldsymbol{x},t) = \sum_{\boldsymbol{k}_\mathrm{h}}\sum_{k_z} \widehat{(\boldsymbol{u}\cdot\nabla)\,\Theta}\,(\boldsymbol{k}_\mathrm{h},k_z,t)\;e^{\imath\boldsymbol{k}_\mathrm{h}\cdot\boldsymbol{x}_\mathrm{h}}\;\cos(k_z z). \tag{B.17}$$

Due to their simplicity, these descriptions will be used in the following.

Note here that the basis function in the vertical direction of any above spectral expansion is either $\cos(\Phi)$ or $\imath\sin(\Phi)$, the latter of which contains the coefficient $\imath$. This coefficient brings this basis function in accordance with the typical Fourier basis function – in other words, the Fourier coefficient corresponding to $\imath\sin(\Phi)$ coincides with the Fourier coefficient corresponding to $e^{\imath\Phi}$ for any properly periodic sine signal. This allows eventually to apply the well-known convolution without further issues.

Beside the potential symmetry of the domain in physical space, also the Fourier coefficients $\hat{\Phi}$ obey certain symmetry properties. Along the horizontal directions with their typical Fourier transform,

$$\hat{\Phi}\,(-\boldsymbol{k}_\mathrm{h},k_z) = \hat{\Phi}^*\,(\boldsymbol{k}_\mathrm{h},k_z) \tag{B.18}$$

holds. Because of the relation of the trigonometrical basis functions (and their coefficients) to $e^{\imath\boldsymbol{k}_\mathrm{h}\cdot\boldsymbol{x}_\mathrm{h}}$, this can be extended to $\hat{\Phi}\,(-\boldsymbol{k}) = \hat{\Phi}^*\,(\boldsymbol{k})$. Additionally, these sine or cosine expansions introduce

$$\hat{\Phi}\,(\boldsymbol{k}_\mathrm{h},-k_z) = -\hat{\Phi}\,(\boldsymbol{k}_\mathrm{h},k_z) \qquad \text{or} \qquad \hat{\Phi}\,(\boldsymbol{k}_\mathrm{h},-k_z) = \hat{\Phi}\,(\boldsymbol{k}_\mathrm{h},k_z)\,, \tag{B.19}$$

respectively.

Technically, these symmetry properties allow an efficient computation of the Fourier coefficients based on the original domain ($z\in[0,1]$) only. Here one can make use of discrete sine or cosine transforms (via `scipy.fft.dst` or `scipy.fft.dct`, respectively), while the coefficients obtained from the former can be corrected (i.e. multiplied by $-\imath$) to account for the coefficient $\imath$ in the basis functions.

Obtaining the modal governing equations

Once it is clear how to spectrally expand all the individual terms in the governing equations (B.1) – (B.3) and how to obtain all the Fourier coefficients technically, these expansions can be inserted. As it was already the case in appendix A, this introduces again all the infinite sums into these equations. The equations are thus projected onto particular wave numbers – see again eq. (A.66).

As the sine basis function differs here with its coefficient $\imath$ slightly compared to its use in eq. (A.63), so do the inner products between sine and cosine functions that resulted in equations (A.68) – (A.70). For the present basis functions, these products result in

$$\langle \mathrm{S}_i, \mathrm{S}_j \rangle = \begin{cases} -\frac{\pi}{2} & \text{if } i = j \text{ and } (i,j) > 0, \\ 0 & \text{if } i \neq j \text{ and } (i,j) \geq 0 \text{ or just } i = j = 0, \end{cases} \tag{B.20}$$

$$\langle \mathrm{C}_i, \mathrm{C}_j \rangle = \begin{cases} \pi & \text{if } i = j = 0, \\ \frac{\pi}{2} & \text{if } i = j > 0, \\ 0 & \text{if } i \neq j \text{ and } (i,j) \geq 0, \end{cases} \tag{B.21}$$

$$\langle \mathrm{S}_i, \mathrm{C}_j \rangle = \begin{cases} \frac{1-(-1)^i}{i}\ \imath & \text{if } j = 0 \text{ and } i > 0, \\ 0 & \text{if } i = j \text{ and } (i,j) > 0 \text{ or just } i = 0, \\ \frac{2i}{(i+j)(i-j)}\ \imath & \text{if } i \neq j \text{ and } (i,j) > 0 \text{ and } (i+j) \text{ is odd}, \\ 0 & \text{if } i \neq j \text{ and } (i,j) > 0 \text{ and } (i+j) \text{ is even}, \end{cases} \tag{B.22}$$

where $(i,j) \in \mathbb{N}$ are the numbers of complete waves over the periodic length onto which the projection is performed.

In contrast, the projection onto horizontal wave numbers $\boldsymbol{k}'_\mathrm{h}$ yields for every term

$$\int_A \sum_{\boldsymbol{k}_\mathrm{h}} \hat{\Phi}\left(\boldsymbol{k}_\mathrm{h}\right)\ e^{\imath \boldsymbol{k}_\mathrm{h} \cdot \boldsymbol{x}_\mathrm{h}}\ e^{-\imath \boldsymbol{k}'_\mathrm{h} \cdot \boldsymbol{x}_\mathrm{h}} dA = \sum_{\boldsymbol{k}_\mathrm{h}} \hat{\Phi}\left(\boldsymbol{k}_\mathrm{h}\right) \underbrace{\int_A e^{\imath \left(\boldsymbol{k}_\mathrm{h} - \boldsymbol{k}'_\mathrm{h}\right) \cdot \boldsymbol{x}_\mathrm{h}} dA}_{=\delta_{\boldsymbol{k}_\mathrm{h} \boldsymbol{k}'_\mathrm{h}}} = \hat{\Phi}\left(\boldsymbol{k}'_\mathrm{h}\right). \tag{B.23}$$

As in appendix A, these projections reduce the sums of almost all terms in these equations to just one single wave number – see also again eq. (A.71). The buoyancy term in eq. (B.2) and the vertical velocity term in eq. (B.3) are the only terms for which mixed products as provided by eq. (B.22) apply. A division of the continuity equation, the x- and y-component of the Navier-Stokes equation, as well as the energy equation by $\langle \mathrm{C}_{n'}, \mathrm{C}_{n'} \rangle$, and a division of the z-component of the Navier-Stokes equation by $\langle \mathrm{S}_{n'}, \mathrm{S}_{n'} \rangle$ results eventually in

$$\imath \boldsymbol{k}' \cdot \hat{\boldsymbol{u}} = 0, \tag{B.24}$$

$$\frac{\partial \hat{\boldsymbol{u}}}{\partial t} + \widehat{\left(\boldsymbol{u} \cdot \nabla\right) \boldsymbol{u}} + \frac{\boldsymbol{e}_z \times \hat{\boldsymbol{u}}}{\mathrm{Ro}} = -\imath \boldsymbol{k}'\, \hat{p} - \sqrt{\frac{\mathrm{Pr}}{\mathrm{Ra}}}\ k'^2 \hat{\boldsymbol{u}} + \boldsymbol{e}_z \sum_n \hat{\Theta}\left(\boldsymbol{k}'_\mathrm{h}, n, t\right)\ \frac{\langle \mathrm{C}_n, \mathrm{S}_{n'} \rangle}{\langle \mathrm{S}_{n'}, \mathrm{S}_{n'} \rangle}, \tag{B.25}$$

$$\frac{\partial \hat{\Theta}}{\partial t} + \widehat{\left(\boldsymbol{u} \cdot \nabla\right) \Theta} = -\frac{1}{\sqrt{\mathrm{RaPr}}}\ k'^2 \hat{\Theta} + \sum_n \hat{u}_z\left(\boldsymbol{k}'_\mathrm{h}, n, t\right)\ \frac{\langle \mathrm{S}_n, \mathrm{C}_{n'} \rangle}{\langle \mathrm{C}_{n'}, \mathrm{C}_{n'} \rangle}. \tag{B.26}$$

If not mentioned explicitly, terms are functions of $(\boldsymbol{k}_\mathrm{h}', n', t)$ due to the performed projection.

The remaining infinite sum in the buoyancy (vertical velocity) term – which does not cancel out – represents a projection of the corresponding quantity onto sine (cosine) basis functions. Roughly speaking, this has become necessary as the evolution equation of the vertical velocity (temperature) describes its evolution in the 'coordinate system' of sine (cosine) functions along the vertical direction – contributions provided in other coordinates need thus to be translated. Note that such a projection is not necessary in the Dirichlet case when the temperature field is expanded as a sine series. Furthermore, the disappearance of such projections for the pressure confirm its proper expansion in eq. (B.12).

There are basically two options on how to compute the projections of the temperature or vertical velocity field onto the complementary trigonometrical basis functions. First and most obvious, one can compute the infinite sums as included in the above equations. Thus, one may define the sine (sp) and cosine projection (cp)

$$\hat{\Theta}_\mathrm{sp}\left(\boldsymbol{k}_\mathrm{h}', n', t\right) := \sum_n \hat{\Theta}\left(\boldsymbol{k}_\mathrm{h}', n, t\right) \frac{\langle \mathrm{C}_n, \mathrm{S}_{n'} \rangle}{\langle \mathrm{S}_{n'}, \mathrm{S}_{n'} \rangle}, \tag{B.27}$$

$$\hat{u}_{z,\,\mathrm{cp}}\left(\boldsymbol{k}_\mathrm{h}', n', t\right) := \sum_n \hat{u}_z\left(\boldsymbol{k}_\mathrm{h}', n, t\right) \frac{\langle \mathrm{S}_n, \mathrm{C}_{n'} \rangle}{\langle \mathrm{C}_{n'}, \mathrm{C}_{n'} \rangle}. \tag{B.28}$$

Alternatively, one may directly expand the quantity for this particular term in the complementary basis and define equivalently the sine (se) and cosine expansion (ce)

$$\Theta\left(\boldsymbol{x}, t\right) := \sum_{\boldsymbol{k}_\mathrm{h}} \sum_{k_z} \hat{\Theta}_\mathrm{se}\ \left(\boldsymbol{k}_\mathrm{h}, k_z, t\right) e^{\imath \boldsymbol{k}_\mathrm{h} \cdot \boldsymbol{x}_\mathrm{h}}\, \imath \sin\left(k_z z\right), \tag{B.29}$$

$$u_z\left(\boldsymbol{x}, t\right) := \sum_{\boldsymbol{k}_\mathrm{h}} \sum_{k_z} \hat{u}_{z,\,\mathrm{ce}}(\boldsymbol{k}_\mathrm{h}, k_z, t)\, e^{\imath \boldsymbol{k}_\mathrm{h} \cdot \boldsymbol{x}_\mathrm{h}}\ \cos\left(k_z z\right) \tag{B.30}$$

with $k_z = n\,\pi$. The infinite sums, as well as the basis functions to the right of the Fourier coefficients disappear when projecting these quantities onto particular wave numbers in the course of the derivation. Albeit the results of both options coincide, the direct expansion via the complementary basis is technically simpler.

Making use of these abbreviations and skipping the dashes again for improved clarity,

$$\imath \boldsymbol{k} \cdot \hat{\boldsymbol{u}} = 0, \tag{B.31}$$

$$\frac{\partial \hat{\boldsymbol{u}}}{\partial t} + \widehat{(\boldsymbol{u} \cdot \nabla)\, \boldsymbol{u}} + \frac{1}{\mathrm{Ro}}\, \boldsymbol{e}_z \times \hat{\boldsymbol{u}}, = -\imath \boldsymbol{k}\, \hat{p} - \sqrt{\frac{\mathrm{Pr}}{\mathrm{Ra}}}\, k^2 \hat{\boldsymbol{u}} + \hat{\Theta}_\mathrm{se}\, \boldsymbol{e}_z, \tag{B.32}$$

$$\frac{\partial \hat{\Theta}}{\partial t} + \widehat{(\boldsymbol{u} \cdot \nabla)\, \Theta} = -\frac{1}{\sqrt{\mathrm{RaPr}}}\, k^2 \hat{\Theta} + \hat{u}_{z,\,\mathrm{ce}} \tag{B.33}$$

result as the final modal governing equations and correspond to equations (3.38) – (3.40) from the main text.

Bibliography

List of peer-reviewed publications

[V1] P. P. Vieweg, J. D. Scheel and J. Schumacher, 'Supergranule aggregation for constant heat flux-driven turbulent convection', Phys. Rev. Research **3**, 013231 (2021).

[V2] P. P. Vieweg, C. Schneide, K. Padberg-Gehle and J. Schumacher, 'Lagrangian heat transport in turbulent three-dimensional convection', Phys. Rev. Fluids **6**, L041501 (2021).

[V3] C. Schneide, P. P. Vieweg, J. Schumacher and K. Padberg-Gehle, 'Evolutionary clustering of Lagrangian trajectories in turbulent Rayleigh–Bénard convection flows', Chaos **32**, 013123 (2022).

[V4] P. P. Vieweg, Y. Kolesnikov and C. Karcher, 'Experimental study of a liquid metal film flow in a streamwise magnetic field', Magnetohydrodynamics **58**, 5–12 (2022).

[V5] P. P. Vieweg, J. D. Scheel, R. Stepanov and J. Schumacher, 'Inverse cascades of kinetic energy and thermal variance in three-dimensional horizontally extended turbulent convection', Phys. Rev. Research **4**, 043098 (2022).

[V6] T. Käufer, P. P. Vieweg, J. Schumacher and C. Cierpka, 'Thermal boundary condition studies in large aspect ratio Rayleigh–Bénard convection', Eur. J. Mech. B-Fluids **101**, 283–293 (2023).

[V7] P. P. Vieweg, A. Klünker, J. Schumacher and K. Padberg-Gehle, 'Lagrangian studies of coherent sets and heat transport in constant heat flux-driven turbulent Rayleigh–Bénard convection', Eur. J. Mech. B-Fluids **103**, 69–85 (2024).

List of non-peer-reviewed scientific contributions

Beside the before-mentioned publications, several additional scientific contributions have been made during the time of the PhD which are not (comparably) peer-reviewed. These comprise articles in conference proceedings [V8, V9, V12, V13], as well as poster presentations at conferences and universities [V10, V11, V15, V16] and other contributions [V14, V17] – also, [V10] was awarded with the 3rd place for one of the best poster

contributions at the conference, and figure 3.13 (a) decorates the front page of [V17]. Especially [V11, V14, V15] served for public relations, allowing a non-scientific audience to capture important aspects of research in fluid mechanics and its relevance to everyday life.

[V8] J. Schumacher, P. P. Vieweg, C. Schneide and K. Padberg-Gehle, 'Lagrangian Coherent Sets as transport barriers in convection', B. Am. Phys. Soc. **65**, F16.00009 (2020).

[V9] P. P. Vieweg, J. Schumacher and J. D. Scheel, 'Large-scale cell formation in turbulent Rayleigh-Bénard convection', B. Am. Phys. Soc. **65**, F16.00002 (2020).

[V10] P. P. Vieweg, 'Experimental study of a liquid metal film flow in a streamwise magnetic field', poster presentation, Electromagnetic Processing of Materials (EPM) 2021 (Riga, Latvia), 2021.

[V11] P. P. Vieweg, 'Structure formation in the Sun (Original German title: Strukturbildung in der Sonne)', poster presentation, Engineering Sciences Day 2021 (Ilmenau, Germany), 2021.

[V12] P. P. Vieweg, Y. Kolesnikov and C. Karcher, 'Experimental study of a liquid metal film flow in a streamwise magnetic field', in Proc. 10th Int. Conf. Electromagn. Process. Mater. EPM (2021), pp. 150–154.

[V13] P. P. Vieweg and J. Schumacher, 'Controlling supergranule aggregation in convection by weak rotation', B. Am. Phys. Soc. **66**, H06.00009 (2021).

[V14] 'Supercomputing Helps Unravel Mysteries of Turbulent Convection in the Sun', in *Innovatives Supercomputing in Deutschland (InSiDE)*, Autumn 2022, 20-2 (Gauss Centre for Supercomputing e.V., Berlin, 2022), pp. 20–23.

[V15] P. P. Vieweg, 'Pattern formation in natural convection flows', poster presentation, Engineering Sciences Day 2022 (Weimar, Germany), 2022.

[V16] P. P. Vieweg, 'Pattern formation in natural convection flows', poster presentation, Boulder School for Condensed Matter and Materials Physics 2022: Hydrodynamics Across Scales (Boulder, CO, USA), 2022.

[V17] P. P. Vieweg, F. Heyder, J. P. John, J. D. Scheel and J. Schumacher, 'Analysis of the Large-Scale Order in Turbulent Mesoscale Convection', in *NIC Symposium 2022: Proceedings*, Vol. 51 (Forschungszentrum Jülich GmbH, Zentralbibliothek Verlag, Jülich, 2022), pp. 405–414.

References

[1] W. C. Röntgen, *Zur Geschichte der Physik an der Universität Würzburg: Festrede zur Feier des dreihundert und zwölften Stiftungstages der Julius-Maximilians-Universität, gehalten am 2ten Januar 1894* (Druck der Kgl. Universitätsdruckerei von H. Stürtz, 1894).

[2] P. C. W. Davies, *The forces of nature*, 2nd ed. (Cambridge University Press, Cambridge, UK; New York, 1986).

[3] F. Chillà and J. Schumacher, 'New perspectives in turbulent Rayleigh-Bénard convection', Eur. Phys. J. E **35**, 58 (2012).

[4] U. Christensen, 'Effects of Phase Transitions on Mantle Convection', Annu. Rev. Earth Planet. Sci. **23**, 65–87 (1995).

[5] T. Maxworthy and S. Narimousa, 'Unsteady, Turbulent Convection into a Homogeneous, Rotating Fluid, with Oceanographic Applications', J. Phys. Oceanogr. **24**, 865–887 (1994).

[6] B. W. Atkinson and J. Wu Zhang, 'Mesoscale shallow convection in the atmosphere', Rev. Geophys. **34**, 403–431 (1996).

[7] B. E. Mapes and R. A. Houze, 'Cloud Clusters and Superclusters over the Oceanic Warm Pool', Mon. Wea. Rev. **121**, 1398–1416 (1993).

[8] J. Schumacher and K. R. Sreenivasan, '*Colloquium*: Unusual dynamics of convection in the Sun', Rev. Mod. Phys. **92**, 041001 (2020).

[9] Kelvinsong, *Diagram of the Sun*, (2012) `https://en.wikipedia.org/wiki/File:Sun_poster.svg` (visited on 31/01/2022).

[10] F. Rincon and M. Rieutord, 'The Sun's supergranulation', Living Rev. Sol. Phys. **15**, 6 (2018).

[11] J. G. Beck, T. L. Duvall and P. H. Scherrer, 'Long-lived giant cells detected at the surface of the Sun', Nature **394**, 653–655 (1998).

[12] C. S. Hanson, T. L. Duvall, A. C. Birch, L. Gizon and K. R. Sreenivasan, 'Solar east-west flow correlations that persist for months at low latitudes are dominated by active region inflows', A&A **644**, A103 (2020).

[13] J. I. G. De La Rosa, 'Sunspot populations and their relation with the solar cycle', Sol. Phys. **74**, 117–123 (1981).

[14] M. Ossendrijver, 'The solar dynamo', Astron. Astrophys. Rev. **11**, 287–367 (2003).

[15] M. Milankovic, *Mathematische Klimalehre und astronomische Theorie der Klimaschwankungen*, Vol. 1 (Gebrüder Borntraeger, Berlin, 1930).

[16] M. Maslin, D. Seidov and J. Lowe, 'Synthesis of the Nature and Causes of Rapid Climate Transitions During the Quaternary', in *Geophysical Monograph Series* (American Geophysical Union, Washington, D. C., 2001), pp. 9–52.

[17] G. Roe, 'In defense of Milankovitch', Geophys. Res. Lett. **33**, L24703 (2006).

[18] N. Gopalswamy, 'The Sun and Space Weather', Atmosphere **13**, 1781 (2022).

[19] H. Bénard, 'Les tourbillons cellulaires dans une nappe liquide transportant de la chaleur par convection en régime permanent', Ann. Chim. Phys. **23**, 62–144 (1901).

[20] P. Manneville, 'Rayleigh-Bénard Convection: Thirty Years of Experimental, Theoretical, and Modeling Work', in *Dynamics of Spatio-Temporal Cellular Structures*, Vol. 207, Springer Tracts in Modern Physics (Springer New York, New York, NY, 2006), pp. 41–65.

[21] L. Rayleigh, 'On convection currents in a horizontal layer of fluid, when the higher temperature is on the under side', The London, Edinburgh, and Dublin Philosophical Magazine and Journal of Science **32**, 529–546 (1916).

[22] R. J. A. M. Stevens, A. Blass, X. Zhu, R. Verzicco and D. Lohse, 'Turbulent thermal superstructures in Rayleigh-Bénard convection', Phys. Rev. Fluids **3**, 041501 (2018).

[23] M. Cross and H. Greenside, *Pattern Formation and Dynamics in Nonequilibrium Systems* (Cambridge University Press, Cambridge, UK; New York, 2009).

[24] V. Valori, G. Elsinga, M. Rohde, M. Tummers, J. Westerweel and T. van der Hagen, 'Experimental velocity study of non-Boussinesq Rayleigh-Bénard convection', Phys. Rev. E **95**, 053113 (2017).

[25] H. Yik, V. Valori and S. Weiss, 'Turbulent Rayleigh-Bénard convection under strong non-Oberbeck-Boussinesq conditions', Phys. Rev. Fluids **5**, 103502 (2020).

[26] A. Pandey, J. Schumacher and K. R. Sreenivasan, 'Non-Boussinesq Low-Prandtl-number Convection with a Temperature-dependent Thermal Diffusivity', ApJ **907**, 56 (2021).

[27] P. Oresta, R. Verzicco, D. Lohse and A. Prosperetti, 'Heat transfer mechanisms in bubbly Rayleigh-Bénard convection', Phys. Rev. E **80**, 026304 (2009).

[28] L. E. Schmidt, P. Oresta, F. Toschi, R. Verzicco, D. Lohse and A. Prosperetti, 'Modification of turbulence in Rayleigh–Bénard convection by phase change', New J. Phys. **13**, 025002 (2011).

[29] S.-i. Takehiro, M. Ishiwatari, K. Nakajima and Y.-Y. Hayashi, 'Linear Stability of Thermal Convection in Rotating Systems with Fixed Heat Flux Boundaries', Geophys. Astro. Fluid **96**, 439–459 (2002).

[30] R. J. Stevens, H. J. Clercx and D. Lohse, 'Heat transport and flow structure in rotating Rayleigh–Bénard convection', Eur. J. Mech. B-Fluids **40**, 41–49 (2013).

[31] U. Burr and U. Müller, 'Rayleigh–Bénard convection in liquid metal layers under the influence of a vertical magnetic field', Phys. Fluids **13**, 3247–3257 (2001).

[32] U. Burr and U. Müller, 'Rayleigh–Bénard convection in liquid metal layers under the influence of a horizontal magnetic field', J. Fluid Mech. **453**, 345–369 (2002).

[33] T. Zürner, F. Schindler, T. Vogt, S. Eckert and J. Schumacher, 'Flow regimes of Rayleigh–Bénard convection in a vertical magnetic field', J. Fluid Mech. **894**, A21 (2020).

[34] J. R. A. Pearson, 'On convection cells induced by surface tension', J. Fluid Mech. **4**, 489–500 (1958).

[35] E. L. Koschmieder, *Bénard cells and Taylor vortices*, Cambridge Monographs on Mechanics and Applied Mathematics (Cambridge University Press, Cambridge, UK; New York, 1993).

[36] T. Boeck, *Bénard-Marangoni convection at low Prandtl numbers: results of direct numerical simulations*, Berichte aus der Physik (Shaker, Aachen, 2000).

[37] E. M. Sparrow, R. J. Goldstein and V. K. Jonsson, 'Thermal instability in a horizontal fluid layer: Effect of boundary conditions and non-linear temperature profile', J. Fluid Mech. **18**, 513–528 (1964).

[38] D. T. J. Hurle, E. Jakeman and E. R. Pike, 'On the solution of the Bénard problem with boundaries of finite conductivity', Proc. R. Soc. Lond. A **296**, 469–475 (1967).

[39] S. Chandrasekhar, 'The instability of a layer of fluid heated below and subject to Coriolis forces', Proc. R. Soc. Lond. A **217**, 306–327 (1953).

[40] T. E. Dowling, 'Rotating Rayleigh-Bénard Convection with Fixed Flux Boundaries', in *1988 Summer Study Program in Geophysical Fluid Dynamics: The Influence of Convection on Large-Scale Circulations* (Woods Hole Oceanographic Institution, Woods Hole Oceanographic Institution, Massachusetts, 1988), pp. 230–247.

[41] M. Bestehorn, *Hydrodynamik und Strukturbildung: mit einer kurzen Einführung in die Kontinuumsmechanik* (Springer, Berlin Heidelberg, 2006).

[42] A. Pellew and R. V. Southwell, 'On maintained convective motion in a fluid heated from below', Proc. R. Soc. Lond. A **176**, 312–343 (1940).

[43] A. Oberbeck, 'Ueber die Wärmeleitung der Flüssigkeiten bei Berücksichtigung der Strömungen infolge von Temperaturdifferenzen', Ann. Phys. Chem. **243**, 271–292 (1879).

[44] J. V. Boussinesq, *Théorie Analytique de la Chaleur*, Vol. 2 (Gauthier-Villars, Paris, France, 1903).

[45] S. Chandrasekhar, *Hydrodynamic and Hydromagnetic Stability* (Oxford University Press, Oxford, UK, 1961).

[46] E. A. Spiegel and G. Veronis, 'On the Boussinesq Approximation for a Compressible Fluid', ApJ **131**, 442–447 (1960).

[47] D. D. Gray and A. Giorgini, 'The validity of the Boussinesq approximation for liquids and gases', Int. J. Heat Mass Tran. **19**, 545–551 (1976).

[48] P. Mayeli and G. J. Sheard, 'Buoyancy-driven flows beyond the Boussinesq approximation: A brief review', Int. Commun. Heat Mass **125**, 105316 (2021).

[49] C.-L. Navier, 'Mémoire sur les lois du mouvement des fluides', Mém. Acad. Sci. Paris **6**, 389–440 (1822).

[50] G. G. Stokes, 'On the Theories of the Internal Friction of Fluids in Motion, and of the Equilibrium and Motion of Elastic Solids', Trans. Camb. Phil. Soc. **8**, 287–305 (1845).

[51] I. Gallagher, 'From Newton to Navier–Stokes, or how to connect fluid mechanics equations from microscopic to macroscopic scales', Bull. Amer. Math. Soc. **56**, 65–85 (2018).

[52] J. M. Aurnou, S. Horn and K. Julien, 'Connections between nonrotating, slowly rotating, and rapidly rotating turbulent convection transport scalings', Phys. Rev. Research **2**, 043115 (2020).

[53] P. A. Davidson, *Turbulence in rotating, stratified and electrically conducting fluids* (Cambridge University Press, Cambridge, United Kingdom, 2013).

[54] N. Becker, J. D. Scheel, M. C. Cross and G. Ahlers, 'Effect of the centrifugal force on domain chaos in Rayleigh-Bénard convection', Phys. Rev. E **73**, 066309 (2006).

[55] P. A. Davidson, *Turbulence: an introduction for scientists and engineers* (Oxford University Press, Oxford, UK; New York, 2004).

[56] M. K. Verma, *Physics of Buoyant Flows: From Instabilities to Turbulence* (World Scientific, New Jersey, 2018).

[57] J. H. Argyris, G. Faust, M. Haase and R. Friedrich, *Die Erforschung des Chaos: dynamische Systeme*, 3rd ed. (Springer Vieweg, Berlin, Heidelberg, 2017).

[58] N. Foroozani, D. Krasnov and J. Schumacher, 'Turbulent convection for different thermal boundary conditions at the plates', J. Fluid Mech. **907**, A27 (2021).

[59] T. Vogt, S. Horn and J. M. Aurnou, 'Oscillatory thermal–inertial flows in liquid metal rotating convection', J. Fluid Mech. **911**, A5 (2021).

[60] J. von Hardenberg, D. Goluskin, A. Provenzale and E. A. Spiegel, 'Generation of Large-Scale Winds in Horizontally Anisotropic Convection', Phys. Rev. Lett. **115**, 134501 (2015).

[61] A. Pandey, D. Krasnov, K. R. Sreenivasan and J. Schumacher, 'Convective mesoscale turbulence at very low Prandtl numbers', J. Fluid Mech. **948**, A23 (2022).

[62] H. Johnston and C. R. Doering, 'Comparison of Turbulent Thermal Convection between Conditions of Constant Temperature and Constant Flux', Phys. Rev. Lett. **102**, 064501 (2009).

[63] E. H. Anders, C. M. Manduca, B. P. Brown, J. S. Oishi and G. M. Vasil, 'Predicting the Rossby Number in Convective Experiments', ApJ **872**, 138 (2019).

[64] S. Horn and J. M. Aurnou, 'Regimes of Coriolis-Centrifugal Convection', Phys. Rev. Lett. **120**, 204502 (2018).

[65] M. K. Verma, A. Kumar and A. Pandey, 'Phenomenology of buoyancy-driven turbulence: recent results', New J. Phys. **19**, 025012 (2017).

[66] P. Olson and G. M. Corcos, 'A boundary layer model for mantle convection with surface plates', Geophys. J. Int. **62**, 195–219 (1980).

[67] J. Marshall and F. Schott, 'Open-ocean convection: Observations, theory, and models', Rev. Geophys. **37**, 1–64 (1999).

[68] C. Navier, 'Mémoire sur les lois de l'équilibre et du mouvement des corps élastiques', Mém. Académie R. Sci. Inst. Fr. **7**, 375–393 (1827).

[69] C. Nobili, 'The role of boundary conditions in scaling laws for turbulent heat transport', MINE **5**, 1–41 (2023).

[70] H. Park, 'A method to determine zeta potential and Navier slip coefficient of microchannels', J. Colloid Interf. Sci. **347**, 132–141 (2010).

[71] C. Chapman, S. Childress and M. Proctor, 'Long wavelength thermal convection between non-conducting boundaries', Earth Planet. Sc. Lett. **51**, 362–369 (1980).

[72] W. Arendt, 'The Laplacian with Robin Boundary Conditions on Arbitrary Domains', Potential Anal. **19**, 341–363 (2003).

[73] F. H. Busse, 'Non-linear properties of thermal convection', Rep. Prog. Phys. **41**, 1929–1967 (1978).

[74] F. H. Busse, 'The Sequence-of-Bifurcations Approach towards Understanding Turbulent Fluid Flow', Surv. Geophys. **24**, 269–288 (2003).

[75] A. Pandey, J. D. Scheel and J. Schumacher, 'Turbulent superstructures in Rayleigh-Bénard convection', Nat. Commun. **9**, 2118 (2018).

[76] T. Zürner, F. Schindler, T. Vogt, S. Eckert and J. Schumacher, 'Combined measurement of velocity and temperature in liquid metal convection', J. Fluid Mech. **876**, 1108–1128 (2019).

[77] S. Zhong, M. T. Zuber, L. Moresi and M. Gurnis, 'Role of temperature-dependent viscosity and surface plates in spherical shell models of mantle convection', J. Geophys. Res. **105**, 11063–11082 (2000).

[78] N. Coltice, M. Gérault and M. Ulvrová, 'A mantle convection perspective on global tectonics', Earth-Sci. Rev. **165**, 120–150 (2017).

[79] G. Schubert, P. Olson and D. L. Turcotte, *Mantle Convection in the Earth and Planets* (Cambridge University Press, Cambridge, 2001).

[80] R. W. Garwood, S. M. Isakari and P. C. Gallacher, 'Thermobaric Convection', in *The Polar Oceans and Their Role in Shaping the Global Environment* (American Geophysical Union, Washington, D. C., 1994), pp. 199–209.

[81] S. Raasch and D. Etling, 'Modeling Deep Ocean Convection: Large Eddy Simulation in Comparison with Laboratory Experiments', J. Phys. Oceanogr. **28**, 1786–1802 (1998).

[82] A. Pal and V. K. Chalamalla, 'Evolution of plumes and turbulent dynamics in deep-ocean convection', J. Fluid Mech. **889**, A35 (2020).

[83] T. Weidauer and J. Schumacher, 'Moist turbulent Rayleigh-Bénard convection with Neumann and Dirichlet boundary conditions', Phys. Fluids **24**, 076604 (2012).

[84] G. K. Vallis, *Atmospheric and Oceanic Fluid Dynamics: Fundamentals and Large-Scale Circulation*, 2nd ed. (Cambridge University Press, Cambridge, 2017).

[85] G. K. Vallis, D. J. Parker and S. M. Tobias, 'A simple system for moist convection: the Rainy–Bénard model', J. Fluid Mech. **862**, 162–199 (2019).

[86] S. Lee and M. H. van Putten, 'Global climate by Rossby number in the solar system planets', New Astron. **72**, 15–18 (2019).

[87] J. Aurnou, M. Calkins, J. Cheng, K. Julien, E. King, D. Nieves, K. Soderlund and S. Stellmach, 'Rotating convective turbulence in Earth and planetary cores', Phys. Earth Planet. In. **246**, 52–71 (2015).

[88] C. Guervilly, P. Cardin and N. Schaeffer, 'Turbulent convective length scale in planetary cores', Nature **570**, 368–371 (2019).

[89] C. C. Finlay and H. Amit, 'On flow magnitude and field-flow alignment at Earth's core surface', Geophys. J. Int. **186**, 175–192 (2011).

[90] P. Garaud, 'Journey to the center of stars: The realm of low Prandtl number fluid dynamics', Phys. Rev. Fluids **6**, 030501 (2021).

[91] M. S. Miesch, A. S. Brun, M. L. DeRosa and J. Toomre, 'Structure and Evolution of Giant Cells in Global Models of Solar Convection', ApJ **673**, 557–575 (2008).

[92] C. R. Cowley, 'Second viscosity of the gas in the outer solar envelope', ApJ **348**, 328–332 (1990).

[93] J. Otero, R. W. Wittenberg, R. A. Worthing and C. R. Doering, 'Bounds on Rayleigh–Bénard convection with an imposed heat flux', J. Fluid Mech. **473**, 191–199 (2002).

[94] J. D. Scheel and J. Schumacher, 'Predicting transition ranges to fully turbulent viscous boundary layers in low Prandtl number convection flows', Phys. Rev. Fluids **2**, 123501 (2017).

[95] M. Plumley and K. Julien, 'Scaling Laws in Rayleigh-Bénard Convection', Earth Space Sci. **6**, 1580–1592 (2019).

[96] D. Krug, D. Lohse and R. J. A. M. Stevens, 'Coherence of temperature and velocity superstructures in turbulent Rayleigh–Bénard flow', J. Fluid Mech. **887**, A2 (2020).

[97] G. Ahlers, S. Grossmann and D. Lohse, 'Heat transfer and large scale dynamics in turbulent Rayleigh-Bénard convection', Rev. Mod. Phys. **81**, 503–537 (2009).

[98] J. J. Niemela and K. R. Sreenivasan, 'Confined turbulent convection', J. Fluid Mech. **481**, 355–384 (2003).

[99] K. P. Iyer, J. D. Scheel, J. Schumacher and K. R. Sreenivasan, 'Classical 1/3 scaling of convection holds up to Ra = 10^{15}', Proc. Natl. Acad. Sci. U.S.A. **117**, 7594–7598 (2020).

[100] P. K. Kundu and I. M. Cohen, *Fluid mechanics*, in collab. with H. H. Hu, 2nd ed. (Elsevier Academic Press, San Diego, 2002).

[101] M. O. Deville, P. F. Fischer and E. H. Mund, *High-order methods for incompressible fluid flow*, Cambridge Monographs on Applied and Computational Mathematics 9 (Cambridge University Press, Cambridge, UK; New York, 2002).

[102] P. Moin and K. Mahesh, 'Direct Numerical Simulation: A Tool in Turbulence Research', Annu. Rev. Fluid Mech. **30**, 539–578 (1998).

[103] O. Zikanov, *Essential Computational Fluid Dynamics* (Wiley, Hoboken, N.J, 2010).

[104] J. B. Marston and S. M. Tobias, 'Recent Developments in Theories of Inhomogeneous and Anisotropic Turbulence', Annu. Rev. Fluid Mech. **55**, 1–29 (2023).

[105] E. Boström, 'Investigation of Outflow Boundary Conditions for Convection-Dominated Incompressible Fluid Flows in a Spectral Element Framework', MA thesis (KTH Royal Institute of Technology, Stockholm, 2015).

[106] M. R. Paul, M. C. Cross, P. F. Fischer and H. S. Greenside, 'Power-Law Behavior of Power Spectra in Low Prandtl Number Rayleigh-Bénard Convection', Phys. Rev. Lett. **87**, 154501 (2001).

[107] G. L. Kooij, M. A. Botchev, E. M. Frederix, B. J. Geurts, S. Horn, D. Lohse, E. P. van der Poel, O. Shishkina, R. J. Stevens and R. Verzicco, 'Comparison of computational codes for direct numerical simulations of turbulent Rayleigh–Bénard convection', Comput. Fluids **166**, 1–8 (2018).

[108] J. D. Scheel, M. S. Emran and J. Schumacher, 'Resolving the fine-scale structure in turbulent Rayleigh–Bénard convection', New J. Phys. **15**, 113063 (2013).

[109] P. Fischer, A. Obabko, S. Kerkemeier, M. Min, J. Lottes, K. Heisey, S. Aithal and Y. Peet, *Nek5000 Tutorial*, (2010) `https://www.mcs.anl.gov/~fischer/nek5000/fischer_nek5000_dec2010.pdf` (visited on 24/10/2019).

[110] B. Fornberg and J. Zuev, 'The Runge phenomenon and spatially variable shape parameters in RBF interpolation', Comput. Math. Appl. **54**, 379–398 (2007).

[111] P. Fischer, J. Lottes, S. Kerkemeier, O. Marin, K. Heisey, A. Obabko, E. Merzari and Y. Peet, *Nek5000 User Documentation* (Argonne National Laboratories, Argonne, Illinois, 2015).

[112] U. M. Ascher, *Numerical methods for evolutionary differential equations*, Computational Science and Engineering 5 (SIAM, Soc. for Industrial and Applied Mathematics, Philadelphia, Pa, 2008).

[113] P. F. Fischer, 'An Overlapping Schwarz Method for Spectral Element Solution of the Incompressible Navier–Stokes Equations', J. Comput. Phys. **133**, 84–101 (1997).

[114] R. Verzicco and K. R. Sreenivasan, 'A comparison of turbulent thermal convection between conditions of constant temperature and constant heat flux', J. Fluid Mech. **595**, 203–219 (2008).

[115] A. Parodi, J. von Hardenberg, G. Passoni, A. Provenzale and E. A. Spiegel, 'Clustering of Plumes in Turbulent Convection', Phys. Rev. Lett. **92**, 194503 (2004).

[116] J. Liu and G. Ahlers, 'Rayleigh-Bénard convection in binary-gas mixtures: Thermophysical properties and the onset of convection', Phys. Rev. E **55**, 6950–6968 (1997).

[117] M. A. Calkins, K. Hale, K. Julien, D. Nieves, D. Driggs and P. Marti, 'The asymptotic equivalence of fixed heat flux and fixed temperature thermal boundary conditions for rapidly rotating convection', J. Fluid Mech. **784**, R2 (2015).

[118] C. J. Chapman and M. R. E. Proctor, 'Nonlinear Rayleigh–Bénard convection between poorly conducting boundaries', J. Fluid Mech. **101**, 759–782 (1980).

[119] R. Ding and J. Li, 'Nonlinear finite-time Lyapunov exponent and predictability', Phys. Lett. A **364**, 396–400 (2007).

[120] A. Jayaraman, J. D. Scheel, H. S. Greenside and P. F. Fischer, 'Characterization of the domain chaos convection state by the largest Lyapunov exponent', Phys. Rev. E **74**, 016209 (2006).

[121] M. Xu and M. R. Paul, 'Spatiotemporal dynamics of the covariant Lyapunov vectors of chaotic convection', Phys. Rev. E **97**, 032216 (2018).

[122] R. Levanger, M. Xu, J. Cyranka, M. F. Schatz, K. Mischaikow and M. R. Paul, 'Correlations between the leading Lyapunov vector and pattern defects for chaotic Rayleigh-Bénard convection', Chaos **29**, 053103 (2019).

[123] H. G. Schuster and W. Just, *Deterministic chaos: an introduction*, 4th rev. and enl. ed. (Wiley-VCH, Weinheim, 2005).

[124] J. D. Scheel and M. C. Cross, 'Lyapunov exponents for small aspect ratio Rayleigh-Bénard convection', Phys. Rev. E **74**, 066301 (2006).

[125] D. A. Egolf, I. V. Melnikov, W. Pesch and R. E. Ecke, 'Mechanisms of extensive spatiotemporal chaos in Rayleigh–Bénard convection', Nature **404**, 733–736 (2000).

[126] A. N. Kolmogorov, 'The Local Structure of Turbulence in Incompressible Viscous Fluid for Very Large Reynolds Numbers', Proc. Math. Phys. Sci. **434**, 9–13 (1991).

[127] C. Gualtieri, A. Angeloudis, F. Bombardelli, S. Jha and T. Stoesser, 'On the Values for the Turbulent Schmidt Number in Environmental Flows', Fluids **2**, 17 (2017).

[128] S. Corrsin, 'On the Spectrum of Isotropic Temperature Fluctuations in an Isotropic Turbulence', J. Appl. Phys. **22**, 469–473 (1951).

[129] G. K. Batchelor, 'Small-scale variation of convected quantities like temperature in turbulent fluid Part 1. General discussion and the case of small conductivity', J. Fluid Mech. **5**, 113 (1959).

[130] J. Schumacher, 'Sub-Kolmogorov-scale fluctuations in fluid turbulence', Europhys. Lett. **80**, 54001 (2007).

[131] V. Valori and J. Schumacher, 'Connecting boundary layer dynamics with extreme bulk dissipation events in Rayleigh-Bénard flow', Europhys. Lett. **134**, 34004 (2021).

[132] K. Sreenivasan, 'Possible Effects of Small-Scale Intermittency in Turbulent Reacting Flows', Flow Turbul. Combust. **72**, 115–131 (2004).

[133] P. M. Sadler, R. R. Gould, P. S. Leiker, P. R. A. Antonucci, R. Kimberk, F. S. Deutsch, B. Hoffman, M. Dussault, A. Contos, K. Brecher and L. French, 'MicroObservatory Net: A Network of Automated Remote Telescopes Dedicated to Educational Use', J. Sci. Educ. Technol. **10**, 39–55 (2001).

[134] H. T. Rossby, 'A study of Bénard convection with and without rotation', J. Fluid Mech. **36**, 309–335 (1969).

[135] S. S. Hough, 'IX. On the Application of Harmonic Analysis to the Dynamical Theory of the Tides. — Part I. On Laplace's "Oscillations of the First Species," and on the Dynamics of Ocean Currents', Phil. Trans. R. Soc. Lond. A **189**, 201–257 (1897).

[136] J. Proudman, 'On the motion of solids in a liquid possessing vorticity', Proc. R. Soc. Lond. A **92**, 408–424 (1916).

[137] G. I. Taylor, 'Motion of solids in fluids when the flow is not irrotational', Proc. R. Soc. Lond. A **93**, 99–113 (1917).

[138] R. J. A. M. Stevens, J.-Q. Zhong, H. J. H. Clercx, G. Ahlers and D. Lohse, 'Transitions between Turbulent States in Rotating Rayleigh-Bénard Convection', Phys. Rev. Lett. **103**, 024503 (2009).

[139] T. Cai, K. L. Chan and H. G. Mayr, 'Deep, Closely Packed, Long-lived Cyclones on Jupiter's Poles', Planet. Sci. J. **2**, 81 (2021).

[140] R. J. A. M. Stevens, H. J. H. Clercx and D. Lohse, 'Optimal Prandtl number for heat transfer in rotating Rayleigh–Bénard convection', New J. Phys. **12**, 075005 (2010).

[141] D. H. Lenschow and B. B. Stankov, 'Length Scales in the Convective Boundary Layer', J. Atmos. Sci. **43**, 1198–1209 (1986).

[142] S. B. Pope, *Turbulent flows* (Cambridge University Press, Cambridge; New York, 2000).

[143] J. Paret and P. Tabeling, 'Experimental Observation of the Two-Dimensional Inverse Energy Cascade', Phys. Rev. Lett. **79**, 4162–4165 (1997).

[144] M. A. Rutgers, 'Forced 2D Turbulence: Experimental Evidence of Simultaneous Inverse Energy and Forward Enstrophy Cascades', Phys. Rev. Lett. **81**, 2244–2247 (1998).

[145] G. Boffetta, 'Energy and enstrophy fluxes in the double cascade of two-dimensional turbulence', J. Fluid Mech. **589**, 253–260 (2007).

[146] G. Boffetta and R. E. Ecke, 'Two-Dimensional Turbulence', Annu. Rev. Fluid Mech. **44**, 427–451 (2012).

[147] K. Julien, A. Rubio, I. Grooms and E. Knobloch, 'Statistical and physical balances in low Rossby number Rayleigh–Bénard convection', Geophys. Astro. Fluid **106**, 392–428 (2012).

[148] B. Favier, L. J. Silvers and M. R. E. Proctor, 'Inverse cascade and symmetry breaking in rapidly rotating Boussinesq convection', Phys. Fluids **26**, 096605 (2014).

[149] S. Musacchio and G. Boffetta, 'Condensate in quasi-two-dimensional turbulence', Phys. Rev. Fluids **4**, 022602 (2019).

[150] A. van Kan and A. Alexakis, 'Condensates in thin-layer turbulence', J. Fluid Mech. **864**, 490–518 (2019).

[151] M. Carbone and A. D. Bragg, 'Is vortex stretching the main cause of the turbulent energy cascade?', J. Fluid Mech. **883**, R2 (2020).

[152] P. L. Johnson, 'Energy Transfer from Large to Small Scales in Turbulence by Multiscale Nonlinear Strain and Vorticity Interactions', Phys. Rev. Lett. **124**, 104501 (2020).

[153] W. J. Bos, 'Three-dimensional turbulence without vortex stretching', J. Fluid Mech. **915**, A121 (2021).

[154] D. Lohse and K.-Q. Xia, 'Small-Scale Properties of Turbulent Rayleigh-Bénard Convection', Annu. Rev. Fluid Mech. **42**, 335–364 (2010).

[155] G. Falkovich, *Fluid mechanics: a short course for physicists* (Cambridge University Press, Cambridge, UK; New York, 2011).

[156] L. F. Richardson, *Weather Prediction by Numerical Process*, 1st ed. (Cambridge University Press, Cambridge, 1922).

[157] M. Voßkuhle, 'Statistische Analysen zweidimensionaler Turbulenz' (Westfälische Wilhelms-Universität Münster, Münster, 2009).

[158] K. R. Sreenivasan and G. Stolovitzky, 'Turbulent cascades', J. Stat. Phys. **78**, 311–333 (1995).

[159] M. K. Verma, *Energy Transfers in Fluid Flows: Multiscale and Spectral Perspectives* (Cambridge University Press, Cambridge; New York, NY, 2019).

[160] A. N. Kolmogorov, 'A refinement of previous hypotheses concerning the local structure of turbulence in a viscous incompressible fluid at high Reynolds number', J. Fluid Mech. **13**, 82–85 (1962).

[161] R. Fjørtoft, 'On the Changes in the Spectral Distribution of Kinetic Energy for Twodimensional, Nondivergent Flow', Tellus **5**, 225–230 (1953).

[162] R. H. Kraichnan, 'Inertial Ranges in Two-Dimensional Turbulence', Phys. Fluids **10**, 1417 (1967).

[163] L. Soucasse, B. Podvin, P. Rivière and A. Soufiani, 'Proper orthogonal decomposition analysis and modelling of large-scale flow reorientations in a cubic Rayleigh–Bénard cell', J. Fluid Mech. **881**, 23–50 (2019).

[164] C. Verbeeck, P. A. Higgins, T. Colak, F. T. Watson, V. Delouille, B. Mampaey and R. Qahwaji, 'A Multi-wavelength Analysis of Active Regions and Sunspots by Comparison of Automatic Detection Algorithms', Sol. Phys. **283**, 67–95 (2013).

[165] D. Choi, D. Banfield, P. Gierasch and A. Showman, 'Velocity and vorticity measurements of Jupiter's Great Red Spot using automated cloud feature tracking', Icarus **188**, 35–46 (2007).

[166] R. Lumpkin, T. Özgökmen and L. Centurioni, 'Advances in the Application of Surface Drifters', Annu. Rev. Mar. Sci. **9**, 59–81 (2017).

[167] J. M. C. Denissen, R. Orth, H. Wouters, D. G. Miralles, C. C. van Heerwaarden, J. V.-G. de Arellano and A. J. Teuling, 'Soil moisture signature in global weather balloon soundings', NPJ Clim. Atmos. Sci. **4**, 13 (2021).

[168] R. A. Preston, C. E. Hildebrand, G. H. Purcell, J. Ellis, C. T. Stelzried, S. G. Finley, R. Z. Sagdeev, V. M. Linkin, V. V. Kerzhanovich, V. I. Altunin, L. R. Kogan, V. I. Kostenko, L. I. Matveenko, S. V. Pogrebenko, I. A. Strukov, E. L. Akim, Y. N. Alexandrov, N. A. Armand, R. N. Bakitko, A. S. Vyshlov, A. F. Bogomolov, Y. N. Gorchankov, A. S. Selivanov, N. M. Ivanov, V. F. Tichonov, J. E. Blamont, L. Boloh, G. Laurans, A. Boischot, F. Biraud, A. Ortega-Molina, C. Rosolen and G. Petit, 'Determination of Venus Winds by Ground-Based Radio Tracking of the VEGA Balloons', Science **231**, 1414–1416 (1986).

[169] N. G. Stewart and R. N. Crooks, 'Long-Range Travel of the Radioactive Cloud from the Accident at Windscale', Nature **182**, 627–628 (1958).

[170] P. Ballereau, *Kyshtym riddle: possible kind of the accident*, CEA-BIB–244 (France, 1988).

[171] D. A. Wheeler, 'Atmospheric dispersal and deposition of radioactive material from Chernobyl', Atmos. Environ. **22**, 853–863 (1988).

[172] O. Masson, A. Baeza, J. Bieringer, K. Brudecki, S. Bucci, M. Cappai, F. Carvalho, O. Connan, C. Cosma, A. Dalheimer, D. Didier, G. Depuydt, L. De Geer, A. De Vismes, L. Gini, F. Groppi, K. Gudnason, R. Gurriaran, D. Hainz, Ó. Halldórsson, D. Hammond, O. Hanley, K. Holeý, Z. Homoki, A. Ioannidou, K. Isajenko, M. Jankovic, C. Katzlberger, M. Kettunen, R. Kierepko, R. Kontro, P. Kwakman, M. Lecomte, L. Leon Vintro, A.-P. Leppänen, B. Lind, G. Lujaniene, P. Mc Ginnity, C. M. Mahon, H. Malá, S. Manenti, M. Manolopoulou, A. Mattila, A. Mauring, J. Mietelski, B. Møller, S. Nielsen, J. Nikolic, R. Overwater, S. E. Pálsson, C. Papastefanou, I. Penev, M. Pham, P. Povinec, H. Ramebäck, M. Reis, W. Ringer, A. Rodriguez, P. Rulík, P. Saey, V. Samsonov, C. Schlosser, G. Sgorbati, B. V. Silobritiene, C. Söderström, R. Sogni, L. Solier, M. Sonck, G. Steinhauser, T. Steinkopff, P. Steinmann, S. Stoulos, I. Sýkora, D. Todorovic, N. Tooloutalaie, L. Tositti, J. Tschiersch, A. Ugron, E. Vagena, A. Vargas, H. Wershofen and O. Zhukova, 'Tracking of Airborne Radionuclides from the Damaged Fukushima Dai-Ichi Nuclear Reactors by European Networks', Environ. Sci. Technol. **45**, 7670–7677 (2011).

[173] G. Haller, 'Lagrangian Coherent Structures', Annu. Rev. Fluid Mech. **47**, 137–162 (2015).

[174] A. Klünker, C. Schneide, A. Pandey, K. Padberg-Gehle and J. Schumacher, 'Lagrangian perspectives on turbulent superstructures in Rayleigh-Bénard convection', Proc. Appl. Math. Mech. **19**, e201900201 (2019).

[175] R. Banisch, P. Koltai and K. Padberg-Gehle, 'Network measures of mixing', Chaos **29**, 063125 (2019).

[176] M. R. Allshouse and T. Peacock, 'Lagrangian based methods for coherent structure detection', Chaos **25**, 097617 (2015).

[177] A. Hadjighasem, M. Farazmand, D. Blazevski, G. Froyland and G. Haller, 'A critical comparison of Lagrangian methods for coherent structure detection', Chaos **27**, 053104 (2017).

[178] G. Froyland and K. Padberg-Gehle, 'A rough-and-ready cluster-based approach for extracting finite-time coherent sets from sparse and incomplete trajectory data', Chaos **25**, 087406 (2015).

[179] M. R. Maxey, 'Equation of motion for a small rigid sphere in a nonuniform flow', Phys. Fluids **26**, 883 (1983).

[180] L.-P. Wang, B. Rosa, H. Gao, G. He and G. Jin, 'Turbulent collision of inertial particles: Point-particle based, hybrid simulations and beyond', Int. J. Multiphas. Flow **35**, 854–867 (2009).

[181] P. Maity, R. Govindarajan and S. S. Ray, 'Statistics of Lagrangian trajectories in a rotating turbulent flow', Phys. Rev. E **100**, 043110 (2019).

[182] B. L. Sawford, P. K. Yeung and J. F. Hackl, 'Reynolds number dependence of relative dispersion statistics in isotropic turbulence', Phys. Fluids **20**, 065111 (2008).

[183] C. Schneide, A. Pandey, K. Padberg-Gehle and J. Schumacher, 'Probing turbulent superstructures in Rayleigh-Bénard convection by Lagrangian trajectory clusters', Phys. Rev. Fluids **3**, 113501 (2018).

[184] G. Elsinga, T. Ishihara and J. Hunt, 'Non-local dispersion and the reassessment of Richardson's t^3-scaling law', J. Fluid Mech. **932**, A17 (2022).

[185] S. Moller, C. Resagk and C. Cierpka, 'Long-time experimental investigation of turbulent superstructures in Rayleigh–Bénard convection by noninvasive simultaneous measurements of temperature and velocity fields', Exp. Fluids **62**, 64 (2021).

[186] S. Moller, 'Experimental characterization of turbulent superstructures in large aspect ratio Rayleigh-Bénard convection', PhD thesis (TU Ilmenau, Ilmenau, Germany, 2022).

[187] D. R. Durran, 'The Third-Order Adams-Bashforth Method: An Attractive Alternative to Leapfrog Time Differencing', Mon. Weather Rev. **119**, 702–720 (1991).

[188] P. Götzfried, M. S. Emran, E. Villermaux and J. Schumacher, 'Comparison of Lagrangian and Eulerian frames of passive scalar turbulent mixing', Phys. Rev. Fluids **4**, 044607 (2019).

[189] I. Goodfellow, Y. Bengio and A. Courville, *Deep learning*, Adaptive Computation and Machine Learning (The MIT Press, Cambridge, Massachusetts, 2016).

[190] B. Mehlig, *Machine Learning with Neural Networks: An Introduction for Scientists and Engineers*, 1st ed. (Cambridge University Press, Cambridge, 2021).

[191] A. Hadjighasem, D. Karrasch, H. Teramoto and G. Haller, 'Spectral-clustering approach to Lagrangian vortex detection', Phys. Rev. E **93**, 063107 (2016).

[192] C. Schneide, M. Stahn, A. Pandey, O. Junge, P. Koltai, K. Padberg-Gehle and J. Schumacher, 'Lagrangian coherent sets in turbulent Rayleigh-Bénard convection', Phys. Rev. E **100**, 053103 (2019).

[193] G. Froyland, C. P. Rock and K. Sakellariou, 'Sparse eigenbasis approximation: Multiple feature extraction across spatiotemporal scales with application to coherent set identification', Commun. Nonlinear Sci. **77**, 81–107 (2019).

[194] J. de la Porte, B. M. Herbst, W. Heremann and S. van der Walt, 'An Introduction to Diffusion Maps', in Proc. Ninet. Annu. Symp. Pattern Recognit. Assoc. South Afr. (2008), pp. 15–25.

[195] R. Kondor and J. D. Lafferty, 'Diffusion Kernels on Graphs and Other Discrete Input Spaces', in Proc. Ninet. Int. Conf. Mach. Learn. (2002), pp. 315–322.

[196] R. Banisch and P. Koltai, 'Understanding the geometry of transport: Diffusion maps for Lagrangian trajectory data unravel coherent sets', Chaos **27**, 035804 (2017).

[197] P. Koltai and S. Weiss, 'Diffusion maps embedding and transition matrix analysis of the large-scale flow structure in turbulent Rayleigh–Bénard convection', Nonlinearity **33**, 1723–1756 (2020).

[198] R. R. Coifman, S. Lafon, A. B. Lee, M. Maggioni, B. Nadler, F. Warner and S. W. Zucker, 'Geometric diffusions as a tool for harmonic analysis and structure definition of data: Diffusion maps', Proc. Natl. Acad. Sci. U.S.A. **102**, 7426–7431 (2005).

[199] R. R. Coifman and S. Lafon, 'Diffusion maps', Appl. Comput. Harmon. A. **21**, 5–30 (2006).

[200] D. Wagner and F. Wagner, 'Between Min Cut and Graph Bisection', in Proc. 18th Int. Symp. Math. Found. Comput. Sci. 1993, Vol. 711, Lecture Notes in Computer Science (1993), pp. 744–750.

[201] J. Shi and J. Malik, 'Normalized cuts and image segmentation', IEEE Trans. Pattern Anal. Machine Intell. **22**, 888–905 (2000).

[202] R. V. Donner, Y. Zou, J. F. Donges, N. Marwan and J. Kurths, 'Ambiguities in recurrence-based complex network representations of time series', Phys. Rev. E **81**, 015101 (2010).

[203] Y. Chi, X. Song, D. Zhou, K. Hino and B. L. Tseng, 'Evolutionary Spectral Clustering by Incorporating Temporal Smoothness', in Proc. 13th ACM SIGKDD Int. Conf. Knowl. Discov. Data Min. KDD-07 (2007), pp. 153–162.

[204] A. Loesch and R. du Puits, 'The Barrel of Ilmenau: A large-scale convection experiment to study dust devil-like flow structures.', Meteorol. Z. **30**, 89–97 (2021).

[205] S. Sharma, G. Marcucci and A. Mahmud, *A complexity perspective on fluid mechanics*, 2022.

[206] Y. Ben-Ami and A. Manela, 'Effect of heat-flux boundary conditions on the Rayleigh-Bénard instability in a rarefied gas', Phys. Rev. Fluids **4**, 033402 (2019).

[207] N. J. Wagner and J. F. Brady, 'Shear thickening in colloidal dispersions', Phys. Today **62**, 27–32 (2009).

[208] B. Fox-Kemper, S. Bachman, B. Pearson and S. Reckinger, 'Principles and advances in subgrid modelling for eddy-rich simulations', CLIVAR Exch. **65**, 42–46 (2014).

[209] H. Hewitt, B. Fox-Kemper, B. Pearson, M. Roberts and D. Klocke, 'The small scales of the ocean may hold the key to surprises', Nat. Clim. Change **12**, 496–499 (2022).

[210] S. Tobias, 'The turbulent dynamo', J. Fluid Mech. **912**, P1 (2021).

[211] B. Fox-Kemper, R. Ferrari and R. Hallberg, 'Parameterization of Mixed Layer Eddies. Part I: Theory and Diagnosis', J. Phys. Oceanogr. **38**, 1145–1165 (2008).

[212] P. Virtanen et al., 'SciPy 1.0: fundamental algorithms for scientific computing in Python', Nat. Methods **17**, 261–272 (2020).

[213] C. R. Harris, K. J. Millman, S. J. van der Walt, R. Gommers, P. Virtanen, D. Cournapeau, E. Wieser, J. Taylor, S. Berg, N. J. Smith, R. Kern, M. Picus, S. Hoyer, M. H. van Kerkwijk, M. Brett, A. Haldane, J. F. del Río, M. Wiebe, P. Peterson, P. Gérard-Marchant, K. Sheppard, T. Reddy, W. Weckesser, H. Abbasi, C. Gohlke and T. E. Oliphant, 'Array programming with NumPy', Nature **585**, 357–362 (2020).

[214] J. D. Hunter, 'Matplotlib: A 2D Graphics Environment', Comput. Sci. Eng. **9**, 90–95 (2007).

Index

The picture on the cover visualises the instantaneous temperature field within the upper thermal boundary layer of the weakly rotating thermal convection simulation Nfs4_Ro30. The width captures the entire periodic domain with aspect ratio 60.